



Mother Pelican

A Journal of Solidarity and Sustainability

Vol. 18, No. 7, July 2022
Luis T. Gutiérrez, Editor

[Home Page](#)
[Front Page](#)



Social Unsustainability: The Case of Slum Societies

Arup Kanti Konar

July 2022

Abstract: Unsustainability is two dimensional: it encompasses both ecological unsustainability and social unsustainability. Some authors have added one more dimension of unsustainability such as economic unsustainability. But this is incorrect, because economic dimension is included in the social dimension. Unsustainability is a matter of degree, and social unsustainability indicates the quality of the societies. The theoretical and practical concept of social unsustainability has been ignored. Social unsustainability is being aggravated due to the exponential growth of the informal sector in the developing countries. But, first of all, we should know what social unsustainability is and how it is manifested in urban slum societies.

Key Words: Society, Ecology, Nature, Culture, Sustainability, Unsustainability, Stability, Instability

Unsustainability entails ecologically unsustainable social instability, which, in other words, implies the coexistence of persistent social instability and emerging ecological instability *ceteris paribus*. Since every word has its opposite polarity, so sustainability means ecologically sustainable social stability, which, in other words, implies the coexistence of social stability and ecological stability *ceteris paribus*.

Social means what is not natural. It has become both adjective and noun. Further, it is being used in normative (e.g. what we ought to do) and positive sense (e.g. what we do). It consists of various "sub-socials" such as political, economic, psychological, religious, cultural, ethical, spiritual, moral, familial, sexual, gender, scientific, technological, legal, demographic, democratic, marital, etc.

Ecological instability is indicated by depreciation, depletion, degradation, and/or destruction of ecological/natural resources, assets or capital. Social instability consists of various sub-social instabilities such as political instability, economic instability, psychological instability, religious instability, cultural instability, ethical instability, spiritual instability, moral instability, familial instability, sexual instability, gender instability, scientific instability, technological instability, legal instability, demographic instability, democratic instability, marital instability, etc. Social instability is indicated by poverty, unemployment, starvation, malnutrition, inequality (of income, wealth and rights), illiteracy, insecurity, lack of basic needs (food, housing and clothing), injustice, inequity, corruption, killing, lynching, assassination, torture, oppression, subjugation, violence (against women), rape, molestation, tyranny, child-labour, prostitution, trafficking, kidnapping, suicide, witch-hunting, conflict, crime, militarization, war, fundamentalism (religious, cultural, etc) and so forth.

Many authors have written about social sustainability. Alphabetically, the examples of such authors are as follows: Agyeman and Evans (2004); Casula Vifell and Soneryd (2012); Cuthill (2009); Davidson (2009); Dempsey, Bramley, Power and Brown (2011); Dillard, Dujon and King, (2009); Fotzpatrick (2011); Larsen (2009); Lehtonen (2004); Littig and Griessler (2005); Magis and Shinn (2009); Nordstrom Kallstrom and Ljung (2005); Omann and Spangenberg (2002); Pawlowski (2007); Seghezzo (2009); Thin, Lockhart and Yaron (2002); Turkington and Sangster (2006). Further, the Special Issue of the journal: *Sustainability: Science, Practice & Policy* (Volume 8, Issue 12, Winter 2012) is devoted to the discussion of "A Missing Pillar? Challenges in Theorizing and Practicing Social Sustainability", in which there are ten articles.

But, there is hardly any author who has written about social unsustainability. Perhaps, he/she

has not seen or observed with his/her own eyes how social unsustainability is. Fortunately, I have discovered an article on social unsustainability by Sultan Qaboos University Professor, Arif Saeed Malik (2018).

If any author wants to know about social unsustainability, he/she should see with his/her own "eyes and heart" the life and living condition of urban slum societies in developing countries. In some developing countries, as much as 90% of the urban population live in slum society. One in three urban residents lives in slum society in developing countries. One in seven people on the planet currently lives in slum society. The slum population of India exceeds the total population of UK. World's largest slum societies, for example, are Khayelitsha in Cape Town (South Africa), Kibera in Nairobi (Kenya), Dharavi in Mumbai (India), Orangi Town in Karachi (Pakistan). The intensity of social unsustainability of the slum society is unprecedented due to lack of basic needs of their day to day life. They are socially deprived and the poorest of the poor section of urban society.

Social unsustainability can be reduced or ruled out by the following ways:

1. Provision of basic needs (food, housing, clothing, etc).
2. Equitable distribution of income and wealth.
3. Arrangement for intra-generational and inter-generational justice among gender, race, class, etc.
4. Equality of rights, including human rights, land users' rights, tenants' rights, indigenous people's rights, etc.
5. Establishment or promotion of democracy.
6. Establishment of peace.
7. Eradication of poverty.
8. Provision of people's meaningful participation in all aspects of state governance.
9. Elimination of corruption in politics at all levels.
10. Implementation of effective measures for addressing the impact of climate change and reducing greenhouse gas emissions.
11. Arrangement for adequate investment in research and development in order to promote sustainable development based on the needs and priorities.
12. Engagement of local people in planning, implementation and monitoring for the management of natural resources.
13. Investment in alternative energy sources.
14. Development of civil society and social capital.
15. Promotion of quality of life, happiness and well-being.

Social unsustainability and ecological unsustainability are not independent, rather, they are interdependent. If we know the way of reducing or ruling out the unprecedented unsustainability of the slum society, then we will be able to reduce or rule out the global social unsustainability.

The terms like welfare, wellbeing, development, prosperity, happiness, quality of life, standard of living, etc. are pointless to the slum society, because the people of slum society do not even know what the standard of life is. The deplorable and pathetic condition of the slum society is the best example of global social unsustainability.

References

- Agyeman, J. & Evans, B. (2004). Just sustainability: The emerging discourse of environmental justice in Britain? *Geographical Journal*, 170(2), 155-164. <https://www.jstor.org/stable/3451592>
- Casula Vifell, A. & Soneryd, L. (2012). Organizing matters: How the "social dimension" gets lost in sustainability projects. *Sustainable Development*, 20(1), 18-27. <https://doi.org/10.1002/sd.461>
- Cuthill, M. (2009). Strengthening the "social" in sustainable development: Developing a conceptual framework for social sustainability in a rapid urban growth region in Australia. *Sustainable Development*, 18(6), 362-373. <http://doi.org/10.1002/sd.397>
- Davidson, M. (2009). Social sustainability: A potential for politics? *Local Environment*, 14(7), 607-619. <https://doi.org/10.1080/13549830903089291>
- Dempsey, N., Bramley, G., Power, S. & Brown, C. (2011). The social dimension of sustainable development: Defining urban social sustainability. *Sustainable Development*, 19(5), 289-300. <https://doi.org/10.1002/sd.417>

Dillard, J., Dujon, V. & King, M. (Eds.)(2009). *Understanding the social dimension of sustainability*. New York: Routledge. <https://www.routledge.com>

Fotzpatrick, T. (Ed.)(2011). *Understanding the environment and social policy*. Bristol: Policy Press. <https://policy.bristoluniversitypress.co.uk>

Larsen, L. (2009). An inquiry into the theoretical basis sustainability: Ten propositions. In J. Dillard, V. Dujon & M. King(Eds.), *Understanding the social dimension of sustainability*, pp. 45-82. New York: Routledge. <https://www.routledge.com/Understanding-the-Social-Dimension-Of-Sustainability/Dillard-Dujon-King/p/book/9780415536677>

Lehtonen, M. (2004). The environmental-social interface of sustainable development: Capabilities, social capital, institutions. *Ecological Economics*, 49(2), 199-214. <https://www.sciencedirect.com/science/article/abs/pii/S092180090400076X>

Littig, B. & Griessler, E. (2005). Social sustainability: A catchword between political pragmatism and social theory. *International Journal of Sustainable Development*, 8(1-2), 65-79. <https://www.inderscienceonline.com/doi/abs/10.1504/IJSD.2005.007375>

Magis, K. & Shinn, C. (2009). Emergent principles of social sustainability. In J. Dillard, V. Dujon & M. King(Eds.), *Understanding the social dimension of sustainability*, pp. 15-44. New York: Routledge. <https://www.routledge.com/Understanding-the-Social-Dimension-Of-Sustainability/Dillard-Dujon-King/p/book/9780415536677>

Malik, A. (2018). The main driver of social unsustainability and its remedy. *International Journal of Social Economics*, 45(6), 973-988. <https://www.emerald.com/insight/content/doi/10.1108/IJSE-01-2017-0005/full/html>

Nordstrom Kallstrom, H. & Ljung, M. (2005). Social sustainability and collaborative learning. *Ambio*, 34(4-5), 376-382. [https://bioone.org/journals/ambio-a-journal-of-the-human-environment/volume-34/issue-4/0044-7447_2005_034_0376_SSACL_2.0.CO_2/Social-Sustainability-and-Collaborative-Learning/10.1579/0044-7447\(2005\)034\[0376:SSACL\]2.0.CO;2.short](https://bioone.org/journals/ambio-a-journal-of-the-human-environment/volume-34/issue-4/0044-7447_2005_034_0376_SSACL_2.0.CO_2/Social-Sustainability-and-Collaborative-Learning/10.1579/0044-7447(2005)034[0376:SSACL]2.0.CO;2.short)

Omann, I. & Spangenberg, J. (2002). Assessing social sustainability: The social dimension of sustainability in a socio-economic scenario. Seventh Biennial Conference of the International Society for Ecological Economics. March 6-9, Sousse, Tunisia. <https://citeseerx.ist.psu.edu/viewdoc/download?doi=10.1.1.201.987&rep=rep1&type=pdf>

Pawlowski, A. (2007). How many dimensions does sustainable development have? *Sustainable Development*, 16(2), 81-90. <https://onlinelibrary.wiley.com/doi/10.1002/sd.339>

Seghezze, L. (2009). The five dimensions of sustainability. *Environmental Politics*, 18(4), 539-556. <https://www.tandfonline.com/doi/full/10.1080/09644010903063669>

Thin, N. Lockhart, C. & Yaron, G. (2002). *Conceptualizing socially sustainable development*. London: Department for International Development and World Bank. (Link is unavailable)

Turkington, R. & Sangster, K. (2006). From housing to social mix: Housing's contribution to social sustainability. *Town and Country Planning*, 75(6), 184-185. (Link is unavailable)

ABOUT THE AUTHOR

Arup Kanti Konar, PhD, is Principal & Associate Professor of Economics, Achhruram Memorial College, Sidho-Kanho-Birsha University, Jhalda, Purulia West Bengal, India.

[| Back to Title |](#)

[LINK TO THE CURRENT ISSUE](#)

[LINK TO THE HOME PAGE](#)

"A mind at peace does not engender wars."

Sophocles (497-406 BCE)

FREE SUBSCRIPTION



GROUP COMMANDS AND WEBSITES

Write to the [Editor](#)
Send email to [Subscribe](#)
Send email to [Unsubscribe](#)
Link to the [Group Website](#)
Link to the [Home Page](#)



Page 3

Subscribe to the
Mother Pelican Journal
via the Solidarity-Sustainability Group
[Enter your email address:](#)

Inverse exchange bias effects and magnetoelectric coupling of the half-doped perovskite-type chromites $\text{Gd}_{0.5}\text{Sr}_{0.5}\text{CrO}_3$ and $\text{Gd}_{0.5}\text{Ca}_{0.5}\text{CrO}_3$

Biswajit Dalal ^{1,*} Xun Kang,^{1,2} Yoshitaka Matsushita ³ Alexei A. Belik ¹
Yoshihiro Tsujimoto ^{1,2} and Kazunari Yamaura ^{1,2,†}

¹International Center for Materials Nanoarchitectonics (WPI-MANA), National Institute for Materials Science, Namiki 1-1, Tsukuba, Ibaraki 305-0044, Japan

²Graduate School of Chemical Sciences and Engineering, Hokkaido University, North 10 West 8, Kita-ku, Sapporo, Hokkaido 060-0810, Japan

³Materials Analysis Station, National Institute for Materials Science, 1-2-1 Sengen, Tsukuba, Ibaraki 305-0047, Japan



(Received 28 May 2022; revised 31 July 2022; accepted 9 September 2022; published 21 September 2022)

The Cr^{4+} oxidation state with two electrons in the Cr $3d$ shell is not often observed in perovskite-type oxides, as high pressures and temperatures are generally required to stabilize the octahedral coordination. Herein, we present a comparative study of the half-doped perovskite-type chromites $\text{Gd}_{0.5}\text{Sr}_{0.5}\text{CrO}_3$ (GSCO) and $\text{Gd}_{0.5}\text{Ca}_{0.5}\text{CrO}_3$ (GCCO). Fifty percent of the Cr occurs in the Cr^{4+} oxidation state after high-pressure synthesis at 6 GPa and 1200 °C. The materials were investigated using synchrotron x-ray diffraction, magnetization, heat capacity, and dielectric measurements. The diffraction patterns show that GSCO and GCCO crystallize in orthorhombic ($Pnma$) structures with different degrees of local lattice distortion. GSCO exhibits a long-range magnetic order at temperatures of < 98 K, accompanied by magnetization reversal, suggesting that the magnetic ground state is ferrimagnetic. In contrast, GCCO displays antiferromagnetic characters at temperatures $< \sim 100$ K. In addition, GSCO exhibits a crossover between conventional and inverse exchange bias effects at low temperatures (< 50 K). This is likely caused by asymmetric exchange Dzyaloshinskii-Moriya interactions between the Cr ions of different valences ($+3$ and $+4$). Furthermore, significant magnetoelectric coupling at the onset of the magnetic order is supported by temperature-dependent dielectric measurements.

DOI: [10.1103/PhysRevB.106.104425](https://doi.org/10.1103/PhysRevB.106.104425)

I. INTRODUCTION

Perovskite-type orthochromite $R\text{CrO}_3$, where R is a rare-earth element, receives considerable attention owing to its potential applications and unique physical properties, such as negative magnetization, temperature- and field-induced fast spin switching, spin reorientation, field-induced switchable polarization, magnetoelectric effects, spin-driven ferroelectricity, magnetoelastic coupling, and exchange bias (EB) and giant magnetocaloric effects [1–14]. Most orthochromites crystallize in perovskite-type orthorhombic structures (space groups of $Pnma$ or $Pbnm$) and exhibit canted antiferromagnetic (AFM) orders. An antisymmetric exchange Dzyaloshinskii-Moriya (DM) interaction causes a weak ferromagnetic (FM) component between the Cr^{3+} spins to manifest at temperatures below the AFM transition (Néel) temperature (T_N) [15,16]. Superexchange interactions through the $\text{Cr}^{3+}\text{--O--Cr}^{3+}$ bond likely cause the AFM order, and complex, anisotropic interactions between R^{3+} and Cr^{3+} may cause unusual physical phenomena, e.g., the polar order of $R\text{CrO}_3$ may be primarily caused by $R\text{--Cr}$ exchange striction (i.e., an exchange field between the R ion and Cr sublattice) [6].

Furthermore, the onset temperatures of spin-driven ferroelectricity and long-range AFM order of all $R\text{CrO}_3$ remain within the range 110–290 K, regardless of the ionic radius of R^{3+} [7,12].

GdCrO_3 undergoes a canted AFM transition at a T_N of 167 K, with negative magnetization, spin reorientation, and field-induced polar order. These complex features are likely caused by interactions between two magnetic elements, Gd^{3+} ($4f^7$) and Cr^{3+} ($3d^3$) [2,5,6]. In addition, spontaneous spin reorientation of the ordered Cr sublattice occurs at 7 K [2,5]. The DM interactions and strong AFM coupling between Gd moments and Cr sublattices may lead to negative magnetization at a specific compensation temperature (T_{comp}). Recently, an unusual EB effect and fast spin switching were observed in single-crystal GdCrO_3 [17], which exhibited a giant magnetocaloric effect and temperature-induced magnetization jump [18,19]. Owing to these multiple anomalies, additional studies of GdCrO_3 are required to clarify its fundamental nature.

Half-doped perovskite-type transition metal oxides, such as manganite and cobaltite, were extensively investigated over recent decades owing to their strong intercorrelations among various characteristics—spin, charge, orbital, and lattice [20–24]. Studies of half-doped manganite ($\text{La}_{0.5}\text{Ca}_{0.5}\text{MnO}_3$) were conducted by Wollan and Koehler [25] and Goodenough [26]. The charge-exchanged AFM ground state was associated with the spatial order of the $\text{Mn}^{3+}/\text{Mn}^{4+}$ ions localized

*b.dalal.iitd@gmail.com

†YAMAURA.kazunari@nims.go.jp

in alternate planes. The most notable discovery to date is the colossal magnetoresistance of mixed-valence manganite $\text{Pr}_{0.5}\text{Sr}_{0.5}\text{MnO}_3$ [27], with significant competition between the FM metal and AFM insulator states [28]. Notably, however, there are contradictory reports regarding the origin of the colossal magnetoresistance [29–33].

In addition, half-doped manganites exhibit various phenomena, including double-exchange ferromagnetism, metal-insulator transitions, Griffiths phases, charge-order-driven ferroelectricity, strong magnetoelectric coupling, magnetodielectric and EB effects, and magnetoelectric phase separation [34–44]. Conversely, half-doped cobaltites exhibit unconventional phase transitions and unexpected properties, such as spin-state transitions, spin reorientations, valence-state and photoinduced metal-insulator transitions, and charge transfer [45–52].

The syntheses of half-doped manganites and cobaltites with perovskite structures and Mn^{4+} and Co^{4+} in octahedral coordination yield compounds with unprecedented physical properties. However, the synthesis of half-doped chromite receives less attention, likely because high pressures and temperatures are required to stabilize Cr^{4+} in octahedral coordination within the perovskite-type structure. We thus investigated $\text{Gd}_{0.5}\text{A}_{0.5}\text{CrO}_3$, where $A = \text{Sr}$ or Ca , using a high-pressure and high-temperature method, as half-doped alkaline-earth metal ions could cause distinct electrical transport and magnetic phenomena, such as, semiconducting and ferrimagnetic (FiM) ground state, magnetic frustration associated with competing AFM and FiM/FM interactions, magnetostriction, inverse EB effect, and magnetoelectric coupling accompanying with the ferroelectric relaxorlike state.

In this paper, we reveal the magnetic and electric properties of two half-doped chromites, $\text{Gd}_{0.5}\text{Sr}_{0.5}\text{CrO}_3$ (GSCO) and $\text{Gd}_{0.5}\text{Ca}_{0.5}\text{CrO}_3$ (GCCO), which were synthesized at 6 GPa and 1200 °C. GSCO exhibited a FiM ground state, whereas GCCO exhibited an AFM ground state. In addition, GSCO exhibited magnetization reversal, non-Griffith-like clustered FM features at temperatures of $> T_{\text{FiM}}$ (FiM transition temperature), and inverse EB effects. Furthermore, temperature-dependent permittivity studies revealed magnetoelectric coupling in GSCO and GCCO.

II. EXPERIMENTAL DETAILS

Polycrystalline GSCO and GCCO were synthesized via a solid-state reaction using powders of Gd_2O_3 , SrO (prepared using SrCO_3 by heating at 1300 °C in oxygen), CaO (prepared using CaCO_3 by heating at 1300 °C in oxygen), Cr_2O_3 , and CrO_2 . The powders were thoroughly mixed in an agate mortar in a stoichiometric ratio in an Ar-filled glovebox. Each mixture was sealed in a Pt capsule and loaded into a multi-anvil press (CTF-MA1500P, C&T Factory, Tokyo, Japan), and the capsule was compressed statically and isotropically at a pressure of 6 GPa at 1200 °C for 1 h (temperature ramping required 12 min). After heating, the capsule was quenched to a temperature of < 100 °C within 1 min, and the pressure was gradually released over several hours. The resulting material was a dense, polycrystalline, black pellet. A sample was finely ground for use in phase identification using a MiniFlex600

x-ray diffractometer (Rigaku, Tokyo, Japan) with $\text{Cu K}\alpha$ radiation.

Finely ground powders were used in synchrotron x-ray diffraction (XRD) at temperatures between 120 and 750 K using a large Debye-Scherrer camera at the BL15XU beamline at SPring-8, Sayo, Japan [53,54]. The wavelength of the synchrotron XRD was 0.65297 Å, calibrated using a standard material CeO_2 . Synchrotron XRD data were analyzed via the Rietveld method [55] using RIETAN-FP [56] and MAUD software [57]. Crystal structure was drawn using VESTA software [58].

The direct current (dc) magnetic susceptibilities (χ) of the materials were measured using a superconducting quantum interference device magnetometer (MPMS, Quantum Design, San Diego, CA, USA). To correct for the stray magnetic field of the superconducting magnet, the magnet was degaussed before each measurement. Measurements were conducted in the temperature range 2–350 K at various applied magnetic fields (H) under zero-field-cooled (ZFC) and field-cooled (FC) conditions. Isothermal magnetization loops were collected at various temperatures in the magnetic field range ± 70 kOe. The alternating current (ac) χ of GSCO was measured at 5–350 K using the same instrument. The reproducibility of GSCO and GCCO magnetic data was verified using a set of materials prepared in different high-pressure runs.

The electrical resistivity (ρ) of a polycrystalline material was measured as a function of temperature via a 4-probe method using a physical property measurement system (PPMS, Quantum Design). The electrical contacts on the bar-shaped material comprised Au wires and Ag epoxy. The temperature-dependent specific heat capacity (C_{total}) was measured using a thermal relaxation method under a zero field or an applied field of 90 kOe in the PPMS at temperatures of 2–300 K. We used an Apiezon-N grease to thermally connect the material to the holder stage.

The dielectric properties were measured at temperatures of 5–300 K using an Alpha-A high-performance frequency analyzer (Novocontrol Technologies, Montabaur, Germany) in the frequency range 100 Hz–2 MHz at $H = 0$ or 90 kOe in the PPMS. During the measurement of GSCO, an extrinsic contribution to the dielectric constant was observed between 220 and 270 K, which was likely due to ice. However, the extrinsic contribution was no longer observed under a much higher vacuum [59]. The deviation between the material and system temperatures under a high vacuum became significant at < 50 K. Therefore, we combined the data measured under normal and high-vacuum conditions to confirm the dielectric behavior of the material.

III. RESULTS AND DISCUSSION

A. Crystal structure

The crystal structures of GSCO and GCCO at room temperature (~ 297 K) were investigated via synchrotron XRD and data analysis using the Rietveld method, as shown in Figs. 1(a) and 1(b), respectively. Based on the structure of RCrO_3 at room temperature, we initially refined the crystal structure of GSCO using a distorted orthorhombic model ($Pbnm$ or its axial transformed standard setting $Pnma$, No.

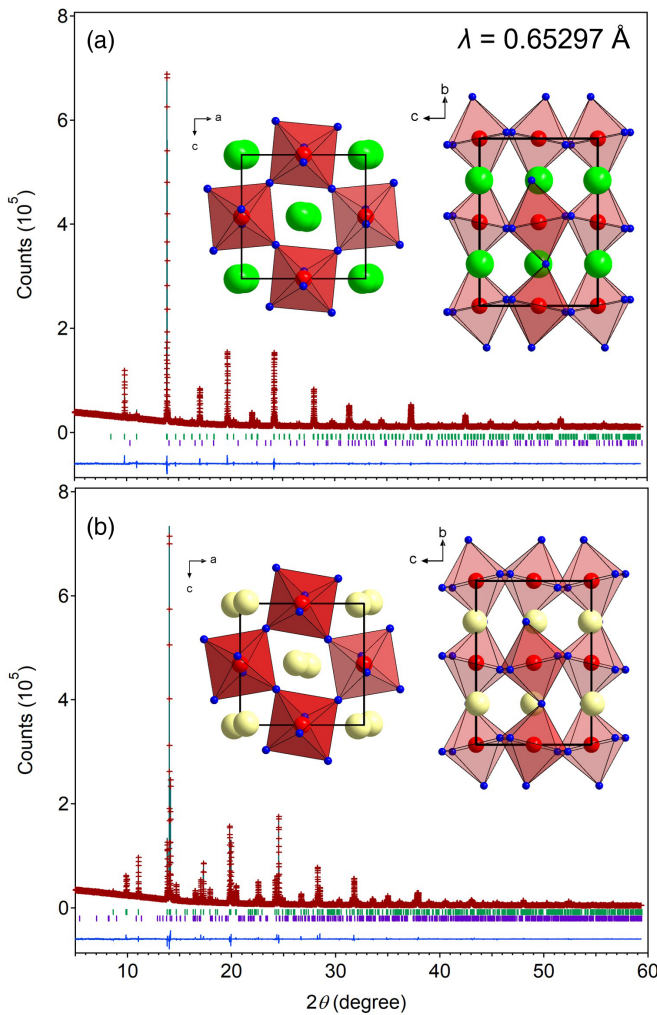


FIG. 1. Rietveld refinement of the synchrotron x-ray diffraction (XRD) patterns of (a) GSCO and (b) GCCO collected at room temperature. The crosses and solid red lines represent the observed and calculated patterns, respectively, with the differences (solid blue lines) shown at the bottom. The vertical ticks indicate the positions of the allowed Bragg reflections. The upper (olive) and bottom (magenta) rows indicate the reflections of the main and secondary phases, respectively. The lattice parameters are $a = 5.41289(2)$ Å, $b = 7.63652(2)$ Å, and $c = 5.39966(2)$ Å for GSCO ($Pnma$), and $a = 5.42543(1)$ Å, $b = 7.54252(1)$ Å, and $c = 5.31059(1)$ Å for GCCO ($Pnma$). The secondary phase is Cr_2O_3 (1.7 wt. %) for GSCO and CaCr_2O_4 (2.5 wt. %) for GCCO. The unit cell of each material is shown as an inset. Green, yellow, blue, and red balls denote Gd/Sr, Gd/Ca, O, and Cr, respectively.

62) and a cubic $Pm\bar{3}m$ model (No. 221). Additionally, we tested a monoclinic $P2_1/c$ model (No. 14) because $P2_1/c$ is in a lower-symmetry subgroup of $Pnma$ and is often observed in double-perovskite materials. As shown in Fig. 1(a), the analysis is successful, indicating that the $Pnma$ model better describes the crystal structure of GSCO. The refined lattice parameters are $a = 5.41289(2)$ Å, $b = 7.63652(2)$ Å, and $c = 5.39966(2)$ Å. The atomic coordinates and isotropic thermal displacement parameters are shown in Table S1 in the Supplemental Material [60]. The inset of Fig. 1(a) shows a structural image of GSCO.

Considering the observed refined tendencies, when we refined the occupation factors for oxygen, the values were slightly > 1 ; the oxygen site is likely occupied fully. Thus, it was reasonable to fix the value to be 1 in the final step. Although the observed pattern was refined to a certain extent using the $P2_1/c$ model, the analysis was unsatisfactory. Detailed inspection, particularly temperature dependence, the standard errors for β angle, and volume increased significantly with temperature. This indicated that GSCO did not crystallize in a monoclinic double-perovskite-based structure with a rock salt-type order.

Meanwhile, GCCO is analyzed well using the orthorhombic $Pnma$ model, which is common in most RCrO_3 materials. Notably, refining the pattern of GCCO using the monoclinic model ($P2_1/c$) failed. Because the end members GdCrO_3 [6] and CaCrO_3 [61] crystallize in the orthorhombic structure ($Pbnm$), GCCO may be regarded as a solid solution. In addition, several small peaks in the synchrotron XRD pattern indicate the presence of 2.5 wt. % orthorhombic CaCr_2O_4 [62]. Rietveld analysis refines the lattice parameters of GCCO and the overall scale factor simultaneously, but the structural parameters of the minor phase remain constant. The final analyzed synchrotron XRD pattern of GCCO is shown in Fig. 1(b), and detailed crystallographic data is shown in Table S2 in the Supplemental Material [60]. The refined lattice parameters are $a = 5.42543(1)$ Å, $b = 7.54252(1)$ Å, and $c = 5.31059(1)$ Å. For comparison, the inset of Fig. 1(b) shows a structural image of GCCO. The overall structure is similar for GSCO and GCCO at this image scale, but the structure has different degrees of local lattice distortion. For example, the Cr–O lengths of the CrO_6 octahedron differ by 0.25% in GSCO and 1.7% in GCCO.

Furthermore, synchrotron XRD patterns were collected at various temperatures from 120 to 750 K to investigate the temperature dependences of the structural properties of GSCO and GCCO. However, neither a change in symmetry nor any additional features were observed. The changes in the lattice parameters of GSCO and GCCO with temperature are shown in Figs. S1(a)–(b) and S1(c)–(d) in the Supplemental Material [60], respectively. All GSCO lattice parameters increase with increasing temperature, exhibiting the expected thermal behavior. The lattice parameters a and c almost converge at ~ 750 K (Fig. S1(a) in the Supplemental Material [60]), indicating that GSCO may approach a structural transition or thermal decomposition. In contrast, the GCCO lattice parameter a decreases with increasing temperature (Fig. S1(c) in the Supplemental Material [60]), although the cause remains unknown. This issue should be investigated in future research.

B. Magnetization

The temperature-dependent dc- χ of GSCO under an applied field of 0.1 kOe, as shown in Fig. 2(a), displays a clear anomaly in the FC curve at ~ 98 K [first derivative spectrum in the inset of Fig. 2(a)], revealing the onset of magnetic order. Below this temperature, the FC curve exhibits a small hump that intersects the zero line at $T_{\text{comp}} = 48$ K. With further cooling, χ decreases until the technical limit (2 K), which is commonly known as magnetization reversal. Conversely, the ZFC curve shows a very weak response at 98 K. Notably,

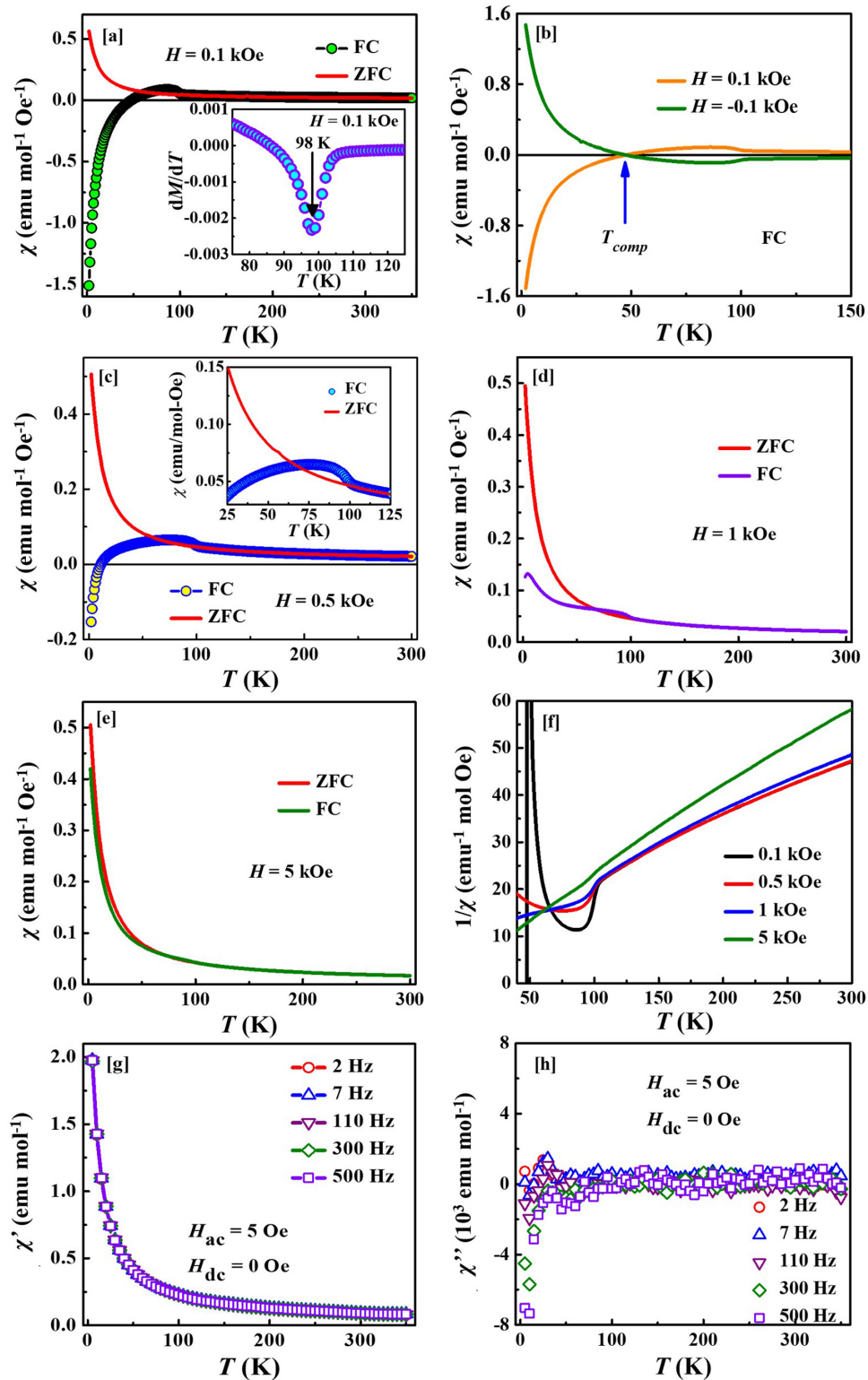


FIG. 2. (a) Zero-field-cooled (ZFC)- and field-cooled (FC)- $\chi(T)$ curves of GSCO measured in a magnetic field of $H = 0.1$ kOe. The inset shows the derivative curve of the FC curve. (b) FC- $\chi(T)$ curves of GSCO measured at $H = 0.1$ and -0.1 kOe. (c)–(e) ZFC- and FC- $\chi(T)$ curves measured at $H = 0.5, 1,$ or 5 kOe, respectively. The inset of (c) displays an enlarged view of the ZFC- and FC- $\chi(T)$ curves at $H = 0.5$ kOe. (f) Inverse χ ($1/\chi$) as a function of temperature and applied field. (g) In-phase (χ') and (h) out-of-phase (χ'') parts of ac- $\chi(T)$ of GSCO measured in an ac magnetic field of 5 Oe at various frequencies.

the FC and post-FC (when heated) curves follow the same trend, unlike those observed for GdCrO₃. Furthermore, GSCO exhibits no features related to the spin reorientation that occurs in GdCrO₃ [2,5].

As suggested by the GSCO structural analysis, Cr ions with different valences are likely connected by AFM exchange interactions and may induce long-range magnetic order at 98 K. Early studies report a similar magnetic behavior, i.e., by the canted FiM order of the double perovskite La₂Ni_{1.19}Os_{0.81}O₆ [63]. Thus, the developed magnetic order of GSCO is likely a canted FiM order, with a transition temperature $T_{\text{FiM}} = 98$ K. Moreover, the negative internal field on the Gd³⁺ moments produced by the weak FM component of canted Cr³⁺/Cr⁴⁺ moments are responsible for the observed compensated magnetization and the magnetization reversal phenomenon below T_{comp} . The net moment from the two canted Cr³⁺/Cr⁴⁺ moments and the Gd³⁺ moments have antiparallel coupling, thus exhibiting FiM ground state in GSCO. Nevertheless, in some ordered double perovskites ($R_2\text{BB}'\text{O}_6$, monoclinic structure with space group $P2_1/n$), the neutron powder diffraction studies confirmed that the FiM ground state is only identified by the coupling between rare-earth moments and FM component of B/B' sublattices and not from the ordered B/B' sublattice magnetization [64–66]. More importantly, the compensated magnetization and/or magnetization reversal phenomenon gives an exceptional indication about the FiM ground state in these kinds of materials, as well as in GSCO.

Under the ZFC condition, when a magnetic field is applied at the lowest temperature, the easy axes of the randomly oriented Gd moments are aligned along the magnetic field direction, and GSCO displays a positive χ . When heated from 2 K, the Gd moments are thermally disturbed and χ decreases. As the magnetizations of the sublattices (Gd and Cr) are unequal, there is no compensation phenomenon.

The FC- χ curve at $H = -0.1$ kOe was also recorded to analyze whether the stray magnetic field plays a role in the observed magnetization reversal. The FC- χ curves measured at $H = 0.1$ and -0.1 kOe are plotted in Fig. 2(b). While measuring the FC- χ curve in the negative field, χ remains negative at $> T_{\text{comp}}$ and becomes positive at $< T_{\text{comp}}$, resembling the inverse behavior of that under the positive field. Because the curves exhibit mirror symmetry in terms of sign reversal, the stray magnetic field exerts little effect on the magnetization reversal.

Figures 2(c)–2(e) show the ZFC- and FC- χ curves measured in different fields ($H = 0.5, 1, \text{ or } 5$ kOe). The magnetization reversal observed at $H = 0.1$ kOe gradually disappears as H increases, and at $H \geq 1$ kOe, the magnetization reversal is challenging to observe. Notably, T_{comp} decreases with increasing H ($T_{\text{comp}} = 11$ K at $H = 0.5$ kOe), indicating the presence of a weaker negative internal field on the Gd moments (produced by weak FM components of the canted Cr moments in opposition to H).

The inverse susceptibility plots ($1/\chi$ vs T) shown in Fig. 2(f) reveal two main features: (i) a sharp decrease in $1/\chi$ at the onset temperature of the long-range magnetic order, which is reminiscent of the canted FiM order. (ii) True paramagnetic behavior is observed at temperatures of

$\gg T_{\text{FiM}} (> \sim 200$ K), suggesting a short-range magnetic correlation between T_{FiM} and ~ 200 K.

The sharp decrease in the $1/\chi$ curve softens with an increasing field, possibly due to the formation of short-range FM clusters. To confirm this, we analyzed the $1/\chi$ vs T curves at 105 K $< T < 200$ K using the power law expression of the Griffith singularity effect.

$$\frac{1}{\chi(T)} = A(T - T_C^R)^{1-\lambda},$$

where A is a constant, T_C^R is the critical temperature below which χ diverges, and λ is an exponent [32,67]. Here, $1/\chi$ does not follow the power law expression well, signifying that the possible magnetic cluster behavior is non-Griffith-like. Similar non-Griffith-like behavior is observed in the half-doped cobaltite La_{0.5}Sr_{0.5}CoO₃, wherein AFM clusters are formed in the paramagnetic matrix [68].

Because we observe increasing magnetization of the pure paramagnetic phase by extrapolating the high-temperature Curie-Weiss (CW) line, short-range FM clusters, not AFM clusters, cause the observed non-Griffith-like behavior. Furthermore, T_C^R is much lower than T_{FiM} , which is inconsistent with the anticipated behavior of a Griffiths phase (i.e., $T_C^R > T_{\text{FiM}}$). However, the short-range FM clusters are assumed to originate from the Cr³⁺-O-Cr⁴⁺ exchange interactions.

The ac- χ ($= \chi' + i\chi''$) of GSCO was measured in an ac magnetic field of 5 Oe at frequencies in the range 2–500 Hz. The in-phase (χ') and out-of-phase (χ'') parts of the zero-field ac- χ as functions of T are shown in Figs. 2(g) and 2(h), respectively. No sharp peak is observed at T_{FiM} , which is consistent with the weak responses of the dc ZFC- χ curves. No additional anomalies or magnetically glassy features are detected. Note that, if a cluster glasslike state is present in the material, a frequency range of up to 500 Hz is usually sufficient to detect it through ac- χ measurements [69–72].

In contrast, GCCO exhibits a completely different magnetic behavior. Figures 3(a)–3(c) show the dc ZFC- and FC- χ curves measured under various magnetic fields ($H = 0.05, 0.1, \text{ or } 0.5$ kOe). The ZFC- and FC- χ curves are identical, increasing continuously as the temperature decreases. No onset of magnetic order is observed, as shown in the inset of Fig. 3(b). However, there is a clear difference between the ZFC and FC curves at < 100 K, as indicated by the arrows shown in Fig. 3(d). The divergence is much more pronounced in the first derivative, as shown in the inset of Fig. 3(d). The random substitution of Ca with Gd may lead to competition between the Cr³⁺-O-Cr³⁺ AFM superexchange and the Cr³⁺-O-Cr⁴⁺ FM double-exchange interactions, causing a magnetically disordered state. However, the divergence between the ZFC and FC curves may indicate that AFM interactions are slightly dominant. Thus, we specified the point of divergence as T_N of GCCO. Since the local lattice distortion of GCCO is different from that of GSCO, its impact on the magnetic exchange interactions differs reasonably. Thus, the possible magnetic ground states of GSCO and GCCO are different owing to the strong dependence on the local structural properties. Notably, β -CaCr₂O₄ undergoes a magnetic transition characterized by the propagation vector

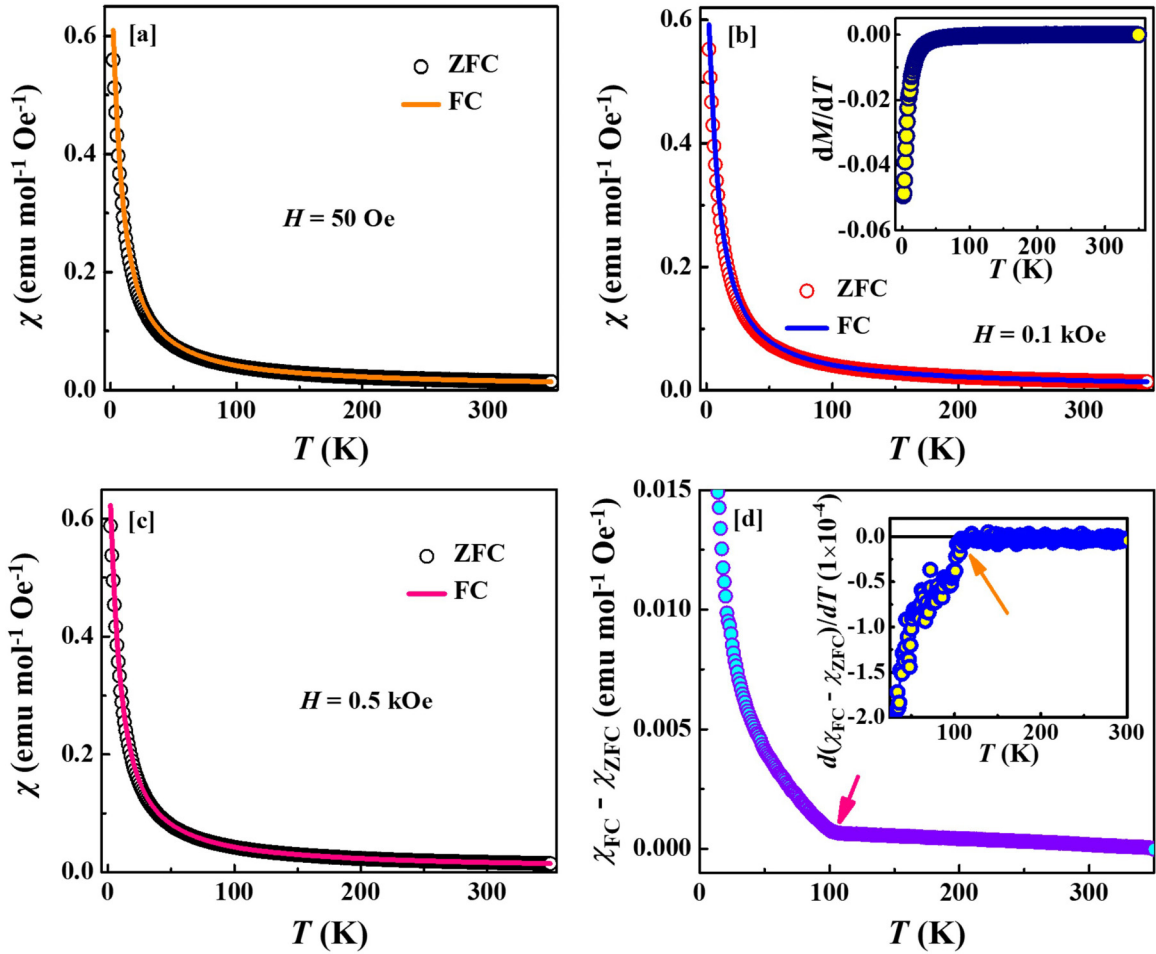


FIG. 3. (a)–(c) Zero-field-cooled (ZFC)- and field-cooled (FC)- $\chi(T)$ curves of GCCO measured at $H = 50$ Oe or 0.1 or 0.5 kOe, respectively. The inset of (b) shows the derivative curve at $H = 0.1$ kOe. (d) Difference between the ZFC- and FC- $\chi(T)$ curves at $H = 0.1$ kOe. Inset of (d) shows the derivative curve of $(\chi_{\text{FC}} - \chi_{\text{ZFC}})$.

$\mathbf{k} = (0, 0, \sim 0.477)$ at $T_N = 21$ K [62]. Although a small amount of β - CaCr_2O_4 (2.5 wt. %) is detected in GCCO, no corresponding feature is observed in the χ vs T or dM_{FC}/dT vs T plots.

The thermal remanent magnetizations (M_{TRM}) of both materials were measured to further elucidate the onsets of the long-range magnetic order and short-range magnetic correlation. During measurement, the magnetic field was set to zero at 2 K immediately after cooling the sample from the paramagnetic state (350 K) in the presence of $H (= 0.5$ kOe), and the sample was then heated to measure the magnetization. Similar protocols are often used to study the spin dynamics of glassy magnetic materials. In addition, M_{TRM} exhibits clear anomalies at the onset of the magnetic order [73,74]. Here, M_{TRM} of GSCO and GCCO as functions of T are shown in Figs. 4(a) and 4(b), respectively. The magnetization reversal of GSCO is again confirmed by the M_{TRM} measurement. However, the thermal variation of M_{TRM} differs slightly from that observed in the dc FC- χ measurement. In addition to the sharp increase in magnetization at the onset of long-range magnetic order at T_{FIM} , a clear anomaly is detected at ~ 150 K for GSCO [inset of Fig. 4(a)]. This indicates that a significant contribution from the short-range magnetic correlation begins at 150 K, which is $\gg T_{\text{FIM}}$. Conversely, GCCO exhibits an

increase in magnetization at ~ 100 K [Fig. 4(b)], which highlights the presence of the magnetic anomaly.

Figures 5(a) and 5(b) show the temperature-dependent $1/\chi$ values of GSCO ($H = 5$ kOe) and GCCO ($H = 0.1$ kOe), respectively. A moderately high magnetic field was used for GSCO to avoid other dilute magnetic interactions. The solid straight lines (red) shown in both plots are guidelines to aid in identifying deviations from CW behavior. The $1/\chi$ curves of GSCO and GCCO deviate from CW behavior at $< \sim 160$ and $< \sim 105$ K, respectively.

To obtain the CW parameters, we fitted the high-temperature $1/\chi$ curves to the CW equation $1/\chi = (T - \Theta)/C$, where $C = N_A \mu_{\text{eff}}^2 / 3k_B$ is the Curie constant, N_A is Avogadro's number, μ_{eff} is the effective magnetic moment, k_B is the Boltzmann constant, and Θ is the Weiss temperature. The fitted curves of GSCO and GCCO are displayed in the insets of Figs. 5(a) and 5(b), respectively, and the respective μ_{eff} values of GSCO and GCCO are 7.04 and 6.75 $\mu_B/\text{f.u.}$. Because half of the Cr^{3+} ions transform to Cr^{4+} ions upon half-doping of Sr^{2+} (Ca^{2+}) at the Gd site of GdCrO_3 , the theoretical moments should be $\mu_{\text{eff}} = 6.53 \mu_B/\text{f.u.}$, based on the equation:

$$\mu_{\text{eff}} = \sqrt{0.5\mu_{\text{Gd}}^2 + 0.5\mu_{\text{Cr}^{3+}}^2 + 0.5\mu_{\text{Cr}^{4+}}^2},$$

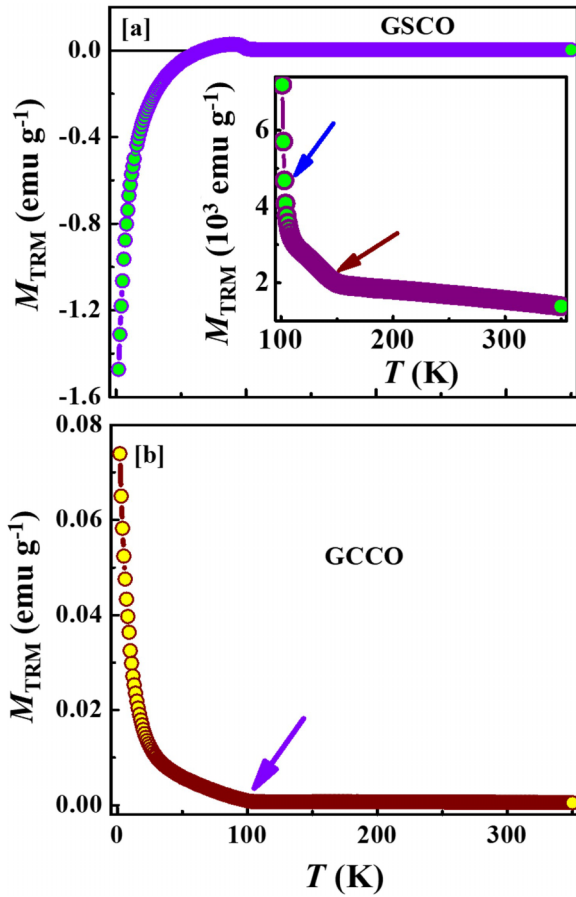


FIG. 4. Thermal remanent magnetizations (M_{TRM}) of (a) GSCO and (b) GCCO, which indicate the onset of magnetic ordering (arrows). The inset shows an enlarged view.

where $\mu_{\text{Gd}} = 7.90 \mu_{\text{B}}$, $\mu_{\text{Cr}^{3+}} = 3.87 \mu_{\text{B}}$ (spin-only due to the quenched $3d$ orbital), and $\mu_{\text{Cr}^{4+}} = 2.82 \mu_{\text{B}}$ (spin-only). This value is close to the experimentally observed values of GCCO and GSCO. In addition, the Θ values of GSCO and GCCO are -63 and -52 K, respectively, with the negative values indicating that AFM interactions are dominant in both materials.

To further elucidate the contrasting magnetic behaviors of these two materials, we recorded isothermal field-dependent magnetization (M vs H) curves under ZFC conditions. Before the measurement of each M - H curve, the material was cooled from well above the onset temperature of magnetic order to the targeted temperature under a zero magnetic field. Figure 6(a) shows the M - H curves of GSCO at temperatures of 2, 10, 40, 60, and 85 K (all less than T_{FiM}). At $T = 40$, 60, or 85 K, linear changes in M vs H are observed in the high-field regions, but weak hystereses are observed in the low-field regions. Much wider hysteresis loops are observed at $T = 2$ or 10 K, indicating the presence of FM and AFM correlations below T_{FiM} .

Regarding the hysteresis loops, we plotted the values of the coercive field (H_{C}) based on the M - H curves at different temperatures in Fig. 6(b). The decrease in H_{C} at < 85 K may be related to the opposite orientation of the Gd sublattice owing to the negative internal field (i.e., the compensation

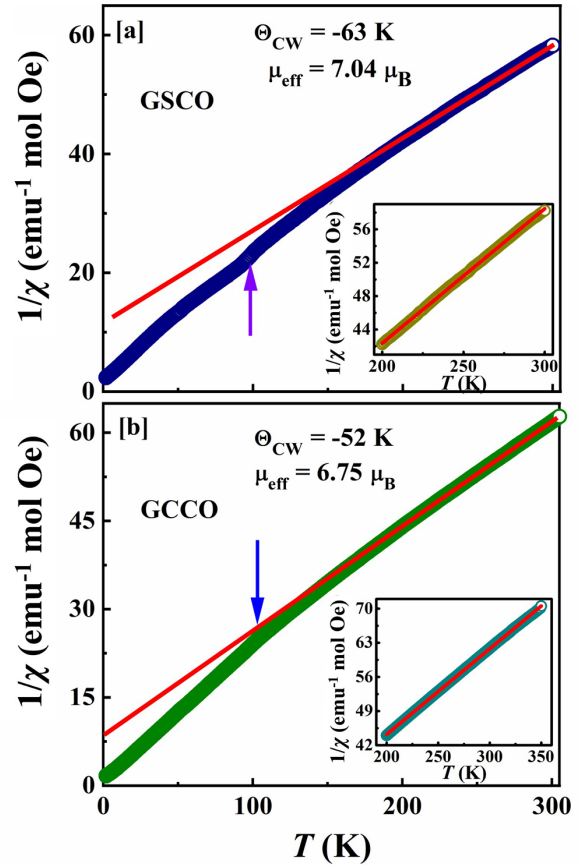


FIG. 5. Inverse magnetic susceptibilities ($1/\chi$) of (a) GSCO (at $H = 5$ kOe) and (b) GCCO (at $H = 0.1$ kOe) as functions of temperature. The solid red lines are guidelines for linear behavior, and the insets show the Curie-Weiss fittings of the high-temperature regions.

phenomenon) with respect to the applied field. An enlarged view of the isotherm at $T = 2$ K is shown in the inset of Fig. 6(b), which indicates that the M - H loop closes within the range ± 20 kOe.

Figure 6(c) shows the M - H isotherms of GCCO at $T = 2, 10, 40, 60,$ and 85 K. Here, H_{C} is 40 Oe at 2 K, which is likely related to the AFM spin correlation. Moreover, even at 70 kOe, the M - H curves are unsaturated, which is typical for materials with AFM-exchange interactions. Nevertheless, the significant S-shapes of the M - H loops of GSCO and GCCO at $T = 2$ or 10 K may be due to the contributions from the much larger Gd³⁺ moments.

To compare the magnetic properties of these two materials, we plotted the isothermal M - H curves measured at $T = 2$ K, as shown in Fig. 6(d), with the inset showing an enlarged view. Notably, there is a small difference in the saturation magnetizations of these compounds at 70 kOe (3.05 and 3.17 μ_{B} /f.u. for GSCO and GCCO, respectively), possibly due to the impurities in GCCO. Notably, the H_{C} of GSCO ($= 1089$ Oe) is 27-fold larger than that of GCCO, which demonstrates its different magnetic nature. Generally, materials with canted FiM structures exhibit higher H_{C} values than those of regular AFM materials. Current observations are in line with the general view.

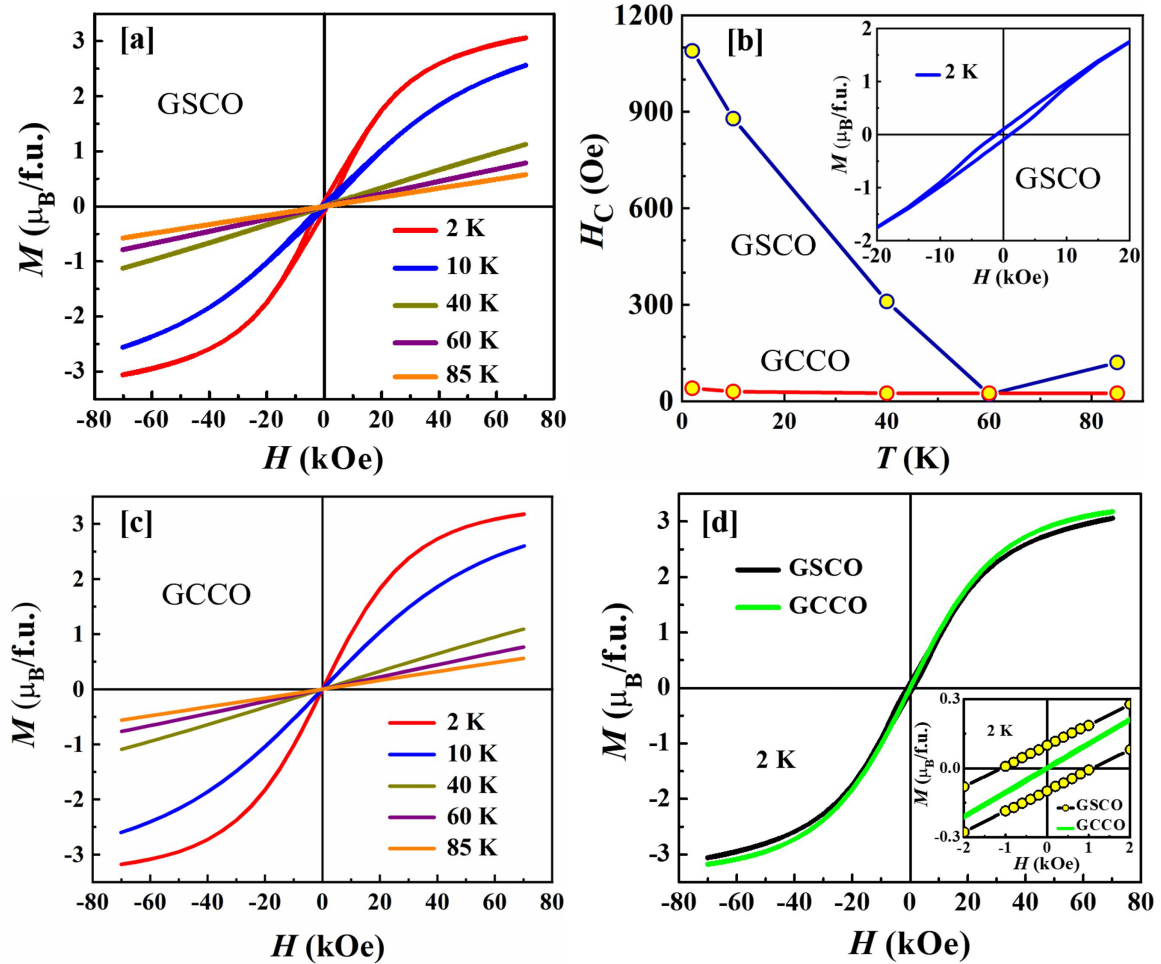


FIG. 6. (a) Isothermal magnetization (M) of GSCO as a function of magnetic field (H) measured under the zero-field-cooled (ZFC) condition at several temperatures ($T = 2, 10, 40, 60,$ and 85 K). (b) Thermal variation of the coercive field (H_C), and the inset shows a magnified view of the ZFC M - H loop at $T = 2$ K. (c) ZFC M - H loops of GCCO measured at temperatures of 2, 10, 40, 60, and 85 K. (d) Comparison of the ZFC M - H loops of GSCO and GCCO at 2 K. The inset shows an enlarged view.

In general, a heterogeneous material with two different magnetic states, such as FM and AFM states [75,76], an FM state and a spin glass [51,52], and FM and FiM states [77], sometimes results in the EB effect. This phenomenon, which is related to the shift of the M - H loop along the magnetic field axis, has considerable applications in spintronic devices. Recently, the EB effect was also observed in a magnetically homogeneous material, i.e., FiM [14]. Because non-Griffith-like FM clusters and canted FiM states coexist in GSCO, we investigated the EB effects by measuring the FC M - H loop at several temperatures. If the cooling field (H_{cool}) is positive, the FC M - H loop shifts toward the negative field axis, which is widely recognized as the conventional EB effect. The EB field (H_{EB}) is a measure of EB anisotropy and defined as $H_{\text{EB}} = (H_1 + H_2)/2$, where H_1 and H_2 are the first (negative) and second (positive) coercive fields at the first and second magnetization reversals, respectively [51]. Notably, H_{EB} should be negative in the conventional EB effect [76].

Figure 7(a) shows the FC M - H loops of GSCO at $H_{\text{cool}} = 20$ kOe at various temperatures ($T = 2, 10, 15,$ or 20 K) below T_{FiM} . Notably, the FC loops were measured within a maximum field (H_{max}) of ± 20 kOe. Contrary to the symmetric

nature of a regular M - H loop at the origin (absence of EB), the FC loop shifts slightly along the field direction from the origin, suggesting that EB anisotropy is induced upon field cooling. The FC loops at $T = 2$ K measured in different directions of $H_{\text{cool}} = 20$ and -20 kOe are shown in Fig. 7(b). The magnitude of the shift may be small, but the loop shifts in the opposite direction.

The enlarged views (within ± 3 kOe) of the FC loops collected in the different directions of H_{cool} at $T = 10, 15, 20, 30,$ or 50 K are shown in Figs. 7(c)–7(g), respectively. Each loop shifts alternatively, i.e., the EB anisotropy undergoes sign reversal when H_{cool} changes direction. Remarkably, the FC loop shifts toward the positive field axis when the material is cooled in the positive field, which contradicts the expectation of the conventional EB effect. This is known as the inverse EB (IEB) effect [78], and the FC loop exhibits the IEB effect at $T \leq 50$ K, whereas the conventional EB effect is observed at $T \geq 70$ K, e.g., an enlarged view of the FC loop within ± 1 kOe at $T = 90$ K [Fig. 7(h)] reveals the conventional EB effect.

Figure 8 shows the temperature dependences of H_1 , H_2 , H_C , and H_{EB} measured at a positive H_{cool} . Here, H_1 and H_2 are

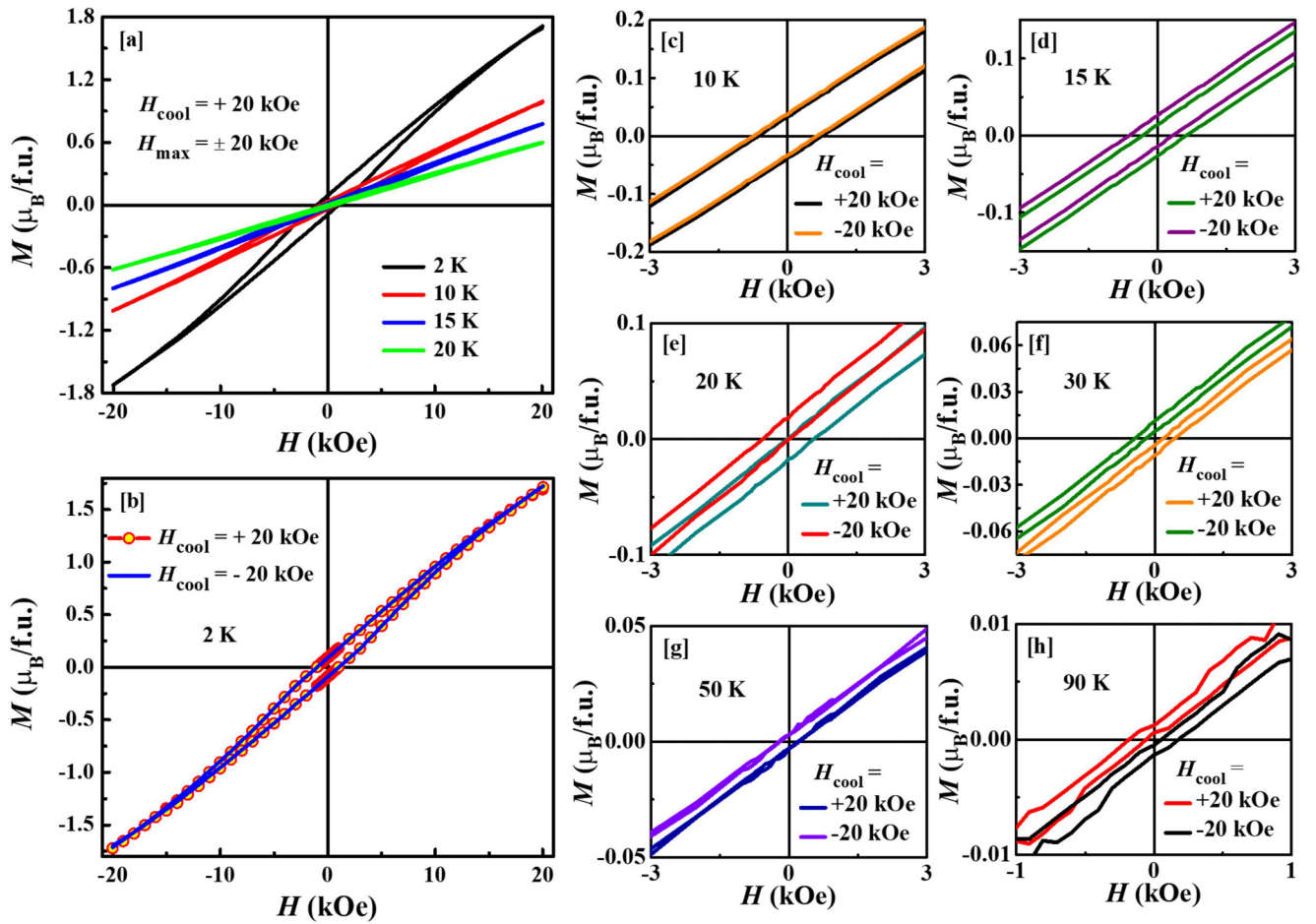


FIG. 7. (a) M - H loops of GSCO measured at $H_{\text{cool}} = 20$ kOe. The maximum field is ± 20 kOe, and the temperatures are $< T_{\text{FiM}}$. (b) Hysteresis loops measured at $T = 2$ K and $H_{\text{cool}} = 20$ or -20 kOe. (c)–(h) Magnified views of the field-cooled (FC) M - H loops measured at $H_{\text{cool}} = \pm 20$ kOe and $T = 10, 15, 20, 30, 50$, or 90 K, respectively.

negative between 70 and 100 K but positive at < 70 K. Also, H_2 remains positive at ≥ 2 K, and H_1 becomes negative again at < 20 K. Clearly, the H_1 and H_2 curves are not monotonous, and thus, a crossover from conventional EB to IEB effects (i.e., negative-to-positive sign inversion of H_{EB}) is observed in GSCO, which may be related to the observed magnetization reversal. Here, H_{EB} approaches zero at < 10 K, confirming the absence of any EB effect. Apart from the small peak at $< T_{\text{FiM}}$, H_C changes monotonically with temperature.

In general, in a strongly anisotropic system, where M does not saturate at the highest H , the minor hysteresis loops hinder us from accurately estimating the EB parameters, which may ultimately lead to erroneous results. Therefore, to detect the true EB effect in such a system, considering an effectively saturated hysteresis loop is recommended [79]. When the loop is closed, M is likely effectively saturated [51]. In this scenario, the FC and ZFC M - H loops are fully closed at 2 K within $H_{\text{max}} = \pm 20$ kOe, as shown in Fig. 7(a) and the inset of Fig. 6(b), respectively. Therefore, the FM component may be saturated, and the minor hysteresis loops may exhibit little effect on the current analysis.

To study the effect of H_{max} on the observed EB phenomenon, we investigated the FC loops at different H_{max} values. FC loops measured at $T = 15$ K

(randomly selected) at a constant $H_{\text{cool}} (= 20$ kOe) and different $H_{\text{max}} (= \pm 20, \pm 25, \pm 30, \text{ or } \pm 70$ kOe) are shown in Fig. 9(a), and an enlarged view of the origin is shown in Fig. 9(b). The magnitude of H_1 increases with increasing H_{max} , and that of H_2 does not change, and thus, the EB effect is reduced by increasing H_{max} . Here, H_C and H_{EB} are plotted as functions of H_{max} at $T = 15$ K in Fig. 9(c), with H_C increasing rapidly up to $H_{\text{max}} = 35$ kOe, beyond which it increases only slightly. Conversely, H_{EB} decreases sharply as H_{max} increases from 20 to 30 kOe and is almost zero at > 30 kOe. In addition, the almost complete suppression of H_{EB} at higher H_{max} values may be associated with suppressed FM contributions from $\text{Cr}^{3+}/\text{Cr}^{4+}$ ions in the FiM structure. At $H_{\text{max}} \geq 30$ kOe, a large paramagnetic Gd^{3+} moment dominates the entire magnetism, which inevitably reduces the exchange anisotropy between the FM clusters and FiM state.

Visualizing the origin of the EB effect, particularly the IEB effect, is rather complex, particularly in single-phase polycrystalline materials with invisible physical boundaries between the two different magnetic phases. Owing to the presence of FM clusters at high-temperatures, complex interfacial magnetic interactions between these clusters and the FiM state may induce EB anisotropy, causing the conventional EB effect in GSCO. Nevertheless, the presence of FM and

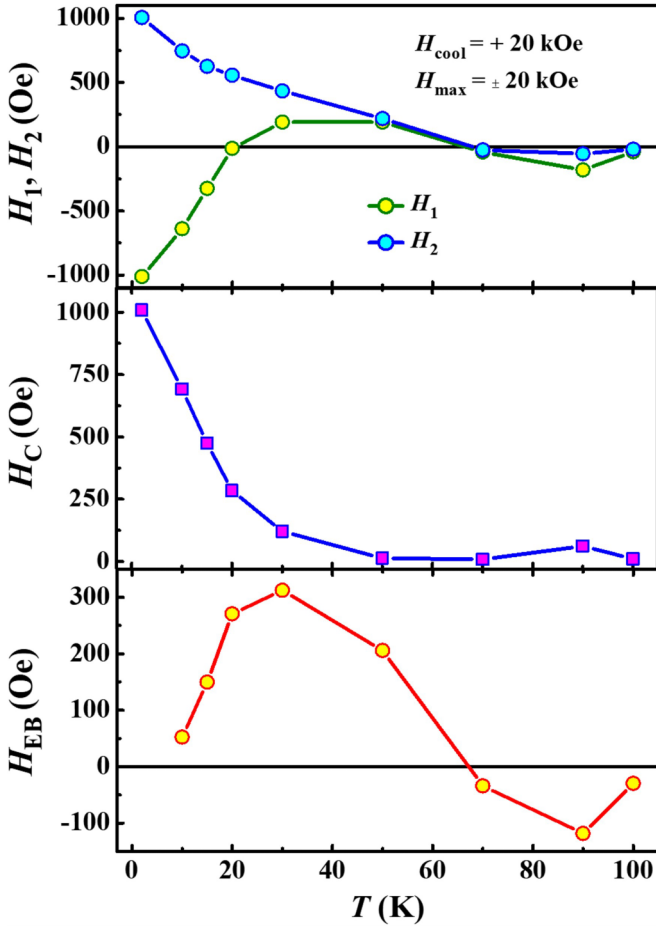


FIG. 8. Thermal profiles of H_1 , H_2 , H_C , and H_{EB} obtained from the field-cooled (FC) M - H loops of GSCO at $H_{cool} = 20$ kOe and $H_{max} = \pm 20$ kOe. Notably, the sign reversal of H_{EB} from negative to positive occurs upon cooling.

AFM components specific to the FiM state may be the real cause of the observed conventional EB behavior.

To gain deeper insight into the IEB phenomenon, we analyzed possible mechanisms to elucidate its origin. In most earlier investigations [80–83], the phenomena of IEB manifest with increasing strength of H_{cool} , in addition to the conventional EB effect at lower H_{cool} values. The sign reversal of H_{EB} is successfully explained for a system wherein FM nanodroplets are embedded in a charge-ordered AFM host using the following equation:

$$-H_{EB} \propto J^2 A L(\mu, H_{cool}, T_f) + J H_{cool},$$

where J is the surface exchange constant, A is a constant (multiplication factor), and L is the Langevin function of the magnetic moment μ of the FM nanodroplets H_{cool} and freezing temperature T_f of the interfacial spin [82]. Clearly, the competition between the surface exchange interaction and H_{cool} may induce the sign reversal of H_{EB} . This equation shows that, for a lower H_{cool} , the first term dominates, and H_{EB} becomes negative, as J^2 is always positive. For a higher H_{cool} , the second term may be significant, and in the case of AFM interfacial coupling, i.e., $J < 0$, sign reversal of H_{EB} may be anticipated.

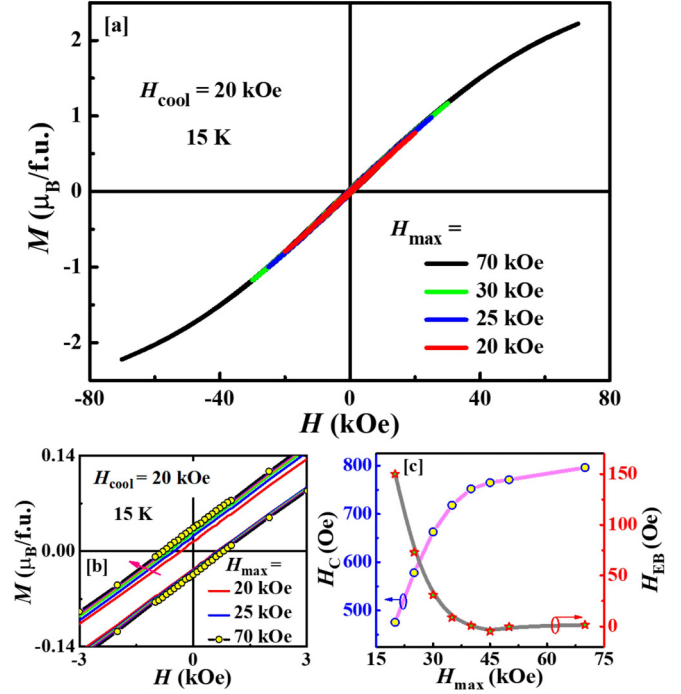


FIG. 9. (a) Field-cooled (FC) M - H loops of GSCO measured at $T = 15$ K at $H_{cool} = 20$ kOe and $H_{max} = \pm 20, \pm 25, \pm 30, \text{ or } \pm 70$ kOe. (b) Enlarged view of the loops. (c) H_C and H_{EB} as functions of H_{max} ($H_{cool} = 20$ kOe) at $T = 15$ K.

In contrast, in this investigation, when T is varied at a fixed H_{cool} and the sign of H_{cool} is changed at a fixed T , sign inversion of H_{EB} is observed. Because the H_{EB} equation does not contain T -dependent terms, the above prediction is unlikely. Another possibility in achieving the IEB effect is a magnetization reversal in the FiM state at $< T_{comp}$, which causes the IEB effect of $\text{LuFe}_{0.5}\text{Cr}_{0.5}\text{O}_3$ [78]. Because sign inversion of H_{EB} is also detected at $< T_{comp}$ of the canted FiM GSCO, these two materials should share a basic physical mechanism. In addition, the various possible pathways of the DM interaction between two Cr ions (with different oxidation states) may lead to a reversal of the magnetic moment, thereby producing the IEB effect. Furthermore, the rough interface between the magnetic layers yields spatially varying mixed AFM and FM couplings, which may generate the IEB effect, even at a lower H_{cool} [81]. In this paper, definitively identifying the origin of the IEB behavior of GSCO is challenging.

C. Heat capacity

To better understand the magnetic properties, the specific heat capacities (C_{total}) of GSCO and GCCO were measured at $H = 0$ and 90 kOe. Figure 10(a) shows the zero-field ($H = 0$ kOe) $C_{total}(T)$ curve of GSCO, which exhibits no λ -like anomaly, which is a common feature of AFM transitions. Instead, a clear anomaly is observed close to $T_{FiM} = 98$ K [Fig. 2(a)]. To estimate the change in magnetic entropy (S_m) by subtracting the lattice contribution ($C_{lattice}$) from C_{total} , combinations of the Debye and Einstein [84] or the two Debye functions [85] were used to fit the high-temperature region of

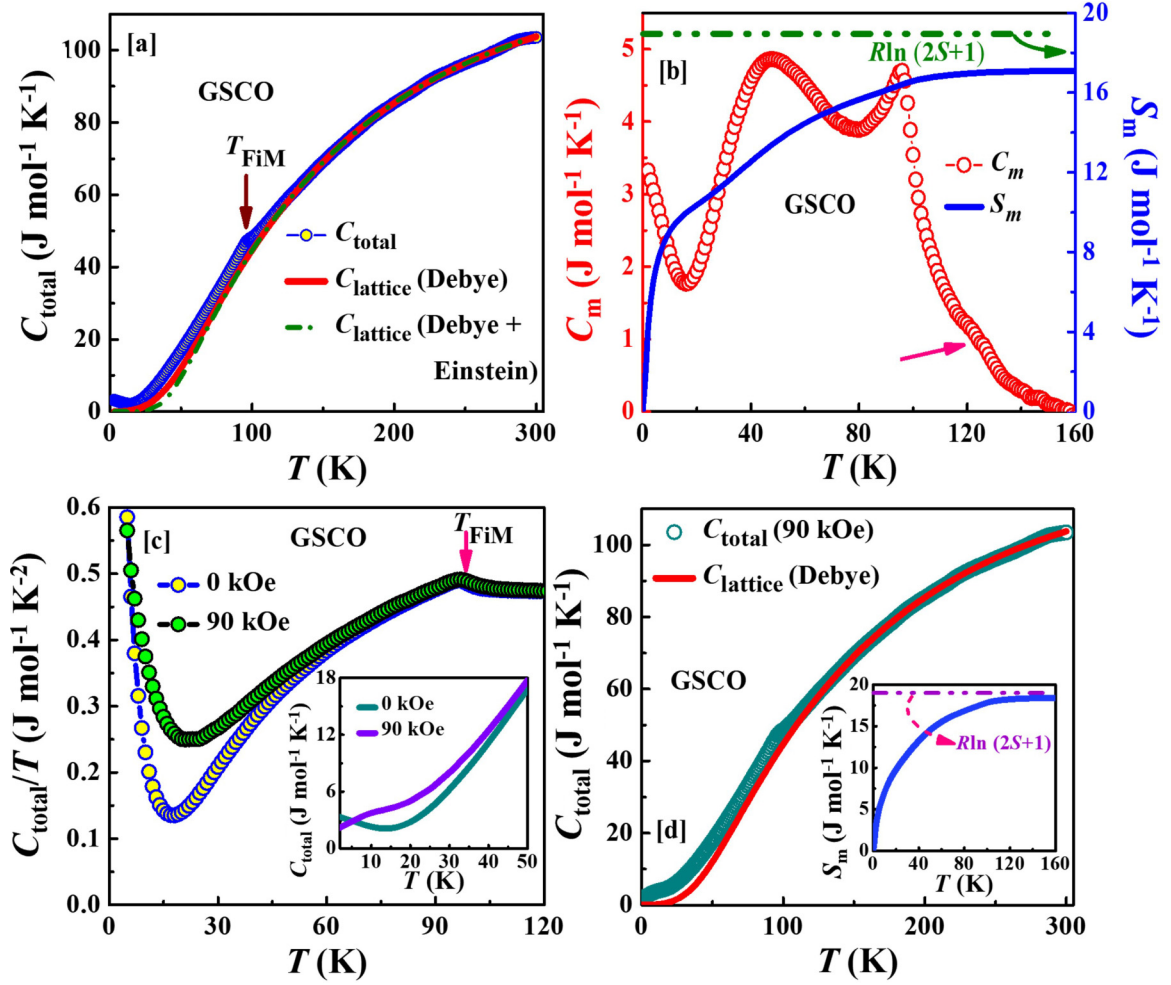


FIG. 10. (a) Temperature dependence of the specific heat capacity (C_{total}) of GSCO under a zero field. The solid and dashed curves show the lattice heat capacities (C_{lattice}) obtained by fitting to the high-temperature region with combinations of two Debye functions or Debye and Einstein functions, respectively. (b) Temperature dependences of the magnetic heat capacity (C_m), which is obtained by subtracting C_{lattice} from C_{total} , and the magnetic entropy (S_m). The dash-dotted straight line represents the theoretical S_m . (c) C_{total}/T vs T plots of GSCO at $H = 0$ and 90 kOe. The inset shows the C_{total} vs T plots. (d) C_{total} of GSCO at $H = 90$ kOe. The solid red curve represents C_{lattice} obtained by fitting to the high-temperature region with a combination of two Debye functions. The inset displays the S_m vs T curve.

$C_{\text{total}} (\gg T_{\text{FiM}})$. In the first case, the formula used is as follows:

$$C_{\text{total}}(T) = n_D \mathcal{D}(T, \Theta_D) + n_E \mathcal{E}(T, \Theta_E),$$

where \mathcal{D} and \mathcal{E} are the Debye and Einstein functions, respectively. Here, Θ_D and Θ_E are the respective Debye and Einstein temperatures, and the scale factors n_D and n_E correspond to the numbers of vibrational modes per formula unit in the Debye and Einstein models, respectively. In the latter case, the heat capacity is approximated by

$$C_{\text{total}}(T) = m_1 \mathcal{D}(T, \Theta_{D1}) + m_2 \mathcal{D}(T, \Theta_{D2}),$$

where m_1 and m_2 are the coefficients related to the vibrational modes per formula unit and Θ_{D1} and Θ_{D2} are the characteristic Debye temperatures. In both cases, proper fitting is observed with the parameters $n_D = 2.34$, $\Theta_D = 859$ K, $n_E = 2.73$, $\Theta_E = 273$ K, $m_1 = 2.09$, $m_2 = 2.99$, $\Theta_{D1} = 888$ K, and $\Theta_{D2} = 385$ K. The total number of vibrational modes in both cases is ~ 5 (i.e., $n_D + n_E \approx 5$ and $m_1 + m_2 \approx 5$), which validates the presence of five atoms per formula unit of GSCO.

Here, C_{lattice} dominates C_{total} at temperatures of $\gg T_{\text{FiM}}$, and thus, the fitted parameters enable the extrapolation of C_{lattice} to the low-temperature limit, as shown by the solid and dotted lines [for C_{lattice} (Debye) and C_{lattice} (Debye + Einstein), respectively] displayed in Fig. 10(a). Because the observed C_{total} and Debye (only) models are very similar, we adopted C_{lattice} (Debye) as a reference to examine the lattice contribution for further analysis. Notably, there is no similar nonmagnetic material that may be used as a reference to properly estimate C_{lattice} of GSCO.

The magnetic contribution to the heat capacity (C_m) is estimated by subtracting C_{lattice} from C_{total} , i.e., $C_m(T) = C_{\text{total}}(T) - C_{\text{lattice}}(T)$. Figure 10(b) shows C_m as a function of T , revealing a sharp peak close to $T_{\text{FiM}} = 98$ K. Additionally, the data show a broad peak at ~ 45 K, with another increase at < 15 K. The broad peak at < 45 K is unusual and is likely due to magnetization reversal, and the increase at < 15 K may be due to the short-range AFM ordering of the Gd moments. Similar increases in C_{total} are also reported in single-crystal and polycrystalline $\text{Gd}_2\text{CoMnO}_6$ [86,87] and single-crystal

Tb₂CoMnO₆ [88]. In addition, an extended plateau of the peak at $\sim T_{\text{FIM}}$ is observed in the high-temperature region of C_m , which suggests the possible presence of short-range magnetic correlations at $> T_{\text{FIM}}$. Moreover, the $C_m(T)$ curve displays several remarkable features but is too complicated to understand clearly.

Finally, S_m is estimated by integrating $C_m(T)/T$ over the studied temperature range [Fig. 10(b)]. Here, S_m increases rapidly with increasing temperature at ≤ 10 K, then gradually increases with increasing temperature, and plateaus at $17 \text{ J mol}^{-1} \text{ K}^{-1}$ at > 130 K. However, the saturation value of S_m is slightly smaller than the expected Boltzmann entropy [$S_m = R \ln(2S + 1) \approx 19 \text{ J mol}^{-1} \text{ K}^{-1}$] based on the mean-field theory for localized Cr^{3+} ($S = \frac{3}{2}$), Cr^{4+} ($S = 1$), and Gd^{3+} ($S = \frac{7}{2}$, $L = 0$). The dashed line in Fig. 10(b) represents the Boltzmann entropy. Several factors may cause the slight discrepancy between the observed and expected S_m , one of which is the short-range AFM ordering of Gd^{3+} moments. In addition, the inadequate estimation of C_m at very low temperatures by extrapolating the high-temperature C_{lattice} may be another cause of the discrepancy. Furthermore, increasing C_{total} at the lowest temperature [2 K, inset in Fig. 10(c)] hinders the proper estimation of C_m .

The C_{total}/T vs T curves of GSCO at $H = 0$ or 90 kOe are plotted in Fig. 10(c). Even at $H = 90$ kOe, no noticeable suppression at $\sim T_{\text{FIM}}$ is observed. Instead, the valleylike features centered at ~ 15 K are moderately suppressed. As shown in the inset of Fig. 10(c), C_{total} at $H = 90$ kOe does not increase as it does under the zero-field but decreases toward zero at < 5 K. Additionally, the short-range ordering of Gd^{3+} moments are significantly disturbed by the application of the 90 kOe field (due to the increased Gd^{3+} polarization). We attempted to estimate the saturation value of S_m again by determining C_{lattice} by fitting the high-temperature region of the C_{total} (90 kOe) curve using the combination of the two Debye functions and extrapolating to $T = 0$ K [Fig. 10(d)]. Remarkably, the temperature dependence of S_m [inset in Fig. 10(d)] shows that S_m generally saturates at a value much closer to the Boltzmann entropy than that at $H = 0$ kOe. Thus, the discrepancy between the observed ($H = 0$ kOe) and expected S_m is likely caused by short-range AFM ordering of Gd^{3+} moments.

To facilitate further comparative studies, we performed a detailed analysis of C_{total} of GCCO. Remarkably, the temperature dependences of the zero-field $C_{\text{total}}(T)$ of both materials are very similar [Figs. 10(a) and 11(a) show those of GSCO and GCCO, respectively], but a clear anomaly is observed at ~ 100 K in the $C_{\text{total}}(T)$ curve of GCCO. The observed anomalies and magnetization data indicate that GCCO undergoes AFM ordering at ~ 100 K. The solid red line shown in Fig. 11(a) represents the GCCO C_{lattice} estimated by combining the two Debye functions. Anomalies are detected at ~ 100 K, but no sharp peaks are observed in the $C_m(T)$ plot close to this temperature (not shown). Instead, a broad peak and an upturn at ~ 75 and < 15 K are observed, respectively.

As shown in the inset of Fig. 11(a), when the temperature is > 130 K, S_m saturates at $17.5 \text{ J mol}^{-1} \text{ K}^{-1}$, which is slightly smaller than the expected Boltzmann entropy. At $H = 90$ kOe, $C_{\text{total}}(T)$ displays no significant change in the

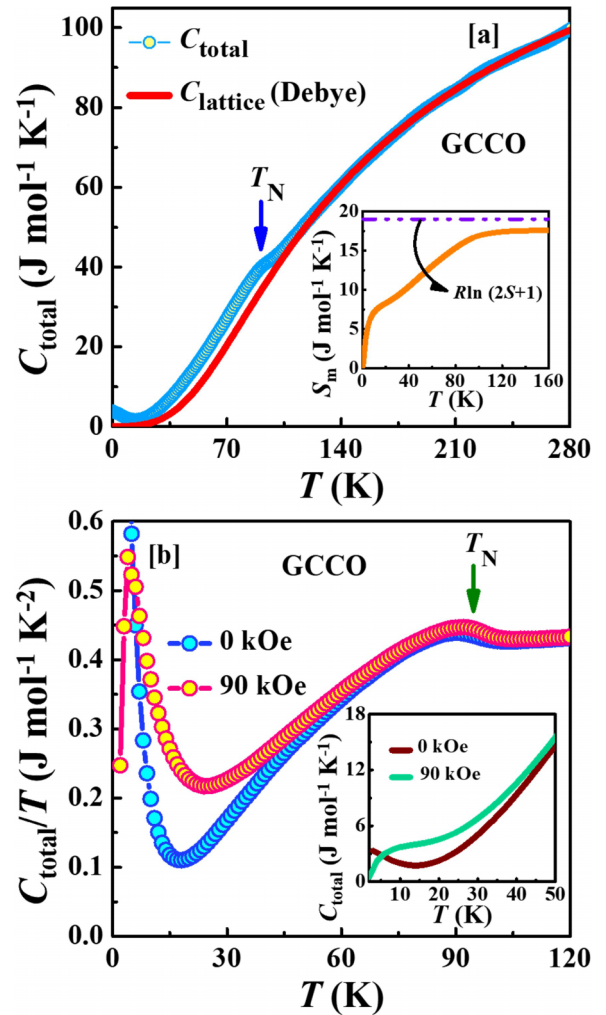


FIG. 11. (a) Specific heat capacity of GCCO as a function of temperature. The red solid curve shows a fitting to a combination of Debye functions, and the inset shows the thermal profile of S_m of GCCO and the theoretical value. (b) C/T vs T plots of GCCO at $H = 0$ or 90 kOe. The inset shows the C_{total} vs T plots.

magnetic transition at 100 K [C/T vs T plot in Fig. 11(b)]. Conversely, valleylike features at 15 K, such as those observed for GSCO, are strongly influenced by the application of H . The inset in Fig. 11(b) shows an enlarged view of the $C_{\text{total}}(T)$ curves at $H = 0$ or 90 kOe, revealing that they intersect at $T = 5$ K.

D. Resistivity

Figure 12(a) shows the temperature-dependent resistivities $\rho(T)$ of GSCO and GCCO. The increase in resistivity with decreasing temperature should yield semiconductorlike behavior. In this context, measuring $\rho(T)$ at temperatures of < 70 K was impossible because of the high resistance which was above the instrumental limit. At room temperature, ρ of GSCO is almost 14-fold higher than that of GCCO ($\rho_{300 \text{ K}} = 57.01$ and $4.19 \text{ } \Omega\text{-cm}$ for GSCO and GCCO, respectively). No metallic behavior is observed within the investigated temperature range, and these features contrast with the electrical

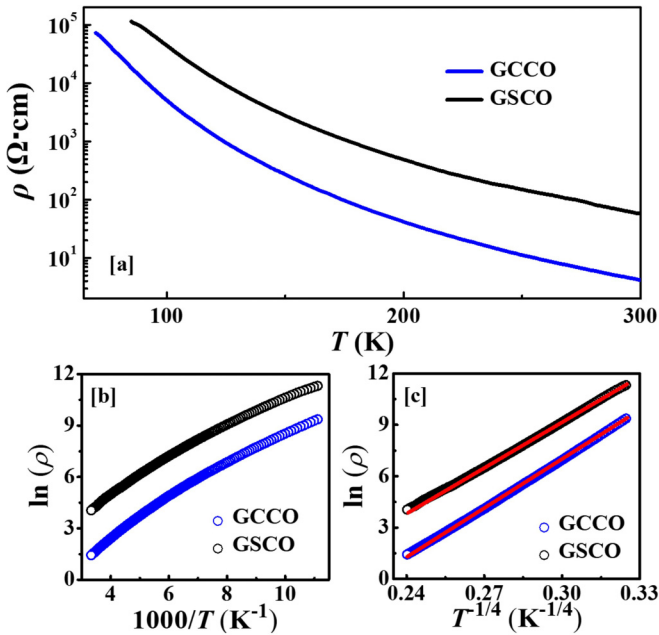


FIG. 12. (a) Temperature dependences of ρ of GSCO and GCCO. (b) Alternative plot of the data. (c) Variable-range-hopping plot of the data. The red solid lines are guidelines.

behaviors of half-doped manganites and cobaltites [36,50]. The resistivity data were analyzed using the Arrhenius model, $\ln\rho$ vs $1000/T$, to investigate the possible conduction mechanisms, as shown in Fig. 12(b). Owing to the nonlinear behaviors of the curves, the $\rho(T)$ curves of both materials are not well modeled by the Arrhenius model. Instead, the linear behavior of the $\ln\rho$ vs $T^{-1/4}$ plot [Fig. 12(c)] shows that variable-range hopping better explains the observed electronic behaviors of GSCO and GCCO.

E. Dielectric behavior

Several $R\text{CrO}_3$ materials (excluding $R = \text{Sc-Pr, Pm, Eu, Dy, Yb}$) should exhibit significant magnetoelectric coupling at temperatures of $< T_N$, and thus, they are potential multi-ferroic materials. Temperature-dependent relative permittivity (ϵ_r) measurements of GSCO and GCCO were performed at various frequencies to investigate possible magnetoelectric coupling. The thermal changes in ϵ_r and its loss factor ($\tan\delta$) are shown in Figs. 13(a)–13(d). The $\epsilon_r(T)$ curves of both materials display three main characteristics: (i) low- T plateaus at ϵ_r of ~ 60 ; (ii) sharply increasing ϵ_r close to $T = 30$ K (at 100 Hz), which is strongly frequency-dependent; and (iii) significant anomalies at $T \approx 100$ K (magnetic transition temperatures of GSCO and GCCO). These are also strongly frequency dependent and shift toward a higher T as the frequency increases [Figs. 13(a) and 13(b)].

In addition, the dielectric anomalies observed at T_{FiM} (for GSCO) and T_N (for GCCO) confirm the presence of significant magnetoelectric coupling in both materials. The frequency dependence of the dielectric anomaly ($\sim T_{\text{FiM}}$ and $\sim T_N$) is characteristic of a ferroelectric relaxorlike state, e.g., spontaneous electrical polarization associated with the anomaly is observed in $R\text{CrO}_3$ [12] and the stepwise

increase in ϵ_r at ~ 30 K may be associated with a large frequency-dependent Maxwell-Wagner relaxation [89]. This usually manifests itself as a depletion layer contribution at the interface between the sample and the electrodes or at some grain boundaries. Most importantly, it is not an inherent property of the material but an extrinsic issue. Conversely, the derivative spectra of $\epsilon_r(T)$ exhibit two peaks at $T \approx 100$ K (T_{FiM} and T_N), and the stepped increase in ϵ_r at this temperature indicates the presence of magnetic coupling. For clarity, the derivative spectra of the data measured at 2.71 kHz are shown as examples [insets in Figs. 13(a) and 13(b)].

Strong dielectric losses are observed at this temperature, with stepwise increases in ϵ_r observed [Figs. 13(c) and 13(d)]. The dielectric loss peaks depend on the frequency for both materials. No additional anomalies are observed in these spectra at the magnetic transition temperature, but the derivatives of the loss spectra reveal sharp increases at $\sim T_{\text{FiM}}$ and $\sim T_N$ [as indicated by the arrows and insets in Figs. 13(c) and 13(d)]. Therefore, the dielectric loss spectra reveal the magnetoelectric coupling of both materials. In addition, the application of a magnetic field of 90 kOe results in no significant changes in the $\epsilon_r(T)$ curves and dielectric loss spectra (not shown).

IV. SUMMARY AND CONCLUSIONS

We successfully synthesized the half-doped perovskite-type chromites GSCO and GCCO. These polycrystalline materials were obtained via solid-state reactions at a high pressure and temperature (6 GPa and 1200 °C). Synchrotron XRD at room temperature revealed that GSCO and GCCO crystallized in orthorhombic structures (space group: $Pnma$) with different degrees of local lattice distortion.

We observed magnetization reversal in GSCO, but GCCO displayed a little anomaly. The magnetic ground state of GSCO is FiM, while it is AFM for GCCO. Therefore, the magnetic ground state of half-doped GdCrO_3 could be tuned via substitution with various alkaline-earth ions. Moreover, the different magnetic ground states of GSCO and GCCO possibly originate from the different degrees of local lattice distortions, as evident from the structural analysis. In addition, thermal residual magnetization studies confirmed the presence of short-range magnetic correlations within GSCO at temperatures of $> T_{\text{FiM}}$. This was further supported by the heat capacity measurements.

Remarkably, GSCO displayed a crossover from the conventional EB effect to the IEB effect upon cooling. Such a crossover could be caused by the reversal of the magnetic moment due to various competing DM interactions. In general, the key factors of producing DM interaction between two atomic spins are the structural inversion symmetry breaking and the strong spin-orbit coupling (SOC) with magnetic exchange energy. In most cases, the strong SOC is provided by the neighboring atoms in the structure. However, in this paper, since $L = 0$ (for Gd^{3+}), the orbital contribution from the neighboring Gd^{3+} cannot be expected. Therefore, the crystal structure itself may stabilize spin canting by minimizing some free energy [71,90,91]. Moreover, the complex interfacial magnetic interactions between the high-temperature FM clusters and the FiM state is the plausible origin of the

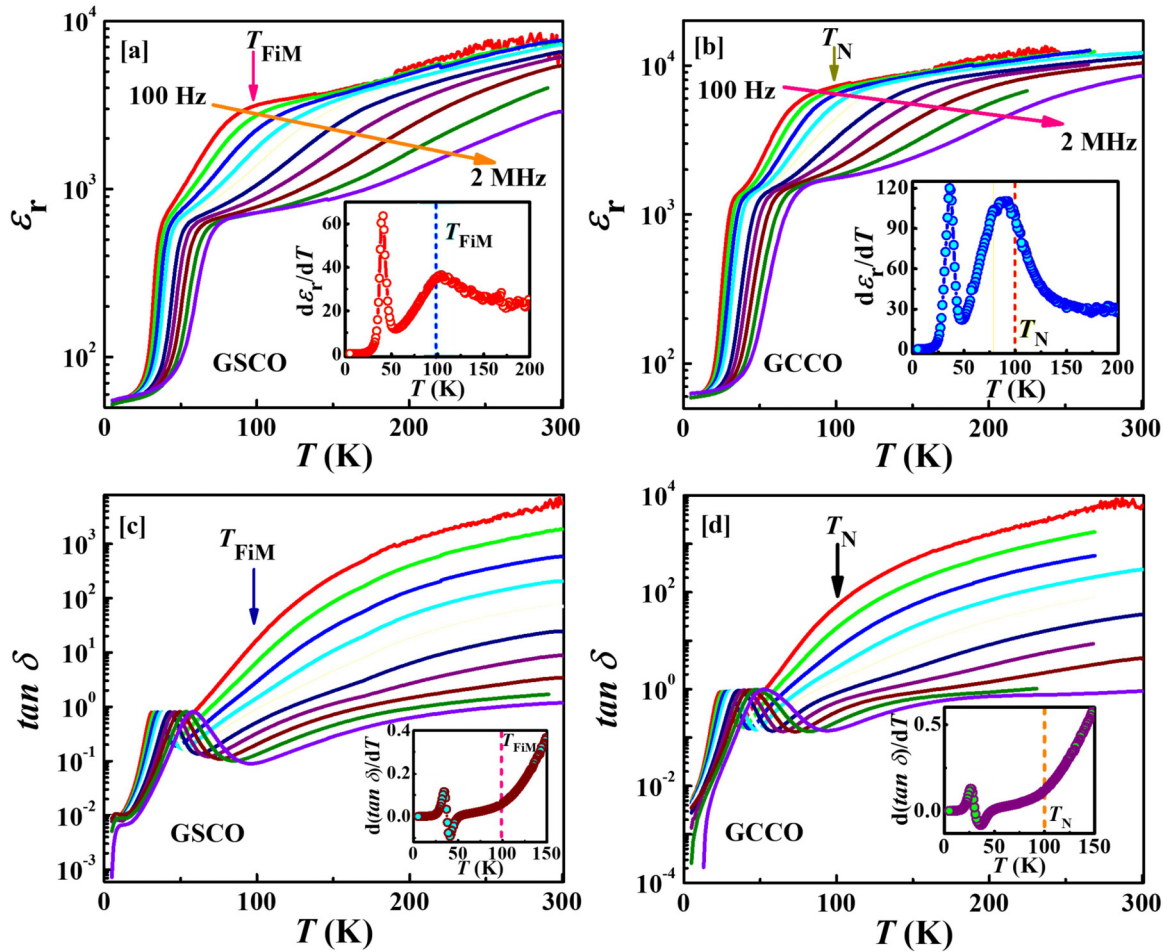


FIG. 13. (a)–(b) Temperature dependences of the dielectric constants (ϵ_r) of GSCO and GCCO, respectively, as recorded at several frequencies in the range 100 Hz–2 MHz ($f = 100$ Hz, 300 Hz, 903 Hz, 2.71 kHz, 8.15 kHz, 24.51 kHz, 73.68 kHz, 221.43 kHz, 665.48 kHz, and 2 MHz). The insets show representative differential curves (at 2.71 kHz). The blue and red dashed lines in the insets indicate the temperature corresponding to the onset of magnetic order of each material. (c)–(d) Temperature-dependent dielectric losses ($\tan \delta$) of GSCO and GCCO, respectively. The insets show representative differential curves (at 2.71 kHz).

conventional EB behavior in GSCO. Although several mechanisms including the competition between interfacial exchange coupling and H_{cool} , the reversal of magnetic moments below T_{comp} , and the spatially varying mixed AFM and FM couplings at the rough interface have been discussed to understand the origin of IEB, we can predict that the IEB effect in GSCO arises due to the magnetization reversal phenomenon. In addition, significant magnetoelectric coupling with ferroelectric relaxorlike states was identified at the onsets of magnetic order of both materials. The presence of the EB effect, particularly the IEB effect, and magnetoelectric coupling yields considerable prospects for application in magnetic memory and spintronic devices.

We interpreted the possible magnetic ground states of both materials as much as possible based on the experimental data, but the exact magnetic structures remain unclear because conducting neutron diffraction studies of highly

neutron-absorbing materials is technically challenging. Further combined studies, such as x-ray magnetic circular dichroism and density functional theory calculations, should contribute to a comprehensive understanding of the magnetic and electronic properties of these half-doped perovskite-type chromites.

ACKNOWLEDGMENTS

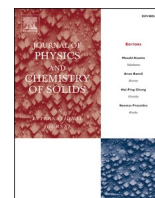
Synchrotron radiation was performed at the beamlines for powder diffraction (BL15XU and BL02B2) at SPring-8 with the approval of the Japan Synchrotron Radiation Research Institute (Proposals No. 2020A4501 and No. 2021A1169). This paper was partially supported by Japan Society for the Promotion of Science KAKENHI Grants No. JP20H05276 and No. JP22H04601.

[1] L. Holmes, M. Eibschitz, and L. G. Van Uitert, *J. Appl. Phys.* **41**, 1184 (1970).

[2] A. H. Cooke, D. M. Martin, and M. R. Wells, *J. Phys. C: Solid State Phys.* **7**, 3133 (1974).

- [3] T. Morishita, K. Aoyagi, K. Tsushima, and T. Kigawa, *Solid State Commun.* **20**, 123 (1976).
- [4] K. Toyokawa, S. Kurita, and K. Tsushima, *Phys. Rev. B* **19**, 274 (1979).
- [5] K. Yoshii, *J. Solid State Chem.* **159**, 204 (2001).
- [6] B. Rajeswaran, D. I. Khomskii, A. K. Zvezdin, C. N. R. Rao, and A. Sundaresan, *Phys. Rev. B* **86**, 214409 (2012).
- [7] S. Lei, L. Liu, C. Wang, C. Wang, D. Guo, S. Zeng, B. Cheng, Y. Xiao, and L. Zhou, *J. Mater. Chem. A* **1**, 11982 (2013).
- [8] K. R. S. Preethi Meher, A. Wahl, A. Maignan, C. Martin, and O. I. Lebedev, *Phys. Rev. B* **89**, 144401 (2014).
- [9] A. McDannald, C. R. delaCruz, M. S. Seehra, and M. Jain, *Phys. Rev. B* **93**, 184430 (2016).
- [10] B. Dalal, B. Sarkar, V. D. Ashok, and S. K. De, *J. Phys.: Condens. Matter* **28**, 426001 (2016).
- [11] M. Taheri, F. S. Razavi, Z. Yamani, R. Flacau, P. G. Reuvekamp, A. Schulz, and R. K. Kremer, *Phys. Rev. B* **93**, 104414 (2016).
- [12] A. Indra, K. Dey, A. Midya, P. Mandal, O. Gutowski, U. Rütt, S. Majumdar, and S. Giri, *J. Phys.: Condens. Matter* **28**, 166005 (2016).
- [13] M. Tripathi, R. J. Choudhary, D. M. Phase, T. Chatterji, and H. E. Fischer, *Phys. Rev. B* **96**, 174421 (2017).
- [14] B. Dalal, B. Sarkar, S. Rayaprol, M. Das, V. Siruguri, P. Mandal, and S. K. De, *Phys. Rev. B* **101**, 144418 (2020).
- [15] I. Dzyaloshinsky, *J. Phys. Chem. Solids* **4**, 241 (1958).
- [16] T. Moriya, *Phys. Rev.* **120**, 91 (1960).
- [17] I. Fita, R. Puzniak, A. Wisniewski, and V. Markovich, *Phys. Rev. B* **100**, 144426 (2019).
- [18] L. H. Yin, J. Yang, X. C. Kan, W. H. Song, J. M. Dai, and Y. P. Sun, *J. Appl. Phys.* **117**, 133901 (2015).
- [19] Y. Zhu, P. Zhou, T. Li, J. Xia, S. Wu, Y. Fu, K. Sun, Q. Zhao, Z. Li, Z. Tang *et al.*, *Phys. Rev. B* **102**, 144425 (2020).
- [20] J. van den Brink, G. Khaliullin, and D. I. Khomskii, *Phys. Rev. Lett.* **83**, 5118 (1999).
- [21] F. Damay, C. Martin, A. Maignan, M. Hervieu, B. Raveau, Z. Jirak, G. André, and F. Bourée, *Chem. Mater.* **11**, 536 (1999).
- [22] R. J. Goff and J. P. Attfield, *Phys. Rev. B* **70**, 140404(R) (2004).
- [23] J. Padilla-Pantoja, J. Herrero-Martín, P. Gargiani, S. M. Valvidares, V. Cuartero, K. Kummer, O. Watson, N. B. Brookes, and J. L. García-Muñoz, *Inorg. Chem.* **53**, 8854 (2014).
- [24] J. Padilla-Pantoja, J. Herrero-Martín, E. Pellegrin, P. Gargiani, S. M. Valvidares, A. Barla, and J. L. García-Muñoz, *Phys. Rev. B* **92**, 245136 (2015).
- [25] E. O. Wollan and W. C. Koehler, *Phys. Rev.* **100**, 545 (1955).
- [26] J. B. Goodenough, *Phys. Rev.* **100**, 564 (1955).
- [27] Y. Tomioka, A. Asamitsu, Y. Moritomo, H. Kuwahara, and Y. Tokura, *Phys. Rev. Lett.* **74**, 5108 (1995).
- [28] Y. Tokura, *Rep. Prog. Phys.* **69**, 797 (2006).
- [29] E. Dagotto, *New J. Phys.* **7**, 67 (2005).
- [30] E. Dagotto, *Science* **309**, 257 (2005).
- [31] J. A. Souza, J. J. Neumeier, and Y. -K. Yu, *Phys. Rev. B* **78**, 014436 (2008).
- [32] M. B. Salamon, P. Lin, and S. H. Chun, *Phys. Rev. Lett.* **88**, 197203 (2002).
- [33] J. Fan, L. Pi, Y. He, L. Ling, J. Dai, and Y. Zhang, *J. Appl. Phys.* **101**, 123910 (2007).
- [34] C. Autret, C. Martin, M. Hervieu, A. Maignan, B. Raveau, G. André, F. Bourée, and Z. Jirak, *J. Magn. Magn. Mater.* **270**, 194 (2004).
- [35] K. Tobe, T. Kimura, and Y. Tokura, *Phys. Rev. B* **69**, 014407 (2004).
- [36] H. Kawano, R. Kajimoto, H. Yoshizawa, Y. Tomioka, H. Kuwahara, and Y. Tokura, *Phys. Rev. Lett.* **78**, 4253 (1997).
- [37] V. K. Shukla and S. Mukhopadhyay, *Phys. Rev. B* **97**, 054421 (2018).
- [38] C. R. Serrao, A. Sundaresan, and C. N. R. Rao, *J. Phys.: Condens. Matter* **19**, 496217 (2007).
- [39] T. Zou, F. Wang, Y. Liu, L.-Q. Yan, and Y. Sun, *Appl. Phys. Lett.* **97**, 092501 (2010).
- [40] S. Dash, A. Banerjee, and P. Chaddah, *J. Appl. Phys.* **113**, 17D912 (2013).
- [41] S. M. Zhou, L. Shi, H. P. Yang, Y. Wang, L. F. He, and J. Y. Zhao, *Appl. Phys. Lett.* **93**, 182509 (2008).
- [42] E. Dagotto, *Nanoscale Phase Separation and Colossal Magnetoresistance: The Physics of Manganites and Related Compounds* (Springer-Verlag, Berlin, Heidelberg, 2003).
- [43] A. I. Kurbakov, V. A. Ryzhov, V. V. Runov, E. O. Bykov, I. I. Larionov, V. V. Deriglazov, C. Martin, and A. Maignan, *Phys. Rev. B* **100**, 184424 (2019).
- [44] H. Zhou, Q. Feng, Y. Hou, M. Nakamura, Y. Tokura M. Kawasaki, Z. Sheng, and Q. Lu, *npj Quantum Mater.* **6**, 56 (2021).
- [45] I. O. Troyanchuk, N. V. Kasper, D. D. Khalyavin, H. Szymczak, R. Szymczak, and M. Baran, *Phys. Rev. Lett.* **80**, 3380 (1998).
- [46] J. L. Garcia-Munoz, J. Padilla-Pantoja, X. Torrelles, J. Blasco, J. Herrero-Martín, B. Bozzo, and J. A. Rodríguez-Velamazán, *Phys. Rev. B* **94**, 014411 (2016).
- [47] M. Kriener, C. Zobel, A. Reichl, J. Baier, M. Cwik, K. Berggold, H. Kierspel, O. Zabara, A. Freimuth, and T. Lorenz, *Phys. Rev. B* **69**, 094417 (2004).
- [48] Y. Okimoto, X. Peng, M. Tamura, T. Morita, K. Onda, T. Ishikawa, S. Koshihara, N. Todoroki, T. Kyomen, and M. Itoh, *Phys. Rev. Lett.* **103**, 027402 (2009).
- [49] J. L. Garcia-Munoz, C. Frontera, A. J. Barón-González, S. Valencia, J. Blasco, R. Feyerherm, E. Dudzik, R. Abrudan, and F. Radu, *Phys. Rev. B* **84**, 045104 (2011).
- [50] K. H. Kim, T. Qian, and Bog G. Kim, *J. Appl. Phys.* **102**, 033910 (2007).
- [51] I. Fita, I. O. Troyanchuk, T. Zajarniuk, P. Iwanowski, A. Wisniewski, and R. Puzniak, *Phys. Rev. B* **98**, 214445 (2018).
- [52] I. Fita, I. O. Troyanchuk, T. Zajarniuk, A. Wisniewski, and R. Puzniak, *Phys. Rev. B* **101**, 224433 (2020).
- [53] M. Tanaka, Y. Katsuya, and A. Yamamoto, *Rev. Sci. Instrum.* **79**, 075106 (2008).
- [54] M. Tanaka, Y. Katsuya, Y. Matsushita, and O. Sakata, *J. Ceram. Soc. Jpn.* **121**, 287 (2013).
- [55] H. M. Rietveld, *J. Appl. Cryst.* **2**, 65 (1969).
- [56] F. Izumi and T. Ikeda, *Mater. Sci. Forum* **321–324**, 198 (2000).
- [57] L. Lutterotti, *Nuclear Inst. Methods Phys. Res. B* **268**, 334 (2010).
- [58] K. Momma and F. Izumi, *J. Appl. Crystallogr.* **44**, 1272 (2011).
- [59] R. Liu, R. Scatena, D. D. Khalyavin, R. D. Johnson, Y. Inaguma, M. Tanaka, Y. Matsushita, K. Yamaura, and A. A. Belik, *Inorg. Chem.* **59**, 9065 (2020).
- [60] See Supplemental Material at <http://link.aps.org/supplemental/10.1103/PhysRevB.106.104425> for the atomic positions, occupancies, and thermal displacement parameters of the structures

- of GSCO and GCCO obtained using synchrotron XRD, temperature dependence of the lattice parameters, and volume of the orthorhombic unit cells of GSCO and GCCO.
- [61] A. C. Komarek, T. Möller, M. Isobe, Y. Drees, H. Ulbrich, M. Azuma, M. T. Fernández-Díaz, A. Senyshyn, M. Hoelzel, G. André *et al.*, *Phys. Rev. B* **84**, 125114 (2011).
- [62] F. Damay, C. Martin, V. Hardy, A. Maignan, G. André, K. Knight, S. R. Giblin, and L. C. Chapon, *Phys. Rev. B* **81**, 214405 (2010).
- [63] H. L. Feng, M. Reehuis, P. Adler, Z. Hu, M. Nicklas, A. Hoser, S.-C. Weng, C. Felser, and M. Jansen, *Phys. Rev. B* **97**, 184407 (2018).
- [64] A. B. Antunes, O. Peña, C. Moure, V. Gil, and G. André, *J. Magn. Magn. Mater.* **316**, e652 (2007).
- [65] J. Blasco, J. L. García-Muñoz, J. García, G. Subías, J. Stankiewicz, J. A. Rodríguez-Velamazán, and C. Ritter, *Phys. Rev. B* **96**, 024409 (2017).
- [66] M. K. Kim, J. Y. Moon, S. H. Oh, D. G. Oh, Y. J. Choi, and N. Lee, *Sci Rep.* **9**, 5456 (2019).
- [67] R. B. Griffiths, *Phys. Rev. Lett.* **23**, 17 (1969).
- [68] C. He, M. A. Torija, J. Wu, J. W. Lynn, H. Zheng, J. F. Mitchell, and C. Leighton, *Phys. Rev. B* **76**, 014401 (2007).
- [69] A. Haldar, K. G. Suresh, and A. K. Nigam, *Europhys. Lett.* **91**, 67006 (2010).
- [70] M. Balanda, *Acta Phys. Pol. A* **124**, 964 (2013).
- [71] K. Manna, A. K. Bera, M. Jain, S. Elizabeth, S. M. Yusuf, and P. S. Anil Kumar, *Phys. Rev. B* **91**, 224420 (2015).
- [72] R. Kumar, P. Yanda, and A. Sundaresan, *Phys. Rev. B* **103**, 214427 (2021).
- [73] R. Mathieu, P. Jönsson, D. N. H. Nam, and P. Nordblad, *Phys. Rev. B* **63**, 092401 (2001).
- [74] B. Mali, H. S. Nair, T. W. Heitmann, H. Nhalil, D. Antonio, K. Gofryk, S. R. Bhandari, M. P. Ghimire, and S. Elizabeth, *Phys. Rev. B* **102**, 014418 (2020).
- [75] A. E. Berkowitz and K. Takano, *J. Magn. Magn. Mater.* **200**, 552 (1999).
- [76] J. Nogués, J. Sort, V. Langlais, V. Skumryev, S. Suriñach, J. S. Muñoz, and M. D. Baró, *Phys. Rep.* **422**, 65 (2005).
- [77] M. Patra, M. Thakur, S. Majumdar, and S. Giri, *J. Phys.: Condens. Matter* **21**, 236004 (2009).
- [78] I. Fita, V. Markovich, A. S. Moskvin, A. Wisniewski, R. Puzniak, P. Iwanowski, C. Martin, A. Maignan, R. E. Carbonio, M. U. Gutowska *et al.*, *Phys. Rev. B* **97**, 104416 (2018).
- [79] J. Geshev, *J. Appl. Phys.* **105**, 066108 (2009).
- [80] J. Nogués, D. Lederman, T. J. Moran, and I. K. Schuller, *Phys. Rev. Lett.* **76**, 4624 (1996).
- [81] J. Nogués, C. Leighton, and I. K. Schuller, *Phys. Rev. B* **61**, 1315 (2000).
- [82] D. Niebieskikwiat and M. B. Salamon, *Phys. Rev. B* **72**, 174422 (2005).
- [83] J. Krishna Murthy and P. S. Anil Kumar, *Sci. Rep.* **7**, 6919 (2017).
- [84] Y. Y. Jiao, Q. Cui, P. Shahi, N. N. Wang, N. Su, B. S. Wang, M. T. Fernández-Díaz, J. A. Alonso, and J. -G. Cheng, *Phys. Rev. B* **97**, 014426 (2018).
- [85] D. A. Salamatin, N. Martin, V. A. Sidorov, N. M. Chtchelkatchev, M. V. Magnitskaya, A. E. Petrova, I. P. Zibrov, L. N. Fomicheva, J. Guo, C. Huang *et al.*, *Phys. Rev. B* **101**, 100406(R) (2020).
- [86] J. Y. Moon, M. K. Kim, Y. J. Choi, and N. Lee, *Sci. Rep.* **7**, 16099 (2017).
- [87] M. Das, P. Sarkar, and P. Mandal, *Phys. Rev. B* **101**, 144433 (2020).
- [88] J. Y. Moon, M. K. Kim, D. G. Oh, J. H. Kim, H. J. Shin, Y. J. Choi, and N. Lee, *Phys. Rev. B* **98**, 174424 (2018).
- [89] P. Mandal, V. S. Bhadram, Y. Sundarayya, C. Narayana, A. Sundaresan, and C. N. R. Rao, *Phys. Rev. Lett.* **107**, 137202 (2011).
- [90] A. Shaw, A. Mitra, S. D. Kaushik, V. Siruguri, and P. K. Chakrabarti, *J. Magn. Magn. Mater.* **488**, 165338 (2019).
- [91] M. Goto, T. Oguchi, and Y. Shimakawa, *J. Am. Chem. Soc.* **143**, 19207 (2021).



Spectroscopic and magnetic investigations of the dilute magnetically doped semiconductors $\text{BaSn}_{1-x}\text{Mn}_x\text{O}_3$ ($0.02 \leq x \leq 0.1$)

Ankita Sarkar^{a,1}, Biswajit Dalal^{b,*}, Subodh Kumar De^{a,**}

^a School of Materials Sciences, Indian Association for the Cultivation of Science, 2A & 2B Raja S. C. Mullick Road, Jadavpur, Kolkata, 700032, India

^b Department of Physics, Achhruram Memorial College, Jhalda, Purulia, West Bengal, 723202, India

ARTICLE INFO

Keywords:

Perovskite oxide
Dilute magnetic semiconductor
Antiferromagnetic interaction
Electron paramagnetic resonance
Singly ionized oxygen vacancy

ABSTRACT

Dilute magnetically doped semiconductors (DMSs) are key to fabricating novel spintronic devices with high functionalities, which could be utilized for the next-generation technological development. BaSnO_3 is a transparent wide band gap (~ 3.1 eV) semiconductor, in which magnetism can be induced through a subtle amount of magnetic impurity doping without deterring its optical transparency. In this work, we report an experimental investigation on the optical spectroscopic and magnetic properties of the DMSs $\text{BaSn}_{1-x}\text{Mn}_x\text{O}_3$ ($0 \leq x \leq 0.1$), synthesized using standard solid-state-reaction method at high-temperature and ambient pressure, through various spectroscopic, electron paramagnetic resonance (EPR) and temperature- and field-dependent magnetization measurements. All samples are found to be crystallize in the cubic structure with space group $Pm\bar{3}m$, in which Mn ions are stabilized in the 4+ valence state. We find that the optical band gap monotonically decreases (from 3.1 eV to 2.08 eV) with increase in Mn doping concentration, which in turn leads to an increase in absorption efficiency in the visible region. An enhanced *sp-d* hybridization between localized *d* electrons of Mn ions and band electrons is likely the main reason for such band gap reduction. Interestingly, theoretical simulation of EPR spectra suggests that the signal is primarily arising from a combination of two spin systems, i.e., Mn^{4+} ions and singly ionized oxygen vacancies. The strength of magnetic interaction between Mn^{4+} ions is also increased for higher doped samples. Moreover, the nature of magnetic interaction is predominantly antiferromagnetic in higher doped samples, as corroborated by the negative value of Curie-Weiss temperature from the inverse susceptibility fitting.

1. Introduction

The discovery of ferromagnetism above room-temperature in dilute magnetically doped semiconductors (DMSs), first theoretically predicted by Dietl et al. [1] and later confirmed by numerous experimental results [2–7], has opened up a new window for the development of the spintronic devices, which can simultaneously make use of both the spin and charge degrees of freedom in a materials system. In particular, the wide band gap semiconductors, such as ZnO, SnO_2 , TiO_2 , and In_2O_3 , were extensively investigated through transition-metal (especially Mn and Co) ion doping over the past few decades to achieve the room-temperature ferromagnetism (RTFM) in DMSs [2–11]. Till date, several binary oxides have been widely studied in the progress of the research on DMSs; but they have few limitations, such as, the lack of

high operation speed and good oxygen stability.

Oxide materials with the perovskite structure are known to have extremely good oxygen stability, and have shown a plethora of excellent electronic, optical and magnetic properties, such as, ferroelectricity, multiferroicity, superconductivity, high mobility and transparency, which could introduce new functionalities to spintronic devices [12–14]. In view of this, more comprehensive research effort has been given to obtain new DMSs with high functionalities using such diverse physical properties of perovskite-structured oxides. Till now, several transition-metal doping studies, for example, Co-doped BaTiO_3 and $\text{Ba}_{0.5}\text{Sr}_{0.5}\text{TiO}_3$, and Co- or Fe-doped SrTiO_3 [15–19], have been performed for realizing the RTFM in nonmagnetic perovskite oxides. Moreover, they belong to a class of materials having wide band gap, which could also facilitate them to become a potential candidate for

* Corresponding author.

** Corresponding author.

E-mail addresses: b.dalal.iitd@gmail.com (B. Dalal), msskd@iacs.res.in (S.K. De).

¹ AS and BD contributed equally to this work.

transparent conducting oxides.

In the perovskite family of oxides, the alkaline-earth stannates with the general chemical formula ASnO_3 ($A = \text{Ba, Ca or Sr}$) have attracted much greater attention from researchers due to their interesting physical properties and potential applications, such as photovoltaic and/or photoelectrochemical energy conversions, stable capacitors, humidity sensors, and gas sensors, in semiconductor industry [20–22]. Among ASnO_3 compounds, BaSnO_3 (BSO) usually crystallizes in an ideal cubic structure, and has emerged as a transparent wide band gap semiconductor with an optical band gap of ~ 3.1 eV [23]. Recently, several dopants have been chosen to substitute both the Ba and Sn sites of BSO in order to enhance the electrical conductivity and induce the magnetism. For example, the high electrical conductivity and mobility at room-temperature was found in the transparent perovskite oxides (Ba, La) SnO_3 and $\text{Ba}(\text{Sn,Sb})\text{O}_3$ [14,24]. Nevertheless, the RTFM has been reported for Mn and Fe-doped BSO compounds [25–27], and the origin of such ferromagnetism has been explained on the basis of either the F-center exchange mechanism (for bulk powder samples) or the coalescence of the magnetic polarons (for thin films). However, more comprehensive research using various experimental tools is necessary in order to unveil the change in the structural, optical and magnetic properties of such semiconductor systems due to magnetic ion doping.

In this article, we report the optical spectroscopic and magnetic properties of the polycrystalline $\text{BaSn}_{1-x}\text{Mn}_x\text{O}_3$ ($0 \leq x \leq 0.1$) samples, which typically form an ideal cubic perovskite structure with space group $Pm\bar{3}m$ and contain only Mn^{4+} ions. The vibrational spectroscopy study confirms the successful incorporation of Mn ions into the host lattice and the presence of oxygen vacancy in the doped samples. Optical absorption spectra reveals that the band gap reduces drastically from 3.1 eV for $x = 0$ to 2.08 eV for $x = 0.1$ due to the enhanced $sp-d$ hybridization between localized d electrons of Mn ions and band electrons. Moreover, precise analyses of the EPR and magnetization data suggested that the observed behavior of both these data can only be analyzed by considering the contributions from both Mn^{4+} ions and singly ionized oxygen vacancies. More importantly, the higher doped samples (for example, $x = 0.1$) showed predominant antiferromagnetic interaction, instead of ferromagnetic behavior.

2. Experimental details

High quality single-phase polycrystalline samples with compositions $\text{BaSn}_{1-x}\text{Mn}_x\text{O}_3$ ($0 \leq x \leq 0.1$) were prepared by the standard solid-state-reaction method at high-temperature and ambient pressure. Stoichiometric quantities of high purity oxides BaCO_3 (Sigma Aldrich; 99.999%), SnO_2 (Sigma Aldrich; 99.9%) and MnO_2 (Sigma Aldrich; 99%) were mixed thoroughly in an agate mortar for 1 h and calcined at 1200 °C for 6 h in air. After furnace cooled, these samples were reground thoroughly for better homogeneity and pressed into a cylindrical pellet using uniaxial hydraulic press. The pellets were then sintered twice in air at 1300 °C for 12 h with intermediate grinding to obtain better crystalline phases.

The phase purity of the as-synthesized samples was checked by x-ray powder diffraction (XRD) measurements using X-Pert Pro, PANalytical diffractometer (equipped with $\text{CuK}\alpha$ radiation, $\lambda = 1.5418$ Å) in the 2θ range 10° – 90° . In order to get more information about the crystal structures of the samples, XRD patterns were analyzed by the Rietveld refinement method [28] using the software MAUD [29]. Raman spectra were collected at room-temperature by an He–Ne laser of $\lambda = 632$ nm using a J-Y Horiba (model T64000) Raman spectrophotometer. Fourier transform infrared (FTIR) spectra of the samples were taken using a PerkinElmer Spectrochem 100 FTIR spectrometer. To analyze the chemical states of the constituent atoms, room-temperature core-level x-ray photoelectron spectroscopy (XPS) measurements were carried out with an SSX-100 ESCA spectrometer (Omicron, model: 1712-62-11) using Al $K\alpha$ radiation, 1486.6 eV line, and a spot size of 800 nm.

Room-temperature optical reflectance data of the samples was recorded by a Varian Cary 5000 ultraviolet (UV)-vis-near-infrared (NIR) spectrophotometer. Electron paramagnetic resonance (EPR) measurements at room-temperature were performed at X-band (9.5 GHz) using JEOL spectrometer. The dc magnetization (M) measurements were carried out in a Quantum Design's MPMS 3 superconducting quantum interference device-vibrating sample magnetometer within the temperature (T) interval 2–300 K and a magnetic field (H) up to ± 50 kOe.

3. Results and discussion

3.1. Crystal structure

The XRD patterns of undoped and Mn-doped BSO samples are shown in Fig. 1(a). Pure BSO usually crystallizes in a perfectly cubic structure with space group $Pm\bar{3}m$ (No. 221) at ambient condition [23]. The presence of diffraction peaks (110), (111), (200), (211), (220), (310), (222) and (321) related to the cubic $Pm\bar{3}m$ phase clearly suggests the single-phase nature of the pure BSO. Further, all of the diffraction peaks of Mn-doped BSO samples can be well indexed with the cubic structure (space group: $Pm\bar{3}m$) of pure BSO. No impurity peaks owing to the evolution of any secondary phases are found in the XRD patterns of $x = 0$ – 0.1 samples. However, an attempt to synthesize the higher doped samples (such as, $x > 0.1$) dictates that the single-phase remains intact only up to $x = 0.1$ doping limit in the present synthesis condition.

To identify the subtle structural changes with doping, Rietveld analyses were carried out by refining the structural and microstructural parameters. The Rietveld-fitted XRD patterns along with the difference between the observed and calculated spectra for $x = 0$ and 0.1 are shown in Fig. 1(b) and (c), respectively. No such anomalous changes, which can be attributed to the structural phase changes, with doping is observed from the Rietveld refinements. It is seen that the lattice parameter (a) monotonously decreases with the increases in the Mn-doping level at the Sn-site of pure BSO [see Fig. 1(d)]. The contraction in the lattice parameter is due to the lower effective ionic radius of the six-coordinated (octahedrally) Mn^{4+} ion (0.53 Å) than that of the six-coordinated Sn^{4+} ion (0.69 Å) [30]. This clearly ratifies the successful incorporation of Mn ions into the lattice of BSO.

3.2. X-ray photoelectron spectroscopy

To investigate the chemical valence state of dopant Mn ions, and to probe the existence of surface adsorptive oxygen in the sample, the core-level XPS spectra of Mn and O have been analyzed using XPSPEAK 4.1 software. The Mn $2p$ core-level XPS spectra for $x = 0.06$ is shown in Fig. 2(a). It is seen that the Mn $2p$ spectrum consists of two high intense peaks centered at 639.8 eV and 651.5 eV, and a shoulder peak centered at 643.7 eV. These two high intense peaks mainly correspond to $2p_{3/2}$ and $2p_{1/2}$ spin-orbit (SO) doublets. Thus, the Mn $2p$ SO doublet is separated by about 11.7 eV. It is worthwhile to mention that the energy separation of the SO doublet depends on the strength of SO coupling, and thus on the valence state of the particular ion [31]. An energetic separation of the SO doublets about 11.7 eV confirms that $x = 0.06$ sample contains only Mn^{4+} ions, which is consistent with the earlier reports [32,33]. A small shoulder peak at 643.7 eV can be attributed to Mn^{4+} satellite [32]. Moreover, the satellite to Mn $2p_{3/2}$ peak is reported to be observed on the higher binding energy side, while maintaining the separation energy nearly equal to 12 eV between two satellite peaks [32].

The O $1s$ spectra for $x = 0.06$ is shown in Fig. 2(b). Due to the asymmetric and broad nature of the O $1s$ spectra, deconvolution of the peak profile was done using a Gaussian-Lorentzian distribution function. The O $1s$ peak was fitted considering two peaks, and the obtained peaks are centered at 528.59 eV and 529.77 eV for $x = 0.06$. The peak at lower binding energy is normally associated with the lattice oxygen in

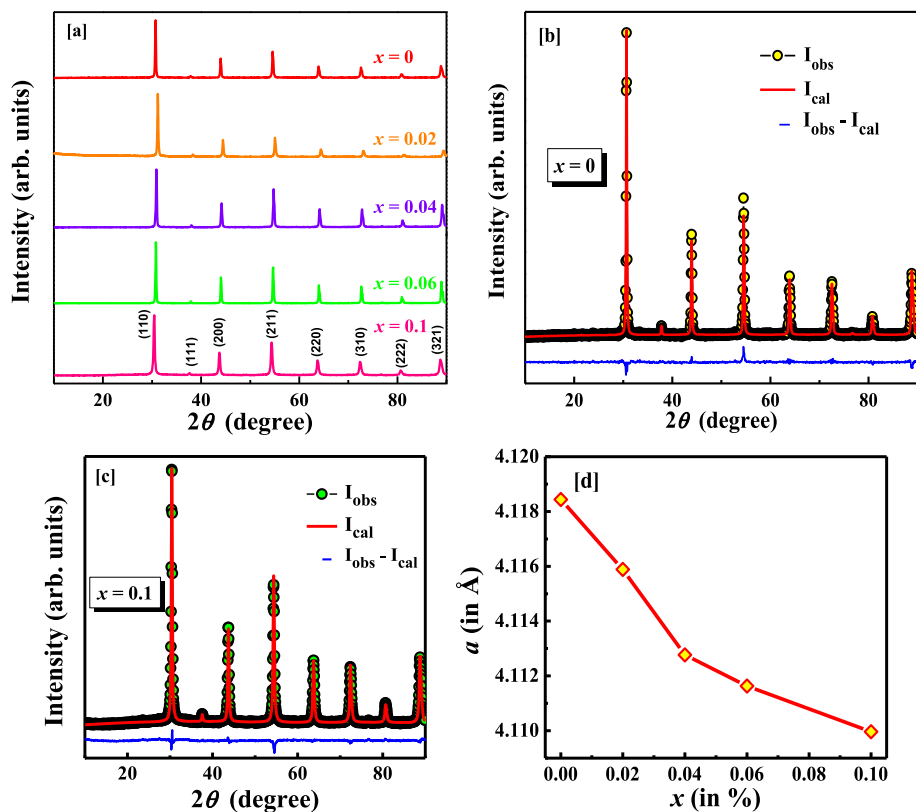


Fig. 1. (a) Room-temperature powder XRD pattern $\text{BaSn}_{1-x}\text{Mn}_x\text{O}_3$ ($0 \leq x \leq 0.1$) samples. Rietveld refinement of powder XRD pattern for (b) $x = 0$ and (c) $x = 0.1$ samples at room-temperature. The black filled circles and solid red line represents the observed and calculated XRD patterns, respectively. The blue line represents the difference between the observed and calculated patterns. (d) The variation of lattice parameter (a) with compositions.

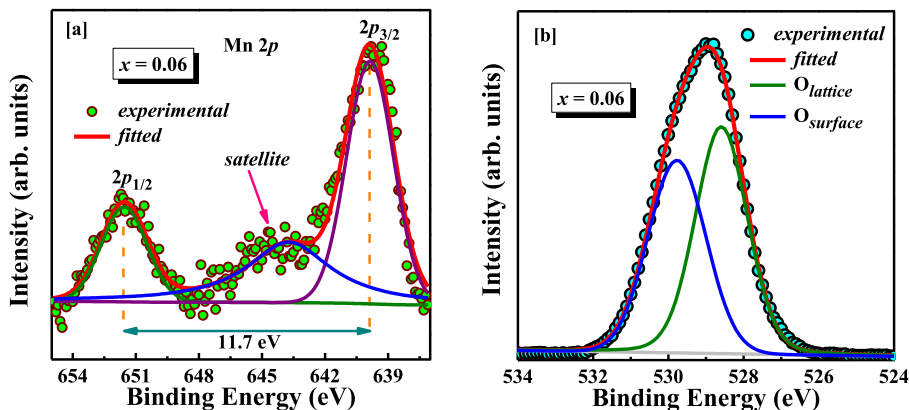


Fig. 2. (a) Core-level XPS spectra of Mn $2p$ level for $x = 0.06$ sample in $\text{BaSn}_{1-x}\text{Mn}_x\text{O}_3$ series at room temperature. (b) The O $1s$ spectra for $x = 0.06$, which shows the presence of surface adsorbed oxygen in the sample.

perovskite oxides. However, according to earlier report [34], the peak at higher binding energy is mainly related to the surface adsorptive oxygen, which has close resemblance to the oxygen vacancy, which has close resemblance to the oxygen vacancy. Note that synthesis procedure can play a crucial role for the creation of oxygen vacancy in the BSO lattice. As the sintering process occurs in air, oxygen is exchanged with the surrounding medium [35].

3.3. Raman spectra

Raman spectroscopy is indeed a powerful experimental technique to probe the dopant incorporation and lattice defects, and to detect the evolution of new phases in the host lattice. Despite the fact that no first-

order Raman-active modes seem to be appeared in the ideal cubic perovskite structure, such as, in highly symmetric cubic BSO with space group $Pm\bar{3}m$, the Raman spectrum for $x = 0$ in Fig. 3 shows some prominent peaks [36,37]. Since the dopant atoms and/or, oxygen vacancies truly affect the translational periodicity of the lattice, the observation of these Raman modes can be ascribed to the local loss of symmetry. Moreover, the most intense Raman bands at 135 cm^{-1} and 154 cm^{-1} for $x = 0$ are quite common in the rhombohedrally distorted perovskite structures [38]. Besides, the lattice-dynamical calculations have predicted that the Raman lines at 135 and 154 cm^{-1} can be assigned to A_{1g} and A_{2g} symmetries, respectively; while, the peak at 570 cm^{-1} is appeared due to Sn-O vibrational mode [37]. So, it can be

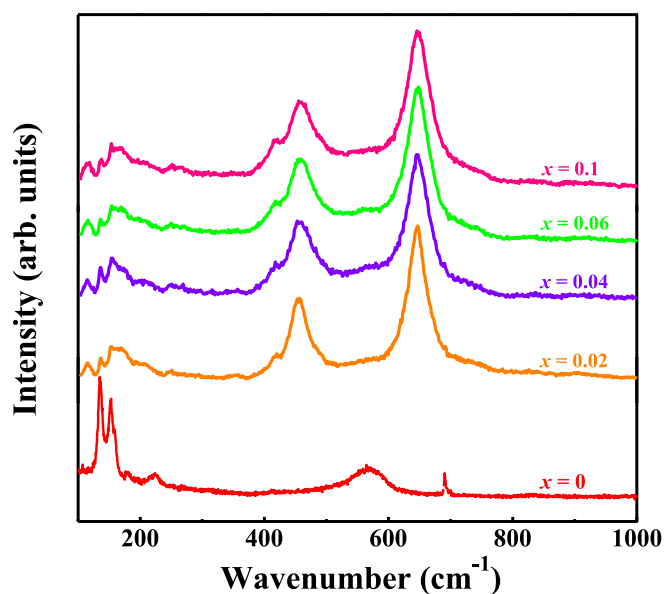


Fig. 3. Raman spectra for $\text{BaSn}_{1-x}\text{Mn}_x\text{O}_3$ ($0 \leq x \leq 0.1$) samples in the wavenumber region $100\text{--}1000\text{ cm}^{-1}$.

concluded that the oxygen vacancies presumably have an important role for the observation of Raman-active modes in $x = 0$.

Furthermore, the breaking of the translational symmetry by virtue of the substitution of Mn^{4+} ion at the Sn-site, in addition to the oxygen vacancy, plays a significant role for the appearance of Raman-active modes in the doped samples [see Fig. 3] [39]. The peak at 570 cm^{-1} for $x = 0$ is completely disappeared with Mn doping; whereas, three new Raman lines centered at 116 , 454 and 648 cm^{-1} appear in the doped samples. The intensity of the Raman lines at 135 and 154 cm^{-1} also reduces with Mn doping, and the Raman modes at 454 cm^{-1} and 648 cm^{-1} become the most intense peaks in doped samples. From our XPS analysis of O 1s spectra, it is evident that the doped samples contain surface adsorptive oxygen and/or, oxygen vacancy, and the percentage of which increases with the increase of doping concentration. The new mode centered at 454 cm^{-1} mainly involved with the oxygen motion, which means the formation of specific defects in host lattice i.e., oxygen vacancies [40,41]. The mode at 648 cm^{-1} is likely to be associated with the Mn–O stretching vibration [42]. Thus, the appearance of a number of Raman-active modes unequivocally fortifies the local lattice distortion induced by oxygen vacancies and dopants in the cubic phase of undoped and doped BSO samples.

3.4. Fourier transform infrared (FTIR) spectra

The FTIR spectra for $x = 0\text{--}0.1$ samples are shown in Fig. 4. A strong minimum in the transmittance data for pure BSO is appeared at 635 cm^{-1} , which can be attributed to the asymmetric stretching vibrational mode of Sn–O bond [43]. It is to be noted that the characteristic vibration of Mn–O and O–Mn–O bonds in the Mn-based oxides usually arise at 522 and 1407 cm^{-1} , respectively [44,45]. Thus, the band centered at 635 cm^{-1} broadens with Mn doping due to the overlap between the Sn–O bond and Mn–O bond. In addition, the vibration of Sn–OH group is most likely to be responsible for the band observed at 1422 cm^{-1} for $x = 0$ [46]. However, the overlapping of O–Mn–O bond and Sn–OH bond causes the band broadening, and as a result, we observe a broader band at 1422 cm^{-1} for the Mn-doped samples. Another broad band centered around 1630 cm^{-1} is seen in the FTIR spectra of $x > 0$, which can be assigned to the stretching mode of OH^- bond [46]. A sharp dip at 860 cm^{-1} for $x > 0$ mainly corresponds to the C–O stretching modes of the CO_3^{2-} ions, signifying that CO_2 is absorbed

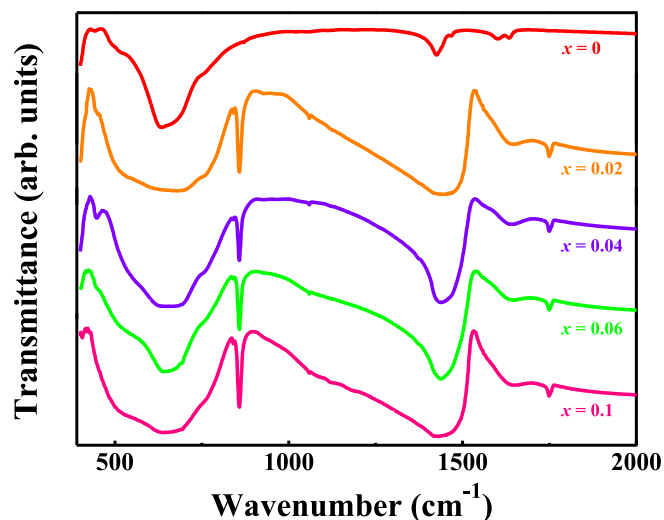


Fig. 4. FTIR spectra for $\text{BaSn}_{1-x}\text{Mn}_x\text{O}_3$ ($0 \leq x \leq 0.1$) samples in the wavenumber region $390\text{--}2000\text{ cm}^{-1}$.

by the samples during the measurement [47].

3.5. Optical absorption spectra

The diffuse reflectance spectra for $x = 0\text{--}0.1$ are displayed in Fig. 5 (a). However, using Kubelka-Munk transformation, we can determine the optical absorbance coefficient (α) for all the samples. The Kubelka-Munk function $F(R)$, which approximately gives us the absorbance, can be defined as [48,49]:

$$F(R) = \frac{(1 - R)^2}{2R} \quad (1)$$

where R is the reflectance. Here, the function $F(R)$ is proportional to optical absorption coefficient (α). The absorption spectra for all the samples are shown in Fig. 5(b). Further, the optical band gap (E_g) can be estimated from the calculated absorption coefficient using the following relation:

$$\alpha h\nu = C(h\nu - E_g)^n \quad (2)$$

where h is the Planck's constant, ν is the incident light frequency, C is the absorption constant, $n = 1/2$ for a direct allowed transition and $n = 2$ for an indirect allowed transition. In this study, the direct band gap for $x = 0\text{--}0.1$ samples has been calculated by extrapolating a straight line towards the $h\nu$ -axis of the Tauc plot [$(\alpha h\nu)^2$ vs $h\nu$], as shown in Fig. 5(c).

The band gap of pure BSO is usually defined as the energy difference between the conduction band minima of Sn 5s bands which are completely vacant for Sn^{4+} ($4d^{10}5s^05p^0$) and the valence band maxima of O 2p bands. From the Tauc plot, the direct band gap of pure BSO is found to be 3.1 eV , which is consistent with the direct band gap value predicted in earlier studies [23]. The hybridization between O 2p orbitals and Sn 5s orbitals results in a clear optical absorption edge at 400 nm [see Fig. 5(b)], thus also confirming the band gap of 3.1 eV for $x = 0$. It is seen that the band gap reduces drastically from 3.1 eV for $x = 0$ to 2.08 eV for $x = 0.1$. Incorporation of Mn^{4+} ions into the lattice of BSO unequivocally enhances the sp - d hybridization between localized d electrons of Mn ions and band electrons, and as a result, the band gap decreases monotonously with increasing doping concentration. In addition, the doped samples appear as darker in color due to the enhanced absorption of light, and thus, increase the absorption efficiency in visible region.

The charge-transfer excitation between O 2p and Mn 3d is considered to be an important precursor for the observed band gap absorption in the

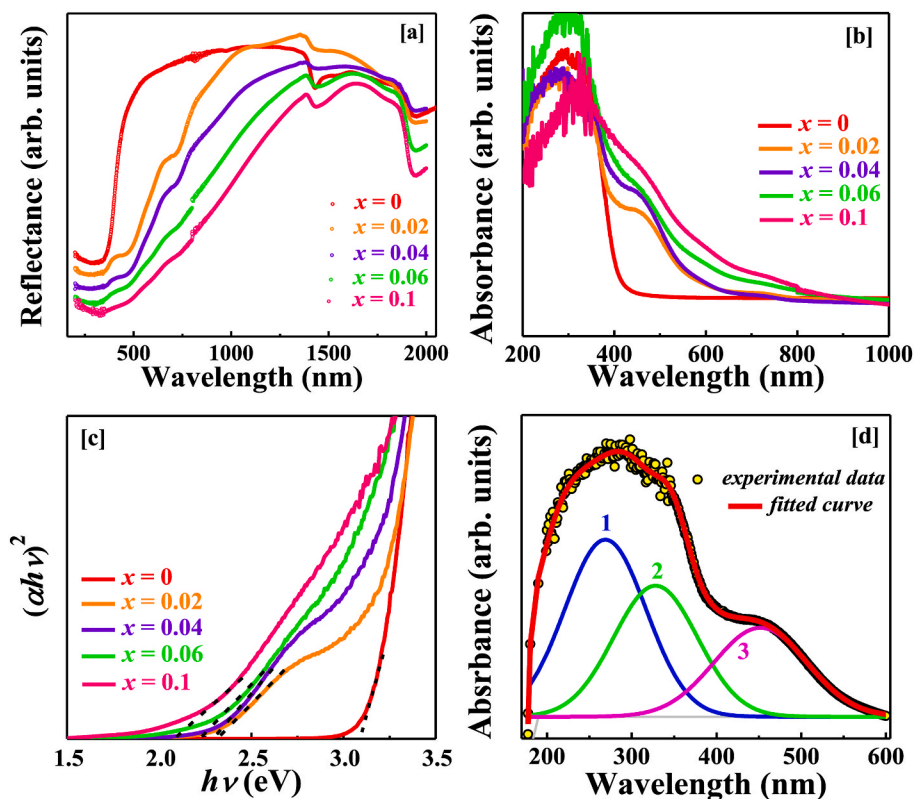


Fig. 5. (a) Optical reflectance spectra for $\text{BaSn}_{1-x}\text{Mn}_x\text{O}_3$ ($0 \leq x \leq 0.1$) samples. (b) UV-vis-NIR optical absorption spectra for $\text{BaSn}_{1-x}\text{Mn}_x\text{O}_3$ ($0 \leq x \leq 0.1$) samples. (c) Tauc plot of $\text{BaSn}_{1-x}\text{Mn}_x\text{O}_3$ ($0 \leq x \leq 0.1$) samples in UV-vis-NIR region for the determination of optical band gap. (d) The deconvoluted optical absorption spectra for $x = 0.02$. The peak 1 corresponds to the charge-transfer excitation band; while, peaks 2 and 3 correspond to the spin-allowed transition bands.

doped samples. To further analyze the origin of broad absorption spectrum, we have deconvoluted the spectrum for $x = 0.02$ with multiple peaks [see Fig. 5(d)]. The absorption band centered at ~ 270 nm (in UV region) mainly appears due to $\text{Mn}^{4+}\text{-O}^{2-}$ charge-transfer transition [50–52]. Besides, the absorption band located at ~ 450 nm can be assigned to the spin-allowed transition of Mn^{4+} : ${}^4\text{A}_{2g} \rightarrow {}^4\text{T}_{2g}$ [51]. Another spin-allowed transition of Mn^{4+} : ${}^4\text{A}_{2g} \rightarrow {}^4\text{T}_{1g}$ results in an absorption band at ~ 320 nm. The overlapping of the charge-transfer band at 270 nm and the spin-allowed transition band at 320 nm leads to a broad absorption band centered at 300 nm in the Mn-doped samples.

3.6. Electron paramagnetic resonance (EPR)

EPR has tuned into an important tool in order to investigate the spin dynamics of the dilute magnetically doped semiconductors (DMSs) having wide band gap. In particular, EPR spectrum provides the information about the nature of spin-spin interactions and the distribution of internal molecular magnetic field, which give us the accessibility to realize the various magnetic phases (such as, paramagnetic, antiferromagnetic cluster, spin-glass) that the materials possess. The EPR spectra at room-temperature for $x = 0.02\text{--}0.1$ are shown in Fig. 6. The EPR spectra showed a predominant sextet hyperfine structure, arising from the nuclear spin $I = 5/2$ of the isotope Mn^{55} . In this context, it is worthwhile to mention that pure BSO normally shows EPR signal due to the singly ionized oxygen vacancies ($\text{V}_\text{o}^\bullet$) [34].

In order to get a comprehensive idea about the nature of magnetism, the EPR spectrum for each sample was simulated using the *Easyspin* package based on MATLAB [53]. Each spectrum has been simulated by considering a combination of two spin systems (here, *System 1* and *System 2*). *System 1* has spin value $S = 3/2$ with g value centered on 1.958 in rhombic symmetry corresponding to the Mn^{4+} ions, and *System 2* has isotropic g value originating from V_o centers. For d^3 electronic system (S

$= 3/2$), the EPR spectra generally exhibits orthorhombicity [54], which is observed for the doped samples. The ground state of d^3 system ($S = 3/2$) in an octahedral field is ${}^4\text{A}_2$, which interact with excited T_{2g} state by spin-orbit coupling. In an external magnetic field, the degeneracy of the ground state is lifted, and the ground state splits into two Kramer's doublets separated by $2D$ where D is the zero-field splitting parameter. The g value shifts due to the mixing of the ground state and the excited ${}^4\text{T}_2$ state, which splits into an orbital singlet and orbital doublet states. Thus, the mixing with ${}^4\text{T}_2$ state, interaction with other levels and the spin-orbit coupling collectively lead to the zero-field splitting. The spin-Hamiltonian for d^3 electron system ($I = 5/2, S = 3/2$) in octahedral environment is

$$H = \beta B g \cdot S + D \left[S_z^2 - \frac{S(S+1)}{3} \right] + I \cdot A \cdot S \quad (3)$$

where the first term is Zeeman interaction, the second term is zero-field splitting, and the third term is hyperfine interaction between electron and nuclear spins.

The value of g , line width (lw) of each component, hyperfine splitting constants, and zero-field splitting parameters have been estimated based on the simulation of experimental data for $x = 0.02\text{--}0.1$, as shown in Table 1. Thus, each spectrum consists of a hyperfine split sextet line with splitting constant (A) 78 Oe and a broad signal coming from oxygen vacancy [see Fig. 6(a)–(d)]. This hyperfine structure centered on the parameter $g = 1.958$ and having a hyperfine splitting constant A nearly equal to 78 G (220 MHz) can be attributed to the Mn^{4+} ($3d^3, S = 3/2$) ion [55,56]. It is to be noted that the line width (lw) and the hyperfine splitting constant (A) have one-to-one correspondence between them. Moreover, the combined values of these two parameters result in a measurement of overall width of the sextet. From the obtained simulation results, it is found that the combined value of lw and A for *System 1* increases with increasing Mn doping concentration, suggesting an

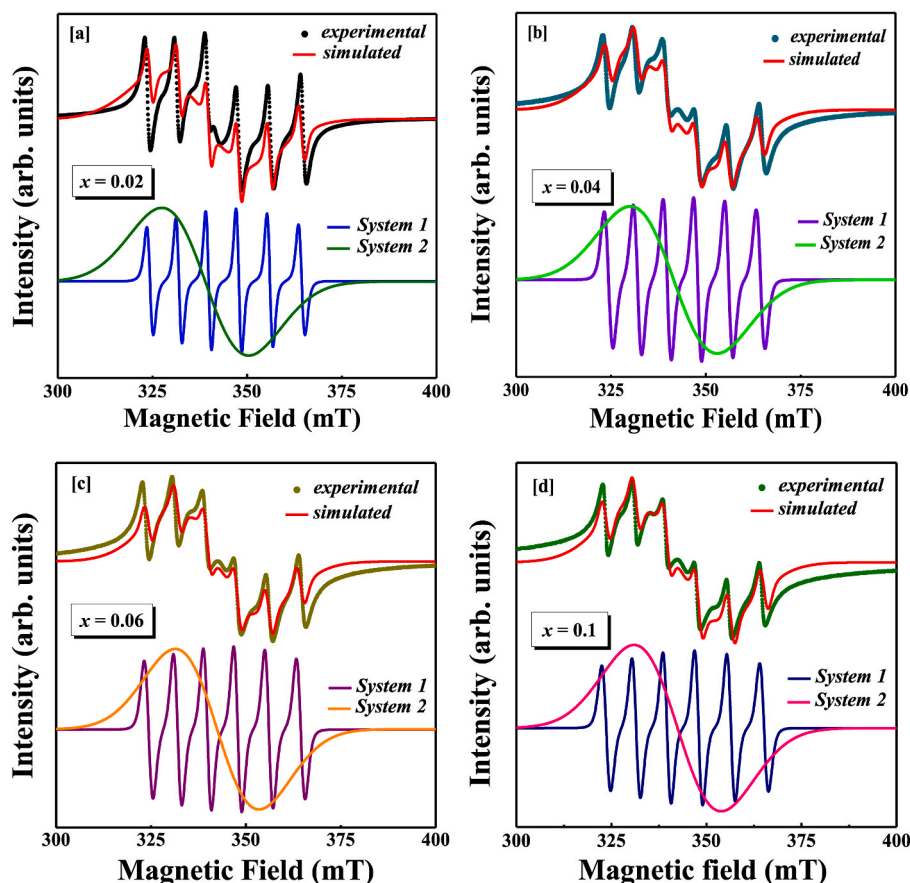


Fig. 6. Experimental (symbols) and simulated (red line) EPR spectra for (a) $x = 0.02$, (b) $x = 0.04$, (c) $x = 0.06$, and (d) $x = 0.1$ at room-temperature. System 1 and System 2 correspond to the contributions from Mn^{4+} ions and V_0 centers, respectively.

Table 1
Simulated parameters of EPR data for different samples at room-temperature.

Doping Concentration (x)	System 1 ($S = 3/2$)					System 2 ($S = 1/2$)	
	g_x	g_y	g_z	A (MHz)	lw (mT)	g	lw (mT)
0.02	1.954	1.958	1.960	220	1.5	1.990	27
0.04	1.954	1.958	1.960	220	2.2	1.975	27
0.06	1.954	1.958	1.960	222	2.2	1.971	27
0.1	1.954	1.958	1.960	228	2.2	1.970	27

increased magnetic interaction between Mn^{4+} ions in the higher doped samples. This also indicates that dipole-dipole interaction is acting among all the paramagnetic centers simultaneously [25]. In contrast, the g value for System 2 slightly decreases with increasing Mn concentration, indicating an enhanced effective molecular magnetic field. However, these g -values for the singly ionized oxygen vacancy lie in the range ~ 1.970 – 1.990 , which is very close to the reported g -value range ~ 1.963 – 1.9920 of singly ionized oxygen vacancy [57].

3.7. Magnetization

The temperature (T) dependence of the zero-field-cooled (ZFC) and field-cooled (FC) magnetic susceptibilities (χ) measured under an applied magnetic field (H) of 500 Oe for $x = 0.06$ and 0.1 are displayed in Fig. 7(a) and (b), respectively. On heating from extreme low temperature (here 2 K), both ZFC and FC susceptibilities for $x = 0.06$ and 0.1 show a decrease in the value with increasing temperature. However, no evidence of long-range magnetic ordering and significant divergence

between ZFC and FC susceptibilities are found for both samples within the investigated temperature range 2–300 K. Although, the samples seem to be paramagnetic (PM) from χ vs. T plots, the inverse susceptibility (χ^{-1}) data do not follow the Curie-Weiss behavior (see the inset in Fig. 7(b)). The observed behavior of $\chi^{-1}(T)$ is quite uncommon in DMSs, and we argue that it may be arising from a combination of two magnetic phases and/or, elements.

As evident from our EPR analysis, both $x = 0.06$ and 0.1 samples contain $3d \text{Mn}^{4+}$ ions and singly ionized oxygen vacancies. Considering that the unusual behavior of $\chi^{-1}(T)$ is arising from a combination of Mn^{4+} ions and singly ionized oxygen vacancies, the $\chi^{-1}(T)$ data is fitted to the equation

$$\chi = \left[(1-y) \frac{C}{T-\theta} + \chi_0 \right] + y \frac{0.363}{T} \quad (4)$$

where y indicates the amount of singly ionized oxygen vacancy, χ_0 is a temperature-independent contribution to the magnetic susceptibility, and C and θ are Curie constant and Curie-Weiss temperature, respectively. The well-fitting to the inverse susceptibility data using above equation for $x = 0.1$ is displayed in Fig. 7(c), which confirms the contributions from both Mn^{4+} ion and singly ionized oxygen vacancy towards the magnetism. The obtained values of y , C , θ and χ_0 are 0.128, 0.0388 (emu-K)/(mol-Oe), -16 K and 6.89×10^{-4} emu mol $^{-1}$ Oe $^{-1}$, respectively. The negative value of θ suggests that the antiferromagnetic (AFM) interaction is dominant in $x = 0.1$ sample, arising from Mn^{4+} -O-Mn $^{4+}$ superexchange interaction. In case of lower doped samples, the non-interacting distant Mn^{4+} ions at the randomly substituted matrix of BSO perhaps induces the paramagnetic nature. Due to the availability of decent Mn^{4+} ions, the AFM coupling becomes stronger in the higher doped sample (e.g., $x = 0.1$).

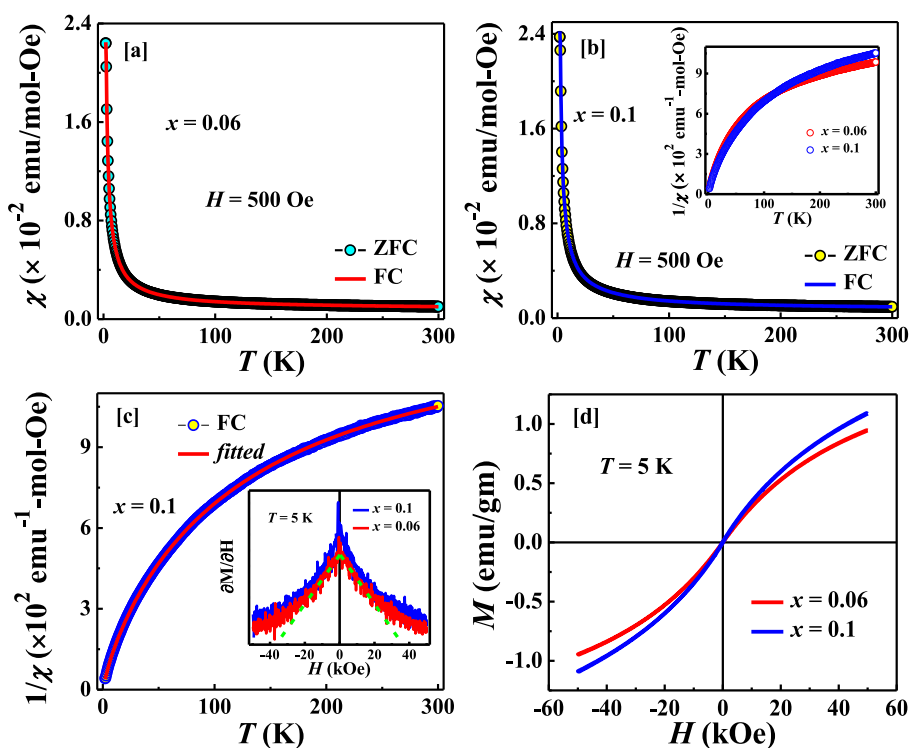


Fig. 7. Temperature dependence of the ZFC (symbols) and FC (lines) magnetic susceptibilities for (a) $x = 0.06$ and (b) $x = 0.1$, measured with an applied magnetic field H of 500 Oe in the temperature range of 2–300 K. Inset in (b) shows the temperature dependence of the inverse susceptibilities for $x = 0.06$ and 0.1, using FC data. The red line in (c) depicts the fit to the inverse susceptibility data using equation (4) for $x = 0.1$. (d) Isothermal magnetic field-dependent magnetization (M – H) curves at $T = 5$ K for $x = 0.06$ and 0.1. Inset in (c) displays the first derivative of magnetization with respect to magnetic field $\partial M/\partial H$ as a function of H for $x = 0.06$ and 0.1.

Isothermal magnetization curves (M versus H) at $T = 5$ K for $x = 0.06$ and 0.1 are shown in Fig. 7(d). The observed M – H curves having negligible coercive field are akin to that of previously reported Mn-based DMS systems [58]. The magnetization does not saturate in both the cases for fields as large as 50 kOe, clearly indicating the PM/AFM nature of the samples. However, a closer inspection of the first derivative of magnetization $\partial M/\partial H$ (see the inset in Fig. 7(c)) reveals a much more complex phenomenon of magnetic interactions, other than simple PM phase. It should be noted that one would expect the constant value of $\partial M/\partial H$ for linear response of magnetization with field in case of an ideal paramagnet.

4. Conclusions

In conclusion, we have successfully synthesized the polycrystalline samples of DMSs $\text{BaSn}_{1-x}\text{Mn}_x\text{O}_3$ ($0 \leq x \leq 0.1$) by standard solid-state-reaction method, and investigated the structural, optical spectroscopic and magnetic properties. Precise analysis of the XRD data reveals that all samples crystallize in the cubic structure with space group $Pm\bar{3}m$, and the lattice parameter monotonously decreases owing to the incorporation of smaller ionic radii Mn^{4+} ions into the lattice of BSO. The optical band gap decreases with increase of Mn dopants concentration due to the enhanced sp – d hybridization between localized d electrons of Mn ions and band electrons. An in-depth analysis of both EPR and magnetization data confirms that Mn^{4+} ions and singly ionized oxygen vacancies are collectively responsible for the observed magnetization behavior in the doped samples, and the nature of magnetic interaction is especially antiferromagnetic in the higher doped samples. We hope the present study provides a deeper understanding of the nature of magnetic interaction in DMSs $\text{BaSn}_{1-x}\text{Mn}_x\text{O}_3$, which allows researchers to design DMSs having unique physical properties based on BaSnO_3 perovskite oxides for potential technological applications.

Declaration of competing interest

The authors declare that they have no known competing financial

interests or personal relationships that could have appeared to influence the work reported in this paper.

Data availability

No data was used for the research described in the article.

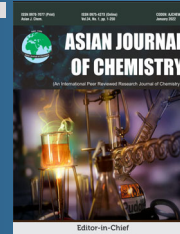
Acknowledgments

Ankita Sarkar (IF150001) would like to thank the Department of Science and Technology (DST), Government of India for providing a DST-INSPIRE Fellowship during the tenure of work.

References

- [1] T. Dietl, H. Ohno, F. Matsukura, J. Cibert, D. Ferrand, *Science* 287 (2000) 1019.
- [2] Y. Matsumoto, M. Murakami, T. Shono, T. Hasegawa, T. Fukumura, M. Kawasaki, P. Ahmet, T. Chikyow, S.-Y. Koshihara, H. Koinuma, *Science* 291 (2001) 854.
- [3] K. Ueda, H. Tabata, T. Kawai, *Appl. Phys. Lett.* 79 (2001) 988.
- [4] J.H. Kim, H. Kim, D. Kim, Y.E. Ihm, W.K. Choo, *J. Appl. Phys.* 92 (2002) 6066.
- [5] P.A. Stamp, R.J. Kennedy, Y. Xin, J.S. Parker, *J. Appl. Phys.* 93 (2003) 7864.
- [6] P. Sharma, A. Gupta, K.V. Rao, F.J. Owens, R. Sharma, R. Ahuja, J.M.O. Guillen, B. Johansson, G.A. Gehring, *Nat. Mater.* 2 (2003) 673.
- [7] S.S. Farvid, L. Ju, M. Worden, P.V. Radovanovic, *J. Phys. Chem. C* 112 (2008), 17755.
- [8] J.L. MacManus-Driscoll, N. Khare, Y. Liu, M.E. Vickers, *Adv. Mater.* 19 (2007) 2925.
- [9] S.Y. Park, P.J. Kim, Y.P. Lee, S.W. Shin, T.H. Kim, J.-H. Kang, J.Y. Rhee, *Adv. Mater.* 19 (2007) 3496.
- [10] H.-S. Kim, L. Bi, G.F. Dionne, C.A. Ross, H.-J. Paik, *Phys. Rev. B* 77 (2008), 214436.
- [11] K.G. Roberts, M. Varela, S. Rashkeev, S.T. Pantelides, S.J. Pennycook, K. M. Krishnan, *Phys. Rev. B* 78 (2008), 014409.
- [12] T. Kimura, T. Goto, H. Shintani, K. Ishizaka, T. Arima, Y. Tokura, *Nature (London)* 426 (2003) 55.
- [13] R.J. Cava, B. Batlogg, J.J. Krajewski, R. Farrow, L.W. Rupp Jr., A.E. White, K. Short, W.F. Peck, T. Komietani, *Nature (London)* 332 (1988) 814.
- [14] H.J. Kim, U. Kim, T.H. Kim, J. Kim, H.M. Kim, B.-G. Jeon, W.-J. Lee, H.S. Sik Mun, K.T. Hong, J. Yu, K. Char, K.H. Kim, *Phys. Rev. B* 86 (2012), 165205.
- [15] Y.-H. Lin, S. Zhang, C. Deng, Y. Zhang, X. Wang, C.-W. Nan, *Appl. Phys. Lett.* 92 (2008), 112501.
- [16] L.B. Luo, Y.G. Zhao, H.F. Tian, J.J. Yang, H.Y. Zhang, J.Q. Li, J.J. Ding, B. He, S. Q. Wei, C. Gao, *Appl. Phys. Lett.* 92 (2008), 232507.

- [17] A.B. Posadas, C. Mitra, C. Lin, A. Dhamdhere, D.J. Smith, M. Tsoi, A.A. Demkov, *Phys. Rev. B* 87 (2013), 144422.
- [18] H.-S. Kim, L. Bi, G.F. Dionne, C.A. Ross, *Appl. Phys. Lett.* 93 (2008), 092506.
- [19] H.-S. Kim, L. Bi, D.H. Kim, D.-J. Yang, Y.J. Choi, J.W. Lee, J.K. Kang, Y.C. Park, G. F. Dionne, C.A. Ross, *J. Mater. Chem.* 21 (2011), 10364.
- [20] B. Hadjarab, A. Bouguelia, M. Trari, *J. Phys. Chem. Solid.* 68 (2007) 1491.
- [21] P. Singh, D. Kumar, O. Parkash, *J. Appl. Phys.* 97 (2005), 074103.
- [22] U. Lampe, J. Gerblinger, H. Meixner, *Sens. Actuators, B* 24–25 (1995) 657.
- [23] H. Mizoguchi, H.W. Eng, P.M. Woodward, *Inorg. Chem.* 43 (2004) 1667.
- [24] H.J. Kim, J. Kim, T.H. Kim, W.-J. Lee, B.-G. Jeon, J.-Y. Park, W.S. Choi, D. W. Jeong, S.H. Lee, J. Yu, T.W. Noh, K.H. Kim, *Phys. Rev. B* 88 (2013), 125204.
- [25] K. Balamurugan, N. Harish Kumar, B. Ramachandran, M.S. Ramachandra Rao, J. Arout Chelvane, P.N. Santhosh, *Solid State Commun.* 149 (2009) 884.
- [26] K. Balamurugan, N. Harish Kumar, J. Arout Chelvane, P.N. Santhosh, *J. Alloys Compd.* 472 (2009) 9.
- [27] Q. Liu, Y. He, H. Li, B. Li, G. Gao, L. Fan, J. Dai, *APEX* 7 (2014), 033006.
- [28] H.M. Rietveld, *J. Appl. Crystallogr.* 2 (1969) 65.
- [29] M. Ferrari, L. Lutterotti, *J. Appl. Phys.* 76 (1994) 7246.
- [30] R.D. Shannon, *Acta Crystallogr. A* 32 (1976) 751.
- [31] B. Dalal, B. Sarkar, S.K. De, *J. Phys. Condens. Matter* 29 (2017), 495803.
- [32] S. Li, S. Wang, Y. Lu, C. Zhang, X. Yang, J. Gao, D. Li, Y. Zhu, W. Liu, *AIP Adv.* 8 (2018), 015009.
- [33] Y.-K. Hsu, Y.-C. Chen, Y.-G. Lin, L.-C. Chen, K.-H. Chen, *J. Mater. Chem.* 22 (2012) 2733.
- [34] A. Sarkar, S.K. De, *Semicond. Sci. Technol.* 33 (2018), 035018.
- [35] I.A. Alagdal, A.R. West, *J. Mater. Chem. C* 4 (2016) 4770.
- [36] T.C. Damen, S.P.S. Porto, B. Tell, *Phys. Rev.* 142 (1966) 570.
- [37] C. Bundesmann, N. Ashkenov, M. Schubert, D. Spemann, T. Butz, E.M. Kaidashev, M. Lorenz, M. Grundmann, *Appl. Phys. Lett.* 83 (2003) 1974.
- [38] M.V. Abrashev, A.P. Litvinchuk, M.N. Iliev, R.L. Meng, V.N. Popov, V.G. Ivanov, R. A. Chakalov, C. Thomsen, *Phys. Rev. B* 59 (1999) 4146.
- [39] B. Cheng, Y. Xiao, G. Wu, L. Zhang, *Appl. Phys. Lett.* 84 (2004) 416.
- [40] J.B. Wang, G.J. Huang, X.L. Zhong, L.Z. Sun, Y.C. Zhou, *Appl. Phys. Lett.* 88 (2006), 252502.
- [41] Y. Sun, X. Zhang, N. Li, X. Xing, H. Yang, F. Zhang, J. Cheng, Z. Zhang, Z. Hao, *Appl. Catal., B* 251 (2019) 295.
- [42] J. Xu, J.H. Park, H.M. Jang, *Phys. Rev. B* 75 (2007), 012409.
- [43] C. Shan, T. Huang, J. Zhang, M. Han, Y. Li, Z. Hu, J. Chu, *J. Phys. Chem. C* 118 (2014) 6994.
- [44] S. Maiti, A. Pramanik, S. Mahanty, *ACS Appl. Mater. Interfaces* 6 (2014), 10754.
- [45] D. Ghosh, S. Bhandari, D. Khastgir, *Phys. Chem. Chem. Phys.* 18 (2016), 32876.
- [46] C. Huang, X. Wang, Q. Shi, X. Liu, Y. Zhang, F. Huang, T. Zhang, *Inorg. Chem.* 54 (8) (2015) 4002.
- [47] W. Lu, H. Schmidt, *Ceram. Int.* 34 (3) (2008) 645.
- [48] R.A. Zargar, M. Arora, R.A. Bhat, *Appl. Phys.* 124 (2018) 36.
- [49] R.A. Zargar, *Sci. Rep.* 12 (2022), 10096.
- [50] C. Tian, H. Lin, D. Zhang, P. Zhang, R. Hong, Z. Han, X. Qian, J. Zou, *Opt Express* 27 (22) (2019), 32666.
- [51] R. Cao, F. Zhang, C. Cao, X. Yu, A. Liang, S. Guo, H. Xue, *Opt. Mater.* 38 (2014) 53.
- [52] K. Drdlikova, D. Drdlik, H. Hadraba, R. Klement, K. Maca, *J. Eur. Ceram. Soc.* 40 (14) (2020) 4894.
- [53] S. Stoll, A. Schweiger, *J. Magn. Reson.* 178 (1) (2006) 42.
- [54] A. Zorko, M. Pregelj, H. Luetkens, A.-K. Axelsson, M. Valant, *Phys. Rev. B* 89 (2014), 094418.
- [55] K. Alexander Müller, *Phys. Rev. Lett.* 2 (8) (1959) 341.
- [56] J.M. Peloquin, K.A. Campbell, D.W. Randall, M.A. Evanchik, V.L. Pecoraro, W. H. Armstrong, R. David Britt, *J. Am. Chem. Soc.* 122 (44) (2000), 10926.
- [57] R.A. Zargar, K. Kumar, M. Arora, M. Shkir, H.H. Smaili, H. Algarni, S. AlFaify, *J. Lumin.* 245 (2022), 118769.
- [58] S. Paul, B. Dalal, M. Das, P. Mandal, S.K. De, *Chem. Mater.* 31 (2019) 8191.



REVIEW

Catalytic Organic Reactions in Liquid Phase by Perovskite Oxides: A Review

RAJIB MISTRI

Department of Chemistry, Achhruram Memorial College, Jhalda, Purulia-723202, India

Corresponding author: E-mail: rajibmistri@yahoo.co.in

Received: 20 June 2022;

Accepted: 22 July 2022;

Published online: 19 September 2022;

AJC-20949

The structural flexibility and controllable physico-chemical characters of perovskite oxides have drawn major attention of researchers for catalytic reactions. Perovskite oxide are mainly used as catalysts for electrochemical, high temperature gas-phase and photocatalytic reactions but their uses for catalytic organic reactions in liquid phase are limited. Various porous and nano-perovskite oxides have been prepared by different methods are effectively used as catalyst for different types of organic reactions in liquid phase. The liquid-phase catalytic organic reactions over perovskite oxides have been classified mainly into three groups: (i) acid/base catalyzed, (ii) selective oxidation and (iii) cross-coupling reactions. This review article mainly emphasizes on different examples of perovskite oxides catalyzed organic reactions in liquid phase along with the relationships among the unique catalytic performance with the structural and the physico-chemical properties of perovskites.

Keywords: Organic reactions, Liquid-phase, catalyst, Perovskite oxides, Structures.

INTRODUCTION

Modern day's chemical industry is in need of technology for generation of sustainable as well as environmentally-safe chemical processes [1-12]. In state of conventional technologies, catalytic processes can apply for the production of various industrially important chemicals due to its economic and environmental benefits. Numerous homogeneous catalysts have been industrially applied for catalytic organic reactions in liquid phase through green synthetic route. These catalysts are highly active as well as selective due to their structure and precisely controllable reactivity [13]. However, the major disadvantages of homogeneous catalysts for large scale application in industrial processes are catalyst separation and various problems in reuse of these costly catalysts [14-16]. These disadvantages can be circumvented through the use of easily recyclable heterogeneous catalysts for the environmental friendly synthesis of expensive important chemicals. Several metal hydroxides or oxides [17-20], polyoxometalates [21,22], zeolites [23,24], metal nanoparticles [25,26], metal-organic frameworks [27,28], polymers [29,30], dendrimers [31] and carbon-based materials [32,33] have been efficiently applied as heterogeneous catalysts for organic reactions in liquid-phase.

Recently, perovskite oxides (with common formula ABO_3) have drawn much attention due to their versatile applications likes magnetic, multi-ferroelectric, piezoelectric, superconducting and also heterogeneous catalytic properties [34-51]. Different perovskite oxides were studied as catalyst for electrochemical reactions [34-38], high temperature gas-phase reactions [39-49] and photocatalytic [47-51] due to their structural stability, flexibility, diversity and controllable physico-chemical properties. Though industrially important perovskite catalyzed organic reactions in liquid-phase have been limited reports [52-88]. Recently several researchers reported porous nano perovskite oxide synthesized by different methods could be used as heterogeneous catalyst for organic reactions in liquid-phase such as acid/base-catalyzed organic reactions [52-57], selective oxidations [58-76], cross-coupling reactions [77-81] and some other hydrogenation/oxidation reactions [82-88]. Table-1 listed various examples of perovskite oxide-based materials as heterogeneous catalyst for organic reactions in liquid phase.

Numerous examples of perovskite oxide catalyzed organic reactions in liquid-phase are highlighted in this review. In addition, their synthesis, structures, physico-chemical properties and environmental-friendly catalytic applications are also summarized.

TABLE-1
 VARIOUS HETEROGENEOUS PEROVSKITE OXIDE CATALYSTS FOR ORGANIC REACTIONS IN LIQUID PHASE

Catalyst/additive	Reaction	Yield	Time (h)	Ref.
Acid/base-catalyzed reaction				
BaZrO ₃		53	1.5	[52]
HTiNbO ₅ nanosheets		17	6	[53]
SmFeO ₃		98	1	[54]
Mesoporous ZnTiO ₃		90-94	14-24	[55]
Mesoporous ZnTiO ₃		73-92	15-18	[55]
ZnTiO ₃ /CTAB		71-94	8	[56]
BiFeO ₃		63-88	-	[57]
Selective oxidation				
Cu/LaFeO ₃		99	3	[58]
LaCrO ₃		84-97	7-8.5	[60]
KNbO ₃		30, 70	1	[61]
Y ₂ BaCuO _{3+x}		18, 14, <1	0.5	[62,63]
CuZrO ₃		69	2	[64]
AuPd/LaMnO ₃ NaOH		70, 17	6	[65]

$\text{Pd}_{0.002}\text{K}_{0.17}\text{Ti}_{1.86}\text{Sr}_{0.20}\text{O}_4$ $\text{Pd}_{0.03}\text{K}_{0.03}\text{Ti}_{1.47}\text{Sr}_{1.02}\text{O}_4$		30-99	24	[66]
La_2CuO_4		70-90	–	[67]
SrMnO_3		81-99	1-10	[68]
SrMnO_3		81-94	8-24	[70]
$\text{BaFeO}_{3.6}$		14-59	72-96	[71]
BaRuO_3		50-90	12-60	[72]
$(\text{La,Sr})_{0.5}(\text{Co,Mn})_{0.5}\text{O}_{3.8}/\text{NHPI}$		99	99	[73]
KTaO_3		58	4	[74]
$\text{BaFeO}_{3.6}$		75	30	[76]
Coupling Reaction				
$\text{LaFe}_{0.57}\text{Co}_{0.38}\text{Pd}_{0.05}\text{O}_3$ /base-TBABr		26-95	0.5-18	[77,78]
$\text{La}_{0.9}\text{Ce}_{0.1}\text{Co}_{0.6}\text{Cu}_{0.4}\text{O}_3$ /base-EtOAc		46-90	48	[79]
$\text{La}_{0.9}\text{Ce}_{0.1}\text{Co}_{0.6}\text{Cu}_{0.4}\text{O}_3$ /base		47-96	6-24	[80]
$\text{Bi}_{1.97}\text{Eu}_{0.03}\text{MoO}_6$		90-97	0.5-1	[81]

Other Reaction				
LaFeO ₃ /KOH		78-98	2-6	[82]
LaCo _{0.8} Fe _{0.2} O ₃		89	6	[84]
Pt/YCo _{0.3} Fe _{0.7} O ₃		95	0.5	[85]
LaMnO ₃		99	24	[86]
LaMnO ₃		66	24	[86]
LaMo _{0.1} Fe _{0.9} O ₃		92	0.3	[87]
LaMnO ₃		95	3	[88]

Synthesis and structure of perovskite catalysts: A number of combination of A- and B-site is possible to procedure ABO₃ structure of perovskite oxide [46,89,90]. Partial substitution of either or both sites (A and B) by other metals can control metal cation's oxidation states and oxygen stoichiometry in multi-component perovskite compositions. Therefore, the adjustable composition of perovskites could lead to structure flexibility with useful physico-chemical characters. Many wonderful books and articles presented the synthesis, structures, characteristic features and uses of perovskite oxides in detail [34-51].

Synthesis of perovskite catalysts: The purity, surface area, particles size or shape and pores size/amounts of perovskite oxides are strongly depending on their synthesis methods [34,89,90]. Ultrapure perovskites can be prepared from pure metal component by the solid-state synthesis method but these synthesized perovskites are mainly use for electrical and electronic applications. But the enormously low surface area (~ 1 m² g⁻¹) of these perovskite limits their overall performance as effective bulk catalyst [4]. Liquid-phase organic reactions are

mainly performed under mild reaction conditions; therefore, relatively high surface area of perovskite catalysts is one of most important factor for a highly efficient catalytic system. Generally, perovskite oxide catalysts are prepared by co-precipitation [65,67-69], solgel [61,64,65,69-73], solution combustion [57,58] and hard-soft templating [82] methods. In co-precipitation, a suitable precipitant (NaOH, ammonia, amines) is slowly mixed to an aqueous two or more metal salts solution generally as metal nitrate and gives a homogeneous mixture. The resultant precipitates wash with pure solvents then calcine at a proper temperature. Different perovskites, ABO₃ (A = La, Sm, Pr and B = Fe, Cr, Mn, Ni, Co), are synthesized by co-precipitation method using *n*-butyl amine as a precipitant [68]. A super-critical anti-solvent precipitation method is also used for the synthesis of LaBO₃ (B = Fe, Cr, Co, Ni, Mn) with high surface areas (22-52 m² g⁻¹) [65]. In co-precipitation method, soluble metal complexes are produced in precipitation step and particular cations are also loss in washing step. Thus controlling the composition of perovskites is difficult in this method.

Perovskites with controlled chemical composition as well as relatively high surface areas are prepared by simple and useful sol-gel method. Malic acid and citric acid most frequently used in sol-gel method for synthesis of perovskites [91,92]. $\text{La}_{0.8}\text{Sr}_{0.2}\text{MO}_3$ ($M = \text{Co}$ and Mn with surface area $20 \text{ m}^2 \text{ g}^{-1}$ and $37 \text{ m}^2 \text{ g}^{-1}$, respectively) with high surface-area have synthesized from aqueous metal salts solution and malic acid at pH 3-4 [92]. The polymerized complex method and the Pechini method have also been well-studied for perovskites synthesis [93,94]. Hexagonal SrMnO_3 (surface area $25 \text{ m}^2 \text{ g}^{-1}$) have synthesized by polymerized complex method [69]. SrMnO_3 with appreciable large surface area ($\leq 47 \text{ m}^2 \text{ g}^{-1}$) also fruitfully synthesized without pH adjustment by using metal acetates and aspartic acid rather than metal nitrates [70] and other hexagonal perovskite materials was also synthesized by this method [71,72].

The single step solution combustion method is also use for synthesis of perovskite nanoparticles, which involves the combustion of corresponding metal salts (mostly nitrates and chlorides in some cases) with appropriate organic fuels (citric acid, urea, glycine, glycerol, *etc.*). The reaction itself supplied the required heat for phase formation. Therefore, heating temperature is lower than the conventional paths and calcination step is not required. The copper substituted LaMO_3 ($M = \text{Fe}$, Mn , Co) catalysts with surface area $10\text{-}27 \text{ m}^2 \text{ g}^{-1}$ was synthesis by single-step solution combustion method [58]. This synthesis method has also been useful for rapid synthesis of different multicomponent perovskites. But, it is difficult to control parameters of the process and maintains the quality of final product by using this preparation method.

Soft and hard templating methods most comprehensively studied for the preparation of porous perovskite materials by using porous silicates and polymeric materials [48]. The perovskite nanoparticles have no pores and the reaction happens only on the surface of the catalyst, which restrict the overall catalytic performance [68]. The ZnTiO_3 , mesoporous perovskite, with $136 \text{ m}^2 \text{ g}^{-1}$ surface area and 5.1 nm averaged pore dimension was synthesized by using a nonionic surfactant template (Pluronic P123) in a new evaporation-induced self-assembly method [61]. Hence, the soft and hard templating methods provide large surface areas ($> 100 \text{ m}^2 \text{ g}^{-1}$) with orderly pore structures but the method complicity, requirement of costly templates and also difficulty in their successive removal makes the applicability of this method is limited.

Although, nanosized and porous suitable perovskite oxides prepared by the aforesaid methods are mainly applied as efficient catalysts. The typically inactive perovskite oxides may be used as supports for different supported metal catalysts and a synergistic effect of perovskite oxide and metal nanoparticles has been suggested for some reactions [65,73,85]. The details applications of all these perovskite oxides for catalytic organic reactions in liquid-phase are described as follows:

Structure of perovskite catalysts: The perovskite oxides are ideally cubic in crystal structure, where large cations (A) have twelve-fold and smaller cations (B) have six-fold coordination with BO_6 octahedra corner-sharing [4]. The tolerance factor (t) is used for indexing the deviation from this ideal structure and is estimated from eqn. 1 (r_A = cationic radius of

A, r_B = cationic radius of B and r_O = anionic radius of O^{2-}) [89,90].

$$t = \frac{(r_A + r_B)}{\sqrt{2(r_B + r_O)}} \quad (1)$$

The ideal cubic perovskite has t value 1. When the t value is lower than 1 (0.75 to 1), the perovskite gives tetragonal, rhombohedral, or lower symmetric structure [89]. The greater t values (> 1) are obtained when we use large alkaline-earth metal cations (A^{2+}) or small B cations and showing hexagonal crystal structure with BO_6 octahedra face-sharing [70,71]. Two-dimensional perovskite with inter leaved cations are showing layered structures is also reported [89].

Different perovskite oxides are design for catalytic organic reactions in liquid-phase. The crystalline structure, formation of oxygen vacancy and the oxidation state of B can be changed by controlling the chemical composition of perovskite oxides. When an A^{3+} ion is replaced by an A^{2+} cation from $\text{A}^{3+}\text{B}^{3+}\text{O}_3$ then increased the oxidation state of B or formed oxygen vacancy [4]. The details applications of all these perovskite oxides as catalyst for organic reaction in liquid-phase along with the relationships between the unique catalytic properties and the structural, the physico-chemical properties are also discussed.

Catalytic applications of perovskite oxide for organic reactions in liquid-phase: The catalytic activity of perovskite oxides strongly depends on their physico-chemical properties. It has been reported that crystalline structure [69,70], formation energy for oxygen vacancy [71], oxygen adsorption capacity [65], surface oxygen vacancy [64,73] and oxidation state of B cation [72] play significant roles for the perovskite oxide catalyzed organic reactions in liquid phase. Several absorptions, spectroscopic and computational methods have been used for characterization of the redox and acidic-basic properties of perovskite oxides [21-23,25,26,29]. The oxygen mobility and reducibility are usually analyzed by hydrogen temperature programmed reduction (TPR), isotopic exchange experiments and temperature programmed desorption (TPD) for the characterization of redox properties. Adsorption micro-calorimetry, site titration using Hammett indicators, TPD and spectroscopy are exclusively used for the analysis of surface acidity/basicity of perovskites. The bulk and surface structures are characterized by infrared spectroscopy (IR), X-ray diffraction (XRD), extended X-ray absorption fine structure (EXAFS), X-ray photoelectron spectroscopy (XPS), Raman spectroscopy and high resolution transmission electron microscope (HRTEM) measurements. However, most publications mainly focus on development of perovskite oxide-catalyzed organic reactions in liquid-phase. Hence, such characterizations in most systems are incomplete and lack of comprehensive mechanistic studies. In this review, the important catalytic property of perovskite oxides in liquid phase is comprehensively summarized and some of the reaction mechanism along with the characterization results is also discussed.

Acid/base-catalyzed reactions: The petroleum refining and petrochemical industry have been utilized solid acid-bases as catalysts for lots of important processes [95-100]. Zeolites,

clays, resins, hetero polyacids, mono or mixed metal oxides and a catalyst with surface modification have been extensively examined as acid-base catalyst. However, the performance of perovskite oxides as acid-base catalyst are still under explored. In recent times, a review article systematically summarized catalytic performance of perovskites as acid-base catalyst [42]. The effects of density, strength, surface modification, exposed faces and type of acid-base sites of perovskite oxides to their performance as catalyst have been studied for the conversion of 2-propanol [53]. In contrast, acid-base catalysis in liquid-phase and comprehensive reaction mechanisms studies are still limited.

$\text{HSr}_2\text{Nb}_3\text{O}_{10}$ and HTiNbO_5 nanosheets with modified surface area were reported as acid catalysts for acetic acid esterification, cumene cracking and 2-propanol dehydration [53]. Cyano-silylation with trimethylsilyl cyanide (TMSCN) of carbonyl compounds to corresponding cyanohydrins trimethylsilyl ethers is a key reaction for production of α -hydroxy aldehydes or acids and β -amino alcohols. SmFeO_3 showed significant activity towards the catalytic cyano-silylation of benzaldehyde by trimethylsilyl cyanide in comparison to other catalysts used for this reaction [54]. But, it is proposed that the active sites of SmFeO_3 was the Brønsted acid sites but results were lack of detail characterization. A new mesoporous ZnTiO_3 perovskite was developed as an efficient catalyst for Friedel-Crafts alkylation by benzyl chloride along with the esterification of C_{12} - C_{18} carboxylic acids [55,56]. A probable mechanism was suggested for the ZnTiO_3 -catalyzed esterification that carboxylic acid was activated through coordination with the Lewis acid site. The same group also stated that reusable nano ZnTiO_3 base catalyst with cubic structure prepared *via* sol-gel method for 1,6-naphthyridine synthesis in water [56]. The cooperative action of Ti^{4+} as Lewis acid site and O^{2-} as base site for the probable reaction mechanism is also proposed.

Preparation of hydroxypivaldehyde is a key reaction, since the product gives neopentyl glycol on successive hydrogenation and it is an intermediate of plasticizers, polyesters, lubricants and synthetic paints. SrZrO_3 and BaZrO_3 exhibited good catalytic activity towards this base-catalyzed aldol condensation reaction of isobutyl aldehyde by formaldehyde with 53% yield along with 91% conversion [52].

Different dihydro-2-oxypyrrroles was synthesized by one-pot synthesis from dimethyl acetylene dicarboxylate, formaldehyde and anilines in methanol over BiFeO_3 catalyst at room temperature [57]. An external magnet could easily recover the used catalyst from the reaction medium and the recovered catalyst was efficiently reused. The authors proposed that an imine intermediate was activated through Lewis acid sites of BiFeO_3 helps a Mannich type reactions by successive cyclization reactions, even though there was no physico-chemical evidence regarding this acid sites.

Selective catalytic oxidation: Selective catalytic oxidation of petroleum-based feed stocks into suitable compounds is a significant reaction since the products are extensively applied for synthesis of valuable products and important chemicals [101-108]. The CO oxidation and total oxidation of different hydrocarbons are extensively reported over perovskite oxide

catalysts [39-43,84]. Several efficient perovskite oxides catalysts are used for selective oxidation reactions in liquid phase by using molecular oxygen (O_2), hydrogen peroxide (H_2O_2) and *tert*-butyl hydroperoxide (TBHP) as oxidant [58-76]. The kinds of catalyst and oxidant played important role for the catalytic efficiency as well as for the reaction mechanism. Preparation of particular widely used important carbonyl compounds from corresponding alcohols *via* selective oxidation due to production of fine chemicals and pharmaceuticals products. Copper-substituted $\text{LaFeO}_3(\text{Cu}/\text{LaFeO}_3)$ perovskite developed as a reusable catalyst for selective oxidation of benzyl alcohol with TBHP [58]. The combustion synthesized catalyst showed higher activity due to the presence of a peculiar poorly-defined amorphous CuO along with substitutional Cu^{2+} phase on the top of LaFeO_3 particle. Cerium doped rhombohedral $\text{La}_{1-x}\text{Ce}_x\text{CoO}_3$ nano perovskite was also act as an effective catalyst for the same reaction in liquid medium under atmospheric pressure using highly pure oxygen as oxidant. Under optimum reaction conditions, among the prepared catalysts $\text{La}_{0.95}\text{Co}_{0.05}\text{O}_3$ catalyst showed higher catalytic activity (> 35%) with ~ 100% selectivity upto four cycles [59]. Reusable LaCrO_3 catalyst also reported for the oxidation of alkyl arenes using TBHP under solvent-free condition [60]. However, H_2O_2 and O_2 have received much consideration than organic hydroperoxides due to their environmental-friendly nature (gives water only as byproduct) and also content high active oxygen species. Titanium loaded potassium niobates ($\text{KTi}_{0.2}\text{Nb}_{0.8}\text{O}_3$ and $\text{KTi}_{0.1}\text{Nb}_{0.9}\text{O}_3$) perovskite developed for the selective catalytic oxidation of 2-(methyl-thio)benzothiazole with excess H_2O_2 to the analogous sulfone and sulfoxide [61]. The electronic and structural defects were due to incorporation of titanium ions into the perovskite lattice for the higher activity of titanium substituted catalyst than the pure potassium niobates (KNbO_3). The $\text{Y}_2\text{BaCuO}_{5\pm x}$ perovskite was also reported as recyclable efficient catalyst for the selective catalytic oxidation of phenol to hydroquinone and catechol using H_2O_2 [62,63]. A radical substitution mechanism is proposed but the complete mechanism was still uncertain for the oxidation reactions with H_2O_2 .

Catalytic oxidative promoting reactions of biomass-derived substance into valuable chemicals with O_2 are an important matter to make a sustainable society due to the replacement of non-renewable fossil resources [7-12,109]. However, still now the selective liquid-phase heterogeneous catalytic oxidation under mild conditions with O_2 are limited [101-108,110]. The CuO and CuZrO_3 mixture was developed as heterogeneous catalytic oxidation of vanillyl alcohol (a model compound representing lignin) [64]. The redox properties of the catalyst improved due to the presence of Cu-O-Zr linkages in high concentration as active phase. The perovskite-catalyzed aerobic oxidation of common organic substances was also examined by various researchers. The effect of perovskites supports on glycerol aerobic oxidation was exclusively studied over AuPt nanoparticles supported on lanthanum based oxides LaMO_3 ($\text{M} = \text{Fe}, \text{Cr}, \text{Mn}, \text{Ni}, \text{Co}$) [65]. This oxidation gives different products and the selectivity of the products was depending on the perovskite supports. From mechanistic studies, it was suggested that the oxygen adsorption capacity supports strongly

influence selectivity of the product and LaMnO_3 support inhibits the lactic acid production due to high oxygen capacity. The Pd-containing perovskite oxide ($\text{Pd}/\text{K}_{0.6}\text{Ti}_{1.85}\text{O}_4$) was reported as a highly stable and reusable catalyst for allylic and benzylic alcohols oxidation by using oxygen [66]. Various substituted benzaldehyde with electron-withdrawing and electron-donating groups were selectively oxidized to the desired products over La_2CuO_4 catalyst [67].

The catalytic oxidation over various types of pure rhombohedral and hexagonal perovskite oxides ($\text{BaFeO}_{3-\delta}$, BaRuO_3 and SrMnO_3) with relatively high surface areas are also reported as efficient catalyst for oxidative dehydrogenation of alcohols and other difficult aerobic oxidation of alkanes and sulfides [69-72]. These hexagonal perovskites also selectively catalyzed alcohols, alkanes, alkyl arenes and sulfides in presence of O_2 . Many allylic, aromatic and heteroatom-incorporated primary or secondary alcohols were selectively transformed to the desired carbonyl compounds over hexagonal SrMnO_3 [69]. But the catalyst showed low catalytic activity towards aliphatic alcohols oxidation. The kinetics measurement showed non-dissociative alcohol and oxygen adsorption and Langmuir-Hinshelwood mechanism was proposed for this catalyzed oxidation reaction. The C-H bond breaking was suggested for the rate determination step from kinetic isotope effect. This type of O_2 -activation was also used for oxidative homocoupling reactions of phenols and amines and the selective oxidation of alkyl arenes to corresponding oxygenated/dehydrogenated products. This is the first example of reductive O_2 activation for selective catalytic oxidation over SrMnO_3 in liquid-phase. The kinetic measurement showed that an oxygen species generated from the solid compare to SrMnO_3 is responsible for this oxidation process and Mars-van Krevelen mechanism was proposed for this reaction [111]. Various aromatic and aliphatic sulfides could also efficiently catalyze to the corresponding sulfones and sulfoxides by using O_2 over recyclable rhombohedral BaRuO_3 [71]. The oxygen transfer reactivity of ruthenium based oxides was significantly affected by the crystal structure of oxides. Thus, the oxygen easily transferred to a sulfide from BaRuO_3 and oxygen also re-oxidized the partially reduced BaRuO_{3-x} than other Ru-based perovskites. The aliphatic C-H bond oxidation of alkanes produces industrially important chemicals and it is still challenging in the chemical industries [72]. There are few Ru- and V-based perovskites used as recoverable as well as a reusable heterogeneous catalyst for aerobic oxidation of adamantane [112,113]. Hexagonal, recyclable $6\text{H-BaFeO}_{3-\delta}$ ($\delta = 0.1$) was efficiently catalyzed this oxidation as well as other various hydrocarbons in presence of oxygen [72]. The author proposed that the adamantane oxidation gates through a radical-mediated pathway and abstraction of hydrogen by $\text{BaFeO}_{3-\delta}$ suggested for the rate determining step. The oxygen-deficient, orthorhombic, recyclable $(\text{La,Sr})_{0.5}(\text{Co,Mn})_{0.5}\text{O}_{3-\delta}$ perovskite was basically applied for the selective oxidation of ethylbenzene and toluene to acetophenone and benzoic acid, respectively with *N*-hydroxyphthalimide (NHPI) [73]. It has been proposed that the large oxygen vacancies of this perovskite could activated NHPI to produce phthalimide *N*-oxyl radical (PINO) and the radical promoting the formation of an alkyl radical through hydrogen

abstraction from hydrocarbons. However, mechanistic detail is still required.

A sets of alkaline tantalates (NaTaO_3 , LiTaO_3 , KTaO_3) also selectively catalyzed styrene to form benzaldehyde. The highest conversion ($\sim 58\%$) with 77% selectivity was achieved for KTaO_3 upto six catalytic cycles. It is suggested that the increasing catalytic performance was attributed to crystalline structure of perovskites, the atomic radius of the alkaline-metals and the presence of segregated phases in the component [74]. Sol-gel methods synthesized, pure and Co loaded nano-lanthanum ferrite ($\text{LaFe}_{1-x}\text{Co}_x\text{O}_3$; $x = 0$ to 1) were also examined for selective catalytic oxidation of styrene to benzaldehyde using H_2O_2 as oxidant [75]. The catalyst showed the higher activity at lowest substitution than other higher cobalt loaded ferrite and also than for pure LaFeO_3 .

$\text{BaFeO}_{3-\delta}$ perovskite may well affectively catalyzed oxidative C=C bond cleavage of numerous aromatic alkenes to preferred carbonyl compounds ($\sim 75\%$ yield) under the additive free condition with O_2 as oxidant [76].

Cross-coupling reactions: Several significant organic chemicals (drugs, materials, optical devices, *etc.*) are manufactured by using cross-coupling reactions over transition metal catalyst [114-118]. Palladium(II) complexes are generally used as homogeneous catalyst in case of cross-coupling reactions in environment friendly mild conditions. Thus development of Pd-based easily recoverable and recyclable heterogeneous catalysts are predominantly required for industrial applications. Along with other approaches impregnation and encapsulation have been tried for the immobilization of Pd particles [78]. But Pd leaching is a big problem for this types of catalysts. Thus, the improvement of Pd-based catalysts as actually heterogeneous remains an interesting tusk for researchers.

Furthermore, palladium containing perovskite oxides also developed as efficient popular automotive three-way catalyst with expressively developed stability due to the self-reformative role of Pd [119,120]. Against such a background, Pd-loading $\text{LaFe}_{0.57}\text{Co}_{0.38}\text{Pd}_{0.05}\text{O}_3$ perovskite is developed for the Suzuki reactions of aryl halides with boronic acids [77]. A number of aryl halides and boronic acids combinations were affectively transformed to the analogous bi-aryls and the catalytic efficiency enhanced with tetra-*n*-butyl ammonium bromide (TBABr) addition in several difficult transformations. The reaction between 4-bromoanisole and phenyl boronic acid over $\text{LaFe}_{0.57}\text{Co}_{0.38}\text{Pd}_{0.05}\text{O}_3$ was taken as a model reaction for this coupling reaction and the reaction mechanism was investigated by using kinetics, microscopy, catalyst poisoning and three-phase tests [78]. On the basis of these results, it was proposed that the Pd particles first reduced to Pd^0 by aqueous alcohol solvents and trapped to a solid surface. The soluble Pd species produces by oxidative-addition of aryl halides helped the Suzuki coupling reaction in a usual way. Transmission electron microscopy (TEM) studies showed that there is no Pd black generated. Thus, low amount (2 ppm) of leached Pd particles (confirm from hot filtration test) after reaction indicated that bulk inorganic phase was recaptured the Pd^0 particles.

Furthermore, Ullmann-type condensation of different aryl halides using thiols and phenols to the analogous sulfides and

biaryl ethers could efficiently catalyze by $\text{La}_{0.9}\text{Ce}_{0.1}\text{Co}_{0.6}\text{Cu}_{0.4}\text{O}_3$ perovskite catalyst [79]. Several phenolic compound could effectively couple with an aryl halide in presence of ethyl acetate and Cs_2CO_3 additives. Three Pd-loaded $\text{Na}_{2.04}\text{Cu}_{0.95}\text{Pd}_{0.05}\text{O}_4$, $\text{LaFe}_{0.57}\text{Cu}_{0.38}\text{Pd}_{0.05}\text{O}_3$ and $\text{LaFe}_{0.57}\text{Co}_{0.38}\text{Pd}_{0.05}\text{O}_3$ perovskites developed for Sonogashira coupling of aryl halides with alkynes is also reported [79]. $\text{LaFe}_{0.95}\text{Pd}_{0.05}\text{O}_3$ perovskite deposited CeO_2 was also reported as efficient catalyst for Sonogashira and Heck cross-coupling reactions by flow chemistry technology [80]. But the reaction time profile is very slow and controlling the byproducts formation should be enhanced catalytic efficiency.

The $\text{Bi}_{1.97}\text{Eu}_{0.03}\text{MoO}_6$ double perovskite catalyst was also reported as an effective catalyst for the formation of substituted quinolones from different aliphatic ketones and 2-amino aryl ketones at ambient temperature in water [81].

Other reactions: LaMO_3 ($M = \text{Mn, Fe, Co, Cr, Al}$) catalyst applied for the hydrogenation of substituted and unsubstituted nitrobenzene to synthesize corresponding aniline in presence of KOH promoter in 2-propanol medium [82,83]. Among the catalysts, LaFeO_3 showed highest catalytic activity for this hydrogenation reaction. The same group also examined the strontium loading effect in the $\text{La}_{1-x}\text{Sr}_x\text{FeO}_3$ for nitrobenzene hydrogenation and found $\text{La}_{0.8}\text{Sr}_{0.2}\text{FeO}_3$ as the best active as well as recyclable catalysts [82,83].

Spray-flame synthesized $\text{LaCo}_{0.8}\text{Fe}_{0.2}\text{O}_3$ perovskite nanoparticles catalyst used for the oxidation of cinnamyl alcohol to cinnamaldehyde in liquid phase with TBHP under mild conditions. Waffel *et al.* [84] suggested a synergistic effect of Co and Fe for the best catalytic activity. Platinum nanoparticles supported on modified sol-gel method synthesized $\text{YCo}_{0.3}\text{Fe}_{0.7}\text{O}_3$ catalyst selectively hydrogenated cinnamaldehyde to cinnamyl alcohol with ~95% selectivity and 100% conversion [85].

Metal-free LaMnO_3 perovskite was reported as an exceptionally effective oxidation catalyst for the conversion of alkyl arenes to corresponding ketones and also for the preparation of 1,1-binaphthyl-2,2-diol (BINOL) through oxidative dimerization of 2-naphthol in presence of molecular oxygen [86]. Citric acid based sol-gel route prepared crumpled nanosheets of molybdenum-doped LaFeO_3 ($\text{LaMo}_{0.1}\text{Fe}_{0.9}\text{O}_3$) were used for the green synthesis of naphthopyrimidines from solvent-free one-pot reaction of different substituted aromatic aldehydes, 2-naphthol and barbituric acid or its derivatives [87]. The oxygen vacancy-rich mesoporous LaMnO_3 prepared through a modified molecular-assembly method, act as a significantly active as well as stable hydrogenation catalyst for synthesis of furfuryl alcohol from furfural with ~100% conversion and 96% selectivity. The author proposed from density functional theory calculation that the interaction of catalyst surface with catalytic substrate facilitated by the expose oxygen deficiency sites of porous LaMnO_3 , which lead to a lower energy barrier for this hydrogenation process [88].

Conclusion

In spite of low surface areas, structurally modified perovskite oxides show a unique catalytic efficiency for various organic reactions in liquid phase. Various porous and nano

perovskite oxides prepared by different conventional methods as well as modified methods can used as catalyst for the preparation of value-added chemicals. Perovskite oxides can efficiently use as acid-base catalysts for aldol condensation, esterification, Friedel-Crafts alkylation, cyanosilylation and one-pot synthesis. However, the connection of the catalytic efficiency with acid/base properties is still not properly discussed. Alkanes, alcohols, arenes, sulfides, *etc.* can selectively oxidized to the corresponding products over precious metal-supported, oxygen deficient, hexagonal and layered perovskite oxides catalyst with O_2 , H_2O_2 and *tert*-butyl hydroperoxide (TBHP) oxidants. Palladium and copper loaded multi-component perovskite oxides can also effectively catalyze Suzuki, Ullmann and Sonogashira type cross-coupling reactions. Several reactions are employed to increase the surface areas of perovskites, which subsequently increases the catalytic activities. However, the procedures complexity and inapplicability to versatile chemical compositions is the fundamental disadvantages of present synthesis methods. Thus a simple, efficient synthesis methods are still required for synthesis of various perovskite oxides with enhanced surface areas ($\geq 100 \text{ m}^2 \text{ g}^{-1}$) at mild condition. Furthermore, elucidation of proper reaction mechanisms along with the connection of catalytic efficiency of perovskite oxides with the substrate activation modes have to be properly clarified. Therefore, appropriate explanation of the mechanistic data can lead to develop efficient perovskite oxide catalysts with proper composition for different organic reactions in the liquid phase under mild reaction conditions.

CONFLICT OF INTEREST

The authors declare that there is no conflict of interests regarding the publication of this article.

REFERENCES

- C.-J. Li and B.M. Trost, *PNAS*, **105**, 13197 (2008) <https://doi.org/10.1073/pnas.0804348105>
- R.A. Sheldon, *Chem. Soc. Rev.*, **41**, 1437 (2012); <https://doi.org/10.1039/C1CS15219J>
- C.J. Clarke, W.-C. Tu, O. Levers, A. Bröhl and J.P. Hallett, *Chem. Rev.*, **118**, 747 (2018); <https://doi.org/10.1021/acs.chemrev.7b00571>
- K. Kamata, *Bull. Chem. Soc. Jpn.*, **92**, 133 (2019); <https://doi.org/10.1246/bcsj.20180260>
- V.L. Sushkevich, D. Palagin, M. Ranocchiarri and J.A. van Bokhoven, *Science*, **356**, 523 (2017); <https://doi.org/10.1126/science.aam9035>
- S.H. Morejudo, R. Zanón, S. Escolástico, I. Yuste-Tirados, H. Malerød-Fjeld, P.K. Vestre, W.G. Coors, A. Martínez, T. Norby, J.M. Serra and C. Kjøseth, *Science*, **353**, 563 (2016); <https://doi.org/10.1126/science.aag0274>
- T. Komanoya, T. Kinemura, Y. Kita, K. Kamata and M. Hara, *J. Am. Chem. Soc.*, **139**, 11493 (2017); <https://doi.org/10.1021/jacs.7b04481>
- S. Kanai, I. Nagahara, Y. Kita, K. Kamata and M. Hara, *Chem. Sci.*, **8**, 3146 (2017); <https://doi.org/10.1039/C6SC05642C>
- M.J. C liment, A. Corma and S. Iborra, *Green Chem.*, **16**, 516 (2014); <https://doi.org/10.1039/C3GC41492B>
- M. Hara, K. Nakajima and K. Kamata, *Sci. Technol. Adv. Mater.*, **16**, 034903 (2015); <https://doi.org/10.1088/1468-6996/16/3/034903>

11. D.M. Alonso, S.G. Wettstein and J.A. Dumesic, *Chem. Soc. Rev.*, **41**, 8075 (2012); <https://doi.org/10.1039/c2cs35188a>
12. M. Besson, P. Gallezot and C. Pinel, *Chem. Rev.*, **114**, 1827 (2014); <https://doi.org/10.1021/cr4002269>
13. B. Cornils, W.A. Herrmann, M. Beller and R. Paciello, *Applied Homogeneous Catalysis with Organometallic Compounds: A Comprehensive Handbook in Four Volumes*, Ed.: 3, Wiley-VCH: Weinheim (2017).
14. J. Hagen, *Industrial Catalysis: A Practical Approach*, Wiley-VCH: Weinheim (1999).
15. G. Ertl, H. Knözinger and J. Weitkamp, *Handbook of Heterogeneous Catalysis*, Ed. 2, Wiley-VCH: Weinheim (2008).
16. N. Mizuno, *Modern Heterogeneous Oxidation Catalysis*, Wiley-VCH: Weinheim (2009).
17. K. Yamaguchi and N. Mizuno, *Syn. Lett.*, 2365 (2010); <https://doi.org/10.1055/s-0030-1258565>
18. A. Takagaki, C. Tagusagawa, S. Hayashi, M. Hara and K. Domen, *Energy Environ. Sci.*, **3**, 82 (2010); <https://doi.org/10.1039/B918563A>
19. M. Hechelski, A. Ghinet, B. Louvel, P. Dufrenoy, B. Rigo, A. Daïch and C. Waterlot, *ChemSusChem*, **11**, 1249 (2018); <https://doi.org/10.1002/cssc.201702435>
20. S. Ishikawa, Z. Zhang and W. Ueda, *ACS Catal.*, **8**, 2935 (2018); <https://doi.org/10.1021/acscatal.7b02244>
21. N. Mizuno, K. Yamaguchi and K. Kamata, *Catal. Surv. Asia*, **15**, 68 (2011); <https://doi.org/10.1007/s10563-011-9111-2>
22. A. Enferadi-Kerenkan, T.-O. Do and S. Kaliaguine, *Catal. Sci. Technol.*, **8**, 2257 (2018); <https://doi.org/10.1039/C8CY00281A>
23. C. Martínez and A. Corma, *Coord. Chem. Rev.*, **255**, 1558 (2011); <https://doi.org/10.1016/j.ccr.2011.03.014>
24. J. Liang, Z. Liang, R. Zou and Y. Zhao, *Adv. Mater.*, **29**, 1701139 (2017); <https://doi.org/10.1002/adma.201701139>
25. K. Kaneda and T. Mizugaki, *ACS Catal.*, **7**, 920 (2017); <https://doi.org/10.1021/acscatal.6b02585>
26. D. Astruc, F. Lu and J.R. Aranzaes, *Angew. Chem. Int. Ed. Engl.*, **44**, 7852 (2005); <https://doi.org/10.1002/anie.200500766>
27. A. Dhakshinamoorthy, M. Alvaro and H. Garcia, *Chem. Commun.*, **48**, 11275 (2012); <https://doi.org/10.1039/c2cc34329k>
28. J. Liu, L. Chen, H. Cui, J. Zhang, L. Zhang and C.-Y. Su, *Chem. Soc. Rev.*, **43**, 6011 (2014); <https://doi.org/10.1039/C4CS00094C>
29. R. Akiyama and S. Kobayashi, *Chem. Rev.*, **109**, 594 (2009); <https://doi.org/10.1021/cr800529d>
30. Q. Sun, Z. Dai, X. Meng and F.-S. Xiao, *Chem. Soc. Rev.*, **44**, 6018 (2015); <https://doi.org/10.1039/C5CS00198F>
31. D. Wang and D. Astruc, *Coord. Chem. Rev.*, **257**, 2317 (2013); <https://doi.org/10.1016/j.ccr.2013.03.032>
32. K. Nakajima and M. Hara, *ACS Catal.*, **2**, 1296 (2012); <https://doi.org/10.1021/cs300103k>
33. Y. Wang, X. Wang and M. Antonietti, *Angew. Chem. Int. Ed.*, **51**, 68 (2012); <https://doi.org/10.1002/anie.201101182>
34. D. Chen, C. Chen, Z.M. Baiyee, Z. Shao and F. Ciucci, *Chem. Rev.*, **115**, 9869 (2015); <https://doi.org/10.1021/acs.chemrev.5b00073>
35. F. Cheng and J. Chen, *Chem. Soc. Rev.*, **41**, 2172 (2012); <https://doi.org/10.1039/c1cs15228a>
36. D.U. Lee, P. Xu, Z.P. Cano, A.G. Kashkooli, M.G. Park and Z. Chen, *J. Mater. Chem. A Mater. Energy Sustain.*, **4**, 7107 (2016); <https://doi.org/10.1039/C6TA00173D>
37. X. Ge, A. Sumboja, D. Wu, T. An, B. Li, F.W.T. Goh, T.S.A. Hor, Y. Zong and Z. Liu, *ACS Catal.*, **5**, 4643 (2015); <https://doi.org/10.1021/acscatal.5b00524>
38. P. Tan, M. Liu, Z. Shao and M. Ni, *Adv. Energy Mater.*, **7**, 1602674 (2017); <https://doi.org/10.1002/aenm.201602674>
39. S. Royer, D. Duprez, F. Can, X. Courtois, C. Batiot-Dupeyrat, S. Laassiri and H. Alamdari, *Chem. Rev.*, **114**, 10292 (2014); <https://doi.org/10.1021/cr500032a>
40. N. Labhassetwar, G. Saravanan, S.K. Megarajan, N. Manwar, R. Khobragade, P. Daggali and F. Grasset, *Sci. Technol. Adv. Mater.*, **16**, 036002 (2015); <https://doi.org/10.1088/1468-6996/16/3/036002>
41. J. Zhu, H. Li, L. Zhong, P. Xiao, X. Xu, X. Yang, Z. Zhao and J. Li, *ACS Catal.*, **4**, 2917 (2014); <https://doi.org/10.1021/cs500606g>
42. F. Polo-Garzon and Z. Wu, *J. Mater. Chem. A Mater. Energy Sustain.*, **6**, 2877 (2018); <https://doi.org/10.1039/C7TA10591F>
43. H. Zhu, P. Zhang and S. Dai, *ACS Catal.*, **5**, 6370 (2015); <https://doi.org/10.1021/acscatal.5b01667>
44. M. Konsolakis, *ACS Catal.*, **5**, 6397 (2015); <https://doi.org/10.1021/acscatal.5b01605>
45. E.A.R. Assirey, *Saudi Pharm. J.*, **27**, 817 (2019); <https://doi.org/10.1016/j.jsps.2019.05.003>
46. P. Yadav, S. Yadav and R. Tomar, *ChemistrySelect*, **6**, 12947 (2021); <https://doi.org/10.1002/slct.202102292>
47. E. Grabowska, *Appl. Catal. B*, **186**, 97 (2016); <https://doi.org/10.1016/j.apcatb.2015.12.035>
48. W. Wang, M.O. Tadé and Z. Shao, *Chem. Soc. Rev.*, **44**, 5371 (2015); <https://doi.org/10.1039/C5CS00113G>
49. M. Kubicek, A.H. Bork and J.L.M. Rupp, *J. Mater. Chem. A Mater. Energy Sustain.*, **5**, 11983 (2017); <https://doi.org/10.1039/C7TA00987A>
50. P. Chandra, *ChemistrySelect*, **6**, 7557 (2021); <https://doi.org/10.1002/slct.202101434>
51. G.F. Teixeira, E. Silva Junior, R. Vilela, M.A. Zaghete and F. Colmati, *Catalysts*, **9**, 721 (2019); <https://doi.org/10.3390/catal9090721>
52. H. Kleineberg, M. Eisenacher, H. Lange, H. Strutz and R. Palkovits, *Catal. Sci. Technol.*, **6**, 6057 (2016); <https://doi.org/10.1039/C5CY01479D>
53. A. Takagaki, M. Sugisawa, D. Lu, J.N. Kondo, M. Hara, K. Domen and S. Hayashi, *J. Am. Chem. Soc.*, **125**, 5479 (2003); <https://doi.org/10.1021/ja034085q>
54. S. Yamaguchi, T. Okuwa, H. Wada, H. Yamaura and H. Yahiro, *Res. Chem. Intermed.*, **41**, 9551 (2015); <https://doi.org/10.1007/s11164-015-1980-y>
55. N. Pal, M. Paul and A. Bhaumik, *Appl. Catal. A*, **393**, 153 (2011); <https://doi.org/10.1016/j.apcata.2010.11.037>
56. S. Ray, P. Das, B. Banerjee, A. Bhaumik and C. Mukhopadhyay, *ChemPlusChem*, **80**, 731 (2015); <https://doi.org/10.1002/cplu.201402405>
57. H. Singh and J.K. Rajput, *J. Mater. Sci.*, **53**, 3163 (2018); <https://doi.org/10.1007/s10853-017-1790-2>
58. R. Mistri, D. Das, J. Llorca, M. Dominguez, T.K. Mandal, P. Mohanty, B.C. Ray and A. Gayen, *RSC Adv.*, **6**, 4469 (2016); <https://doi.org/10.1039/C5RA22592B>
59. A.A. Ansari, S.F. Adil, M. Alam, N. Ahmad, M.E. Assal, J.P. Labis and A. Alwarthan, *Sci. Rep.*, **10**, 15012 (2020); <https://doi.org/10.1038/s41598-020-71869-z>
60. S.J. Singh and R.V. Jayaram, *Catal. Commun.*, **10**, 2004 (2009); <https://doi.org/10.1016/j.catcom.2009.07.018>
61. C. Saux, C. Leal Marchena, R. Dinamarca, G. Pecchi and L. Pierella, *Catal. Commun.*, **76**, 58 (2016); <https://doi.org/10.1016/j.catcom.2015.12.023>
62. C. Liu, Z. Zhao, X. Yang, X. Ye and Y. Wu, *Chin. J. Chem.*, **14**, 516 (1996).
63. C. Liu, Z. Zhao, X. Yang, X. Ye and Y. Wu, *Chem. Commun.*, 1019 (1996); <https://doi.org/10.1039/CC9960001019>
64. S. Saha and S.B. Abd Hamid, *RSC Adv.*, **7**, 9914 (2017); <https://doi.org/10.1039/C6RA26370D>
65. C.D. Evans, S.A. Kondrat, P.J. Smith, T.D. Manning, P.J. Miedziak, G.L. Brett, R.D. Armstrong, J.K. Bartley, S.H. Taylor, M.J. Rosseinsky and G.J. Hutchings, *Faraday Discuss.*, **188**, 427 (2016); <https://doi.org/10.1039/C5FD00187K>
66. I.B. Adilina, T. Hara, N. Ichikuni, N. Kumada and S. Shimazu, *Bull. Chem. Soc. Jpn.*, **86**, 146 (2013); <https://doi.org/10.1246/bcsj.20120215>
67. A. Rahmani and J. Saari, *J. Nanostruct.*, **6**, 301 (2016); <https://doi.org/10.22052/JNS.2016.34270>

68. S. Sugunan and V. Meera, *Indian J. Chem.*, **34A**, 984 (1995).
69. S. Kawasaki, K. Kamata and M. Hara, *ChemCatChem*, **8**, 3247 (2016); <https://doi.org/10.1002/cctc.201600613>
70. K. Sugahara, K. Kamata, S. Muratsugu and M. Hara, *ACS Omega*, **2**, 1608 (2017); <https://doi.org/10.1021/acsomega.7b00146>
71. K. Kamata, K. Sugahara, Y. Kato, S. Muratsugu, Y. Kumagai, F. Oba and M. Hara, *ACS Appl. Mater. Interfaces*, **10**, 23792 (2018); <https://doi.org/10.1021/acsami.8b05343>
72. S. Shibata, K. Sugahara, K. Kamata and M. Hara, *Chem. Commun.*, **54**, 6772 (2018); <https://doi.org/10.1039/C8CC02185F>
73. A. Aguadero, H. Falcon, J.M. Campos-Martin, S.M. Al-Zahrani, J.L.G. Fierro and J.A. Alonso, *Angew. Chem. Int. Ed. Engl.*, **50**, 6557 (2011); <https://doi.org/10.1002/anie.201007941>
74. C. Leal Marchena, G.A. Pecchi and L.B. Pierella, *Catal. Commun.*, **119**, 28 (2019); <https://doi.org/10.1016/j.catcom.2018.10.016>
75. I. Jaouali, N. Moussa, M.F. Nsib and M.A. Centeno, Proceedings of 2nd Euro-Mediterranean Conference for Environmental Integration (EMCEI-2), p. 429 (2019).
76. S. Shibata, K. Kamata and M. Hara, *Catal. Sci. Technol.*, **11**, 2369 (2021); <https://doi.org/10.1039/D1CY00245G>
77. M.D. Smith, A.F. Stepan, C. Ramarao, P.E. Brennan and S.V. Ley, *Chem. Commun.*, 2652 (2003); <https://doi.org/10.1039/b308465e>
78. S.P. Andrews, A.F. Stepan, H. Tanaka, S.V. Ley and M.D. Smith, *Adv. Synth. Catal.*, **347**, 647 (2005); <https://doi.org/10.1002/adsc.200404331>
79. S. Lohmann, S.P. Andrews, B.J. Burke, M.D. Smith, J.P. Atteld, H. Tanaka, K. Kaneko and S.V. Ley, *Synlett*, 1291 (2005); <https://doi.org/10.1055/s-2005-865233>
80. C. Battilocchio, B.N. Bhawal, R. Chorghade, B.J. Deadman, J.M. Hawkins and S.V. Ley, *Isr. J. Chem.*, **54**, 371 (2014); <https://doi.org/10.1002/ijch.201300049>
81. T. Dharmana and B.N. Naidu, *Asian J. Chem.*, **34**, 437 (2022); <https://doi.org/10.14233/ajchem.2022.23428>
82. A.S. Kulkarni and R.V. Jayaram, *Appl. Catal.*, **A**, **252**, 225 (2003); [https://doi.org/10.1016/S0926-860X\(03\)00417-4](https://doi.org/10.1016/S0926-860X(03)00417-4)
83. A.S. Kulkarni and R.V. Jayaram, *J. Mol. Catal. Chem.*, **223**, 107 (2004); <https://doi.org/10.1016/j.molcata.2003.12.042>
84. D. Waffel, B. Alkan, Q. Fu, Y.T. Chen, S. Schmidt, C. Schulz, H. Wiggers, M. Muhler and B. Peng, *ChemPlusChem*, **84**, 1155 (2019); <https://doi.org/10.1002/cplu.201900429>
85. Y. Xue, H. Xin, W. Xie, P. Wu and X. Li, *Chem. Commun.*, **55**, 3363 (2019); <https://doi.org/10.1039/C9CC00318E>
86. Y. Sahin, A.T. Sika-Nartey, K.E. Ercan, Y. Kocak, S. Senol, E. Ozensoy and Y.E. Turkmen, *ACS Appl. Mater. Interfaces*, **13**, 5099 (2021); <https://doi.org/10.1021/acsami.0c20490>
87. S. Rahmatinejad and H. Naeimi, *Polyhedron*, **177**, 114318 (2020); <https://doi.org/10.1016/j.poly.2019.114318>
88. Y. Zheng, R. Zhang, L. Zhang, Q. Gu and Z.A. Qiao, *Angew. Chem. Int.*, **60**, 4774 (2021); <https://doi.org/10.1002/anie.202012416>
89. P. Granger, V.I. Parvulescu, V.I. Parvulescu and W. Prellier, *Perovskites and Related Mixed Oxides*, Wiley-VCH: Weinheim (2016).
90. Y. Wang, H. Arandiyani, J. Scott, A. Bagheri, H. Dai and R. Amal, *J. Mater. Chem. A Mater. Energy Sustain.*, **5**, 8825 (2017); <https://doi.org/10.1039/C6TA10896B>
91. C. Marcilly, P. Courty and B. Delmon, *J. Am. Ceram. Soc.*, **53**, 56 (1970); <https://doi.org/10.1111/j.1151-2916.1970.tb12003.x>
92. Y. Teraoka, H. Kakebayashi, I. Moriguchi and S. Kagawa, *Chem. Lett.*, **20**, 673 (1991); <https://doi.org/10.1246/cl.1991.673>
93. M.P. Pechini, Method of Preparing Lead and Alkaline Earth Titanates and Niobates and Coating Method Using the Same to Form a Capacitor, US Patent, US3330697 (1967).
94. M. Kakihana, *J. Sol-Gel Sci. Technol.*, **6**, 7 (1996); <https://doi.org/10.1007/BF00402588>
95. H. Hattori and Y. Ono, *Solid Acid Catalysis: From Fundamentals to Applications*, CRC Press: Boca Raton (2015).
96. Y. Ono and H. Hattori, *Solid Base Catalysis*, Springer: Berlin/Heidelberg (2011).
97. G. Busca, *Chem. Rev.*, **107**, 5366 (2007); <https://doi.org/10.1021/cr068042e>
98. T. Okuhara, N. Mizuno and M. Misono, *Adv. Catal.*, **41**, 113 (1996); [https://doi.org/10.1016/S0360-0564\(08\)60041-3](https://doi.org/10.1016/S0360-0564(08)60041-3)
99. K. Kamata and K. Sugahara, *Catalysts*, **7**, 345 (2017); <https://doi.org/10.3390/catal7110345>
100. A. Corma and H. Garcia, *Chem. Rev.*, **103**, 4307 (2003); <https://doi.org/10.1021/cr030680z>
101. T. Punniyamurthy, S. Velusamy and J. Iqbal, *Chem. Rev.*, **105**, 2329 (2005); <https://doi.org/10.1021/cr050523v>
102. F. Cavani and J.H. Teles, *ChemSusChem*, **2**, 508 (2009); <https://doi.org/10.1002/cssc.200900020>
103. K. Kamata, *Bull. Chem. Soc. Jpn.*, **88**, 1017 (2015); <https://doi.org/10.1246/bcsj.20150154>
104. N. Mizuno and K. Kamata, *Coord. Chem. Rev.*, **255**, 2358 (2011); <https://doi.org/10.1016/j.ccr.2011.01.041>
105. X. Engelmann, I. Monte-Pérez and K. Ray, *Angew. Chem. Int. Ed.*, **55**, 7632 (2016); <https://doi.org/10.1002/anie.201600507>
106. S.S. Stahl, *Angew. Chem. Int. Ed.*, **43**, 3400 (2004); <https://doi.org/10.1002/anie.200300630>
107. I.A. Weinstock, R.E. Schreiber and R. Neumann, *Chem. Rev.*, **118**, 2680 (2018); <https://doi.org/10.1021/acs.chemrev.7b00444>
108. S. Ishikawa and W. Ueda, *Catal. Sci. Technol.*, **6**, 617 (2016); <https://doi.org/10.1039/C5CY01435B>
109. E. Hayashi, T. Komanoya, K. Kamata and M. Hara, *ChemSusChem*, **10**, 654 (2017); <https://doi.org/10.1002/cssc.201601443>
110. Q. Gao, C. Giordano and M. Antonietti, *Angew. Chem. Int. Ed.*, **51**, 11740 (2012); <https://doi.org/10.1002/anie.201206542>
111. M.A. Vannice, *Catal. Today*, **123**, 18 (2007); <https://doi.org/10.1016/j.cattod.2007.02.002>
112. K. Yamaguchi and N. Mizuno, *New J. Chem.*, **26**, 972 (2002); <https://doi.org/10.1039/b203262g>
113. T. Mitsudome, N. Nosaka, K. Mori, T. Mizugaki, K. Ebitani and K. Kaneda, *Chem. Lett.*, **34**, 1626 (2005); <https://doi.org/10.1246/cl.2005.1626>
114. J.P. Corbet and G. Mignani, *Chem. Rev.*, **106**, 2651 (2006); <https://doi.org/10.1021/cr0505268>
115. S.R. Chemler, D. Trauner and S.J. Danishefsky, *Angew. Chem. Int. Ed.*, **40**, 4544 (2001); [https://doi.org/10.1002/1521-3773\(20011217\)40:24<4544::AID-ANIE4544>3.0.CO;2-N](https://doi.org/10.1002/1521-3773(20011217)40:24<4544::AID-ANIE4544>3.0.CO;2-N)
116. N. Miyaura and A. Suzuki, *Chem. Rev.*, **95**, 2457 (1995); <https://doi.org/10.1021/cr00039a007>
117. F. Bellina, A. Carpita and R. Rossi, *Synthesis*, 2419 (2004); <https://doi.org/10.1055/s-2004-831223>
118. N. Miyaura, T. Yanagi and A. Suzuki, *Synth. Commun.*, **11**, 513 (1981); <https://doi.org/10.1080/00397918108063618>
119. Y. Nishihata, J. Mizuki, T. Akao, H. Tanaka, M. Uenishi, M. Kimura, T. Okamoto and N. Hamada, *Nature*, **418**, 164 (2002); <https://doi.org/10.1038/nature00893>
120. I. Jarrige, K. Ishii, D. Matsumura, Y. Nishihata, M. Yoshida, H. Kishi, M. Taniguchi, M. Uenishi, H. Tanaka, H. Kasai and J. Mizuki, *ACS Catal.*, **5**, 1112 (2015); <https://doi.org/10.1021/cs501608k>

Rajib Mistri*

Selective oxidation of benzene to phenol in the liquid phase over copper-substituted LaFeO₃ perovskite oxide as catalyst

<https://doi.org/10.1515/znb-2023-0016>

Received March 16, 2023; accepted June 10, 2023;

published online June 27, 2023

Abstract: Selective oxidation of benzene to phenol is done in the liquid phase over copper-substituted LaFeO₃ perovskite oxides as catalyst using H₂O₂ as oxidant under mild reaction conditions. Among the different copper-substituted perovskite catalysts synthesized by a novel solution combustion method, the LaFe_{0.90}Cu_{0.10}O₃ catalyst showed highest activity (~56 % with 100 % selectivity of phenol) and also gives better activity than the corresponding catalyst made via incipient wetness impregnation of 10 at % Cu over combustion-synthesized LaFeO₃. XRD analysis revealed formation of the perovskite phase as the predominant one. The greater activity of the combustion-made catalyst has been attributed to the occurrence of a peculiar poorly-defined structure having substitutional copper ion sites on top of the LaFeO₃ particle as observed in HRTEM analysis. Much less occurrence of this phase in the impregnated catalyst, where copper is primarily present as dispersed CuO crystallites, explains its comparatively lower activity in the oxidation reaction. The effect of catalyst recycling shows negligible change of activity for the combustion-made catalyst whereas the analogous impregnated catalyst shows considerable decrease in activity in recycling. This explained to be due to the essentially intact poorly-defined structure in the former and leaching of the finely dispersed CuO crystallites from the latter catalyst during cycling.

Keywords: benzene oxidation; Cu²⁺ ion sites in LaFeO₃; Cu-substituted LaFeO₃ perovskite; reduced copper leaching; solution combustion

1 Introduction

Phenol is a significant chemical compound for preparation of industrially important materials and useful compounds

[1–5]. At present, worldwide almost 95 % of phenol is industrially manufactured through the multi-step “cumene process” from benzene [6]. However, the energy consumption is high due to the requirement of high pressure and high temperature for this process [7]. Additionally, highly explosive cumene hydroperoxide is produced in the “cumene process” as an intermediate [8, 9] and overall yield in this multistage process is low (less than 5 %) [7, 9]. To overcome these disadvantages, the development of more efficient and environmental friendly alternatives for the synthesis of phenol is highly desirable. Hence, great interest is keen to a one-step catalytic oxidation process for phenol production from benzene. Theoretically, the benzene to phenol conversion is well possible by oxidation, but experimentally this goal is difficult [10]. N₂O [11], H₂O₂ [12, 13], O₂ [14] and a mixture of O₂ and H₂ [15] are mostly investigated as oxidant for the direct hydroxylation of benzene to form phenol. Particularly, N₂O allows high selectivity but the limited N₂O sources and requirement of high reaction temperatures are the main drawback for this oxidant. Among the oxidants, H₂O₂ is a particularly useful oxidant due to the formation of only water as by-product. In addition, the procedure is environment-friendly, simple as well as economic [16]. Many homogeneous catalysts have been tested for this oxidation reaction [17–31], such as Cu complexes [22–25], Ni complexes [21], Co complexes [19], iron complexes [26–28] and Os complexes [29]. Polyoxometalate (POM) and phosphovanadomolybdate (V-POM) ionic composites have also been reported as homogeneous catalyst for the benzene to phenol transformation with O₂ as oxidant at room temperature [30, 31].

Different supported transition metal oxides (Fe, Co, Ti, Mo, V, Cr, Mn and others, supported on Al₂O₃, SiO₂ and TiO₂) were exclusively studied as heterogeneous catalysts for the benzene oxidation to form phenol. Among them vanadium-based catalysts showed better activity for the benzene hydroxylation [32–34]. Molecular sieves with incorporated transition metals (like NaY, SBA15, MCM-41, SBA16) also showed excellent catalytic activity for this oxidation due to the presence of isolated, highly dispersed active sites in the silica framework of the molecular sieves [35–37]. Recently, metal-doped carbon nitride [38] has also been reported as active catalyst for benzene hydroxylation using H₂O₂, but

*Corresponding author: Rajib Mistri, Department of Chemistry, Achhruram Memorial College, Jhalda, Purulia 723202, West Bengal, India, E-mail: rajibmistri@yahoo.co.in

further oxidation and the formation of by-products made this process unsatisfactory [16]. Although significant progress has been achieved in the last few years, the reported catalytic systems often showed only limited efficiency due to inherent drawbacks. As an example, the hydrophilic surface of a reported catalyst that adsorbed polar phenol molecules over non-polar benzene, which made benzene conversion lower, and consequently phenol selectivity became poorer [12]. In addition, active species leaching is mainly responsible for the deactivation of the catalysts in some cases [39].

Perovskite oxides (ABO_3) have attracted much attention recently for their useful application as piezoelectric, ferroelectric, magnetic, superconducting and also heterogeneous catalytic properties [40–47]. Various perovskites have been reported as catalyst for industrially important selective oxidation reactions of organic substrates in the liquid phase [48–59]. But the weaker sulphur poisoning resistance and low specific surface area of perovskites as compared to noble metals have restricted their industrial applications [60]. Recently new approaches such as substitutions of the cationic sites (rare earth metals for A and transition metals for B) and using new synthesis methods are applied for the structural modification and enhancement of the catalytic activity [61–66]. Pt-, Pd-, and Rh-substituted $LaMnO_3$ perovskites synthesized by the citrate method have been reported as efficient catalysts for total methane oxidation [66, 67]. Pd-substituted $LaMO_3$ ($M = Fe, Co$) [64, 66], $LaMn_{0.976}Rh_{0.224}O_{3.15}$ [68] and $(La_{0.6}Sr_{0.4})(Co_{0.94}Pt_{0.03}Ru_{0.03})O_3$ [69] were also reported as effective three-way catalysts.

In this study, we report the preparation, characterization and catalytic efficiency of copper-substituted $LaFeO_3$ perovskite oxides for benzene oxidation. Among the prepared perovskite compositions, $LaFe_{0.90}Cu_{0.10}O_3$ has shown the highest activity and selectivity in the formation of phenol by oxidation of benzene in acetonitrile using H_2O_2 under mild reaction conditions.

2 Experimental

2.1 Synthesis of catalysts

Pure $LaFeO_3$ and various copper-substituted $LaFeO_3$ perovskites ($LaFe_{1-x}Cu_xO_3$) ($x = 0.05–0.20$), were synthesized by the solution combustion method (SCS) using oxalyl dihydrazide (ODH; $C_2H_6N_4O_2$) as fuel. In particular, $LaFe_{0.90}Cu_{0.10}O_3$ was prepared by combustion of the metal salts $La(NO_3)_3 \cdot 9H_2O$ (Loba Chem, 99%), $Fe(NO_3)_3 \cdot 9H_2O$ (Merck India, 98%) and $Cu(NO_3)_2 \cdot 3H_2O$ (Merck India, 99%) with oxalyl dihydrazide in molar ratios of 1:0.90:0.10:2.26 at an ignition temperature of $T = \sim 350$ °C. In a specific synthesis, 2 g of $La(NO_3)_3 \cdot 9H_2O$, 1.6794 g of $Fe(NO_3)_3 \cdot 9H_2O$, 1.12 mL of a 10% aqueous $Cu(NO_3)_2 \cdot 3H_2O$ solution and 1.6108 g of ODH

were dissolved in 30 mL of water in a borosilicate dish and then introduced for combustion in a preheated muffle furnace. The surface of the redox mixture got ignited at complete dehydration and gave the perovskite within a minute.

In order for comparison, we prepared $LaFe_{0.90}Cu_{0.10}O_3$ through incipient wetness impregnation (IWI) method. The impregnated catalyst was prepared by impregnation of a proper volume of copper nitrate aqueous solution analogous to the support's pore volume into the combustion-made dried $LaFeO_3$ support. Subsequently it was dried at 100 °C overnight, crushed and calcined at 400 °C in air for 3 h to obtain the $LaFe_{0.90}Cu_{0.10}O_3$ -IWI catalyst.

2.2 Characterization of the catalysts

XRD, BET and HRTEM have been used for characterization of the synthesized materials. Powder X-ray diffraction (PXRD) patterns were collected with a Bruker D8 Advance diffractometer (40 kV, 40 mA) equipped with a Lynxeye detector and using $CuK\alpha$ radiation ($\lambda = 1.5418$ Å). The data was recorded in the 2θ range of 10–100° with 1 s step⁻¹ scanning time and 0.02° step size.

The BET surface areas were estimated with an Autosorb iQ-MP (Quantachrome Instruments, USA) at $T = -196$ °C. The samples were degassed at 300 °C for 7 h before each measurement. The BET equation

$$S_{BET} = V_m \times N_A \times s / V \times a$$

(with S_{BET} = specific surface area, V_m = monolayer adsorbed gas volume, N_A = Avogadro's no., s = cross-section area of adsorbed gas molecule, V = molar volume of adsorbed gas, a = mass of sample) is used for specific surface areas calculation over 0.3 to 0.08 P/P_0 pressure range.

High Resolution Transmission Electron Microscopy (HRTEM) was used for the microstructural characterization with a JEOL 2010F instrument at 200 kV accelerating voltage. The Si standard was used for calibration of the magnification. On prolonged electron beam exposure, no induced damage was observed for the studied samples and all images are raw data only.

2.3 Test of oxidation activity

The benzene oxidation with hydrogen peroxide was performed in the temperature range between room temperature (RT) and 100 °C under atmospheric pressure. In a typical reaction, 0.5 g of the catalyst was added to a liquid mixture containing 5 mL of benzene (56.3 mmol), 10 mL of 30 wt% H_2O_2 (97.9 mmol) and 20 mL of acetonitrile in a 250 mL two-necked round bottom flask under continuous stirring. The reaction system in the beginning consisted of two liquid phases, a benzene- and acetonitrile-containing organic phase and an aqueous phase containing acetonitrile and 30% H_2O_2 . After the start of the reaction the liquid mixture turned into homogeneous.

The homogeneous reaction mixture was analyzed by gas chromatography (Nucon 5765, New Delhi) equipped with a FID detector with a fused silica 30 m × 0.25 mm × 0.25 μm capillary column (EC5) at 220 °C injector and 240 °C detector temperature. The initial and final column temperatures were fixed at 110 and 150 °C respectively, with a temperature rate of 80 K min⁻¹. The standard sample injection method was used for the quantitative analysis.

Recycling tests were carried out for the best active combustion-synthesized $LaFe_{0.90}Cu_{0.10}O_3$ and its analogous impregnated ($LaFe_{0.90}Cu_{0.10}O_3$ -IWI) catalysts only. The solution after each experiment was

filtered and the residue was washed with the solvent. Then the residue was dried at 110 °C overnight and used in the next cycles as catalyst to examine the recycling ability.

Conventional iodometric titration was used for measuring the concentration of consumed H_2O_2 during the oxidation process from which we can calculate the H_2O_2 conversion in mol% (Conv.) and H_2O_2 selectivity in mol% (SE) by using the formulae: Conv. (in mol%) = total H_2O_2 consumption (including self-decomposition)/initial amount of H_2O_2 and SE (in mol%) = consumption of H_2O_2 for phenol formation/total H_2O_2 consumption.

3 Results and discussion

3.1 Screening of catalysts

The catalytic activities of several copper-substituted LaFeO_3 perovskite oxide catalysts for the oxidation of benzene at 70 °C at atmospheric pressure are combined in Table 1. Pure LaFeO_3 is totally inactive for this oxidation. It is clearly marked that the combustion-synthesized $\text{LaFe}_{0.90}\text{Cu}_{0.10}\text{O}_3$ shows much better activity (~56 % conversion with 100 % phenol selectivity) than the other catalysts studied here and any further increase in copper content also decreased the activity as well as selectivity of the catalysts. Thus, the catalyst with the formula $\text{LaFe}_{0.90}\text{Cu}_{0.10}\text{O}_3$ was selected for subsequent studies. Phenol was produced as the predominant oxidation product and hydroquinone (maximum ~8 %) was observed as the byproduct. The analogous IWI catalyst showed much lower conversions (~30 %) with only 95 % selectivity as compared to the combustion-synthesized catalyst (see Table 1).

The catalytic activities of $\text{LaFe}_{0.90}\text{Cu}_{0.10}\text{O}_3$ for the benzene to phenol oxidation in the temperature range 32 °C–80 °C is presented in Figure 1(a). At room temperature (32 °C) benzene was only faintly oxidized, showing more or less no reaction.

Table 1: Benzene oxidation activities of different copper-substituted perovskite catalysts.^a

Catalyst composition	Benzene conversion (%)	Phenol formation (%)	Phenol selectivity (%)
LaFeO_3	–	–	–
$\text{LaFe}_{0.95}\text{Cu}_{0.05}\text{O}_3$	32.6	31.9	97.8
$\text{LaFe}_{0.93}\text{Cu}_{0.07}\text{O}_3$	38.5	37.1	96.4
$\text{LaFe}_{0.90}\text{Cu}_{0.10}\text{O}_3$	56	100	100
$\text{LaFe}_{0.85}\text{Cu}_{0.15}\text{O}_3$	47.9	42.6	88.9
$\text{LaFe}_{0.80}\text{Cu}_{0.20}\text{O}_3$	45.3	38.6	85.2
$\text{LaFe}_{0.90}\text{Cu}_{0.10}$ -IWI	30.4	28.9	95.1

^aReaction conditions: 5 mL benzene + 10 mL H_2O_2 + 0.5 g catalyst + 20 mL MeCN; 6 h at $T = 70$ °C.

After rising the temperature to 40 °C, the oxidation activity increases sharply (around 32 % conversion with 100 % selectivity of phenol). Further increase by 10 K gives rise to an about 12 % increase of benzene conversion and remains almost constant (54–56 %) from 60 °C to 70 °C. However, a decrease of the activity (~47 %) and phenol selectivity (~92 %) was observed at 80 °C due to further oxidation of phenol to 1,4-benzoquinone and hydroquinone at higher temperatures. Benzene vaporization can further lead to decreased activity at this temperature [70].

Figure 1(b) shows the phenol formation percentage as a function of time over $\text{LaFe}_{0.90}\text{Cu}_{0.10}\text{O}_3$ at 70 °C. The catalytic oxidation reaction starts at around 30 min and reaches a maximum (~56 % conversion) beyond 6 h over the catalyst with 100 % selectivity.

3.2 Effect of H_2O_2 concentration on the oxidation of benzene over $\text{LaFe}_{0.90}\text{Cu}_{0.10}\text{O}_3$

The H_2O_2 concentration has a clear impact on the oxidation of benzene. The effect of H_2O_2 concentration was measured by retaining the amount of benzene constant (5 mL or 56.3 mmol) in acetonitrile at $T = 70$ °C (see Figure 2). No oxidation products were observed in the absence of H_2O_2 . 50 mmol H_2O_2 gives ~43 % conversion which reaches the maximum ~56 % at a concentration of 97.9 mmol H_2O_2 . Further increase of H_2O_2 to 195.8 mmol (or a molar ratio of 1:4 after 1:2) did not show any noticeable change in conversion. However, catalytic activity and selectivity decreased from 195.8 mmol H_2O_2 onwards. This can be due to increased water formation at higher concentrations of H_2O_2 which lowers the solubility of phenol. In addition, the formation of byproducts increases due to over oxidation of phenol [71]. Although a theoretical ratio of 1:1 or 56.3 mmol H_2O_2 is needed for this oxidation reaction, in our experiments an optimum ratio of 1:2 (97.9 mmol of H_2O_2) was found. This can be explained by the fact that not all of the H_2O_2 participates actually in the oxidation reaction due to self-decomposition of H_2O_2 , which cannot be avoided under the reaction conditions [72]. Mainly phenol along with small amounts of 1,4-benzoquinone and hydroquinone were identified as products but other oxidized products like catechol were not detected in our study. This may be due to the fact that at low concentrations of H_2O_2 the perovskite-based catalysts mostly form peroxide radicals which subsequently lead to the formation of hydroquinone instead of catechol during the catalytic oxidation [70].

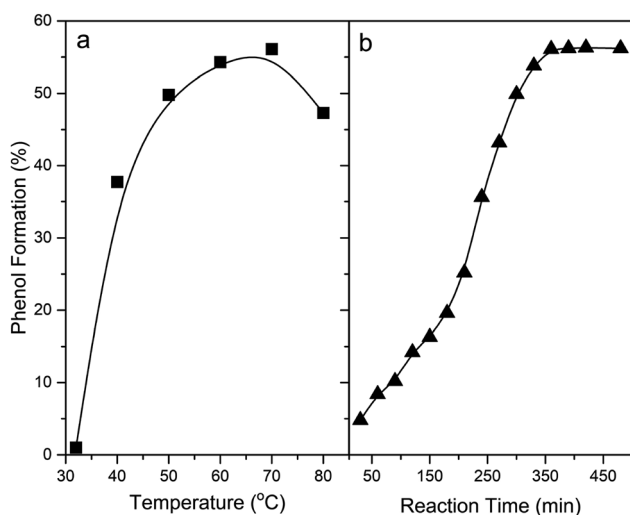


Figure 1: Temperature and time effect on the benzene oxidation. (a) Temperature effect (6 h reaction time) and (b) time effect ($T = 70\text{ }^{\circ}\text{C}$) on the oxidation of benzene over $\text{LaFe}_{0.90}\text{Cu}_{0.10}\text{O}_3$ as catalyst. Reaction conditions: 5 mL benzene + 10 mL H_2O_2 + 0.5 g catalyst + 20 mL MeCN.

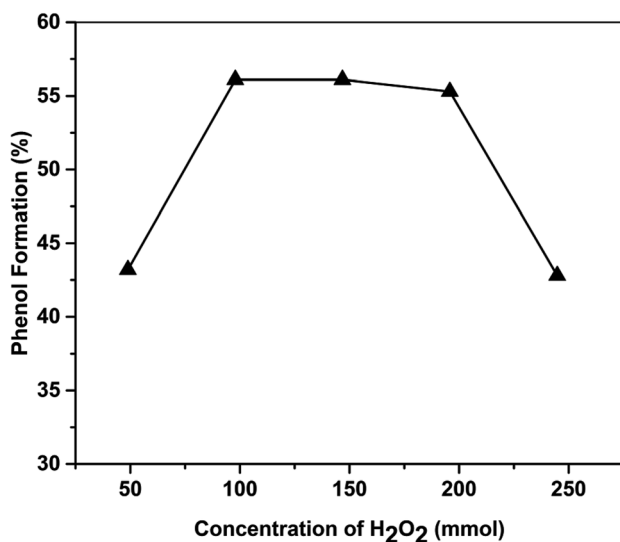


Figure 2: Phenol formation as a function of H_2O_2 concentration over $\text{LaFe}_{0.90}\text{Cu}_{0.10}\text{O}_3$ as catalyst. Reaction conditions: 5 mL benzene + 0.5 g catalyst + 20 mL MeCN; 6 h at $T = 70\text{ }^{\circ}\text{C}$.

3.3 Effect of solvent on the oxidation of benzene over $\text{LaFe}_{0.90}\text{Cu}_{0.10}\text{O}_3$ as catalyst

Different solvents were used for the oxidation of benzene and it was found that the activity decreases in the order acetonitrile > acetic acid > ethanol > water ~ methanol (Figure 3). The highest phenol formation (56 %) with 100 % selectivity was observed in acetonitrile. Although we get high benzene conversion (~30 %) in water, the phenol

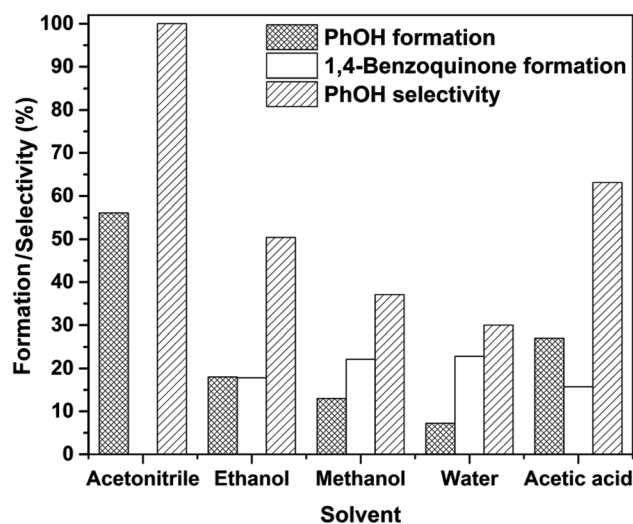


Figure 3: Benzene oxidation activities of $\text{LaFe}_{0.90}\text{Cu}_{0.10}\text{O}_3$ as catalyst in different solvents. Reaction conditions: 5 mL benzene + 0.5 g catalyst + 10 mL H_2O_2 + 20 mL solvent; 6 h at $T = 70\text{ }^{\circ}\text{C}$.

selectivity was very low (~24 %) due to the formation of 1,4-benzoquinone (selectivity ~76 %) mainly by further oxidation. Methanol gave less phenol formation (~13 %) and selectivity (~37 %) mostly due to the lower boiling point (65 °C) of this solvent. On the other hand, ethanol is a higher-boiling solvent than methanol and consequently showed a better phenol formation activity (18 %) as well as selectivity (50 %) which, however, is lower than acetic acid or acetonitrile. Acetic acid as solvent gave higher phenol formation (~27 %) but the phenol selectivity (~63 %) is less than acetonitrile.

Acetonitrile is an aprotic solvent and can easily activate H_2O_2 by formation of a good oxygen transfer intermediate, the perhydroxyl anion, which initiates the oxidation [73]. In addition, the H_2O_2 consumption and its self-decomposition can affect the oxidation activity in various solvents. The effective utilization of H_2O_2 for the oxidation reaction increases when the self-decomposition rate of H_2O_2 is low. Interestingly, the desired product can be obtained by using the appropriate solvent for the oxidation reaction, i.e., water for the formation of 1,4-benzoquinone or acetonitrile for phenol [73, 74].

3.4 Effect of solvent variations on the decomposition of H_2O_2 over $\text{LaFe}_{0.90}\text{Cu}_{0.10}\text{O}_3$

The catalytic activity and selectivity largely depend on the selective H_2O_2 decomposition. The following definitions are used. Decomposition of H_2O_2 means total H_2O_2 consumed

during the entire reaction. H_2O_2 decomposing to water and oxygen is referred to as self-decomposition. H_2O_2 utilized for formation of phenol is referred to as selective decomposition. H_2O_2 utilized for the formation of other by products including self-decomposition is referred as non-selective decomposition.

Thus we estimated the H_2O_2 consumption percentage and its selective decomposition for benzene oxidation over $\text{LaFe}_{0.90}\text{Cu}_{0.10}\text{O}_3$ as catalyst in different solvents by iodometric titration (see Section 2.3, Table 2). The benzene conversion will be higher when the decomposition of H_2O_2 in the overall oxidation process is higher but a high initial decomposition of H_2O_2 will result in nonselective H_2O_2 decomposition and the formation of by-products increases. A high total decomposition of H_2O_2 with minimum initial decomposition (i.e., high selective decomposition of H_2O_2) enhances the effective H_2O_2 utilization and as a result the phenol formation increases. The solvent dependence of the selective conversion of H_2O_2 is following the order: acetonitrile (~56 %) > acetic acid (~29 %) > ethanol (~22 %) > methanol (~14 %) > water (~6 %). The activity of benzene oxidation over $\text{LaFe}_{0.90}\text{Cu}_{0.10}\text{O}_3$ catalyst also follows the same order in different solvents (see Figure 3). In this study, acetonitrile showed the highest conversion with 100 % selectivity under the selected conditions. The poorer selective conversion of peroxide can be made responsible for the lower phenol formation in ethanol, methanol and water. The peroxide radical, which is generated in the oxidation process, acquires additional stability in these polar protic solvents due to the formation of hydrogen bonds. Thus the H_2O_2 decomposition equilibrium is shifted to the right and the self-decomposition rate increases [20].

On the other hand, the peroxide radical does not acquire extra stability in acetonitrile due to the polar aprotic nature of the solvent. In acetic acid, peroxyacetic acid is formed which makes H_2O_2 even more stable and reduces the self-decomposition of H_2O_2 . Thus, the loss of H_2O_2 is lower in these two solvents than in the other polar protic solvents used here and the formation of phenol increases. Interestingly, after 3 h a small decline of peroxide selectivity is observed in acetonitrile and acetic acid. The H_2O_2 self-decomposition is still present up to 3 h of reaction time and some by-products are also formed after this time.

3.5 Test of heterogeneity and recycling ability

In order to see whether the catalytic benzene oxidation was truly heterogeneous or not and also to examine for probable metal leaching, the traditional Sheldon hot-filtration test was performed by using both combustion-made $\text{LaFe}_{0.90}\text{Cu}_{0.10}\text{O}_3$ and incipient wetness-made $\text{LaFe}_{0.90}\text{Cu}_{0.10}\text{O}_3$ -IWI catalysts. For this purpose, after 2 h of catalytic reaction, the catalyst was instantaneously filtered off from the reaction mixture by using a Gooch crucible with a G4 sintered disk to avoid re-adsorption of leached metals onto the catalyst surface. The filtrate was collected in a different preheated round-bottom flask at the same temperature and the reaction was carried on for further 4 h. Gas-chromatographic analysis showed no change in conversion after 2 h up to 6 h (14 %) for the combustion-made $\text{LaFe}_{0.90}\text{Cu}_{0.10}\text{O}_3$ catalyst (see Figure 4). However, a little but definite increase in conversion (from 8 to 15 %) was observed for the $\text{LaFe}_{0.90}\text{Cu}_{0.10}\text{O}_3$ -IWI catalyst in hot-filtration test (see Figure 4). Thus, the nature of this oxidation reaction is purely heterogeneous for combustion-made $\text{LaFe}_{0.90}\text{Cu}_{0.10}\text{O}_3$ catalyst and the possibility of metal leaching or active material decomposition can be excluded.

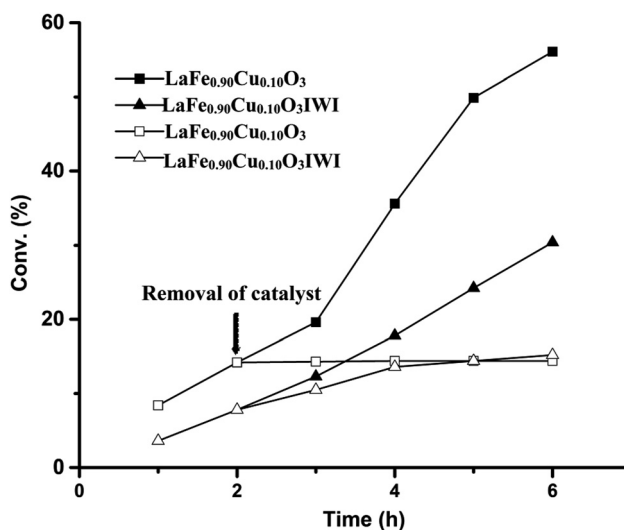


Figure 4: Sheldon hot-filtration test.

Table 2: H_2O_2 conversion (Conv.) and selectivity (SE) in different solvents over $\text{LaFe}_{0.90}\text{Cu}_{0.10}\text{O}_3$ at different time intervals^a.

Time (h)	Acetonitrile		Ethanol		Methanol		Water		Acetic acid	
	Conv.	SE	Conv.	SE	Conv.	SE	Conv.	SE	Conv.	SE
1	30.2	34.6	36.9	12.5	40.2	8.3	47.8	3.2	31.3	17.9
3	62.0	29.8	53.2	14.1	56.3	11.5	67.3	5.6	56.3	15.3
6	99.1	56.1	82.1	22.3	87.6	14.5	95.2	6.4	92.1	29.2

^aReaction conditions: 5 mL benzene + 0.5 g catalyst + 10 mL H_2O_2 + 20 mL solvent; $T = 70^\circ\text{C}$.

The certain enhancement of conversion in the absence of catalyst for $\text{LaFe}_{0.90}\text{Cu}_{0.10}\text{O}_3$ -IWI proves that the nature of catalytic oxidation is not truly heterogeneous in case of this catalyst and a certain amount of active metal is leaching out from this catalyst to the reaction mixture during the oxidation reaction (Figure 5).

The leaching of active metals has been reported to be controlled by using strong metal-supported interactions in $\text{Fe}^{3+}/\text{MgO}$ catalysts and the catalyst is also maintaining the same activity after the first cycle (36 % conversion) [75]. Cu-NaY zeolites were also reported as efficient catalysts with limited metal leaching after the first cycle and the leaching of the metal after the second cycle has almost stopped [76]. The metal leaching problem was controlled in 4 wt% Cu-MCM-41 and the phenol formation was lowered by 5 % only after the third cycle [70]. Bimetallic Co-V-MCM-41 shows reduced metal leaching in the benzene oxidation in acetonitrile with H_2O_2 at 70 °C for 24 h (conversion 48 % and 81 % selectivity of phenol) [77]. The metal leaching was also limited for the $\text{FeVCu}/\text{TiO}_2$ -catalyzed benzene oxidation in ascorbic acid [78]. Thus, the leaching of active metals is an important non-negligible aspect for these catalytic reactions in the literature. In our metal ion-substituted catalyst, where the active metals are incorporated into the perovskite structure, the probability of active metal leaching is expected to be lower. The recycling test of the combustion-made $\text{LaFe}_{0.90}\text{Cu}_{0.10}\text{O}_3$ catalyst retains its activity as well as selectivity in the successive cycles (up to the third cycle) but the conversion as well as the selectivity for the impregnated catalyst ($\text{Cu}_{0.10}\text{LaFe}_{0.90}\text{O}_3$ -IWI) decrease in successive cycles (conversion decreases from ~30 % to 24 % in the second cycle and

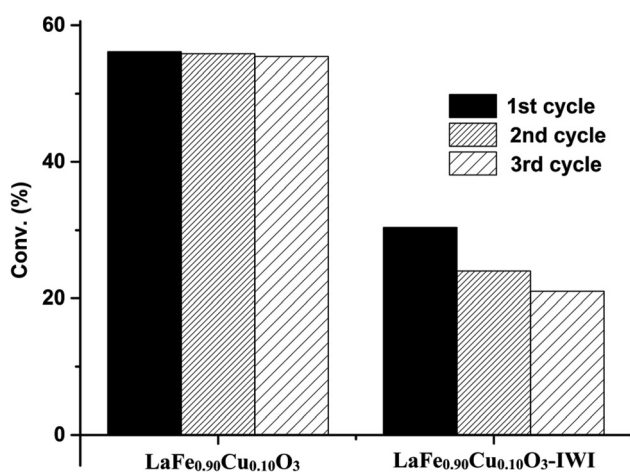


Figure 5: Recycling effect of the catalyst $\text{LaFe}_{0.90}\text{Cu}_{0.10}\text{O}_3$ prepared via (a) solution combustion (SCS), (b) impregnation (IWI) methods on benzene oxidation. Reaction conditions: 0.50 g catalyst + 5 mL benzene + 10 mL H_2O_2 + 20 mL MeCN; 6 h at $T = 70$ °C.

to 21 % in the third cycle). Thus, the reduced conversion in the recycling test of the IWI catalyst is accompanied by considerable copper leaching.

3.6 BET studies of the catalysts

The BET surface areas of the catalysts LaFeO_3 , $\text{LaFe}_{0.95}\text{Cu}_{0.05}\text{O}_3$, $\text{LaCu}_{0.10}\text{Fe}_{0.90}\text{O}_3$, the used $\text{LaFe}_{0.90}\text{Cu}_{0.10}\text{O}_3$ -cy2 (after 2nd cycle) and $\text{LaFe}_{0.90}\text{Cu}_{0.10}\text{O}_3$ -IWI are 12.6, 14.6, 26.6, 21.6 and $9.9 \text{ m}^2 \text{ g}^{-1}$ respectively. Among these catalysts, $\text{La}_{0.90}\text{Cu}_{0.10}\text{FeO}_3$ shows the highest surface area along with highest pore volume of $0.260 \text{ cm}^3 \text{ g}^{-1}$. The pore volume varies from 0.019 to $0.260 \text{ cm}^3 \text{ g}^{-1}$ for the other samples. The LaFeO_3 has very small pores of 1.8 nm width but all other catalysts have pore size distributions between 14.6 and 15.3 nm.

3.7 XRD studies

The powder XRD patterns of different perovskite (pure and Cu-substituted) samples show that the major phase formed in the combustion-synthesized and IWI catalysts is orthorhombic perovskite LaFeO_3 (Figure 6). All the diffraction lines could be indexed to the orthorhombic structure of LaFeO_3 (space group $Pnma$; JCPDS 37-1493). Some additional reflections are also present in our study which clearly

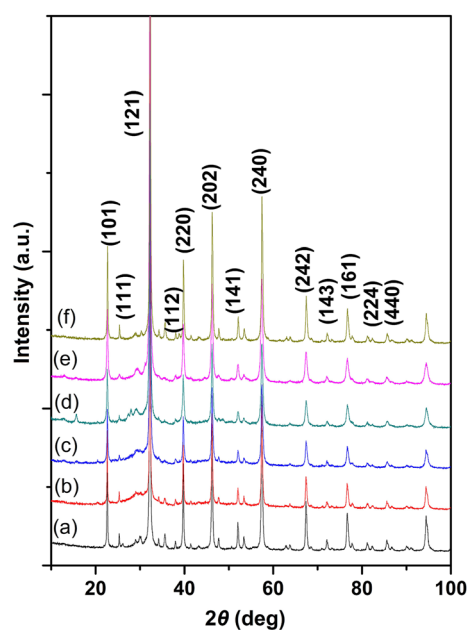


Figure 6: XRD patterns of (a) LaFeO_3 , (b) $\text{LaFe}_{0.95}\text{Cu}_{0.05}\text{O}_3$, (c) $\text{LaFe}_{0.93}\text{Cu}_{0.07}\text{O}_3$, (d) $\text{LaFe}_{0.90}\text{Cu}_{0.10}\text{O}_3$, (e) $\text{LaFe}_{0.85}\text{Cu}_{0.15}\text{O}_3$ and (f) $\text{LaFe}_{0.90}\text{Cu}_{0.10}\text{O}$ -IWI.

indicate the presence of very minor amounts of La_2O_3 and Fe_3O_4 as impurities. However, the parent LaFeO_3 contains more impurity phases which reduces as the Cu content increases. In case of the IWI sample, the peak around 35.6° is broadened and a new peak appears at 38.7° which indicates the formation of an additional phase and the presence of CuO oxide.

3.8 Microstructural studies

The low-magnification TEM image of the as-prepared $\text{LaFe}_{0.90}\text{Cu}_{0.10}\text{O}_{3-\delta}$ sample shows a holey structure with an unusual morphology (Figure 7(a)). The comprehensive HRTEM image of the as-prepared $\text{LaFe}_{0.90}\text{Cu}_{0.10}\text{O}_3$ shows the lattice fringes analogous to the LaFeO_3 phase from Fourier Transform (FT) measurement (Figure 7(b)). Spots at 2.37 and 2.78 Å match exactly the (112) and (121) crystallographic planes of LaFeO_3 , respectively. A poorly-defined structure is also identified over most of the LaFeO_3 crystals by HRTEM. The widening of the area labeled “a” in Figure 7(b) shows the poorly defined structure which comprises 2–4 atomic layers in most cases and an atomic mismatch is also observed among the surface of pure LaFeO_3 crystals with this poorly defined structure.

The $\text{LaFe}_{0.90}\text{Cu}_{0.10}\text{O}_3$ sample after the second cycle ($\text{LaFe}_{0.90}\text{Cu}_{0.10}\text{O}_3\text{-cy2}$) is almost similar to the fresh one and the holey structure is identical as in the as-prepared

sample (Figure 7(c)). Lattice fringes at 2.78 Å are also clearly observable in the areas labeled “a” and “b”, which again corresponds perfectly to the (121) crystallographic planes of LaFeO_3 , but in the enlarged images the existence of the poorly defined phase is marked by arrows (Figure 7(d)).

The general appearance of the sample synthesized by the IWI method ($\text{LaFe}_{0.90}\text{Cu}_{0.10}\text{O}_3\text{-IWI}$) is similar to those defined above for the samples prepared by the SCS method and low magnification image of the sample $\text{LaFe}_{0.90}\text{Cu}_{0.10}\text{O}_3\text{-IWI}$ also shows the characteristic holey structure (Figure 7(e)). However, HRTEM images show well-faceted LaFeO_3 planes and the poorly defined phase is not as common as in the samples prepared by combustion (Figure 7(f)).

Therefore, it can be concluded from HRTEM that the sample is comprised by holey LaFeO_3 crystals and a poorly defined structure located on top of the LaFeO_3 crystals. Cu is likely present as Cu^{2+} ions in the poorly defined areas rather forming a solid solution and an atomic mismatch between the poorly defined structure and the LaFeO_3 crystal surface is also observed. Such poorly defined areas are much more abundant in the sample prepared by combustion with respect to the sample prepared by IWI. In the SCS sample, almost all the LaFeO_3 crystals are covered by the poorly defined phase, whereas in the IWI samples there are abundant clean edges of LaFeO_3 crystals. This suggests that the SCS sample performs better as catalyst due to the existence of the poorly defined phase. Finally, the combustion-made catalyst exhibits a structure after the second cycle similar to

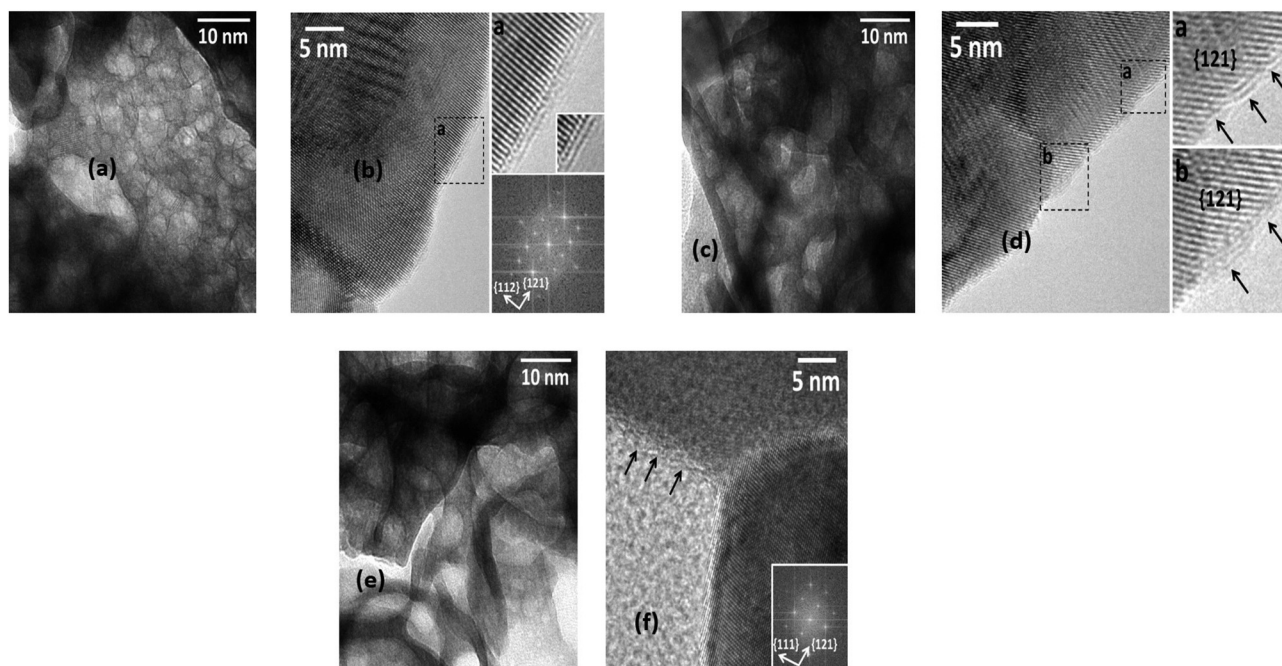


Figure 7: TEM images of (a, b) $\text{LaFe}_{0.90}\text{Cu}_{0.10}\text{O}_3$, (c, d) $\text{LaFe}_{0.90}\text{Cu}_{0.10}\text{O}_3\text{-cy2}$ and (e, f) $\text{Cu}_{0.10}\text{LaFe}_{0.90}\text{O}_3\text{-IWI}$.

the fresh sample at the atomic level, that is, with abundant poorly defined phase over the LaFeO_3 phase. This suggests that the poorly defined phase is not removed in the catalyst recycling.

3.9 General discussion of copper ion-substituted perovskite catalysts for benzene oxidation

Generally, copper in the oxidation state 2+ is believed to act as active site for the catalytic oxidation reaction of benzene to phenol [79–81]. In our study, the combustion-derived $\text{LaFe}_{0.90}\text{Cu}_{0.10}\text{O}_3$ catalyst is surrounded by an unusual surface structure on the surface-subsurface area of perovskite and copper is present as Cu^{2+} atom within the perovskite structure rather than as solid CuO . This unusual structure of $\text{LaFe}_{0.90}\text{Cu}_{0.10}\text{O}_3$ is playing the vital role in the much better oxidation activities of the combustion-synthesized catalyst rather than the corresponding catalyst prepared by incipient wetness impregnation ($\text{LaFe}_{0.90}\text{Cu}_{0.10}\text{O}_3$ -IWI) where finely dispersed CuO is mainly present in the catalyst.

This phenomenon also supports the observation of the best activity of $\text{LaFe}_{0.90}\text{Cu}_{0.10}\text{O}_3$ catalyst among all examined catalysts (Table 1). We surprisingly note that the phenol selectivity increases with longer reaction times (in some cases reaching ~100 %). The decreased decomposition rate of H_2O_2 during reaction progress is primarily responsible for the overall increase of phenol selectivity at longer reaction times (6 h). The H_2O_2 decomposition progressively increases the quantity of water in the reaction mixture and as a result the concentration of oxidant as well as concentration of feebly water-soluble byproducts are decreasing in the presence of water.

Catalytic benzene oxidation in the presence of peroxide is usually following peroxy-metal pathways, similar to Fenton chemistry and the hydroxyl radicals activate the highly stable benzene molecule towards phenol formation [82]. The oxidation of benzene by peroxide over one-electron oxidants like copper is commonly believed to take place through a radical pathway [81, 83]. In the present study, we believe that a similar redox mechanism operates with H_2O_2 in our copper ion-substituted perovskite catalyst. In order to investigate the oxidation mechanism, we have performed the oxidation reaction in the presence of quinone, a radical scavenger. After 2 h of oxidation, the scavenger was added to the reaction mixture and the reaction progression was monitored. The analysis of the reaction aliquot clearly shows that the benzene oxidation is completely paused after the scavenger addition (Figure 8). Thus, we conclude that the

oxidation process over the perovskite catalyst reported in this study proceeds through a radical mechanism similar to previous literature reports [77, 83, 84]. In more detail, the metal ion (here copper) acts as a radical initiator for the auto-oxidation processes by promoting the decomposition of H_2O_2 to radicals mediated by the $\text{Cu}^{2+}/\text{Cu}^+$ redox couple (one-electron transfer process promoted by LaFeO_3 perovskite). Eventually benzyl free radicals are produced by abstraction of hydrogen by homolytic cleavage from benzene. This radical reacts further with the peroxy radical to form phenol and water.

The excellent activity (~56 % conversion with 100 % selectivity) of our $\text{LaFe}_{0.90}\text{Cu}_{0.10}\text{O}_3$ perovskite catalyst becomes even more evident when this system is compared with other catalysts reported previously. Bimetallic Cu-Ce-doped rice husk silica was reported as highly efficient catalyst with a high benzene conversion (84 %) as well as phenol selectivity (96 %) under atmospheric pressure at 70 °C in acetonitrile after 4 h. However, in this study a significant decline in conversion during successive cycles was reported due to active metal leaching [81]. Highly dispersed vanadium oxide on ceria-promoted rice husk silica also acts as a highly selective catalyst for phenol formation from benzene oxidation with H_2O_2 in acetonitrile at 60 °C, but the conversion was much lower (~21 %) [84]. Although our combustion-made catalyst provides lower surface areas than the commonly used supports such as zeolites [74, 77, 85–88], alumina [79], titania [89], magnesia [75] and rice husk silica [81, 83] it still shows significant activity as compared to many other reported catalysts. The peculiar structure of our combustion-made catalyst seems to be an important factor for the significant catalytic activity.

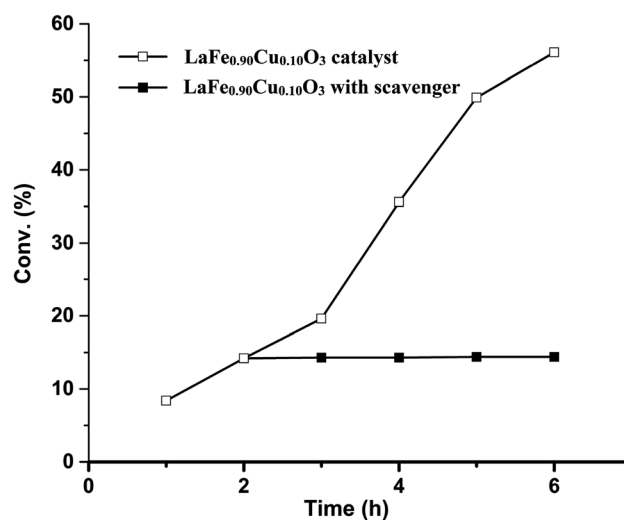


Figure 8: Effect of radical scavenger.

4 Conclusions

Copper-substituted $\text{LaFe}_{1-x}\text{Cu}_x\text{O}_3$ perovskite oxides have been prepared by a simple novel solution combustion method. Combustion-made $\text{LaFe}_{0.90}\text{Cu}_{0.10}\text{O}_3$ is shown to be a very efficient catalyst for the benzene oxidation in acetonitrile at 70 °C (56.1% conversion with 100% phenol selectivity). The effects of different parameters such as copper loading, time, temperature, oxidant concentration and solvent were studied and it was found that acetonitrile is the best solvent at 70 °C with a 1:2 molar ratio of benzene to H_2O_2 . A peculiar poorly defined structure on top of the LaFeO_3 particles in the combustion-made catalyst is characterized by microstructural studies and is probably due to incorporation of copper ion into the perovskite. The probability of active metal leaching is reduced for the combustion-made catalyst as compared to the analogous catalyst made by the incipient wetness impregnation (IWI) method. The recycling experiments also support this phenomenon where the combustion-made catalyst shows almost the same activity up to three cycles whereas the equivalent IWI catalyst shows noticeable loss of activity and selectivity in the successive cycles.

Author contributions: The author has accepted responsibility for the entire content of this submitted manuscript and approved submission.

Research funding: None declared.

Conflict of interest statement: The author declares no conflicts of interest regarding this article.

References

- Schmidt R. J. *Appl. Catal.*, A 2005, 280, 89–103.
- Solyman W. S., Nagiub H. M., Alian N. A., Shaker N. O., Kandil U. F. *J. Radiat. Res. Appl. Sci.* 2017, 10, 72–79.
- Pryde C., Hellman M. *J. Appl. Polym. Sci.* 1980, 25, 2573–2587.
- Takeichi T., Furukawa N. Epoxy resins and phenol-formaldehyde resins. In *Polymer Science: A Comprehensive Reference*. Elsevier BV: Amsterdam, 2021; pp. 723–751.
- Brydson J. A. *Plastics Materials*; Elsevier: Amsterdam, 1999.
- Zakoshansky V. *Pet. Chem.* 2007, 47, 273–284.
- Park H., Choi W. *Catal. Today* 2005, 101, 291–297.
- Fortuin J., Waterman H. *Chem. Eng. Sci.* 1953, 2, 182–192.
- Molinari R., Poerio T. *Asia-Pac. J. Chem. Eng.* 2010, 5, 191–206.
- Mancuso A., Sacco O., Sannino D., Venditto V., Vaiano V. *Catalysts* 2020, 10, 1424–1445.
- Yuranov I., Bulushev D. A., Renken A., Kiwi-Minsker L. *Appl. Catal.*, A 2007, 319, 128–136.
- Hu L., Wang C., Ye L., Wu Y., Yue B., Chen X., He H. *Appl. Catal.*, A 2015, 504, 440–447.
- Jiang T., Wang W., Han B. *New J. Chem.* 2013, 37, 1654–1664.
- Guo H., Chen Z., Mei F., Zhu D., Xiong H., Yin G. *Chem. Asian J.* 2013, 8, 888–891.
- Niwa S., Eswaremoorthy M., Nair J., Raj A., Itoh N., Shoji H., Namba T., Mizukami F. *Science* 2002, 295, 105–107.
- Parida K., Rath D. *Appl. Catal.*, A 2007, 321, 101–108.
- Peng J., Shi F., Gu Y., Deng Y. *Green Chem.* 2003, 5, 224–226.
- Nomiya K., Yagishita K., Nemoto Y., Kamataki T. *J. Mol. Catal. A: Chem.* 1997, 126, 43–53.
- Anandababu K., Muthuramalingam S., Velusamy M., Mayilmurugan R. *Catal. Sci. Technol.* 2020, 10, 2540–2548.
- Mistri R., Rahamana M., Llorca J., Priolkar K. R., Colussi S., Ray B. C., Gayen A. *J. Mol. Catal. A: Chem.* 2014, 390, 187–197.
- Muthuramalingam S., Anandababu K., Velusamy M., Mayilmurugan R. *Catal. Sci. Technol.* 2019, 9, 5991–6001.
- You X., Wei Z., Wang H., Li D., Liu J., Xu B., Liu X. *RSC Adv.* 2014, 4, 61790–61798.
- Tsuji T., Zaoputra A. A., Hitomi Y., Mieda K., Ogura T., Shiota Y., Yoshizawa K., Sato H., Kodera M. *Angew. Chem. Int. Ed.* 2017, 56, 7779–7782.
- Conde A., Diaz-Requejo M. M., Pérez P. *J. Chem. Commun.* 2011, 47, 8154–8156.
- Kumari S., Muthuramalingam S., Dhara A. K., Singh U., Mayilmurugan R., Ghosh K. *Dalton Trans.* 2020, 49, 13829–13839.
- Ramu R., Wanna W. H., Janmanchi D., Tsai Y. F., Liu C. C., Mou C. Y., Yu S. S. *Mol. Catal.* 2017, 441, 114–121.
- Yalymov A. I., Bilyachenko A. N., Levitsky M. M., Korlyukov A. A., Khrustalev V. N., Shul'pina L. S., Dorovatovskii P. V., Es'kova M. A., Lamaty F., Bantreil X., Villemejeanne B., Martinez J., Shubina E., Kozlov Y., Shul'pin G. *Catalysts* 2017, 7, 101–119.
- Carneiro L., Silva A. R. *Catal. Sci. Technol.* 2016, 6, 8166–8176.
- Vinogradov M. M., Kozlov Y. N., Nesterov D. S., Shul'pina L. S., Pombeiro A. J., Shul'pin G. B. *Catal. Sci. Technol.* 2014, 4, 3214–3226.
- Sarma B. B., Carmieli R., Collauto A., Efremenko I., Martin J. M., Neumann R. *ACS Catal.* 2016, 6, 6403–6407.
- Li X., Xue H., Lin Q., Yu A. *Appl. Organomet. Chem.* 2020, 34, 5606–5616.
- Dong Y., Niu X., Song W., Wang D., Chen L., Yuan F., Zhu Y. *Catalysts* 2016, 6, 74–90.
- Shijina A. V., Renuka N. K. *React. Kinet. Catal. Lett.* 2009, 98, 139–147.
- Peng G., Fu Z., Yin D., Zhong S., Yang Y., Yu N., Yin D. A. *Catal. Lett.* 2007, 118, 270–274.
- Tanarungsun G., Kiatkittipong W., Praserttham P., Yamada H., Tagawa T., Assabumrungrat S. *Catal. Commun.* 2008, 9, 1886–1890.
- Gu Y. Y., Zhao X. H., Zhang G. R., Ding H. M., Shan Y. K. *Appl. Catal.*, A 2007, 328, 150–155.
- Jourshabani M., Badiei A., Shariatinia Z., Lashgari N., Ziarani G. M. *Ind. Eng. Chem. Res.* 2016, 55, 3900–3908.
- Zhang T., Zhang D., Han X., Dong T., Guo X., Song C., Si R., Liu W., Liu Y., Zhao Z. *J. Am. Chem. Soc.* 2018, 140, 16936–16940.
- Ito S., Mitarai A., Hikino K., Hiramata M., Sasaki K. *J. Org. Chem.* 1992, 57, 6937–6941.
- Chen D., Chen C., Baiyee Z. M., Shao Z., Ciucci F. *Chem. Rev.* 2015, 115, 9869–9921.
- Cheng F., Chen J. *Chem. Soc. Rev.* 2012, 41, 2172–2192.
- Ge X., Sumboja A., Wu D., An T., Li B., Goh F. W. T., Hor T. S. A., Zong Y., Liu Z. *ACS Catal.* 2015, 5, 4643–4667.
- Zhu J., Li H., Zhong L., Xiao P., Xu X., Yang X., Zhao Z., Li J. *ACS Catal.* 2014, 4, 2917–2940.
- Zhu H., Zhang P., Dai S. *ACS Catal.* 2015, 5, 6370–6385.
- Wang W., Tadé M. O., Shao Z. *Chem. Soc. Rev.* 2015, 44, 5371–5408.
- Chandra P. *ChemistrySelect* 2021, 6, 7557–7597.

47. Teixeira G. F., Junior E. S., Vilela R., Zaghe M. A., Colmati F. *Catalysts* 2019, 9, 721–726.
48. Kleineberg H., Eisenacher M., Lange H., Strutz H., Palkovits R. *Catal. Sci. Technol.* 2016, 6, 6057–6065.
49. Yamaguchi S., Okuwa T., Wada H., Yamaura H., Yahiro H. *Res. Chem. Intermed.* 2015, 41, 9551–9561.
50. Singh H., Rajput J. K. *J. Mater. Sci.* 2018, 53, 3163–3188.
51. Mistri R. *Asian J. Chem.* 2022, 34, 2489–2498.
52. Kawasaki S., Kamata K., Hara M. *Chem. Cat. Chem.* 2016, 8, 3247–3253.
53. Shibata S., Sugahara K., Kamata K., Hara M. *Chem. Commun.* 2018, 54, 6772–6775.
54. Marchena C. L., Pecchi G. A., Pierella L. B. *Catal. Commun.* 2019, 119, 28–32.
55. Shibata S., Kamata K., Hara M. *Catal. Sci. Technol.* 2021, 11, 2369–2373.
56. Dharmana T., Naidu B. N. *Asian J. Chem.* 2022, 34, 437–442.
57. Xue Y., Xin H., Xie W., Wua P., Li X. *Chem. Commun.* 2019, 55, 3363–3366.
58. Zheng Y., Zhang R., Zhang L., Gu Q., Qiao Z. A. *Angew. Chem. Int. Ed.* 2021, 60, 4774–4781.
59. Mistri R., Das D., Llorca J., Dominguez M., Mandal T. K., Mohanty P., Ray B. C., Gayen A. *RSC Adv.* 2016, 6, 4469–4477.
60. Sushkevich V. L., Palagin D., Ranocchiaro M., van Bokhoven J. A. *Science* 2017, 356, 523–527.
61. Anastas P., Warner J. *Green Chemistry: Theory and Practice*; Oxford University Press: New York, 1998.
62. Morejudo S. H., Zanón R., Escolástico S., Tirados I. Y., Fjeld H. M., Vestre P. K., Coors W. G., Martínez A., Norby T., Serra J. M., Kjølseth C. *Science* 2016, 353, 563–566.
63. Komanoya T., Kinemura T., Kita Y., Kamata K., Hara M. *J. Am. Chem. Soc.* 2017, 139, 11493–11499.
64. Kanai S., Nagahara I., Kita Y., Kamata K., Hara M. *Chem. Sci.* 2017, 8, 3146–3153.
65. Climent M. J., Corma A., Iborra S. *Green Chem.* 2014, 16, 516–547.
66. Hara M., Nakajima K., Kamata K. *Sci. Technol. Adv. Mater.* 2015, 16, 034903–034925.
67. Alonso D. M., Wettstein S. G., Dumesic J. A. *Chem. Soc. Rev.* 2012, 41, 8075–8098.
68. Cornils B., Herrmann W. A., Beller M., Paciello R. *Applied Homogeneous Catalysis with Organometallic Compounds: A Comprehensive Handbook in Four Volumes*, 3rd ed.; Wiley-VCH: Weinheim, 2017.
69. Besson M., Gallezot P., Pinel C. *Chem. Rev.* 2014, 114, 1827–1870.
70. Chandran R. S., Ford W. T. *J. Chem. Soc., Chem. Commun.* 1988, 46, 104–105.
71. Guilhaume N., Primet M. *J. Catal.* 1997, 165, 197–204.
72. Berger D., Matei C., Papa F., Voicu G., Fruth V. *Prog. Solid State Chem.* 2007, 35, 183–191.
73. Stuchinskaya T. L., Kozhevnikov I. V. *Catal. Commun.* 2003, 4, 417–422.
74. Ferguson G., Ajjou A. N. *Tetrahedron Lett.* 2003, 44, 9139–9142.
75. Kockritz A., Sebek M., Dittmar A., Radnik J., Bruckner A., Benstrup U., Hugl H., Magerlein W. *J. Mol. Catal. A: Chem.* 2006, 246, 85–99.
76. Peyrovi M. H., Mahdavi V., Salehi M. A., Mahmoodian R. *Catal. Commun.* 2005, 6, 476–479.
77. Choudhary V. R., Dumbre D. K. *Appl. Catal., A* 2010, 375, 252–257.
78. Sheldon R. A., Arends I. W. C. E., Dijkman A. *Catal. Today* 2000, 57, 157–166.
79. Shiono M., Kobayashia K., Nguyen T. L., Hosoda K., Kato T., Ota K., Dokiya M. *Solid State Ionics* 2004, 170, 1–7.
80. Giebel L., Kiebling D., Wendt G. *Chem. Eng. Technol.* 2007, 30, 889–894.
81. Sorenson S. C., Wronkiewicz J. A., Sis L. B., Wirtz G. P. *Am. Ceram. Soc. Bull.* 1974, 53, 446–449.
82. Behera G. C., Parida K. M. *Appl. Catal., A* 2012, 413, 245–253.
83. Brunel D., Fajula F., Nagy J. B., Deroide B., Verhoef M. J., Veum L., Peters J. A., van Bekkum H. *Appl. Catal., A* 2001, 213, 73–82.
84. Choudhary V. R., Dumbre D. K., Uphade B. S., Narkhede V. S. *J. Mol. Catal. A: Chem.* 2004, 215, 129–135.
85. Merino N. A., Barbero B. P., Grange P., Cadús L. E. *J. Catal.* 2005, 231, 232–244.
86. Pena M. A., Fierro J. L. G. *Chem. Rev.* 2001, 101, 1981–2018.
87. Royer S., Berube F., Kaliaguine S. *Appl. Catal., A* 2005, 282, 273–284.
88. Koponen M. J., Suvanto M., Pakkanen T. A., Kallinen K., Kinnunen T. J. J., Haörkönen M. *Solid State Sci.* 2005, 7, 7–12.
89. Tanarungsun G., Kiatkittipong W., Praserttham P., Yamada H., Tagawa T., Assabumrungrat S. *J. Ind. Eng. Chem.* 2008, 14, 596–601.



Cite this: DOI: 10.1039/d2ee04211h

Scalable production of an intermetallic Pt–Co electrocatalyst for high-power proton-exchange-membrane fuel cells†

Tae Yong Yoo,^{‡,ab} Jongmin Lee,^{‡,ab} Sungjun Kim,^{‡,ab} Min Her,^{ab} Shin-Yeong Kim,^{ab} Young-Hoon Lee,^{ab} Heejong Shin,^{ab} Hyunsun Jeong,^{ab} Arun Kumar Sinha,^{ab} Sung-Pyo Cho,^c Yung-Eun Sung^{ab*} and Taeghwan Hyeon^{ab*}

Power performance is the primary bottleneck to the industrial application of proton-exchange-membrane fuel cells, which hinges on catalytic activity, oxygen mass transfer, and proton conduction at the cathode catalyst layer. Tackling all these critical factors requires a holistic design of catalyst, embodied by an elaborate synthesis. Here we present a straightforward synthetic approach to address these practical issues. A bimetallic compound, formulated as $[\text{Co}(2,2'\text{-bipyridine})_3][\text{PtCl}_6]$, thermally decomposes and produces carbon-protected sub-5 nm-sized intermetallic Pt–Co nanoparticles, on which compressively-strained and rigid Pt-skin can be formed. In addition to the high intrinsic activity, we achieved the combined features of high electrochemical surface area, N-doping on the mesoporous carbon support, and highly stabilized Co that could promote oxygen mass transfer and proton conduction. In the single cell configuration, the catalyst achieved unprecedented rated power densities of 1.18 W cm^{-2} and $5.9 \text{ W mg}_{\text{Pt}}^{-1}$ at 0.67 V (with a cathode loading of $0.1 \text{ mg}_{\text{Pt}} \text{ cm}^{-2}$), while experiencing voltage loss of only 29 mV (at 0.8 A cm^{-2}) at the end of the test.

Received 31st December 2022,
Accepted 30th January 2023

DOI: 10.1039/d2ee04211h

rsc.li/ees

Broader context

Hydrogen is a promising alternative to fossil fuels that can be produced in sustainable ways and effectively converted into electricity through fuel cell systems. The economic viability of the fuel cell system is a key factor that determines the transition towards a hydrogen economy. However, despite the huge previous efforts on proton-exchange-membrane fuel cells, we are still facing limited performance, mainly regarding the power density, long-term durability, and cost of platinum catalysts. Therefore, a novel production method for platinum-based electrocatalysts is in urgent need, which requires a precise design of the synthesis to overcome the multiple challenging issues. In this study, we present a straightforward and scalable synthetic platform based on thermal annealing for the practical production of a platinum-based fuel cell catalyst with unprecedented power performance. The overall structure of the catalyst, including the rigid platinum-skin surface, stable intermetallic core, sufficient ECSA, and highly porous and nitrogen-doped carbon support, not only gives high intrinsic activity but also promotes the oxygen mass transfer and proton conduction. We believe that the proposed thermal synthetic method will stimulate the practical production of commercially viable electrocatalysts for the fuel cell industry.

Introduction

Proton-exchange-membrane fuel cells (PEMFCs) are a representative system for the widespread use of hydrogen as a clean

energy carrier.^{1,2} Several critical challenges, including improving the power density, reducing the cost of platinum (Pt)-based catalysts and increasing the durability, need to be overcome for the large-scale commercialization of PEMFCs.^{3–5} The energy efficiency of PEMFCs heavily relies on the cathode catalyst layer (CCL) where sluggish kinetics of the oxygen reduction reaction (ORR) greatly reduces the cell voltage, whilst poor oxygen mass transfer and low proton conduction limit the overall power efficiency.^{3,4} Thanks to the intensive efforts to improve the intrinsic catalytic activity through novel nanomaterials,^{5–14} several reports have surpassed the 2025 target of the U.S. Department of Energy (DOE) for the mass activity at 0.9 V ($0.44 \text{ A mg}_{\text{Pt}}^{-1}$).^{5–11} However, their power performance at 0.67 V is still far below the practical level (1 W cm^{-2} and $8 \text{ W mg}_{\text{Pt}}^{-1}$).¹⁵

^a Center for Nanoparticle Research, Institute for Basic Science (IBS), Seoul 08826, Republic of Korea

^b School of Chemical and Biological Engineering, and Institute of Chemical Processes, Seoul National University, Seoul 08826, Republic of Korea.
E-mail: ysung@snu.ac.kr, thyeon@snu.ac.kr

^c National Center for Inter-University Research Facilities, Seoul National University, Seoul 08826, Republic of Korea

† Electronic supplementary information (ESI) available. See DOI: <https://doi.org/10.1039/d2ee04211h>

‡ These authors contributed equally to this work.

Thus, it is now imperative to seek a high-power and durable PEMFC operation based on a practical and scalable synthetic process of catalysts.^{16–18}

Practical design of catalysts for high-power PEMFCs requires a holistic consideration of multiple factors that affect performance at high current density (HCD, $>0.8 \text{ A cm}^{-2}$).¹⁹ Oxygen mass transfer is mainly responsible for the cell voltage reduction at HCD, and various strategies, which include high electrochemical surface area (ECSA) of Pt-based nanoparticles (close to $50 \text{ m}^2 \text{ g}_{\text{Pt}}^{-1}$ for low Pt loadings),^{4,20,21} high mesoporosity of CCL,^{22,23} and heteroatom doping on carbon supports for uniform distribution of ionomers on the catalyst,^{24,25} have been explored to address this key issue. Poor proton conduction is another dominant issue at HCD, which is affected by the presence of dissolved metal ions and the quality of the ionomer.^{26–28} Recently, various highly-ordered Pt-based intermetallic nanomaterials have been extensively investigated to enhance the catalytic activity and stability, even with a significantly decreased amount of Pt.^{5,8–11} In particular, protection of intermetallic crystal cores, such as $\text{L1}_0\text{-PtCo}$ and $\text{L1}_2\text{-Pt}_3\text{Co}$, with a Pt-skin surface not only allows high intrinsic activity but also provides excellent electrochemical stability by preventing the cobalt dissolution that blocks proton conduction, thereby minimizing Fenton reaction that damages the ionomer and membrane.^{8,29,30}

However, for industrial-scale applications, it is challenging to simplify the current complicated synthetic procedures required to get an ideal form of PEMFC catalyst. Synthesis of intermetallic nanoparticles generally requires a high-temperature annealing to get ordered intermetallic structures, which often results in the severe aggregation of the nanoparticles.³¹ Two representative strategies, including physical protection^{32–34} and strong anchoring^{35,36} of nanoparticles on the support, effectively prevent aggregation, but both methods still require huge efforts to create and remove protective shells or anchoring sites, precluding large-scale production. Furthermore, achieving all the desired structural factors of supported nanoparticles without using toxic organic surfactants and solvents remains elusive, which could cause safety issues in the manufacturing process.³¹

Herein we present a practical and facile synthetic approach that addresses all the aforementioned issues and demonstrate an excellent PEMFC power performance. The electrostatic attraction between two oppositely charged metal complexes enables the facile preparation of a bimetallic compound, which provides a unique carbon-confined environment to produce highly dispersed intermetallic alloy nanoparticles on a commercial mesoporous carbon support *via* a simple thermal annealing process.³⁷ Ketjenblack EC-600JD (KB) is chosen as the support for the uniform formation of alloy nanoparticles due to its mesoporosity and high surface area, enabling an effective decomposition and dispersion of the bimetallic compound upon annealing. The overall structure of the prepared electrocatalyst simultaneously tackled the critical issues in PEMFCs, including ORR kinetics (by the strained Pt-skin surface on the intermetallic Pt–Co core), oxygen mass transfer (by the high ECSA and mesoporous N-doped carbon support), and proton conduction (by stabilized Co species in the intermetallic core and Pt-skin) with desirable durability.

Results and discussion

Synthesis of supported intermetallic Pt–Co nanoparticles

The bimetallic $[\text{Co}(\text{bpy})_3][\text{PtCl}_6]$ compound (Co–Pt compound, bpy = 2,2'-bipyridine) was prepared simply by adding $[\text{PtCl}_6]^{2-}$ solution into $[\text{Co}(\text{bpy})_3]^{2+}$ solution (Fig. 1(a)). We confirmed the morphology of the Co–Pt compound and its high crystallinity by transmission electron microscopy (TEM) and X-ray diffraction (XRD) analyses (Fig. S1, ESI†). Energy-dispersive X-ray spectroscopy (EDS) elemental mapping indicates the homogeneous distribution of Co and Pt in the compound with 1:1 atomic composition (Fig. 1(b) and Table S1, ESI†). The bipyridine ligand plays a central role (Fig. S2, ESI†) not only in the formation of Co–Pt compound (Fig. S3, ESI†) but also in the *in situ* formation of the N-doped carbon shell that protects the nanoparticles from aggregation in the subsequent annealing process.³⁷ The attachment of Co–Pt compound on KB was readily done by either grinding them together or ball milling. Scanning electron microscopy (SEM), TEM, and scanning transmission electron microscopy (STEM) images clearly show both the Co–Pt compound and KB in the composite (Fig. 1(c) and Fig. S4, ESI†). Although every grain of the Co–Pt compound was not completely separated and ideally dispersed on KB during this grinding step, the subsequent thermal annealing could induce an effective decomposition of this compound to uniformly cover all the surface of KB, producing alloy nanoparticles. Brunauer–Emmett–Teller (BET) analysis indicated the retention of the pore structure of KB after grinding with the Co–Pt compound (Fig. S5, ESI†).

We induced a thermal decomposition of the Co–Pt compound on KB by annealing the composite at $900 \text{ }^\circ\text{C}$ (Fig. 1(a)). SEM and TEM analyses indicate that KB retains its mesoporous morphology (Fig. 1(d) and Fig. S6, ESI†), while the XRD pattern of the annealed composite reveals the formation of an intermetallic $\text{L1}_0\text{-CoPt}$ (i-CoPt) phase (Fig. S7, ESI†). The annealed sample (denoted as i-CoPt/KB) accommodates i-CoPt nanoparticles of uniform sizes between 3–4 nm due to the presence of an *in situ*-formed N-doped carbon shell as a physical barrier against aggregation (Fig. 1(e), (f) and Fig. S6, ESI†).³⁸ We performed STEM-EDS mapping to characterize the homogeneous distribution of Co, Pt, and N elements in the entire surface of i-CoPt/KB (Fig. S8, ESI†). The high-angle annular dark-field STEM (HAADF-STEM) image in Fig. 1(g) clearly shows the characteristic inter-atomic arrangement in a single i-CoPt nanoparticle.^{36,37} The presence of an N-doped carbon shell was identified by high-resolution TEM imaging, as shown in Fig. S9 (ESI†). It is noteworthy that the use of bipyridine offers a unique route to produce size-confined intermetallic nanoparticles on an irregular porous carbon support without any use of elaborate colloidal synthesis or anti-aggregation treatment. The high surface area of KB played an essential role in the homogeneous decomposition and dispersion of the Co–Pt compound in the annealing conditions.

We further investigated the specific formation mechanism of compound-derived i-CoPt nanoparticles on KB using *ex situ* XRD measurement. The characteristic peaks of the Co–Pt compound completely disappear at $300 \text{ }^\circ\text{C}$ with no sign of metallic phase (Fig. 2(a)). As the temperature increases, both

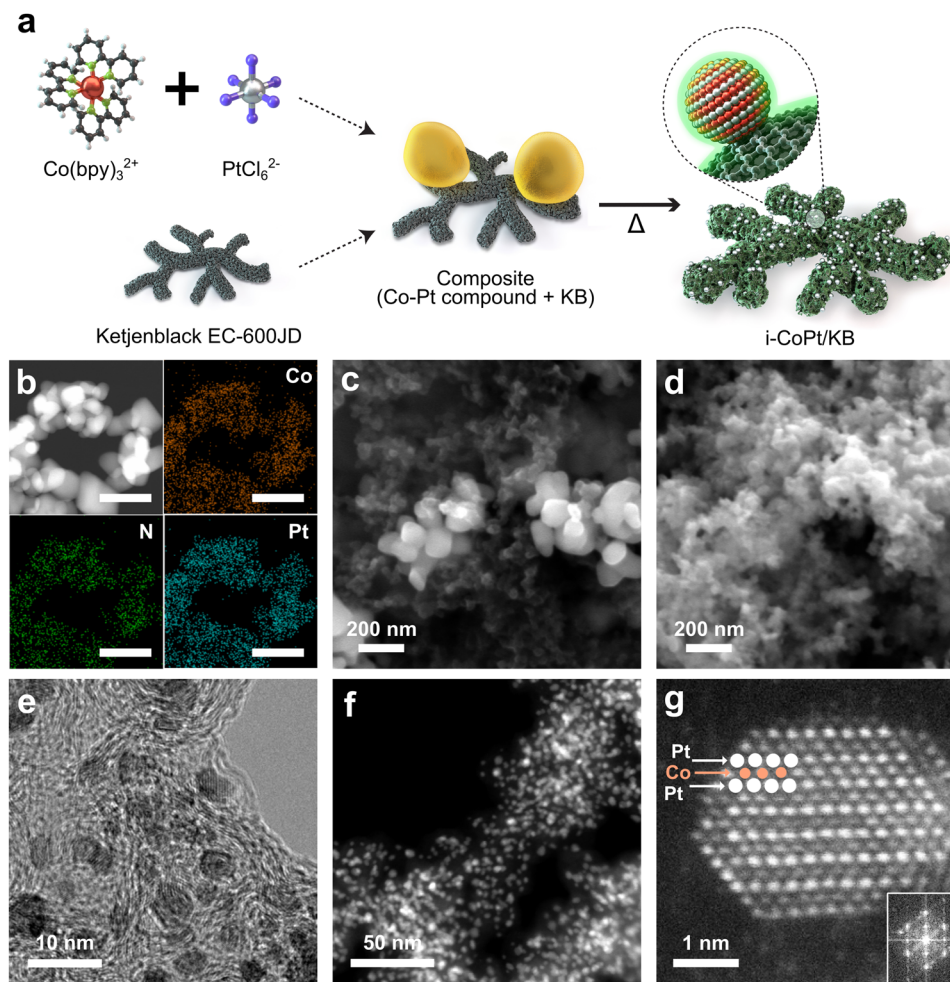


Fig. 1 (a) Schematic illustration of the synthesis of supported Pt–Co nanoparticles. (b) STEM-EDS mapping of the Co–Pt compound. The scale bar is 250 nm. SEM images of the (c) composite, and (d) i-CoPt/KB. (e) TEM, and (f) STEM images of i-CoPt/KB. (g) HAADF-STEM image and its FFT pattern (inset) of i-CoPt/KB. The atomic arrangement of Co and Pt is marked by orange and white colors, respectively.

the Pt-rich Co_xPt_y phase and Co phase evolve at 500 °C, after which the Co phase gradually decreases and finally disappears at 800 °C. The intensity of the main peak at around 41.2 degree continuously increases from 500 to 900 °C, which indicates the growth of CoPt nanoparticles. The clear signs of the intermetallic phase, the (110) peak at around 33.1 degree and two superlattice peaks between 50–65 degree, appear after 2 hours at 900 °C, and become even sharper afterwards. TEM, STEM (Fig. S10, ESI[†]), and X-ray photoelectron spectroscopy (XPS) (Fig. S11, ESI[†]) analyses strongly support the growth mechanism inferred from the XRD data. Based on the above information, we derived four representative stages of nanoparticle formation, as illustrated in Fig. 2(b). Pt and Co ions in carbon (at 300 °C) bond together to form Pt-rich alloys and Co clusters (at 500 °C), which subsequently evolve into CoPt random alloy nanoparticles (at 800 °C) and finally convert into i-CoPt nanoparticles (at 900 °C after 6 hours).

Catalyst activation and structural analysis

We then applied an exquisite thermal activation process to obtain an activated electrocatalyst, denoted as i-CoPt@Pt/KB

(see ESI[†]).³⁹ Air-etching was used to remove the N-doped carbon shell on the surface of the i-CoPt nanoparticles, and the subsequent H_2 -annealing could induce re-alloying of some oxidized Co with CoPt alloy nanoparticles together with the formation of the Pt-skin surface. It is worth noting that the overall thermal process in this study allows consecutive formation and activation of supported i-CoPt nanoparticles in a single furnace, making the entire production simple but highly reproducible. After the activation, 2–3 layers of Pt-skin surface with interior i-CoPt core were obtained without aggregation, which was clearly identified by TEM and HAADF-STEM imaging (Fig. 3(a), (b) and Fig. S12, ESI[†]). The XRD pattern clearly reveals the well-preserved ordered structure of the i-CoPt core after the activation (Fig. S13, ESI[†]). The development of the i-CoPt core and Pt-skin structure was also characterized by X-ray absorption near edge structure (XANES), extended X-ray absorption fine structure (EXAFS), and XPS analyses (Fig. S14 and S15, ESI[†]). The increased white line intensity of i-CoPt@Pt/KB in the Pt L_3 -edge XANES spectrum indicates that the N-doped carbon shell is effectively etched and the Pt-skin is fully exposed to the

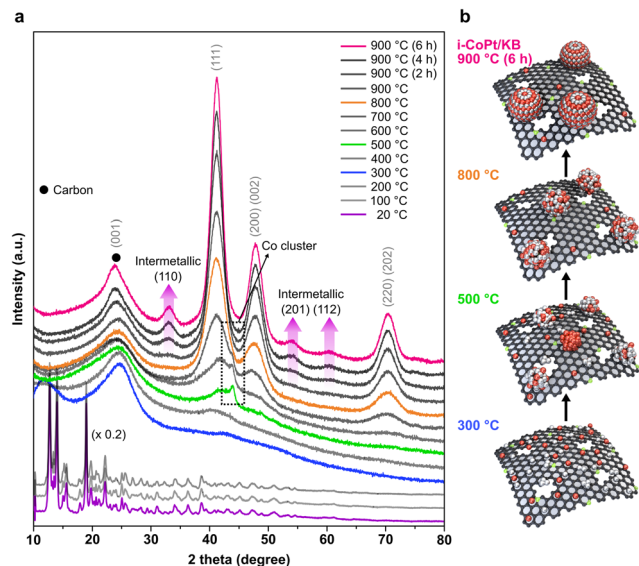


Fig. 2 (a) *Ex situ* XRD patterns at different annealing temperatures from 100 to 900 °C. The intensities of the 20, 100, and 200 °C curves are multiplied by 0.2. (b) Schematic illustration of the formation mechanism of i-CoPt nanoparticles on KB. Each Pt, Co, N, and C atom is colored in gray, red, green, and black, respectively.

air (Fig. 3(c)).⁴⁰ Furthermore, the lattice contraction of Pt in both the i-CoPt core and the Pt-skin was confirmed by Pt EXAFS (Fig. 3(d) and Fig. S16, ESI[†]), and the compressive strain of -4.24% at the outermost surface was observed by HAADF-STEM imaging (Fig. S17, ESI[†]). This compressive strain is

known to tailor the electronic state of the Pt surface by downshift of the d-band center, which is translated to an enhanced ORR activity by weaker binding energy of reaction intermediates compared to pure Pt.^{41–43} Co K-edge XANES and EXAFS spectra demonstrate negligible change after the activation, mainly due to the intact Co species in the i-CoPt core of i-CoPt@Pt nanoparticles (Fig. 3(e) and (f)). XPS analysis on Co further supports this result by the presence of a weak signal of Co⁰ after the activation because of rigid protection by the outermost Pt-skin layer (Fig. S15b, ESI[†]). We confirmed the increment of the Co composition from the surface to the core by controlling the incident photon energy in XPS analysis (Fig. S18, ESI[†]).^{44,45} The exact Pt mass loadings of i-CoPt/KB and i-CoPt@Pt/KB were obtained by inductively coupled plasma atomic emission spectroscopy (ICP-AES), which showed high Co content of 28.4 atom% and Pt mass loading higher than 40 wt% after the activation (Table S2, ESI[†]). This high Pt loading is beneficial for the preparation of a thin CCL that shortens the oxygen transfer pathway (Fig. S19 and S20, ESI[†]). We further confirmed the scalability of the overall synthetic process by gram-scale synthesis of i-CoPt/KB and its activation without compromising the quality of both i-CoPt/KB and i-CoPt@Pt/KB (Fig. S21, ESI[†]).

Electrochemical half-cell performance of i-CoPt@Pt/KB

The electrocatalytic properties of the prepared catalysts were first studied using the rotating-disk electrode (RDE) technique with commercial Pt/C as a benchmark catalyst. We observed a significant difference between the as-prepared i-CoPt/KB and the activated i-CoPt@Pt/KB in their cyclic voltammogram (CV)

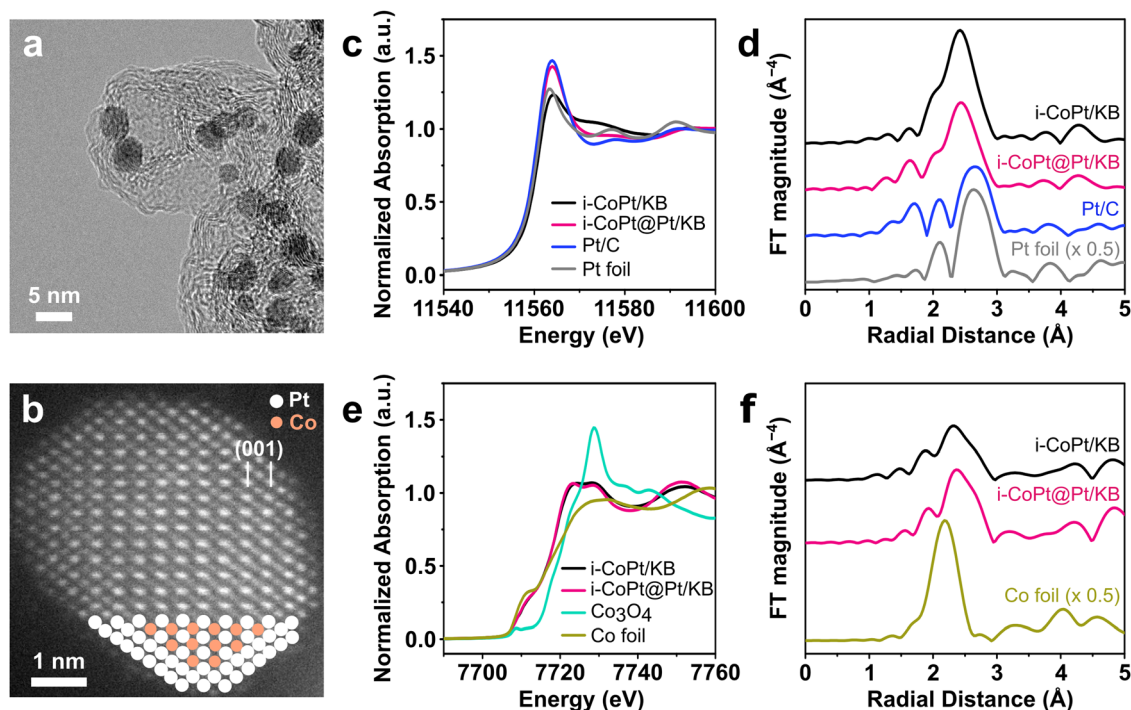


Fig. 3 (a) TEM image of i-CoPt@Pt/KB. (b) HAADF-STEM image of i-CoPt@Pt/KB. The Pt-skin layers and the internal atomic arrangement of Co and Pt are marked by orange and white colors, respectively. (c) Pt L₃-edge XANES, and (d) Pt EXAFS data of i-CoPt@Pt/KB with i-CoPt/KB, commercial Pt/C, and Pt foil. (e) Co K-edge XANES, and (f) Co EXAFS data of i-CoPt@Pt/KB with i-CoPt/KB, Co₃O₄, and Co foil.

curves (Fig. 4(a)). i-CoPt/KB exhibits only the feature of a double layer capacitance due to the complete coverage of i-CoPt nanoparticles with N-doped carbon shell. The facile air etching at 200 °C effectively exposed the Pt surface with no sign of nanoparticle aggregation or loss of KB. The fully exposed Pt-skin surface in i-CoPt@Pt/KB exhibited high ECSA of $58.2 \text{ m}^2 \text{ g}_{\text{Pt}}^{-1}$ as measured by a CO stripping experiment (Fig. 4(b) and Fig. S22, ESI[†]) due to the uniform particle sizes of 3 to 4.5 nm (Fig. S12, ESI[†]). As expected, i-CoPt@Pt/KB showed superior ORR activities (mass activity of $2.07 \text{ A mg}_{\text{Pt}}^{-1}$ and specific activity of $3.95 \text{ mA cm}_{\text{Pt}}^{-2}$) compared to those of Pt/C due to the compressive strain on Pt-skin exerted by the i-CoPt core (Fig. 4(c) and Fig. S23, ESI[†]).^{46–50} We confirmed the electron transfer number of i-CoPt@Pt/KB by rotating ring-disk electrode (RRDE) measurement, which demonstrated an excellent 4-electron reaction pathway at all potential ranges along with the commercial Pt/C (Fig. S24, ESI[†]). Owing to the rigid Pt-skin structure, i-CoPt@Pt/KB showed excellent durability after an accelerated durability test (ADT) for 30 000 cycles with barely changed ECSA (Fig. S25 and S26, ESI[†]) and half-wave potential (Fig. S27, ESI[†]),^{51,52} while commercial Pt/C was severely damaged. We also confirmed that the electrocatalytic properties were not affected even in gram-scale synthesis, which sheds light on the mass production of i-CoPt@Pt/KB for its practical application (Fig. S28, ESI[†]).

Practical fuel cell performance

To demonstrate the practical application of i-CoPt@Pt/KB in PEMFCs, the membrane electrode assembly (MEA) using

i-CoPt@Pt/KB was fabricated, and its performance and durability were evaluated under practical operating conditions. For a benchmark, the MEA with commercial Pt/C (HiSPEC 4000, Johnson Matthey Co.) was prepared and tested under the same conditions. Because all the components used in the tested MEAs were identical except for the cathode catalysts, the MEAs were labeled by the name of the cathode catalysts used. For all MEAs, the Pt loading of the cathode was fixed to $0.1 \text{ mg}_{\text{Pt}} \text{ cm}^{-2}$ to secure reasonable power densities and durability, and the ionomer to carbon weight ratios were optimized to be 0.8 for the i-CoPt@Pt/KB and 0.5 for the Pt/C cathode, respectively (Fig. S29, ESI[†]). SEM images of both catalyst-coated membranes (CCMs) clearly show similar thicknesses and secondary pore geometries of CCLs (Fig. S30, ESI[†]). i-CoPt@Pt/KB exhibited high ECSA of $53.3 \text{ m}^2 \text{ g}_{\text{Pt}}^{-1}$ (roughness factor of $53.3 \text{ cm}_{\text{Pt}}^2 \text{ cm}_{\text{MEA}}^{-2}$) which is close to the value measured in the RDE test (Fig. 4(b) and Fig. S31, ESI[†]). On the contrary, the higher ECSA of the benchmark Pt/C catalyst in RDE (due to the smaller particle size of 3 nm) was not translated to the MEA configuration due to the well-known poisoning of the Pt surface by selective adsorption of the ionomer.¹⁵ Although SEM-EDS mapping data shows comparable distribution of F element for both cathodes (Fig. S32, ESI[†]), this different loss of ECSAs between the two catalysts is mainly attributed to the N-doping in i-CoPt@Pt/KB (Fig. S33, ESI[†]), which enhances the ionomer distribution on the carbon support and contributes to an effective formation of triple phase boundaries (Fig. S34, ESI[†]).²⁴

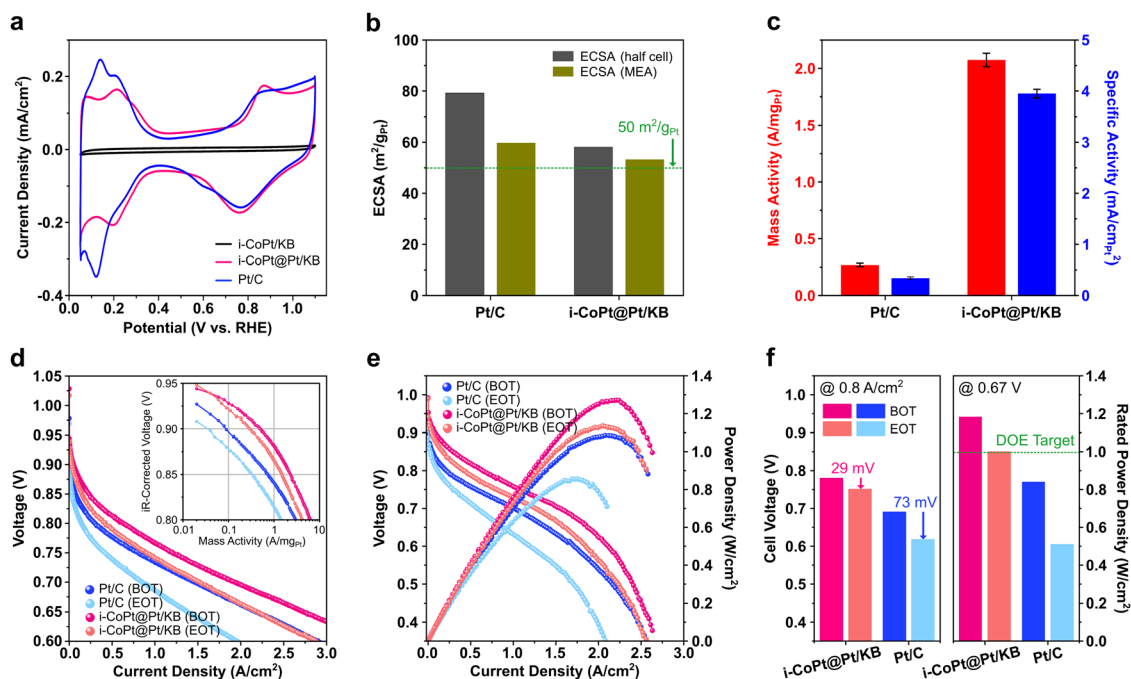


Fig. 4 (a) CV curves of i-CoPt@Pt/KB with i-CoPt/KB, and commercial Pt/C. (b) ECSA of Pt/C and i-CoPt@Pt/KB measured in a half-cell and MEA. (c) Mass and specific activities of i-CoPt@Pt/KB at 0.9 V (versus RHE) compared to commercial Pt/C. (d) H_2 - O_2 fuel cell polarization curves and the derived Tafel plots (inset) before and after ADT cycling. H_2 flow rate = 0.2 L min^{-1} , O_2 flow rate = 0.2 L min^{-1} . (e) H_2 -air fuel cell polarization and power density curves of i-CoPt@Pt/KB and Pt/C before and after ADT cycling. Anode loading (Pt/C): $0.1 \text{ mg}_{\text{Pt}} \text{ cm}^{-2}$, cathode loading (i-CoPt@Pt/KB or Pt/C): $0.1 \text{ mg}_{\text{Pt}} \text{ cm}^{-2}$. Test conditions: 80 °C, 100% relative humidity, 250 kPa_{abs}, H_2 flow rate = 0.2 L min^{-1} , air flow rate = 0.8 L min^{-1} . (f) Cell voltage at 0.8 A cm^{-2} (left) and rated power density at 0.67 V (right) of i-CoPt@Pt/KB and Pt/C before and after ADT cycling.

Fig. 4(d) shows the single cell polarization curve of the tested MEAs under H_2 - O_2 conditions, indicating that i-CoPt@Pt/KB outperforms Pt/C throughout the entire voltage region. The internal resistance (iR)-corrected Tafel plots (inset in Fig. 4(d)) and electrochemical impedance spectra (EIS) at 0.05 A cm^{-2} (Fig. S35, ESI[†]) demonstrated that i-CoPt@Pt/KB exhibits superior activity compared to Pt/C in the single cell configuration. In particular, at 0.9 V (iR-corrected), i-CoPt@Pt/KB exhibited 4.4 times higher mass activity ($0.53 \text{ A mg}_{\text{Pt}}^{-1}$) compared to that of the benchmark catalyst ($0.12 \text{ A mg}_{\text{Pt}}^{-1}$), which exceeds the 2025 DOE activity target for PEMFCs ($0.44 \text{ A mg}_{\text{Pt}}^{-1}$) (Fig. S36, ESI[†]). Likewise, we confirmed the superior performance of i-CoPt@Pt/KB under practical H_2 -air operating conditions (Fig. 4(e) and Fig. S37, ESI[†]). At the kinetic dominant region of 0.8 V, i-CoPt@Pt/KB exhibited much higher current density of 0.64 A cm^{-2} than Pt/C (0.20 A cm^{-2}) (Fig. S38, ESI[†]), far surpassing the 2025 DOE target (0.3 A cm^{-2} at 0.8 V). Moreover, at a practical working voltage of 0.67 V for high power output, i-CoPt@Pt/KB reached a current density of 1.76 A cm^{-2} , corresponding to a power density of 1.18 W cm^{-2} (above the DOE target of 1.0 W cm^{-2} for $\leq 0.1 \text{ mg}_{\text{Pt}} \text{ cm}^{-2}$ in cathode) (Fig. 4(f)). To comprehensively understand the high HCD performance of i-CoPt@Pt/KB, we conducted EIS analysis under H_2 -air conditions (Fig. S39, ESI[†]). Compared to the benchmark Pt/C catalyst, i-CoPt@Pt/KB exhibited a slightly smaller low frequency arc at the current densities above 0.8 A cm^{-2} , which is related to the mass transport resistance in the electrode. Considering that conventional porous carbon-based catalysts have generally shown lower HCD performance due to higher transport resistance than solid carbon-based catalysts (Fig. S40, ESI[†]), it is noteworthy that the porous carbon-based i-CoPt@Pt/KB catalyst showed somewhat lower transport resistance than the benchmark Pt/C catalyst based on solid carbon. Compared to the commercial PtCo/C (Fig. S41, ESI[†]), and the state-of-the-art Pt-based catalysts tested under similar operating conditions (Fig. 5 and Table S3, ESI[†]), i-CoPt@Pt/KB exhibited not only the highest rated power performance but also a notable specific rated power (normalized with the total Pt loading in single cell) in MEA.^{6–11} These results demonstrate that i-CoPt@Pt/KB is a promising ORR catalyst for a

practical PEMFC cathode, as the rated power performance at the critical voltage (0.67 V) is one of the key figures to evaluate the practical applicability of a PEMFC system.^{4,26} This unprecedented power performance originates not only from the intrinsic activity of the strained Pt surface but also from the combination of desirable structural factors that includes sufficient roughness factor ($\text{cm}_{\text{Pt}}^2 \text{ cm}_{\text{MEA}}^{-2}$) higher than 50, mesoporous carbon structure, and nitrogen doping on the support. The major role of Pt roughness factor in low-Pt PEMFC power has been systematically analyzed in a previous study,⁴ which emphasized the rapid voltage loss at HCD (due to high non-Fickian oxygen transport resistance) if the roughness factor falls down to lower than $40 \text{ cm}_{\text{Pt}}^2 \text{ cm}_{\text{MEA}}^{-2}$ despite a reasonably high mass activity. The mesoporous carbon support with N-doping reduces the local oxygen transport resistance by providing a pore network and enabling homogeneous distribution of the ionomer in CCL.^{15,24}

The durability of i-CoPt@Pt/KB was evaluated after ADT of square-wave potential cycling between 0.60 V (3 s) and 0.95 V (3 s), which is much harsher than the triangle-wave protocol between 0.6 and 1.0 V.⁵³ After ADT for 30 000 cycles, i-CoPt@Pt/KB preserved 81.2% of its beginning of test (BOT) ECSA while that of Pt/C largely decreased by 62.9% (Fig. S31, ESI[†]). It is important to note that the optimum size of i-CoPt@Pt nanoparticles (3–4.5 nm) contributed both to the balance of a sufficient initial ECSA and to its high retention after ADT.⁵⁴ i-CoPt@Pt/KB retained 64.5% of its BOT mass activity, meeting the durability target (<40%) for mass activity set by the DOE (Fig. S36, ESI[†]). Notably, in the H_2 -air test, the voltage loss for i-CoPt@Pt/KB at HCD of 0.8 A cm^{-2} was 29 mV, which meets the DOE target (<30 mV) (Fig. 4(f)). The rated power performance of the i-CoPt@Pt/KB MEA decreased by only 15.4% while that of Pt/C decreased by 39.4%. The i-CoPt@Pt/KB MEA still exhibited high H_2 -air performance (0.42 A cm^{-2} at 0.8 V, and 1.0 W cm^{-2} at 0.67 V) that meets the BOT performance targets set by the DOE (0.3 A cm^{-2} at 0.8 V, and 1.0 W cm^{-2} at 0.67 V) (Fig. 4(f) and Fig. S38, ESI[†]). TEM analysis on i-CoPt@Pt/KB at the end of the test (EOT) confirmed that the overall sizes of the i-CoPt@Pt nanoparticles remained close to 5 nm even after the harsh ADT cycling (Fig. S42, ESI[†]). We speculate that the better retention of particle size and ECSA in i-CoPt@Pt/KB compared

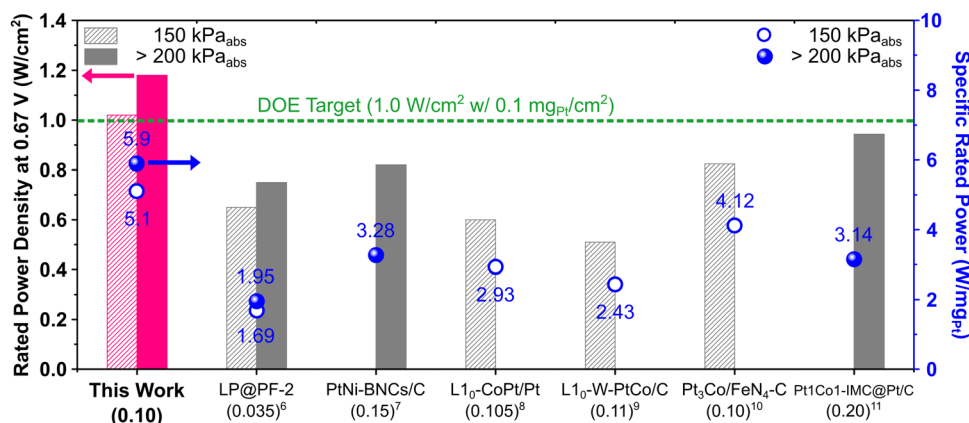


Fig. 5 Comparison of the rated power density and specific rated power at 0.67 V of i-CoPt@Pt/KB and the state-of-the-art Pt-based catalysts in the literature.^{6–11} Cathode Pt loadings ($\text{mg}_{\text{Pt}} \text{ cm}^{-2}$) are written in parentheses.

to Pt/C comes from the superior stabilization of i-CoPt nanoparticles by the high temperature annealing on the high surface area carbon. STEM-EDS detected the remaining Co and Pt elements in i-CoPt@Pt/KB at the EOT (Fig. S43, ESI†), indicating more than twice higher Co/Pt ratio (0.23 for i-CoPt@Pt/KB) compared to the commercial Pt₃Co/C catalysts with random alloy nanoparticles (~0.23 after conditioning, and ~0.098 at the EOT) reported in the previous works.^{55,56} This enhanced durability can be attributed to the intermetallic core and Pt-skin surface, which were also confirmed at the EOT (Fig. S44, ESI†).

Conclusion

We presented a straightforward and delicate synthetic platform based on thermal annealing to get a practical ORR catalyst that satisfies comprehensive requirements for both high intrinsic activity and high rated power performance in a PEMFC system. The crystalline ionic compound, composed of [Co(bpy)₃]²⁺ and [PtCl₆]²⁻, enabled a carbon-confined growth of intermetallic nanoparticles with N-doping on the entire mesoporous carbon support. The active Pt-skin with intermetallic L1₀-CoPt core catalyzed the ORR in efficient ways both in a half-cell and MEA. More importantly, we attained the highest PEMFC rated power per active area (1.18 W cm⁻²) and total platinum loading (5.9 W mg_{Pt}⁻¹) under a practical H₂-air condition owing to the high ECSA, mesoporosity, and N-doping on the carbon support that collectively enhanced oxygen mass transfer. The catalyst endured a harsh durability test with the final rated power density of 1.0 W cm⁻², due to the effective protection of Co dissolution induced by the rigid Pt-skin structure that maintained proton conduction. Overall, this study highlights the importance of meeting all the critical parameters to achieve much higher PEMFC power performance through the development of a facile and scalable production method of the catalyst. Further modifications from this approach, such as doping, tuning the compositions, and using novel metal complexes or carbon supports, could provide enhanced and desirable power performance suited to large-scale industrial applications of PEMFCs.

Data and materials availability

All data that support the findings of this study are available from the corresponding authors upon reasonable request.

Author contributions

T. Y. Y., J. L., S. K., Y.-E. S., and T. H. conceived the ideas, designed the experiments, and wrote the manuscript. T. Y. Y., J. L., S. K., M. H., S.-Y. K., Y.-H. L., H. S., H. J., A. K. S., S.-P. C., Y.-E. S., and T. H. performed the experiments and analysis.

Conflicts of interest

There are no conflicts to declare.

Acknowledgements

This research was supported by the Institute for Basic Science (IBS-R006-D1 and IBS-R006-A2).

References

- 1 K. Jiao, J. Xuan, Q. Du, Z. Bao, B. Xie, B. Wang, Y. Zhao, L. Fan, H. Wang, Z. Hou, S. Huo, N. P. Brandon, Y. Yin and M. D. Guiver, Designing the next generation of proton-exchange membrane fuel cells, *Nature*, 2021, **595**, 361–369.
- 2 O. Z. Sharaf and M. F. Orhan, An overview of fuel cell technology: Fundamentals and applications, *Renewable Sustainable Energy Rev.*, 2014, **32**, 810–853.
- 3 J. Fan, M. Chen, Z. Zhao, Z. Zhang, S. Ye, S. Xu, H. Wang and H. Li, Bridging the gap between highly active oxygen reduction reaction catalysts and effective catalyst layers for proton exchange membrane fuel cells, *Nat. Energy*, 2021, **6**, 475–486.
- 4 A. Kongkanand and M. F. Mathias, The Priority and Challenge of High-Power Performance of Low-Platinum Proton-Exchange Membrane Fuel Cells, *J. Phys. Chem. Lett.*, 2016, **7**, 1127–1137.
- 5 X. X. Wang, M. T. Swihart and G. Wu, Achievements, challenges and perspectives on cathode catalysts in proton exchange membrane fuel cells for transportation, *Nat. Catal.*, 2019, **2**, 578–589.
- 6 L. Chong, J. Wen, J. Kubal, F. G. Sen, J. Zou, J. Greeley, M. Chan, H. Barkholtz, W. Ding and D.-J. Liu, Ultralow-loading platinum-cobalt fuel cell catalysts derived from imidazolate frameworks, *Science*, 2018, **362**, 1276–1281.
- 7 X. Tian, X. Zhao, Y.-Q. Su, L. Wang, H. Wang, D. Dang, B. Chi, H. Liu, E. J. M. Hensen, X. W. Lou and B. Y. Xia, Engineering bunched Pt-Ni alloy nanocages for efficient oxygen reduction in practical fuel cells, *Science*, 2019, **366**, 850–856.
- 8 J. Li, S. Sharma, X. Liu, Y.-T. Pan, J. S. Spendelow, M. Chi, Y. Jia, P. Zhang, D. A. Cullen, Z. Xi, H. Lin, Z. Yin, B. Shen, M. Muzzio, C. Yu, Y. S. Kim, A. A. Peterson, K. L. More, H. Zhu and S. Sun, Hard-Magnet L1₀-CoPt Nanoparticles Advance Fuel Cell Catalysis, *Joule*, 2019, **3**, 124–135.
- 9 J. Liang, N. Li, Z. Zhao, L. Ma, X. Wang, S. Li, X. Liu, T. Wang, Y. Du, G. Lu, J. Han, Y. Huang, D. Su and Q. Li, Tungsten-Doped L1₀-PtCo Ultrasmall Nanoparticles as a High-Performance Fuel Cell Cathode, *Angew. Chem., Int. Ed.*, 2019, **58**, 15471–15477.
- 10 Z. Qiao, C. Wang, C. Li, Y. Zeng, S. Hwang, B. Li, S. Karakalos, J. Park, A. J. Kropf, E. C. Wegener, Q. Gong, H. Xu, G. Wang, D. J. Myers, J. Xie, J. S. Spendelow and G. Wu, Atomically dispersed single iron sites for promoting Pt and Pt₃Co fuel cell catalysts: performance and durability improvements, *Energy Environ. Sci.*, 2021, **14**, 4948–4960.
- 11 Q. Cheng, S. Yang, C. Fu, L. Zou, Z. Zou, Z. Jiang, J. Zhang and H. Yang, High-loaded sub-6 nm Pt₁Co₁ intermetallic compounds with highly efficient performance expression in PEMFCs, *Energy Environ. Sci.*, 2022, **15**, 278–286.

- 12 Z. Peng and H. Yang, Designer platinum nanoparticles: Control of shape, composition in alloy, nanostructure and electrocatalytic property, *Nano Today*, 2009, **4**, 143–164.
- 13 H. You, S. Yang, B. Ding and H. Yang, Synthesis of colloidal metal and metal alloy nanoparticles for electrochemical energy applications, *Chem. Soc. Rev.*, 2013, **42**, 2880–2904.
- 14 L. Zhang, K. Doyle-Davis and X. Sun, Pt-Based electrocatalysts with high atom utilization efficiency: from nanostructures to single atoms, *Energy Environ. Sci.*, 2019, **12**, 492–517.
- 15 T. A. M. Suter, K. Smith, J. Hack, L. Rasha, Z. Rana, G. M. A. Angel, P. R. Shearing, T. S. Miller and D. J. L. Brett, Engineering Catalyst Layers for Next-Generation Polymer Electrolyte Fuel Cells: A Review of Design, Materials, and Methods, *Adv. Energy Mater.*, 2021, **11**, 2101025.
- 16 K. Kodama, T. Nagai, A. Kuwaki, R. Jinnouchi and Y. Morimoto, Challenges in applying highly active Pt-based nanostructured catalysts for oxygen reduction reactions to fuel cell vehicles, *Nat. Nanotechnol.*, 2021, **16**, 140–147.
- 17 M. K. Debe, Electrocatalyst approaches and challenges for automotive fuel cells, *Nature*, 2012, **486**, 43–51.
- 18 X. Tian, X. F. Lu, B. Y. Xia and X. W. Lou, Advanced Electrocatalysts for the Oxygen Reduction Reaction in Energy Conversion Technologies, *Joule*, 2020, **4**, 45–69.
- 19 V. R. Stamenkovic, D. Strmcnik, P. P. Lopes and N. M. Markovic, Energy and fuels from electrochemical interfaces, *Nat. Mater.*, 2017, **16**, 57–69.
- 20 M. Shao, A. Peles and K. Shoemaker, Electrocatalysis on Platinum Nanoparticles: Particle Size Effect on Oxygen Reduction Reaction Activity, *Nano Lett.*, 2011, **11**, 3714–3719.
- 21 G. W. Sievers, A. W. Jensen, J. Quinson, A. Zana, F. Bizzotto, M. Oezaslan, A. Dworzak, J. J. K. Kirkensgaard, T. E. L. Smitshuysen, S. Kadkhodazadeh, M. Juelsholt, K. M. Ø. Jensen, K. Anklam, H. Wan, J. Schäfer, K. Čépe, M. Escudero-Escribano, J. Rossmeisl, A. Quade, V. Brüser and M. Arenz, Self-supported Pt–CoO networks combining high specific activity with high surface area for oxygen reduction, *Nat. Mater.*, 2021, **20**, 208–213.
- 22 N. Ramaswamy, W. Gu, J. M. Ziegelbauer and S. Kumaraguru, Carbon Support Microstructure Impact on High Current Density Transport Resistances in PEMFC Cathode, *J. Electrochem. Soc.*, 2020, **167**, 064515.
- 23 H. Adabi, A. Shakouri, N. U. Hassan, J. R. Varcoe, B. Zulevi, A. Serov, J. R. Regalbuto and W. E. Mustain, High-performing commercial Fe–N–C cathode electrocatalyst for anion-exchange membrane fuel cells, *Nat. Energy*, 2021, **6**, 834–843.
- 24 S. Ott, A. Orfanidi, H. Schmies, B. Anke, H. N. Nong, J. Hübner, U. Gernert, M. Glied, M. Lerch and P. Strasser, Ionomer distribution control in porous carbon-supported catalyst layers for high-power and low Pt-loaded proton exchange membrane fuel cells, *Nat. Mater.*, 2020, **19**, 77–85.
- 25 J. Chang, G. Wang, M. Wang, Q. Wang, B. Li, H. Zhou, Y. Zhu, W. Zhang, M. Omer, N. Orlovskaya, Q. Ma, M. Gu, Z. Feng, G. Wang and Y. Yang, Improving Pd–N–C fuel cell electrocatalysts through fluorination-driven rearrangements of local coordination environment, *Nat. Energy*, 2021, **6**, 1144–1153.
- 26 C.-Y. Ahn, J. E. Park, S. Kim, O.-H. Kim, W. Hwang, M. Her, S. Y. Kang, S. Park, O. J. Kwon, H. S. Park, Y.-H. Cho and Y.-E. Sung, Differences in the Electrochemical Performance of Pt-Based Catalysts Used for Polymer Electrolyte Membrane Fuel Cells in Liquid Half- and Full-Cells, *Chem. Rev.*, 2021, **121**, 15075–15140.
- 27 C. Cui, L. Gan, M. Heggen, S. Rudi and P. Strasser, Compositional segregation in shaped Pt alloy nanoparticles and their structural behaviour during electrocatalysis, *Nat. Mater.*, 2013, **12**, 765–771.
- 28 P. P. Lopes, D. Li, H. Lv, C. Wang, D. Tripkovic, Y. Zhu, R. Schimmenti, H. Daimon, Y. Kang, J. Snyder, N. Becknell, K. L. More, D. Strmcnik, N. M. Markovic, M. Mavrikakis and V. R. Stamenkovic, Eliminating dissolution of platinum-based electrocatalysts at the atomic scale, *Nat. Mater.*, 2020, **19**, 1207–1214.
- 29 V. R. Stamenkovic, B. S. Mun, K. J. J. Mayrhofer, P. N. Ross and N. M. Markovic, Effect of Surface Composition on Electronic Structure, Stability, and Electrocatalytic Properties of Pt-Transition Metal Alloys: Pt-Skin versus Pt-Skeleton Surfaces, *J. Am. Chem. Soc.*, 2006, **128**, 8813–8819.
- 30 F. Xiao, Q. Wang, G.-L. Xu, X. Qin, I. Hwang, C.-J. Sun, M. Liu, W. Hua, H.-W. Wu, S. Zhu, J.-C. Li, J.-G. Wang, Y. Zhu, D. Wu, Z. Wei, M. Gu, K. Amine and M. Shao, Atomically dispersed Pt and Fe sites and Pt–Fe nanoparticles for durable proton exchange membrane fuel cells, *Nat. Catal.*, 2022, **5**, 503–512.
- 31 H. Kim, T. Y. Yoo, M. S. Bootharaju, J. H. Kim, D. Y. Chung and T. Hyeon, Noble Metal-Based Multimetallic Nanoparticles for Electrocatalytic Applications, *Adv. Sci.*, 2022, **9**, 2104054.
- 32 J. Kim, C. Rong, J. P. Liu and S. Sun, Dispersible Ferromagnetic FePt Nanoparticles, *Adv. Mater.*, 2009, **21**, 906–909.
- 33 D. Y. Chung, S. W. Jun, G. Yoon, S. G. Kwon, D. Y. Shin, P. Seo, J. M. Yoo, H. Shin, Y.-H. Chung, H. Kim, B. S. Mun, K.-S. Lee, N.-S. Lee, S. J. Yoo, D.-H. Lim, K. Kang, Y.-E. Sung and T. Hyeon, Highly Durable and Active PtFe Nanocatalyst for Electrochemical Oxygen Reduction Reaction, *J. Am. Chem. Soc.*, 2015, **137**, 15478–15485.
- 34 H. Y. Kim, T. Kwon, Y. Ha, M. Jun, H. Baik, H. Y. Jeong, H. Kim, K. Lee and S. H. Joo, Intermetallic PtCu Nanoframes as Efficient Oxygen Reduction Electrocatalysts, *Nano Lett.*, 2020, **20**, 7413–7421.
- 35 R. Ryoo, J. Kim, C. Jo, S. W. Han, J.-C. Kim, H. Park, J. Han, H. S. Shin and J. W. Shin, Rare-earth–platinum alloy nanoparticles in mesoporous zeolite for catalysis, *Nature*, 2020, **585**, 221–224.
- 36 C.-L. Yang, L.-N. Wang, P. Yin, J. Liu, M.-X. Chen, Q.-Q. Yan, Z.-S. Wang, S.-L. Xu, S.-Q. Chu, C. Cui, H. Ju, J. Zhu, Y. Lin, J. Shui and H.-W. Liang, Sulfur-anchoring synthesis of platinum intermetallic nanoparticle catalysts for fuel cells, *Science*, 2021, **374**, 459–464.
- 37 T. Y. Yoo, J. M. Yoo, A. K. Sinha, M. S. Bootharaju, E. Jung, H. S. Lee, B.-H. Lee, J. Kim, W. H. Antink, Y. M. Kim, J. Lee, E. Lee, D. W. Lee, S.-P. Cho, S. J. Yoo, Y.-E. Sung and T. Hyeon, Direct Synthesis of Intermetallic Platinum–Alloy

- Nanoparticles Highly Loaded on Carbon Supports for Efficient Electrocatalysis, *J. Am. Chem. Soc.*, 2020, **142**, 14190–14200.
- 38 M. Karuppappan, Y. Kim, S. Gok, E. Lee, J. Y. Hwang, J.-H. Jang, Y.-H. Cho, T. Lim, Y.-E. Sung and O. J. Kwon, A highly durable carbon-nanofiber-supported Pt–C core-shell cathode catalyst for ultra-low Pt loading proton exchange membrane fuel cells: facile carbon encapsulation, *Energy Environ. Sci.*, 2019, **12**, 2820–2829.
- 39 D. Li, C. Wang, D. Tripkovic, S. Sun, N. M. Markovic and V. R. Stamenkovic, Surfactant Removal for Colloidal Nanoparticles from Solution Synthesis: The Effect on Catalytic Performance, *ACS Catal.*, 2012, **2**, 1358–1362.
- 40 C. Wang, M. Chi, D. Li, D. Strmcnik, D. V. D. Vliet, G. Wang, V. Komanicky, K.-C. Chang, A. P. Paulikas, D. Tripkovic, J. Pearson, K. L. More, N. M. Markovic and V. R. Stamenkovic, Design and Synthesis of Bimetallic Electrocatalyst with Multilayered Pt-Skin Surfaces, *J. Am. Chem. Soc.*, 2011, **133**, 14396–14403.
- 41 Y. Xu, A. V. Ruban and M. Mavrikakis, Adsorption and Dissociation of O₂ on Pt–Co and Pt–Fe Alloys, *J. Am. Chem. Soc.*, 2004, **126**, 4717–4725.
- 42 P. Strasser, S. Koh, T. Anniyev, J. Greeley, K. More, C. Yu, Z. Liu, S. Kaya, D. Nordlund, H. Ogasawara, M. F. Toney and A. Nilsson, Lattice-strain control of the activity in dealloyed core-shell fuel cell catalysts, *Nat. Chem.*, 2010, **2**, 454–460.
- 43 M. Luo and S. Guo, Strain-controlled electrocatalysis on multimetallic nanomaterials, *Nat. Rev. Mater.*, 2017, **2**, 17059.
- 44 D. Choi, J. Y. Jung, M. J. Lee, S.-H. Kim, S. Lee, D. W. Lee, D.-G. Kim, N. D. Kim, K.-S. Lee, P. Kim and S. J. Yoo, Atomic Rearrangement in Core-Shell Catalysts Induced by Electrochemical Activation for Favorable Oxygen Reduction in Acid Electrolytes, *ACS Catal.*, 2021, **11**, 15098–15109.
- 45 D. Y. Chung, S. Park, H. Lee, H. Kim, Y.-H. Chung, J. M. Yoo, D. Ahn, S.-H. Yu, K.-S. Lee, M. Ahmadi, H. Ju, H. D. Abruña, S. J. Yoo, B. S. Mun and Y.-E. Sung, Activity–Stability Relationship in Au@Pt Nanoparticles for Electrocatalysis, *ACS Energy Lett.*, 2020, **5**, 2827–2834.
- 46 D. Wang, H. L. Xin, R. Hovden, H. Wang, Y. Yu, D. A. Muller, F. J. DiSalvo and H. D. Abruña, Structurally ordered intermetallic platinum–cobalt core-shell nanoparticles with enhanced activity and stability as oxygen reduction electrocatalysts, *Nat. Mater.*, 2013, **12**, 81–87.
- 47 P. Hernandez-Fernandez, F. Masini, D. N. McCarthy, C. E. Strebel, D. Friebe, D. Deiana, P. Malacrida, A. Nierhoff, A. Bodin, A. M. Wise, J. H. Nielsen, T. W. Hansen, A. Nilsson, I. E. L. Stephens and I. Chorkendorff, Mass-selected nanoparticles of Pt_xY as model catalysts for oxygen electroreduction, *Nat. Chem.*, 2014, **6**, 732–738.
- 48 M. Escudero-Escribano, P. Malacrida, M. H. Hansen, U. G. Vej-Hansen, A. Velázquez-Palenzuela, V. Tripkovic, J. Schiøtz, J. Rossmeisl, I. E. L. Stephens and I. Chorkendorff, Tuning the activity of Pt alloy electrocatalysts by means of the lanthanide contraction, *Science*, 2016, **352**, 73–76.
- 49 S. Maiti, K. Maiti, M. T. Curnan, K. Kim, K.-J. Noh and J. W. Han, Engineering electrocatalyst nanosurfaces to enrich the activity by inducing lattice strain, *Energy Environ. Sci.*, 2021, **14**, 3717–3756.
- 50 W. Wang, B. Lei and S. Guo, Engineering Multimetallic Nanocrystals for Highly Efficient Oxygen Reduction Catalysts, *Adv. Energy Mater.*, 2016, **6**, 1600236.
- 51 S. Lee, J.-H. Jang, I. Jang, D. Choi, K.-S. Lee, D. Ahn, Y. S. Kang, H.-Y. Park and S. Y. Yoo, Development of robust Pt shell through organic hydride donor in PtCo@Pt core-shell electrocatalysts for highly stable proton exchange membrane fuel cells, *J. Catal.*, 2019, **379**, 112–120.
- 52 M. Luo, Y. Sun, X. Zhang, Y. Qin, M. Li, Y. Li, C. Li, Y. Yang, L. Wang, P. Gao, G. Lu and S. Guo, Stable High-Index Faceted Pt Skin on Zigzag-Like PtFe Nanowires Enhances Oxygen Reduction Catalysis, *Adv. Mater.*, 2018, **30**, 1705515.
- 53 S. Stariha, N. Macauley, B. T. Sneed, D. Langlois, K. L. More, R. Mukundan and R. L. Borup, Recent Advances in Catalyst Accelerated Stress Tests for Polymer Electrolyte Membrane Fuel Cells, *J. Electrochem. Soc.*, 2018, **165**, F492–F501.
- 54 Z. Yang, S. Ball, D. Condit and M. Gummalla, Systematic Study on the Impact of Pt Particle Size and Operating Conditions on PEMFC Cathode Catalyst Durability, *J. Electrochem. Soc.*, 2011, **158**, B1439.
- 55 N. Ramaswamy, S. Kumaraguru, W. Gu, R. S. Kukreja, K. Yu, D. Groom and P. Ferreira, High-Current Density Durability of Pt/C and PtCo/C Catalysts at Similar Particle Sizes in PEMFCs, *J. Electrochem. Soc.*, 2021, **168**, 024519.
- 56 X. Wang, S. DeCrane, T. Nowicki, N. N. Kariuki, S. C. Ball and D. J. Myers, Effect of Particle Size on the Dissolution of Pt₃Co/C and Pt/C PEMFC Electrocatalysts, *J. Electrochem. Soc.*, 2021, **168**, 054516.

সাহিত্য অঙ্গন

(সাহিত্য অঙ্গন // Sahitya Angan)

ISSN : 2394 4889 Vol : VIII, Issue : XVII 4th March 2023

Website : www.sahityaangan.com

মুখ্য সম্পাদক

ড. জয়গোপাল মণ্ডল

কার্যকরী সম্পাদক

ড. প্রণবকুমার মাহাতো

ড. সৌম্যব্রত বন্দ্যোপাধ্যায়

উজ্জ্বল প্রামাণিক



ড. জয়গোপাল মণ্ডল

অভিষেক টাওয়ার, ৪র্থ তল, ফ্ল্যাট নং-২

কলাকুশমা, ডাক-কে. জি. আশ্রম, খানবাদ-৩২৮১০৯

Website : www.sahityaangan.com

SAHITYA ANGAN
An Exclusive Interdisciplinary & Literary Tri-lingual
Peer-reviewed Journal
ISSN : 2394 4889 Vol : VIII, Issue : XVII 4th March 2023

Chief Editor :
Dr. Jaygopal Mandal

Working Editor :
Dr. Pranab Kumar Mahato
Dr. Soumyabrata Bandyopadhyay
Ujjwal Pramanik

© Publisher

Cover Drawing : Sidhartha Bose

Type Setting & Cover Setting :
Manik Sahu
Mob : 9830950380

Printing and Binding :
B.C.D Offset (Dey's House)

Price : 550.00

Published By :
Dr. Jaygopal Mandal
Abhishek Tower, Block-A.
4th Floor, Flat-2, Kalakushma
P. S. Saraidhela, Dhanbad-828109
Phone : 09830633202 / 7003488354
E-mail : joygopalvbu@gmail.com,
sahityaangan@gmail.com
Website : www.sahityaangan.com

সূচি

প্রবন্ধ

গল্প-কথা—গণেশ বসু	১
উত্তরায়ণের দিন—অমর মিত্র	১৯
নারী স্বাধীনতার মৃদুস্বর : অবতরণিকা—পিউ মণ্ডল	২৩
অচরিতার্থ কামনার লেলিহান আগ্রাসন এবং 'সোনালি মোরগের গল্প'—ড. পৌলোমী রায়	২৯
সৈয়দ মুস্তাফা সিরাজের নির্বাচিত ছোটগল্পে সমাজ বাস্তবতা—মোহ : নূরুল আমিন	৩৮
সমরেশ বসুর ছোটগল্প : এক জীবনবাদী প্রত্যয়ের সুর—দিলরুবা খাতুন	৪২
ভাষা বৈচিত্র্যে সমরেশের ছোটগল্প—চন্দ্রিমা মৈত্র দুবে	৪৮
মধ্যবিত্তের রুচির বিপরীতে : আখতারুজ্জামান ইলিয়াসের কথাসাহিত্য—ড. মাধুরী বিশ্বাস	৫৭
আখতারুজ্জামান ইলিয়াসের ছোটগল্পে মধ্যবিত্ত বাঙালি সমাজের যন্ত্রণা ও প্রত্যয়ের সংকট—অসীম মুখার্জি	৬৪
ভোমের চিতা : নিম্নবর্গের অস্তিত্ববাদী চেতনার আখ্যান—মধুসূদন সাহা	৭০
নারীমুক্তির প্রেক্ষিতে আশাপূর্ণার সুবর্ণলতা : মাতৃত্বের ভিন্ন স্বর—অভিজিৎ শীট	৭৭
গরম ভাত অথবা নিছক ভূতের গল্প : কুসংস্কারমুক্ত সমাজ ভাবনা কিংবা ক্ষুধা ও দারিদ্র্য—অনিন্দিতা দাস	৮৪
গল্পকার ভগীরথ মিশ্রের গল্পে প্রতিফলিত লৌকিক সংস্কৃতির রূপরেখা—মানস ঘোষ	৯১
আবুল বাশারের গল্প রুকু দেওয়ান : এক রূপাজীবীর আলোকোজ্জ্বল পরণকথা—রফিয়া সুলতানা মোল্লা	১০০
উদ্বাস্ত নারীদের জীবনযুদ্ধ : নির্বাচিত উপন্যাসে—গৌতম অধিকারী	১০৬
দুই পৃথিবীর সংঘাত: প্রসঙ্গ রমানাথ রায়ের 'ক্ষত ও অন্যান্য গল্প'—মানসী কুইরী	১১২
সুকান্তি দত্তের 'মহেন-জো-দারোর নগ্নিকা' : মধ্যবিত্ত যৌনজীবন-চেতনার আধুনিক ভাষা—শ্রেয়া ভদ্র	১২০
অভিজিৎ সেনের নির্বাচিত ছোটগল্প : উত্তরবঙ্গের প্রান্তিক মানুষের অনালোকিত যাপনকথা—কৌশিক পান্ডে	১২৬
নলিনী বেরার গল্পে মানবজীবন: 'তরঙ্গহীন ভীষণ মৌন'—উজ্জ্বল প্রামাণিক	১৩৮
বাংলা ছোটগল্পে ছেচল্লিশের দাঙ্গার প্রতিফলন—বিজেন্দ্র দালাল	১৪৩
শান্ত্রিবিলেখী আন্দোলন : বাংলা ছোটগল্পের ভিন্নতর ধারা—বিশ্বজিৎ বিশ্বাস	১৫০
প্রচৈত গুপ্তের উপন্যাস 'ধুলোবালির জীবন' : যৌনতা, প্রেম এবং দাম্পত্য—সম্পদ দে	১৫৯
নজরুল দৃষ্টিতে ও সৃষ্টিতে রবীন্দ্রনাথ—ড. অরুণাভ মুখার্জী	১৬২
প্রবহমান বাংলা কবিতা : অপ্রতিরোধ্য সুভাষ মুখোপাধ্যায়—ড. মহাশ্বেতা চ্যাটার্জি	১৭২

নজরুল দৃষ্টিতে ও সৃষ্টিতে রবীন্দ্রনাথ

ড. অরুণাভ মুখার্জী

বাংলা কাব্যাকাশের দুই উজ্জ্বল জ্যোতিষ্ক রবীন্দ্রনাথ ও নজরুল। একজন সূর্য, অপরজন চন্দ্র। রবিজ্যোতি ও নজরুল-চন্দ্রিমার সমন্বিত কিরণে বাংলা সাহিত্যবিশ্ব আলোকদীপ্ত ও মহৎ মহিমায় আকীর্ণ। উদ্বেলিত যৌবনোচ্ছ্বাসে আত্মহারা কবি কাজী নজরুল ইসলাম পরাধীন জাতির বৃকে মুক্তির আকাঙ্ক্ষা জাগিয়ে তোলার স্বপ্নে বিভোর হয়ে নিজ প্রতিভার স্বতন্ত্র দীপখানি জ্বালালেও রবি-জ্যোতির আলোকে তাঁর হৃদয় হয়েছে মুগ্ধ বিভোর ও তন্দ্রাতুর। আর সেই মুগ্ধতার প্রকাশ বর্তিকা ‘নজরুল দৃষ্টিতে ও সৃষ্টিতে রবীন্দ্রনাথ’ এই শিরোনামে আলোচ্য রচনায় ফুটিয়ে তোলার প্রয়াস নেওয়া হয়েছে।

‘রবীন্দ্র-যুগ’ বলতে আমরা ১৮৬১ সাল থেকে ১৯৪১ সাল পর্যন্ত সময়সীমাকে ধরে থাকি। এই সময় আমরা দেখতে পাই, রবীন্দ্র-নক্ষত্র নিয়ন্ত্রিত নিয়তির মতো বাঙালির শিল্প-সাহিত্য-সংস্কৃতি পরিচালিত হয়েছে। শরৎচন্দ্র লিখেছেন — “কবিগুরু তোমার প্রতি চাহিয়া আমাদের বিস্ময়ের সীমা নাই”^১। আর এই সময় পর্বেই বস্তুত ১৯১৯-’২০ সাল থেকে ১৯৩০-’৩১ সাল পর্যন্ত নজরুলের সাহিত্য সাধনার উৎকৃষ্ট সময়। রবীন্দ্রনাথকে অবলম্বন করে নজরুল কেবলমাত্র কয়েকখানি কবিতাই শুধু রচনা করেন নি, রবীন্দ্রনাথ ছিলেন তাঁর ভাবের গুরু, তাঁর আদর্শের গুরু। রবীন্দ্র প্রসঙ্গ, রবীন্দ্র ভাব-ভাবনা তাঁকে আজীবন যেমন অনুপ্রাণিত করেছে, তেমনি, নজরুলের দৃষ্টিতে রবীন্দ্রনাথ শুধু মাত্র কবি বা ঋষি ছিলেন না, নজরুলের কাছে রবীন্দ্রনাথ ছিলেন ‘প্রিয় পরমসুন্দর’—

“বক্ষে তব চির-রূপ-রসবিলাসীয়ে!
হারায়ে ফেলেছি সেথা সত্তা আপনার
কাঁদিয়াছি রূপমুগ্ধা রাধিকার মতো।
হে কবি, আজিও শুনি সে চির-কিশোর
তোমার বেণুতে গাহে যৌবনের গান।
সেথা তুমি কবি নও, ঋষি নহ তুমি,
সেথা তুমি মোর প্রিয় পরম সুন্দর!”

(‘অশ্রু-পুষ্পাঞ্জলি’, ‘নতুন চাঁদ’)

আসলে নজরুল ছিলেন ‘রবীন্দ্র-বহ্নিলোকে ঝাড়ের পাখি’। কবিতার ক্ষেত্র ছাড়াও নজরুলের গান-গল্প-উপন্যাস-নাটক-চিঠিপত্র-অভিভাষণ—সর্বত্রই একটা রবীন্দ্রভাব-পরিমণ্ডল আমরা লক্ষ করি। রবীন্দ্রনাথ সম্পর্কে নজরুলের অকপট স্বীকারোক্তি — “বিশ্বকবি কে আমি শুধু শ্রদ্ধা নয়, পূজা করে এসেছি সকল হৃদয় মন দিয়ে, ছেলেবেলা থেকে তাঁর ছবি সামনে রেখে গন্ধধূপ ফুল চন্দন দিয়ে সকাল সন্ধ্যা বন্দনা করেছি”^২।

www.abdpindia.net

ISSN 0974-8849

UGC Care Listed Journal : Group-I, Sl. No.-4

दार्शनिक त्रैमासिक

वर्ष-68

अंक-4

अक्टूबर-दिसम्बर, 2022



अखिल भारतीय दर्शन-परिषद्

सन्दर्भ-सूची

1. ऋग्वेद 1.187.1, 20.21.3, 10.92.2, 1.22.18, 5.26.6, 7.43.24, 9.64.1
2. अथर्ववेद 9.9.17
3. श्रीमद्भगवद्गीता 18.46
4. श्रीमद्भगवद्गीता 10.10
5. श्रीमद्भगवद्गीता 12.6-7
6. श्रीमद्भगवत् 6.3.22
7. श्रीमद्भगवत् 1.2.6
8. मनुस्मृति 2.6.12
9. याज्ञवल्क्यस्मृति 1.7
10. मनुस्मृति 6.92, याज्ञवल्क्यस्मृति 1.122, विश्णुस्मृति 2.8-9, वृद्धगौतम स्मृति 12.2-3
11. याज्ञवल्क्यस्मृति 1.8
12. श्रीमद्भगवत् 12.11.31
13. मैत्रायण्युपनिषद् 6, 36
14. बृहदारण्यकोपनिषद् 2.4, 5
15. डॉ. पी.वी. काणे, धर्मशास्त्र का इतिहास, भाग 1, पृ. 4
16. डॉ. राजबाली पाण्डेय, हिन्दू धर्म कोश, पृ. 339
17. कल्याण-धर्मशास्त्र अंक, गीताप्रेस, गोरखपुर, 1996, पृ. 97-99

□

दार्शनिक त्रैमासिक

अभिनिरक्षित (Peer Reviewed)

ISSN 0974-8849

UGC Care Listed Journal : Group-I, SI. No. -4

वर्ष-68, अंक-4, अक्टूबर-दिसम्बर, 2022

अस्तित्व के अद्वैत वेदान्त दर्शन और आस्तिक अस्तित्ववादी दर्शन

डॉ. प्रसित रंजन घोष *

अद्वैत वेदांत सबसे अभीर तत्त्वमीमांसा की पूर्ण वास्तविकता और ब्रह्म के पूर्ण ज्ञान का वर्णन करता है। ब्रह्म शुद्ध चैतन्य है। इस सन्दर्भ में आस्तिक अस्तित्ववाद एक व्यक्ति की आत्म-चेतना के बारे में केवल अस्तित्व के रूप में अध्ययन करता है। तो, दोनों दर्शन उनके ज्ञानमीमांसा और तत्त्वमीमांसा के साथ चेतना के साथ-साथ आत्म चेतना के बारे में चर्चा करते हैं। यह पेपर दिखाना है कि इसका तुलनात्मक अध्ययन गंभीर रूप से है।

1

अस्तित्ववाद के संस्थापक कौर्गेगार्ड ने व्यक्तिपरक सत्य को ही स्वीकार किया। इतना ही नहीं वह हेगेल के वस्तुनिष्ठ सत्य का विशेष करता है और उसने अपने अनुभव में धार्मिक विश्वासों के माध्यम से अनुभव के रूप में ईश्वर के अस्तित्व को स्वीकार किया। उन्होंने परिभाषित किया कि सत्य व्यक्तिपरक सत्य हैं। इसीलिए उन्होंने हेगेल के वस्तुनिष्ठ सत्य को अस्वीकार कर दिया जो उनके दर्शन का आधार है। उन्होंने महसूस किया कि ईश्वर विषय है, शंकर के अद्वैत दर्शन ने दिखाया कि एक व्यक्ति स्वयं का विषय है। व्यक्ति की स्वयं चेतना भी आत्म चेतना के रूप में है।

शंकर का अद्वैत दर्शन आत्म-चेतना सहित चेतना से संबंधित है। उन्होंने सूत्रबद्ध किया कि जीव = चेतना = ब्रह्म = परम वास्तविकता = परम

* एसोसिएट प्रोफेसर, एच.ओ.डी. और दर्शनशास्त्र विभाग, अच्युतम मेमोरियल कॉलेज, झालदा, पुरुलिया, पश्चिम बंगाल

अस्तित्व। तो, शंकर के अद्वैत दर्शन और अस्तित्वाद् ने पाया कि अस्तित्व स्वयं चेतना है जो प्रकृति में चेतना है। मुख्य शब्द : चेतना, आत्म-चेतना, इश्वर, विषयपरकता, स्वतंत्रता, पसंद, अस्तित्व, स्वयं व्यक्ति में।

इस पत्र में शंकर के अद्वैत वेदांत और आस्तिक अस्तित्वाद् के बीच एक तुलनात्मक अध्ययन पर चर्चा की गई है कि चेतना शंकर के अद्वैत वेदांत और ईश्वरवादी अस्तित्वाद् दोनों के दर्शन का प्रमुख विषय है। वर्तमान में चेतना महत्वपूर्ण अंतःविषय है।

2

ऋग्वेद में ऐतरेय उपनिषद् का महावाक्य 'प्रज्ञानं ब्रह्म' है। यह सभी के पूर्ण विवरण के रूप में सार्वभौमिक दर्शन है। यह कहा जा सकता है कि हर चीज का नियम ब्रह्म है। हम प्रज्ञानम को पूर्ण ज्ञान के रूप में नहीं सोच सकते हैं जो कि बिना है एक व्यक्तिगत निज का अस्तित्व। और यह स्पष्ट है कि एक व्यक्ति स्वयं एक व्यक्तिगत व्यक्ति का तात्पर्य है। तो प्रज्ञानं ब्रह्म के महावाक्य से एक समीकरण इस प्रकार बनाया जा सकता है।

प्रज्ञा पूर्ण चेतना = एक व्यक्ति जीव = एक व्यक्तिगत स्व = एक व्यक्तिगत व्यक्ति। पूर्ण चेतन्य से विशेष चेतन्य अथवा व्यक्ति चेतन्य निःसृत होता है शंकर का प्रज्ञा से अस्तित्वादी तथा हुसाल का फेनोमेनोलोजी का ट्रान्ससेनडेन्डाल इगो सभी चेतना निःसृत होता है।

तो एक व्यक्ति का वर्णन, एक व्यक्ति स्वयं अनिवार्य रूप से ब्रह्म है। ब्रह्म वेद ब्रह्म भवति (मुंडक उपनिषद्: 3/2/9)। जब एक व्यक्ति के रूप में एक आकांक्षी, जो ब्रह्म विकार द्वारा वेदांत के श्रावण, मनन और निदिध्यापस के माध्यम से ब्रह्म विद्या का अभ्यास करने का उरसुकता से इशारा रखता है और अंत में एक व्यक्ति ब्रह्म बन जाता है, जो एक व्यक्ति की पूर्ण अभिव्यक्ति है। सर्वज्ञ या ब्रह्म के रूप में मनुष्य हमेशा के लिए ऐतिहासिक खोज है। अद्वैत वेदांत में, जीव, एक व्यक्तिगत विशेष चेतना रूप का आत्मा और ब्रह्म पूर्ण वास्तव या निरपेक्ष होने के रूप में।

जीव = एक व्यक्तिगत आत्म = ब्रह्म = पूर्ण वास्तविकता = अखंडम (अनंत)।

शंकर के अनुसार, एक व्यक्ति स्वयं और ब्रह्म समान हैं। ब्रह्म सच्चिदानंदम है जो सत् (पूर्ण अस्तित्व) के समान शब्द हैं चित् (पूर्ण चेतना) और आनंद (पूर्ण शांति)। तो, हम वेदांत से हर चीज का एक कानून बनाते हैं जो इस प्रकार है।

सत् = चित् = आनंद = सच्चिदानंद = पूर्ण अस्तित्व = निरपेक्ष चैतन्य परम शांति।

उपरोक्त नियम जो वेदांत कहता है वह सब कुछ का खाका है, सभी भाषाओं का कुल विवरण।

तो, यह स्पष्ट है कि वेदांत सभी का पूर्ण विवरण घोषित करता है। सब कुछ अनिवार्य रूप से चेतना है। तो, ब्रह्मांड में केवल और एक चीज स्थिर है वह है शुद्ध चेतना।

शंकर ने कहा कि सभी वेदों, उपनिषदों, गीता को 'केवल अद्वैत वेदांत' के सार के रूप में उन्होंने आधे श्लोक (आधे वाक्य) में ही व्यक्त किया। यह इस प्रकार है :

"ब्रह्म सत्यं, जगत मिथ्या, जिवा ब्रह्मैव नपरा"। ब्रह्म सत्यं जगत (ब्रह्मांड) झुठा है और जीव और ब्रह्मा (व्यक्तिगत मनुष्य और पूर्ण चेतना है साहस्य)।

3

इसका अर्थ है कि ब्रह्म (पूर्ण चेतना) सत्य है। सत्य शाश्वत अस्तित्व है। जगत (ब्रह्मांड) झुठा है। असत्य का अर्थ है जो क्षणिक (अस्तित्व) है और शुद्ध चेतना या पूर्ण ब्रह्म और जीव (व्यक्तिगत स्व) के रूप में भिन्न नहीं हैं। सत्य शाश्वत सत्ता है। अपरिवर्तित युनिवर्सल बीइंग हमेशा के लिए। सार्वभौमिक सत्ता परम वास्तविकता है, शुद्ध चेतना है। सभी नाम और रूप विश्व के रूप में ब्रह्मांड हैं। सभी परिवर्तन नाम और रूपों में भी शामिल हैं। सभी परिवर्तन = सभी रूप = संपूर्ण ब्रह्मांड = जगत = असत्य। लेकिन सभी का सार या शाश्वत के लिए सभी चीजों का मूल आधार अपरिवर्तित शाश्वत पूर्ण चेतना या ब्रह्म है।

प्रज्ञा पूर्ण ज्ञान है जो ब्रह्म के लिए खड़ा है। यहाँ ज्ञानमीमांसा और तत्वमीमांसा एक दूसरे समान हैं। ज्ञान चेतना है। अनुभव चेतना का एक रूप है। वेदांत में यह अनूठा वर्णन और कानून है जो पूरे ब्रह्मांड का स्पष्ट रूप से वर्णन करता है। पूरे ब्रह्मांड की हर चीज का वर्णन और परिभाषित किया गया है केवल और एक शाश्वत चीज चेतना, ब्रह्म।

यहाँ यह भी निष्कर्ष निकाला गया है कि ब्रह्मांड में केवल एक चीज है जो चेतना के रूप में पूर्ण मुक्त है। तो, स्वतंत्रता चेतना, केवल ब्रह्म, शुद्ध

चेतना ही ब्रह्मांड का नियंत्रक है। चेतना या ब्रह्म सब कुछ नियंत्रित करता है।

एकमात्र और अद्वितीय सिद्धांत बिल्कुल स्वतंत्र है और यह अनिर्वाण रूप से केवल चेतना है। अद्वैत वेदांत ने इसे दुनिया में खोजा। ब्रह्म सच्चिदानंद या अस्तित्व, चेतना और साध ही पूर्ण शांति है। तो, स्वतंत्रता चेतना के समान है। ब्रह्म या चेतना के रूप में अस्तित्व मुक्त है। ब्रह्म के रूप में अस्तित्व मुक्त है। ब्रह्म हमेशा के लिए स्वतंत्र रूप से मौजूद है। वेदांत घोषणा करता है कि अस्तित्व चेतना है। अस्तित्व मुक्त है। अद्वैत वेदांत के अनुसार अस्तित्व या चेतना या पूर्ण शांति या ब्रह्म स्वतंत्र है जो सभी को नियंत्रित करता है।

अस्तित्ववाद में, अस्तित्व एक सार उनकी मुख्य चर्चा हैं। वे चेतना, स्वतंत्रता, व्यक्तिगत व्यक्ति, स्वनियमन के बारे में चर्चा करते हैं। वास्तव में अस्तित्ववाद की वे शर्तें कोई नई अवधारणा नहीं है। यह स्पष्ट है कि आत्म-विरोध वास्तव में हमेशा के लिए झूठ है।¹ अद्वैत वेदांत से पता चलता है कि ब्रह्म अस्तित्व या चेतना या शांति के रूप में आत्मा-विरोधभासी शेष पूरी तरह मुक्त है। तो, स्पष्ट है कि अस्तित्व सार से पहले होता है स्वयं विरोधभासी अस्तित्ववाद है। वेदांत से पता चलता है कि, अस्तित्व = चेतना = ब्रह्म = सार।

तो, चेतना से पहले अस्तित्व आत्म-विरोधभासी था। यहाँ अस्तित्व नहीं चेतना है, अस्तित्ववाद है। लेकिन अद्वैत वेदांत में, अस्तित्व चेतना है। सात = चित = आनंद = सच्चिदानंद ब्रह्म।

तो, अस्तित्व और चेतना समान है। वे बिल्कुल अलग नहीं हैं लेकिन एक ही चीज हैं। मनुष्य चेतना है। उसका लक्ष्य ब्रह्म बनना है। सभी व्यक्ति चेतना या आत्म चेतना के रूप में (क्योंकि आत्म चेतना शुद्ध चेतना का एक रूप है) ब्रह्म बन रहे हैं। यह वास्तव में मनुष्य बनाने की प्रक्रिया है जिसे अद्वैत वेदांत को ब्रह्म को प्राप्त करने की प्रक्रिया के रूप में कहा जा सकता है (ब्रह्म वेद, ब्रह्मैव भवती)।

पूर्व-चिंतनशील चेतना और चिंतनशील चेतना प्रकृति में चेतना हैं। वे समान और अद्वैत हैं। यह कहना स्पष्ट है कि चेतना ही अस्तित्व है और सभी से पहले है। इसलिए सत्ता शुद्ध चेतना है। शुद्ध चेतना सभी से मुक्त है। तो,

चेतना और स्वतंत्रता एक ही हैं। स्वतंत्रता का अर्थ है चेतना या आत्म-चेतना। यह निष्कर्ष निकाला जा सकता है कि चेतना पूर्ण अस्तित्व = स्वतंत्रता = अद्वैत = अखंडन या अनंत चेतना है। तर्क यह है कि अद्वैत के रूप में केवल परम वस्तु। शाश्वत अस्तित्व वाले सभी में व्याप्त चेतना है। तो, चेतना सभी चीजों को नियंत्रित करती है, जिसमें सभी व्यक्ति भी शामिल है। केवल एक चीज मौजूद है क्योंकि चेतना सभी बहुलताएं और अंतर है।

सन्दर्भ-सूची

1. स्वामी विश्वरानंद, ब्रह्म सूत्र, अद्वैत आश्रम, पृ. 78
2. शंकराचार्य, पंचिकरणम्, उद्बोधन, कलकता, पृ. 15
3. श्री श्री सदानंद योगिंद्र, वेदांतसर, बी. के. पाल, संस्कृत पुस्तक भंडार, कोलकाता-4, ऐतरयो उपनिषद्।
4. ऐतरयो उपनिषद्।
5. ए. क्रिटिकल स्टडी ऑफ सार्ट्रेस ऑन्टोलोजी ऑफ कॉन्शियसनेस, वर्धमान यूनिवर्सिटी, वर्धमान, 1978, पृ. 71
6. सोरेन कीर्कगार्ड, अवैज्ञानिक पोस्ट्रिक्ट का समापन, ट्रान, डी. स्वेन्सन, प्रिंसटन यूनिवर्सिटी प्रेस, 1941, पृ. 251
7. जीन-पॉल सार्त्र, बीइंग एंड नथिंगनेस, टी. आर. हेजलर्ड, बर्नर्स, पृ. 161

□



Printed by : Satyam Publication, Delhi & Patna, 09386365631

ISSN 2278 - 0688

Volume - XXII

ऋतायनी

A REFEREED RESEARCH JOURNAL OF SANSKRIT

ऋतायनी

VOLUME-XXII

ISSN 2278 - 0688

December 2022

Purulia , West Bengal

December 2022

RITAAAYANI

Vol. - XXII

ISSN 2278 - 0688

Volume -XXII

December 2022

ऋतायनी

RITAAAYANI

A REFEREED RESEARCH JOURNAL OF SANSKRIT

(U.G.C. Approved Journal No. 40947)

Chief Editor

Dr. Chandrakanta Panda

Editor

Dr. Jagamohan Acharya

Associate Editors

Dr. Buddheswar Sarangi

Dr. Jogeswar Mahanta

Sushant Pradhan

Purulia , West Bengal

भक्तिप्रस्थानस्य परिचयः महत्त्वम् अवदानं च

Somen Dutta

भक्तेः स्वरूपम्

भज् इति धानोः भक्तिशब्दस्य निष्पन्नः भवति । हिन्दुधर्मे भक्तिः आराधना तथा उपासनायाः एक-विशेषः रीतिः इति मन्यते । पूजितदेवे व्यक्तित्वं प्रति वा विशेषः स्नेहः प्रेमः वा भक्तिः इति कथ्यते । ईश्वरसमर्पणं पूर्णतया भक्तिः इति पण्डिताः उच्यन्ते । भक्तिमार्गे यः जनः ईश्वरं भजति सः व्यक्तिः भक्तः नाम अभिधीयते । भक्तिदर्शनं भक्तिमार्गः इति उच्यते । भक्तिवादः हिन्दुधर्मस्य अनेकसंप्रदायानाम् आधारः अस्ति । भिन्न-भिन्न-सम्प्रदायाः भक्तिवादस्य भिन्न-भिन्न-प्रकारेण व्याख्यां कुर्वन्ति । भक्तिवादः रीतिनां संस्काराणां च उपरि ईश्वरप्रेमं स्थापयति । प्रमि, मित्रम, माता-पिता-सन्ततिः, गुरु-शिष्यः इव ईश्वर-मनुष्ययोः मानवीयसम्बन्धः भक्तिवादस्य मुख्यस्तम्भः अस्ति । ईश्वरस्य विशिष्टरूपस्य, ईश्वरस्य निराकाररूपस्य वा गुरुं प्रति विशेष-भक्तिः भक्तिवादस्य प्रधान-अङ्गः । हिन्दुधर्मे भिन्नसंप्रदायेषु भक्तिवादस्य विशिष्टरूपाः प्रचलिताः सन्ति । यथा— शैवाः शिवस्य तथा शिवसम्बद्धदेवतानां भक्ताः, वैष्णवः विष्णुः तथा तस्य अवताराणां भक्ताः, शाक्ताः च महाशक्तेः विभिन्नरूपस्य भक्ताः सन्ति ।

वैदिकसाहित्ये देवानां भक्तिसाहचर्यं लक्षते । श्रुत्विकसमर्पितस्य हविर्भागस्य सेवार्थं ते देवाः संहतिं सम्मतिञ्च दर्शयन्ति । यथा—

आस्य जानन्तो नाम चिद्विवक्तन

महस्ते विष्णो सुमतिं भजामहे ।।

भज् सेवायाम् इति धात्वर्थबलेन देवनिष्ठप्रीत्यनुकूलव्यापारो भजेरर्थः ।

यथा गरुडपुराणे उक्तम्—

भज इत्येष वै धातुः सेवायां परिकीर्तितः ।

तस्मात् सेवा बुधैः प्रोक्ता भक्तिः साधनभूयसी ।।

अर्थात् सेव्य-सेवकसम्बन्धमूलतया सेव्य इष्टदेव सेवकश्च जीवो भवति । भक्तेः क्रमविकासे साध्यरूपायाः साधनरूपायाश्च भक्तेः भर्जनं प्रायशो दृश्यते ।

स्मरन्तः स्मारयन्तश्च मिथोघौघहरं हरिम् ।

भक्त्या सञ्जातया भक्त्या बिभ्रत्युत्पुलकां तनुम् ।।

श्रीमद्भागवते नवधाभक्तेः पुंखानुपुंखविवरणमुदाहरणञ्च दृश्यते । तथैव नारदभक्तिसुत्रे अपि भक्तेः स्वरूपस्य विषयो वर्णितः । इक्ष्वरे परमप्रेमारुपा एव भक्तिः सा च अमृत्तारुपा

अस्ति । अर्थात् यथा वृक्षस्य पूर्णत्वं गौरवं च फले प्राप्तं भवति तथैव भक्तेः स्वरूपं गौरवं च भगवति परमप्रेमलक्षणे एव अस्ति । शाण्डिल्येन अपि स्वभक्तिसुत्रे परमतत्त्वं प्रति परानुरक्तिरेव भक्तिः इति उक्तम् । तथैवाध्यात्मरामायणे अपि अगस्त्येन-भक्तिरुपायं विना स्वप्ने अपि मोक्षः न भवेत् इति कथितम् । नारदपञ्चरात्रे अपि देह-मनो-बुद्ध्यहंकारैः रहित ज्ञानयोगावरणात् मुक्तः शुद्धभावेन सर्वैरिन्द्रियैः इन्द्रियाधिपतेः श्रीहृषीकेशस्य पदानुशीलनं नतेव भक्तिरिति उच्यते । बृहदारण्यकश्रुतौ उक्तम्- तमेव धीरो विज्ञानमेव भक्तिरुच्यते । भगवद्गदीतायां भगवता कृष्णेन सर्वेषु भूतेषु समः ब्रह्मभुतः भाव एव भक्तिरिति कथितम् । भक्तिरसामृतसिन्धुः प्रेमरूप सूर्यकिरणवत् स्वकीयकान्तिद्वारा चिन्तमध्ये द्रवीभावोत्पन्नक्षमः शुद्धसत्त्वप्रधानरूपभाव एव भक्तिरिति श्रीरुपगोस्वामिना उक्तम् । छान्दोग्योपनिषदि श्यामाच्छवलं प्रपद । शवलाच्छयामं प्रपद्ये इतीयं प्रपत्तिः शारणागतिर्वा भक्तिरिति कथितम् । भागवते श्रीकपिलेन-यदगुणश्रुतिमात्रेण मयि सर्व-गुहाशये । मनोगतिरविच्छन्ना यथा गंगाम्थसो अम्बुधौ । इति भक्तेः निर्गणस्वरूपमुद्दहत्म् । श्री सुतेन इयम् अहैतुकी भक्तिः जीवस्य श्रेष्ठधर्मरूपेण प्रतिपादिता । यथा—

स वै पुंसां परो धर्मो यतो भक्तिरधोक्षजे ।

अहैतुक्यप्रतिहता ययात्मा सम्प्रसीदति ।।

अर्थात्, येनेन्द्रियज्ञानातीतं श्रीकृष्णं प्रति श्रवणादिलक्षणा फलाभिसंधान-रहिता ऐकान्तिकी निरपेक्षा भक्तिर्जयते सैव पुंसां परोधर्मः भवति तथा भक्त्या आत्मा प्रसीदति ।

एवं भक्तेः सामान्यस्वरूपं वेदोपनिषत्प्रारम्भिकभक्तिसुत्र-शाण्डिल्य भक्तिसुत्र-भागवताध्यात्मरामाणादिषु आर्षग्रन्थेषु समुपलभ्यते ।

वैदिकसाहित्ये भक्तिः

भक्तिः वैदिकसाहित्ये मानवजीवनस्य लक्ष्यरूपेण स्वीक्रियते । वैदिकमंत्रेषु अपि भक्तिधारायाः संकेतः प्राप्तुं शक्यते । श्रवण-कीर्तन-स्मरण-पादसेवनार्चनवन्दन-दास्य सख्यात्मनिवेदनादि रूपेण भक्तेः नवधा वर्णनमुपलभ्यते । तत्र परमात्मनः श्रीविष्णोः यशःकथायाः पुनः पुनः श्रवणाय ऋग्वेदस्य मंत्रे प्रमाणं प्राप्यते । यथा—सेदु श्रवोभिर्यज्यं चिदभ्यसत् । कीर्तनभक्तेः सूचना अपि प्राप्यते तत्र विष्णोर्नु कं वीर्याणि प्रवोचम् अर्थात् श्रीविष्णोः लीलापराक्रमादितत्त्वं वर्णयामि इति परमात्मनः लीला-गुणानुकीर्तनस्य सूचना मंत्रे अस्मिन् प्राप्यते ।

प्रविष्णवे शुषमेतु मन्म गिरिक्षित उरुगायाय वृष्णे ।

अत्र उरुगाये भगवति मम स्मरणं सुदृढं भवत्विति मंत्रे अस्मिन् पादसेवनभक्तेः विषये सूचना प्राप्यते यथा—

यस्य त्री पुर्णा मधुना पदान्यक्षीयमाणा-स्वधया मदन्ति ।

भगवतः विष्णोः माधुर्यमण्डिताक्षयपादत्रयस्य सेवनेन आनन्दः प्राप्यते इति अस्मिन् मंत्रे कथितम् ।

अर्चनभक्तिविषये कथ्यते यथा— प्र वः पान्तमन्धसो धियायते महे शुराय विष्णवे चार्चित अत्र मह्यपराक्रमस्य विष्णोः भगवतः अर्चना सूचिता ।

वन्दनभक्तिविषये कथ्यते यथा— नमोरुचाय ब्राह्मये अस्मिन् मंत्रे ब्रह्म-विग्रहस्य नमस्कारः निर्दिश्यते ।

दास्यभक्तिविषये कथ्यते-ते विष्णो सुमतिं भजामहे अत्र भगवतः विष्णोः सेवां कर्तुं सूचना प्राप्यते । सख्यभक्तिविषये कथ्यते-उरुक्रमस्य स हि बन्धु रित्था विष्णोः अत्र भगवतः उरुक्रमस्य विष्णोः सखरूपेण सेवां कर्तुं सूचना प्राप्यते ।

आत्मनिवेदनात्मकभक्तिविषये कथ्यते—

यः पूर्याय वेधसे नवीयसे सुमज्जानये विष्णवे ददाशति ।

अत्र जगत्-स्रष्टारं, नित्यनवीनं भगवन्तं प्रति आत्मसमर्पणं कर्तुं कामना क्रियते ।

एवं वैदिकसाहित्ये भक्तेः नवसाधनै यथा—श्रवण-कीर्तन-स्मरण-पादसेवनार्चन-वन्दन-दास्य-सख्यात्मनिर्वदनभक्तिभिः प्रभावः परवर्तिश्रीमद्भागवतगीता पुराण सूत्रालंकारसाहित्येषु परिलक्ष्यते ।

वैदिकसाहित्ये देवस्तुनिपरका मन्त्राः भक्तितत्त्वस्य बीजं बहुन्ति । तत्रापि लोभत्यागपूर्वकात्मसमर्पणस्य तथा आत्मनः तुच्छभावस्य निवेदनेन सह स्वस्वेष्टदेवकृपाकटाक्षलाभाय ये प्रत्यक्ष-परोक्षाध्यात्मिकमन्त्राः परिगीताः तत्र भक्तेः गन्धः अनन्तरवर्तितसाहित्यं सुवासयति, इति अत्र नास्ति संशितिलेशः ।

श्रीमद्भागवद्गीतायां भक्तिः

यथा वैदिकसाहित्येषु नवधाभक्तेः सूचना प्राप्यते तथैव सर्वेपनिपदा सारस्वतरूपायां श्रीमद्भागवद्गीतायामपि नवधाभक्तेः प्रमाणमुपलभ्यते । श्रवणभक्तिविषये भगवता कृष्णेन अर्दुनं प्रति उपदिश्यते । यथा—

श्रद्धावानसूयश्च शृणुयादपि यो नरः ।

सोपि मुक्तः शुभान् लोकान् प्राप्नुयात् पुण्यकर्मणाम् ।।

अस्मिन् श्लोके श्रद्धावान अनसुयो गीताश्रवणात् एव मुक्तिं प्राप्नोति इति उक्तम् । कीर्तन-स्मरणभक्तिविषये तत्र सूचनां उपलभ्यते । यथा—

मच्चित्ता मद्गतप्राणा बोधयन्तः परस्परम् ।

कथयन्तश्च मां नित्यं तुष्यन्ति च रमन्ति च ।।

अत्र नित्यं परस्परं बोधयन्त इति पदेन सर्वदा भगवतः कीर्तनं कर्तुं संकेतः लभ्यते। पुनश्च मच्चित्ता मद्गतप्राणा इति पदेन भगवतः स्मरणं ततः पादसेवनभक्तिविषये वर्णयते यथा—

अभ्यासेष्यसमर्थोऽसि मत्तर्मपरमो भव।

मदर्थमपि कर्माणि कुर्वन् सिद्धिमवाप्स्यसि।।

अत्र अभ्यासेयोगे असमर्थोऽपि भगवतकर्मपरायणो भूत्वा तस्य कथाश्रवण-कीर्तन-वंदनार्चन-तन्मन्दिरमार्जन-पुष्पचयन-ततपरिचर्यादि कर्तुं सूचना प्राप्यते। पुनश्च दास्यभक्तिविषये तत्र प्रमाणं प्राप्यते।

मन्मना भव मद्भक्तो मद्याजी मां नमस्कुरु।

मामेवैष्यसि युक्तत्वैवमात्मानं मत्परायणः।

अत्र मद्भक्ताशब्देन भगवान् एव एकमात्रपरमगतिः भर्ता-स्वामी इति मत्वा तत्राम-रूप-गुण-प्रभाव-लीलादी श्रवण-कीर्तन-स्मरणेषु तस्मै सर्वसमर्पणभाव एव दास्यभक्तेः सूचना लभ्यते। ततः सख्यभक्तिविषये प्रमाणं प्राप्यते यथा—

गतिर्भर्ता प्रभुः साक्षी निवासः शरणं सुहृत्।

प्रभवः प्रलयः स्थानं निधानं बीजमव्ययम्।।

अत्र गतिः भर्ता-प्रभुः साक्षी सुहृत् इति मत्वा तस्मिन् शरणापन्नभाव एव सख्यभक्तिरिति कथ्यते इति सूचना प्राप्यते। ततः आत्मनिर्वदन-भक्तिविषये सूचना प्राप्यते यथा—

सर्वधर्मान् परित्यज्य मामेकं शरणं व्रज।

अहं त्वां सर्वपापेभ्यो मोक्षयिष्यामि मा शुचः।

अत्र मामेकं शरणं व्रज इति वाक्येन चिन्ता-सेवा-पूजा-प्रणति पूर्वकं सर्वधर्मपरित्यागेन केवलं भगवतः शरणागतिः एव आत्मनिवेदनात्मिका भक्तिरिति कथ्यते।

भगवद्गीतायां ज्ञानयोगः कर्मयोगः भक्तियोगः इति योगसमुच्चये भक्तियोगस्य विवेचनं कृतम्। तत्र सम्प्रदायभेदेन ज्ञानस्य कर्मणो भक्तेः वा प्रधानाप्रधानताविमर्शः। अन्ततो गत्वा त्रयाणां योगानां समुच्चयविषयः सकलतत्त्वमौलिभूतः प्रतिपादितः। तथापि तत्र उपास्योपासक-सम्बन्धरूपाया भक्तेरपि च पत्रपुष्पफलतोयोत्सर्गपूर्वकं भगवत्प्राप्तिरूपायाः भक्तेश्च अनन्यता संसाधिता।

वैदिकसाहित्यात् श्रीमद्गीतायां च परं पुराणसाहित्ये भक्तितत्त्वस्य पुंखानुपुंखं वर्णनं दृश्यते। उक्तितत्त्वस्य विवेचनं प्रायतः अष्टादशपुराणेषु उपलभ्यते। यद्यपि सर्वेषु पुराणेषु भक्तेः स्वरूपाणां यत्र तत्र वर्णनं दृश्यते तथापि ब्रह्म-पदम-विष्णु-भागवतादि भक्तिप्रधानपुराणेषु भक्तितत्त्वस्य सर्वाधिकं वर्णनमुपलभ्यते।

ब्रह्मपुराणे श्रीकृष्णभक्तितत्त्वस्य विस्तारेण सह वर्णनादनन्तरं तत्सम्बन्धि ज्ञानमिश्रितभक्तितत्त्वं वर्णितम्। यथा—

अप्यन्यचित्तोशुद्धो वा यः सदा कीर्त्तयेद्धरिम्।

सोपि दोषक्षयान् मुक्तिं लभेच्चेदिपतिर्यथा ।।

अत्र भगवतः नामकीर्त्तनेन द्वेष्यभक्तापि मुक्तिः प्राप्ता इति कथितम्।

पद्मपुराणे भक्तेः प्रमुखाङ्गरूपेण ख्याताया कीर्त्तनभक्तेः महत्त्वं वर्णितम्। एवं तत्र भगवतः कीर्त्तनमण्डलीनां नामोल्लेखोपि विद्यते। यथा—

अप्यन्यचित्तोशुद्धो वा यः सदा कीर्त्तयेद्धरिम्।

सोपि दोषक्षयान् मुक्तिं लभेच्चेदिपतिर्यथा ।।

अत्र भगवतः नामकीर्त्तनेन द्वेष्यभक्तापि मुक्तिः प्राप्ता इति कथितम्।

पद्मपुराणे भक्तेः प्रमुखाङ्गरूपेण ख्याताया कीर्त्तनभक्तेः महत्त्वं वर्णितम्। एवं तत्र भगवतः कीर्त्तनमण्डलीनां नामोल्लेखोपि विद्यते। यथा—

प्रहादस्तालधारी तरलगतितया चोद्धवः कांस्यधारी

वीणाधारी सुरर्षिः स्वरकुशलतया रागकर्त्तार्जुनोभूत्।

इन्द्रोवादीन्मृदङ्गं जयजयसुकराः कीर्त्तने ते कुमारा-

सत्राग्रे भाववक्ता सरसरचनया व्यासपुत्रो बभूव ।।

अत्र प्रहादोद्धव-नारदारजुनेन्द्र-सनत्कुमारा इत्यादयः परमभागवताः स्व स्व वाद्ययंत्रैः सह भगवतः नामकीर्त्तनं कृतवन्त इति सूचना प्राप्यते।

ततः विष्णुपुराणे पञ्चमांशे अष्टाध्येषु केवलायाः भक्तेः स्वरूप-वर्णनमुपलभ्यते। भक्तेः प्रमुखसाधनरूपस्मरणभक्तिप्रसङ्गे इत्थं वर्णितम्—

स्मृते सकलकल्याणभाजनं यत्र जायते।

पुरुषस्तमजं नित्यं ब्रजामि शरणं हरिम् ।।

अत्र भगवतः स्मरणमात्रेणैव सर्वकल्याणं भजते पुरुषः इति कथितम्। पुनश्च तत्र अक्रुरेण श्रीकृष्णस्य ब्रह्मस्वरूपमनुभूय तस्मिन् भक्तिः कृता दृश्यते।

तस्मादहं भक्तिविनम्रचेता, ब्रजामि सर्वेश्वरमीश्वराणाम।

अंशावतारं पुरुषोत्तमस्य हनादिमद्धान्तमजस्य विष्णोः ।।

ततः भक्तिप्रधानपुराणेषु भागवतस्य स्थानमन्यतमम्। अस्मिन् पुराणे भक्तेः स्वरूपस्य सभेतं सतत्त्वं वर्णनमुपलभ्यते। अत्र भक्तेः द्विविधः मार्गो वर्णितः। तयोः साध्यसाधनयोः साधनमार्गः भक्तिसाधनस्य सुगमोपाय इति वर्णितम्। यथा—

न साधयति मां योगो न सांख्यं धर्म उद्धव ।

न स्वाध्यायस्तपस्त्यागो यथा भक्तिर्ममोर्जिता ॥

अत्र योग-सांख्य-स्वाध्याय-तपस्त्यागादि विना भगवति भक्तिःसञ्जाता इति सूचना प्राप्यते ।
पुनश्च सप्तमाध्याये परमभक्तप्रहादोपि भक्तेः उपादेयतायाः प्रसङ्गे कथितवान्—

प्रीणनाथ मुकुन्दस्य न वृत्तं न बहुज्ञता

न दानं न तपो नेज्या न शौचं न व्रतानि च ।

प्रीयनेमलया भक्त्या हरिरन्यद् विडम्बनम् ॥

अत्र भगवतः भाक्तिं विना भक्तस्य अन्यसाधनं यथा— दान-तयो-यज्ञ-व्रतादि उपहसमेव
प्राप्नोति किन्तु अमलया भक्त्या एव भगवान् प्रीयते इति सूचना प्राप्यते । तत्र पुनश्च भक्तिरेव
वैराग्यसाधिका तथा कर्मणः उपयोगः वैराग्यस्य हेतोः उवति । यावत् वैराग्यस्योत्पत्तिः न
भवेत् तावत् वर्णक्षमविहिताचाराः सदा पालनीयाः । तथा च उक्तम्—

तावत् कर्माणि कुर्वीत न निर्विद्येत यावता ।

मक्तथाश्रवणादौ वा श्रद्धा यावत्र जायते ॥

पुनश्च कथ्यते तत्र—श्रेयसः मूलस्रोतोरुपिणीं भाक्तिं परिहाय बोध्यते प्राप्यते
उद्योगशीलानां मानवानां प्रयत्नः नथैव निष्कलः तथा कलेशोत्पादकश्च भवति यथा
स्थूलतुषावधातिनाम् ।

श्रेयः श्रुतिं भक्तिमुदस्य ते विभो

क्लिशयन्ति ये केवलबोधलब्धये ।

तेषामसौ क्लेशल एव शिष्यते

नान्यद् यथा स्थूलतुषावधातिनाम् ॥

पुनश्च तत्र ज्ञानपेक्षया भक्तेः उपादेयता प्रतिपादिना । साधनभक्तिः नवधा भवति ।
पुराणसाहित्ये विशेषतः भागवते सत्संगतेः महिमगानं सर्वत्र दृश्यते । साध्यरुपा अथवा फलरुपा
भक्तिः प्रेमलक्षणा इति गृह्यते । प्रेमलक्षणायुक्तभक्ताः बाह्येन्द्रचक्रवर्तिनां पदं तथा योगस्य
श्रेष्ठसिद्धानामपि मोक्षपदं नेच्छन्ति । भगवता सार्धं नित्यवृन्दावने ललितविह्वारार्थमावेशितधीः
भगवच्चञ्चरीकः भक्तः शुष्कां रसशुन्यां मुक्तिमपि तिरस्कारोति । यथा—

न पारमेष्ठ्यं न महेन्द्रधिष्यं

न सार्वभौमं न रसाधिपत्यं ।

न योगसिद्धीरपुनर्भवं वा

मय्यर्पितात्मेच्छति मद् विनान्यत् ॥

पुनश्च तत्र भगवतः दशनिच्छुभक्तानां स्वभाव-विषये वर्णितम्। यथा—

अजातपक्षा इव मातरं खगाः
स्तन्यं यथा वत्सतराः क्षुधार्ताः।
प्रियं प्रियेव व्युषिनं विषण्णा
मनोरविन्दाक्ष दिदृशते त्वाम्॥

उपसंहारः

अयं भक्तिरसः प्रत्यक्षभक्तिरसः परोक्षभक्तिरसः इति द्विधा विभज्यते। पुनश्च प्रत्यक्षभक्तिरसः शान्त-दास्य-सख्य-वात्सल्य-माधुर्यादिरूपेण पञ्चधा विभज्यते। पुनश्च परोक्षभक्तिरसः ह्रास्य-करुण-क्रोध-शौर्य-भय-विस्मय-बीभत्सादिरूपेण सप्तधा विभज्यते। द्वादश-रसानुसारं-कपिल-माधव-उपेन्द्र-नृसिंह-नन्द-नन्दन-वलराम-कूर्म-कल्की-राघव-वराह-मत्स्यादिद्वादशानाम् अवताराणां कल्पना क्रियते।

सन्दर्भग्रन्थसूची—

1. Ujjvalanī'amaḥ of RUpagoswami, Edited by Tukaram JA'vajl', Mumbai, 1835.
2. History of Sanskrit Poetics by S.K. De, Calcutta Oriental Press, Calcutta, 1925.
3. Rasadī'ghikā' of VidyA'rA'ma, Edited by Gopal Narayan BahuDa, Rajasthan Oriental Research Institute, Jodhpur, 1956.
4. The Number of Rasas by V. Raghvan, The Theosophical Publishing House, Adyar, Madras, 1975.
5. Bhaktiramā'ntasindhu of RUpagoswA'mi, Edited by I'rī' Bhakti VedA'ntaSwA'mi, BhaktivedA'nta Book Trust, Mumbai, 1980.
6. 16. EkA'vall' of Vidyadhara, with the Commentary of Tarala by MallinA'tha, Osmania University, Hyderabad, 1981.
7. भक्तिवैभवनटकम्, कविडिण्डिमजीवादेवाचार्यः, Odisha Sahitya Academy, Bhubaneswar, 1981.

Research Scholar
S.K.B. University,
Purulia, West Bengal
Mob : 7384860243



ISSN : 2347-7180

(A Bilingual Research Journal, Indexed in UGC-Care list)

DOGO RANGSANG

Research Journal, Vol-13, Issue. 3, No.3, March 2023

দগো ঝাংছাং

CHIEF EDITOR (HON.)
EDITORS (HON.)

মুখ্য সম্পাদক (অবৈতনিক)
সম্পাদকদ্বয় (অবৈতনিক)

: Dr. Upen Rabha Hakacham
: Dr. Lalit Chandra Rabha
: Dr. Dhaneswar Kavitha
: ড° উপেন ঝাভা হাকাচাম
: ড° ললিত চন্দ্র ঝাভা
: ড° ধনেশ্বর কলিতা

A Peer Reviewed Bilingual Research Journal
(Indexed in UGC-CARE List)

ISSN 2347-7180

DOGO RANGSANG RESEARCH JOURNAL

দগো বাংছাং গবেষণা পত্রিকা

Chief Editor (Hon.) : Dr. Upen Rabha Hakacham
Editors (Hon.) : Dr. Lalit Chandra Rabha
Dr. Dhaneswar Kalita

মুখ্য সম্পাদক (অবৈতনিক) : ড° উপেন বাভা হাকাচাম
সম্পাদকদ্বয় (অবৈতনিক) : ড° ললিত চন্দ্র বাভা
ড° ধনেশ্বর কলিতা



Dogo Rangsang Research Society
Reg. No. KAM-M/263/L/ 595 of 2015-16
দগো বাংছাং গবেষণা সমিতি

HYDRAULIC STRUCTURES IN ANCIENT INDIA: PEOPLE'S WISDOM

Dr. Samar Kanti Chakrabartty, Head, Department of History, Achhruram Memorial College, Jhalda, Purulia (Affiliated to Sidho-Kanho-Birsha University, Purulia, West Bengal, India)

Abstract

Water is the name of life. The dry climate and water scarcity are not phenomena of recent times. They existed in the past just as they do now. In ancient India, different water harvesting practices developed along with high levels of hydraulic structures. This article reviews studies of traditional water collection mechanisms, with two themes. It provides brief descriptions of unique water harvesting systems and the most critical debates on the issue of ancient India. The essay argues that interest in the subject must now attempt to chase great questions as well. Towards the end, it is argued that much insight and theoretical traction may be gained from the 'well water harvesting structures'. This work also explains how ecology-based societies were developed, and how they encountered social threats to maintaining the balance between men and the environment for the future generation.

Key Words: Agricultural Development, Indigenous people, rain-water, Hydraulic structure, Practices

Introduction

The civilizations of ancient India flourished on the banks of rivers and seas over the ages. The importance of water resources is highlighted in the hymns of the Vedas, the Puranas, the Upanishads, the epics, and other classical literature of ancient India. These records show the birth of hydraulic structures and water management systems and the awareness of ancient people prevalent in the country. The people of the Indus-Valley Civilization, Vedic Civilization, and those belonging to Maurya, the Guptas, the Cholas, the Pallavas, and other periods had achieved a high level of excellence in the use and management of water resources. The prime objective of the water management system in early India was to enhance the irrigation system in a decentralized manner. Perhaps this water management system was first implemented across the banks of the rivers in the study area to serve the interests of the local communities. Agriculture was the primary source of livelihood for people in the past. Even today, it is the principal source of income for millions of people worldwide.

Statement of the Problem

Traditional water collection systems can determine if it is possible to mitigate the enormous water crisis at present. Ancient hydraulic structures were formed and functioned well thanks to the comprehensive cooperation, supervision, maintenance, and topographical knowledge of the ancestors. In the early days, long-standing wars and conflicts created a chaotic environment that disrupted the smooth flow of water through the channels. Even minor irrigation systems were not regularly cleaned, and maintainers failed to repair the hydraulic structures owing to the age of decline of the particular kingdom. It is experienced that traditional knowledge-based water management was only appropriate for minor cultivation. In addition, due to the shifting of livelihood patterns of the communities' neglected the local irrigation systems. Irrigation projects, on the other hand, fail due to the patronage of village chiefs and local kings. Traditional knowledge deteriorated massively when extensive cultivation started without regard for the laws of nature. Moreover, natural disasters also hampered the proper functioning of water structures and management in early days. For example, in the Mayura era, Sudarshana Lake was one of the finest examples of this.

Objectives of the study

- Explain topography characteristics based on traditional knowledge.
- Identify the collective cooperation and wisdom of your forefathers.
- Explain how important the laws of nature are.

- > Depicting wars and conflicts hinders the socio-economic structures of communities.

Review of Literature

Anupam Mishra's pioneering work (2013) '*AAj Bhi Khare Hain Talab*' gives a detailed description about the hydraulic structures and its multiple uses and impact on the communities. A *Nagajasthi* or wooden pillar was set up in the middle of the *talab* by the local experts through the ceremony to measure water level of the pond/talab periodically. John M Fritz & George Michell (2017) has highlighted its geographical location, indigenous water harvesting practices, (aqueduct, stone-well, dug well, stepped well), royal's water tapping mechanism from the Tungabhadra rivers and surrounding hills in Vijayanagara. The 'city of victory' Vijayanagara is the growth of meeting not only for its historical importance; its remarkable landscape, the innovative agricultural method in the foothills of the empire, religious association, archaeological evidence, etc had made it an outstanding destination of international significance. Arjun Appadurai' pioneer work (1986) expressed the reality that nature may exist outside society, but natural resources are social phenomena treated by human beings to their benefit. Debasish Sengupta, Paramesh Goswami and Kalyan Rudra (2013) noted that ancient India artificially preserved rainwater by applying traditional knowledge and wisdom.

Research Methodology

Methods have been used to write this article that includes both requisite historical method as well as the basic primary sources. Apart from secondary sources like books, articles, relevant images and archeological sources have been used to find out the hydraulic structure of ancient India's past, and their resource evaluation management in the drought landscapes has been explained in a scientific manner. This study has used four methods; theoretical, observational, experimental and empirical.

Results and Discussion

There are four stages in the result analysis. There are three factors; topographical location, past and present performance analysis, and the number of beneficiaries. This study has investigated the water harvesting practices of some states like West Bengal, Bihar, Assam, and Meghalaya. Traditional water management practices are moribund in West Bengal, whereas Purulia is maintaining the traditional practice perfectly. On the other hand, North Bihar has also been following the same practices from time immemorial. Indigenous communities of south India and the north-western part of the country are trying to revive traditional practices on the basis of the topographical features of the study area, and some conservationists like Rajender Singh, Anna Hazare, and many more are raising their voices to retrieve dying practices on the basis of wisdom.

Table No. 1: Topographical location and Performance of the water Harvesting Management

Names	Location in Foothills	Status of the Past	Status of the Present	Beneficiaries Communities
Ponds, hapa, Johad, well, Step-farming	West Bengal	Fostered well	Almost dried up except Purulia	Santal, munda, Mahato, kumar & Kurmis
Ging	Jammu & Kashmir	Maintained well	maintaining	Balti, Boda, Bot, Bota
Kul	Himachal Pradesh & Uttarakhand	Maintained well	maintaining	Kinnaur, lahul, Pangi
Step farming	Arunachalpradesh, Nagaland	maintained well	maintaining	Aptani tribe
Bamboo Strip	Meghalaya, West Bengal and other North-eastern states	maintained well	maintaining	Modo, Mech, Naga, Lepcha etc
Khadin	Rajasthan	maintained well	Medium	Maldhari, Rabari
Kandi, Johar, panam Keni	Rajasthan & Maharashtra	maintained well	Medium	Maldhari, Rabari, Kuruma tribe
Virdha & Bawali	Gujarat & Rajasthan	maintained well	In moribund condition	Maldhari, Rabari, Bhil, Dholo Bhil
Pat & Kanath	Madhya Pradesh	maintained well	In moribund condition	Agariya, Andh, Baiga, Bhaina.

Eri	Tamil Nadu	maintained well	Medium	Aranadan, Eravallan, Irular, Kadar, Kammara, Adhiyan
Katre & Kere	Karnataka	maintained well	Medium	Adiyan, Barda, Bavacha, Bamcha, Bhil, Bhil, Garasia, Dholi Bhil
Johad	West Bengal	maintained well	Maintaining well in Purulia and Some part of Bankura, Birbhum, Jhargram	Santal, Munda, Kumar, Kurmis
Ahar-pyne	Bihar and West Bengal	maintained well	Limited in North Bihar and Purulia in West Bengal	Santal, Munda, Kumar, Kurmis, Mahatos

The above table shows the names of the water collection practices, the topographic location of the States, past performance vis-à-vis the several services of the traditional knowledge, the current scenarios, and the status of the water managers. This study looked at almost many traditional water collection structures in West Bengal, Bihar, Jharkhand, Meghalaya, Assam, etc. to collect authentic information on traditional water harvesting systems. In addition, it also examines many water management structures at the beginning of India.

Discourse on Hydraulic Structures

Ancient India had several types of water management systems like *johad*, *ahar-pyne*, *kund*, *hapa* (*hapa* means small pond and digs up in corner of field for soil moisture.), pond, *anicut*, *dam*, *bundh*, *indha*, *bawli*, *eri*, *pat*, *rapot*, *jalhara* etc.¹ Their techniques and structures were different due to the different configurations of the lands. These bear ample testimony to the technologies and their mosaic past based on the topographical features and climate of the region. The 'Arthashastra' refers to the method of lifting water from artificial water bodies like lakes, tanks, and wells.² It refers to making tiny heaps of sand before the end of the monsoon. Such rain gauges were used for farming and cultivation in Kerala. During monsoon season, the rainwater was trapped in the heaps to recharge groundwater levels. This practice became popular among the farmers to avoid the evils of the water crisis in drought-prone areas. This practice was also used to remove weeds and loosen up the soil to make it suitable for agriculture. Some water-harvesting management is mentioned below to clarify the theme of the work.

Halagatti is an ancient water-tapping practice. Embankments were constructed at different levels to detain rain-water that runs down the slopes. The aim, however, was not to stop all the water. The remaining water was released into the following field when the field was adequately wet. This method of outflowing water was called *halagatti*. The size and height of the mouth of the *halagatti* (waste-weir) practice were determined based on the rain and the slope. This is generally constructed at a slightly higher level than the field. Stones are laid on the side of the outlet as well as its base.³ These measures are followed for the conservation of topsoil and drought relief.⁴ The Arthashastra also mentions the different water harvesting systems prevalent in ancient India. In Sringerapur, near Allahabad (in the state of Uttar Pradesh), there existed a sophisticated water harvesting system that stored the flood water of the river Ganges on the natural slope of the land. Karikala Chola (c. 120 CE), the greatest among the early Chola Kings of the Sangam Age in South India, built the Grand Anicut or Kallanai (Dam) across the river Kaveri to divert water for irrigation and cultivation.⁵

Jhalara is an age-old water conservation method practiced in Rajasthan to cope with scanty rainfall. *Jhalaras* are typically rectangular-shaped step wells with multi-layer steps on three or four sides. These step-wells collect the subterranean water of an upstream reservoir. *Jhalaras* were built to ensure an easy and regular water supply for religious rites, royal ceremonies, and the daily chores of the local communities. The oldest step wells may date back to 550 AD. However, the most illustrious step wells were constructed in the medieval period. It is roughly estimated that more than 3000 step wells were constructed in two central northern states of India.⁶ The city of Jodhpur has eight such *jhalaras*, the oldest of which is the Mahamandir *Jhalara*, which dates back to 1660 AD. A large number of reservoir outlets were constructed in the tract between the Sutlej and the Ravi rivers in the Montgomery district

of Pakistan. These would be filled during a flood and be transformed into lakes. When the rivers remained dry in summer, the water of the lakes was used for irrigation using jhalara.⁷

The Ahar Pyne system is an indigenous irrigation technology that continues to irrigate areas of south Bihar in India. Nirmal Sengupta, in his article, 'Indigenous Irrigation Organization in South Bihar', has stated that it was introduced around 3000 years ago for tapping rain-water. Ahars (channels) are reservoirs with embankments on three sides and are built at the ends of drainage lines such as rivulets or artificial works like pynes.⁸ Pynes are diversion channels led off from the river for irrigation purposes and impounding water in the ahars. It is mostly to the credit of these that paddy cultivation has been possible in this region owing to the preservation of rain-water by ahar-pyne water management. The system attained its highest development in the district of Gaya. This article provides an account of the ahar-pyne systems in South Bihar and the need to build organizational and institutional capacities of civil society and government agencies to undertake ahar-pyne renovation and management. Nowadays, the ahar-pyne system has witnessed a tendency toward sharp decline, yet even today, it constitutes nearly three-fourths of the total irrigation facilities in South Bihar. More than sixty percent of these are defunct now, and the rest are poorly managed. Nirmal Sengupta has attributed factors to the decline of Ahar-pyne practice in South Bihar, such as the loss of interest among the zamindars (landlords) in maintaining the system and the introduction of a new system by the irrigation department of South Bihar in the 1960s.⁹

Johad, one of the oldest systems of conserving groundwater, has existed since ancient times in the Alwar district of Rajasthan. They are small earthen check dams that capture and store rain-water. Johad, popularly known as a small dam, was dug up to meet the water needs in the non-rainy season. It is a community-owned traditional rain-water principally used for agriculture.¹⁰ Nowadays, such water harvesting management is used for irrigation in several states like Haryana, Punjab, Rajasthan, and Gujarat. Generally, johads are built along the foothills and river basins. Sluice gates were built in every johads on the earthen-*bundh* to discharge water from the water body. Thus, the water-saturated land is then used for crop production. Archaeologists like Sunila Narin and Sunita Narin have dated that this crescent-shaped system of effective water management was introduced by the Paliwal Brahmins of Jaisalmer, Rajasthan, in the 15th century.¹¹

The following picture deals with the structural management of johad which managed the water-related needs in the states of Haryana, Uttar Pradesh, and Rajasthan many years ago. The covered area of johad varies from 2 hectares to 100 hectares in the Alwar district.¹² Essentially, the johad captures runoff water from monsoon floods and allows it to percolate down to lower fields during the dry months.¹³

Panam Kenies were used to store rain-water by the *Kuruma tribe* in Rajasthan. This water management system was also developed many years ago. Wooden cylinders are made by soaking the stems of today's palms in water for a long time so that the core rots away until only the hard outer layer remains. This system is used only for drinking water in the different parts of Rajasthan and Gujarat.¹⁴

In northeastern Meghalaya, a 200-year-old system of tapping stream and spring water using **bamboo pipes** is prevalent. The primitive tribes had developed this simple and effective method of water preservation for irrigation and drinking. Generally, water is collected using different sizes of bamboo pipes from the perennial springs of the hills.¹⁵ fewer watering crops are grown under this water management system. Drops of water are directly put into the roots of the plants. Nowadays, this age-old practice is followed by the farmers of the Khasi and Jaintia hills to cultivate nut orchards and black peppers.

The **Ramtek model** has been named after the water harvesting structures in the town of Ramtek in Maharashtra. It is a series of ponds designed to harvest the seasonal rain-water available in the ponds and lakes of the region. Ramtek management preserves runoff water and recharges the ground or earth during the monsoon. It has been maintained mainly by the *malguzari* (landowners) of the region.¹⁷ Nowadays, about 41000 hectares of agricultural land are being irrigated by this practice.

The **Pat system** had been built in the undulating terrain to divert water from hills-streams to irrigation channels. Such a practice was formed at the Bhitada village in the Jhabua district of Madhya Pradesh.

Diversion *bunds* are made across a stream by the people surrounding the *bunds*. The Pat channel passes through deep ditches, and then water is brought into the rice field through the stone aqueducts.¹⁸

The *Eri* (tank) is one of the oldest water management systems in Tamil Nadu. In most cases, an *Eri* or tank is excavated in the foothills. It is fed by the channels of the diverted river's water. The local people used it for multi- purposes, such as controlling the flood of the area, recharging groundwater, preventing soil erosion, and stopping the wastage of runoff water during the heavy monsoon. Even today, it is widely used for the same purposes.¹⁹ Tanks can supply water to the remotest villages for irrigation and other daily chores. Presently, this water tapping system is prevalent in many districts (Ramnathpuram, Tanjabbhur, and Pudukottai) of Tamilnadu.

The *Kund* is an old water-tapping practice. A plastered *kund* is so foolproof that not a single drop of water ever leaks or gets spoiled, and the water remains clean for the entire year.²⁰ The purpose of it is to harvest rain-water for drinking. *Kunds* dot the sandier tracts of western Rajasthan and Gujarat.²¹ According to Raja Sur Singh, the earliest evidence of this date was discovered in the village of Vadi Ka Milan in the year 1607 AD. Anil Agarwal and Sunita Narain, in their edited book, '*Dying Wisdom: Rise, Fall and Potential of India's Traditional Water Harvesting Systems* (1997) have described in detail the '*community kundis*' that had been built by collective initiative.²²

The excavation of ponds or tababs for tapping rainwater is one of the oldest practices in our country, initiated in very early ages. Anupam Mishra's pioneering work, '*AAj Bhi Khare Hain Talab*' gives a detailed description of its multiple uses and its impact on the lives of the communities. Of course, individual homes in the drought-prone regions of the country have their smaller talabs or ponds for bathing, clothing, fishing, and other daily chores.²³ Besides, this practice was/is found around villages, homes, temples, mosques, and forts. A *Nagajasthi*, or wooden pillar, in the middle of the *talab* was set up by the local people during the ceremony to measure the water level of the pond periodically.²⁴

The traditional eco-friendly systems are viable and cost-effective alternatives to rejuvenate India's depleted water resources.²⁵ These structures, along with modern rainwater-saving techniques, such as percolation tanks, injection wells, and subsurface barriers, can be the answer to India's water scarcity. The indigenous people of ancient India had exercised the traditional water practices, and such old systems formed and operated on the basis of 'laws of nature'.²⁶ Arjun Appadurai's pioneer work (1986) expressed the reality that nature may exist outside society, but natural resources are social phenomena treated by human beings to their benefit.²⁷

Conclusion

This paper attempts to unravel the awareness of indigenous people related to various forms of water preservation systems prevalent in ancient India. Many societies flourished on the banks of rivers and other water bodies in the past, and their fate was essentially linked with effective water hydraulic engineering. Historically, many communities such as Maldhari, Rabari, Gond, and others relied heavily on the various services provided by water bodies. Many kingdoms in ancient India had developed various water management practices in the past and had maintained them well in a decentralized manner to meet local needs without compromising the availability of water resources for future generations. Currently, traditional water harvesting systems (Virdha, Kanath, and Johad) are on the verge of extinction, and many old hydraulic structures have been depleted. The British government implemented an extra tax on water bodies, and it caused a disruption in traditional water conservation systems. During British rule, a whole water-network system developed against individual water harvesting practices. This change not only destroyed ancient hydraulic structures but also made them difficult to retrieve. By demonstrating the ancient water conservation systems, the common people took on the responsibility of public welfare.

Acknowledgement

I am extremely thankful to Professor (Dr.) Pradip Chattopadhyay, Dean of Arts of the University of Burdwan and express my deep respect to Dr. Ranjan Chakrabarti, former Vice-Chancellor, The University of Vidyasagar for facilitating this study. I am also grateful to the editors of DRSR for giving me an opportunity.

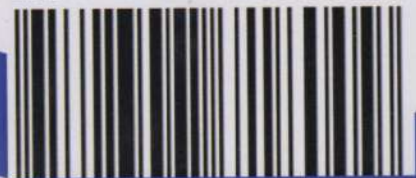
References

1. Sengupta, D., Goswami, D. & Rudra, R. (2014) , “Water”. Avenal Publication: Burdwan, 2014, PP. 211-22 (see detail in A. Agarwal and S. Narain, S. (ed.), (1997), *Dying Wisdom: Rise, Fall and Potential of India's Traditional Water Harvesting Systems*, Center for Science and Environment, New Delhi, PP.73-115.
2. Shah, J. “*The Kautilya's Arthashastra*”, (2014), Jaico Publishing House: Mumbai, P.85
3. Krishna, N. and Sing, A. (2014) (ed.), *Ecological Tradition of India*, C.P.R. Environmental Education Center of Excellence of the Ministry of Environment and Forests, Government of India. P.9.
4. Sengupta, N. “*The Indigenous irrigation Organization in South Bihar*”,(1980) *Indian Economic and Social History Review*, Vol-XVII, NO. 2, PP. 157-189
5. Iyengar, V. “*Waternama, A Collection of Traditional Practices for Water Conservation and Management in Karnataka*”, (2007), Communication for Development and Learning: Karnataka, P. 26.
6. Fisher, M.H. “*An Environmental History of India: From Earliest Times to the Twenty-First Century*” (2018), Cambridge University Press: UK, First Published P. 36
7. Agarwal, A and Narain, S. (ed.), (1997), “*Dying Wisdom: Rise, Fall and Potential of India's Traditional Water Harvesting Systems*”, Center for Science and Environment, New Delhi, 1997, p. 229.
8. Rangarajan, M.& Sivaramakrishnan,K. (eds.), (2012), “*Indian Environmental History: From Ancient Times to Colonial Period*”, Vol. I, Permanent Black: New Delhi, P. 41.
9. Sengupta, N. op.cit., PP. 161-175.
10. Gupta, S. (2011), “ *Demystifying 'Tradition': The Politics of Rainwater Harvesting in Rural Rajasthan*”, India, Vol.4, Issue-3, PP. 347-364.
11. Kashwan, P. (2006), “*Traditional Water Harvesting Structure: Community behind 'Community'*”, *Economic and Political Weekly*. Vol. 41, No. 7, PP. 596-598.
12. Agarwal, A. and Narain, S. (1997), “ *Dying Wisdom: Rise and Fall of India's Traditional Water harvesting System*”, Center for Science and Environment: New Delhi, P. 129.
13. Sengupta, N.op.cit., P.182.
14. Gupta, S. op.cit., P. 359.
15. Kashwan, P. op.cit., PP. 599-601.
16. Fritz , J.M & Michell, M. (2017), “*Hampi Vijayanagara*”, Jaico Publishing House: Mumbai 2017, PP. 29-33.
17. Agarwal, A. and Narine, S.op.cit., PP. 177-180.
18. Pant, N. (1998) “*Indigenous Irrigation in South Bihar: A Case of Congruence of Boundaries*”, *Economic and Political Weekly*, Vol. 33, No. 49 (Dec. 5-11), PP. 3136-3137.
19. Jain, S. K., Agarwal, P. K., and Singh, V. P. (2007), “*Hydrology and Water Resources of India*”, Springer Science & Business Media, Dordrecht, P. 45
20. Sengupta, D., Goswami, D. & Rudra, R. (2014) , “Water”,PP. 211-22.
21. Gupta, S.op.cit., P. 26.
22. Agarwal, A. and Narain, S. op.cit., P.13.
23. Mishra, A. (2013), “ *Ajj Bhi Khare Hain Talab*”, (Hindi), Rajasthani Granthahar: Jodhpur, Third revised edition, PP. 38-43.
24. Ibid. PP. 76
25. Trivedi, A. (2006), “*Management of Environment Through Ages, (History of Ecology and Environment: India)*, International Book Distribution Company: Lucknow, PP. 22-24
26. Niranjana Pant & R.K. Verma, (eds.), *Tanks In Eastern India : A Study in Exploration*, IWMI, Tata Policy Research Programme & Center For Development Studies, 2010, PP. 20-30.
27. Appadurai, A. (1986), *The Social Life of Things: Commodities in Cultural Perspectives*, CUP, P.1



Published by Dr. Angshuman Das, Secretary,
Dogo Rangsang Research Society, Guwahati &
Printed at Dream Graphics, Naokata, Tamulpur (BTR), Assam

ISSN 2347-7180



Cover Designed at Dream Graphics by Kamal K Sarmah



ISSN : 2347-7180

(A Bilingual Research Journal, Indexed in UGC-Care list)

DOGO RANGSANG

Research Journal, Vol-13, Issue-6, No. 09, June 2023

দগো ঝাংছাং

CHIEF EDITOR (HON.)
EDITORS (HON.)

মুখ্য সম্পাদক (অবৈতনিক)
সম্পাদকদ্বয় (অবৈতনিক)

: Dr. Upen Rabha Hakacham
: Dr. Lalit Chandra Rabha
: Dr. Dhaneswar Kavitha
: ড° উপেন ঝাভা হাকাচাম
: ড° ললিত চন্দ্র ঝাভা
: ড° ধনেশ্বর কলিতা

A Peer Reviewed Bilingual Research Journal
(Indexed in UGC-CARE List)

ISSN 2347-7180

DOGO RANGSANG RESEARCH JOURNAL

দগো বাংছাং গবেষণা পত্রিকা

Chief Editor (Hon.) : Dr. Upen Rabha Hakacham
Editors (Hon.) : Dr. Lalit Chandra Rabha
Dr. Dhaneswar Kalita

মুখ্য সম্পাদক (অবৈতনিক)
সম্পাদকদ্বয় (অবৈতনিক)

: ড° উপেন বাভা হাকাচাম
: ড° ললিত চন্দ্র বাভা
: ড° ধনেশ্বর কলিতা



Dogo Rangsang Research Society
Reg. No. KAM-M/263/L/ 595 of 2015-16
দগো বাংছাং গবেষণা সমিতি

SORROW OF SANDBARS: UNDERSTANDING THE HUMAN ROLE IN CHANGING ENVIRONMENT OF DAMODAR RIVER, INDIA

Samar Kanti Chakrabartty Head, Department of History, Achhruram Memorial College, Affiliated to Sidho-Kanho-Birsha University, Purulia, West Bengal, India samarkantichakrabartty@gmail.com

Abstract

Sandbars are narrow ridges of sand formed by the river system in the Bengal delta in eastern India. Some sandbars are often found in the middle of the Damodar River, and they can serve as an essential habitat for some people and animals. Since the beginning of time, the Damodar River has been known for its sandbars (Sorrow of Bengal). 'Sandbars' have been colonized in various stages after the partition of India in 1947. Prior to partition, they were wide fields covered with grass and wild bushes. This essay demonstrates how marginalized Bangladeshis have been living on sandbars while dealing with a variety of problems, including storms, floods, soil erosion, and a lack of access to basic amenities like water, electricity, medical care, as well as connectivity with the outside world. Moreover, sandbars are often isolated from the mainland, making it harder for people to access necessary services such as education and employment. Despite these challenges, many refugees have learned how to adapt to living on passing sandbars. It also explains how they often develop unique techniques and methodologies for mitigating the effects of natural disasters. Overall this research demonstrates that assessments of vulnerability and insecurity are arbitrary and insignificant, however immediate survival is very crucial.

Keywords: Migration, Environmental-crisis, Sandbar, problem, Land-accretion, Refugees

Introduction

EKISTICS first provides background information on the region, the scope of the authority of Damodar Valley, the study's findings and recommendations, and finally the case for a rehabilitation programme for people from submerged lands. The source of the Damodar River is situated around 200 miles west of Calcutta and flows through the Indian states of Bihar and West Bengal. Despite its tiny size (9400 square miles), the Damodar Valley is abundant in natural resources. Nature has provided the valley with the land, water, minerals, and labour it needs to be prosperous. But much of the land particularly in the upper valley is deteriorating rapidly unless it is reconditioned erosion will spread to its lower reaches ultimately the whole valley will be destined to become desert.¹ Due to this, numerous sand bars appeared on the Lower Damodar river's edges as well as in the middle, and the same process is still occurring today. After two steps partition of India in 1947, these alluvial river beds were acquired by empty-handed refugees, and they played a crucial role in converting the remote land accumulations into productive and livable landscapes for their immediate survival. But there are numerous problems, including safety concerns during storms, a lack of access to basic amenities such as water, electricity, and medical facilities, and challenges in transportation. Sandbars are prone to flooding, and people living in these areas have to frequently evacuate their homes during natural disasters. Migration communities from Bihar and Bangladesh settle on the sandbar despite the environmental dangers because the soils are productive and because untitled land is less expensive than the main land.

However, these sandbars are curved or patchy landscapes. Sand bars fluctuate frequently, forcing vulnerable people to move 2-4 times in 15-16 years due to their fluctuating nature.² Their destiny is their present and future gift; they have no voice or option. The inhabitants of the sandbars are stateless and unable to integrate into "main land society" because to their acute destitution.³ Refugees from Bangladesh had a steady existence and were considered as full citizens of Eastern Pakistan before to division. At the same time, indigenous populations in West Bengal used the alluvial land accretions of the Lower Damodar River as pasture fields. In these sand bars, immigrants are dealing with severe environmental problems and socioeconomic hardship as a result of the pain of partition.⁴ This article describes the environmental difficulties that refugees and native submerged settlers deal with on a daily basis on the erratic terrain of Lower Damodar. Still, refugees and local outcasts must

choose the running land accretions as a point of entrance where there are ongoing threats of storms, floods, and land erosion as well as a lack of connectivity, access to healthcare, education, and other essentials.⁵ The capacity of those residing on the sandbars to adapt to what is typically perceived as an unstable environment is a problem that merits more investigation. The investigation detailed in this paper started with a series of queries about potential residents' perceptions of the sandbars as a safe location to live. Why, given the extreme insecurity, do individuals choose to live in the remote environment of sand bars? How many options do they have when choosing a home? Do the residents of sandbars consider them to be permanent homes or do they utilize them as a launching pad to travel to other locations?

Statement of the Problem

In late colonial West Bengal, this approach explains the paradoxical relationship between partition and environment. This study investigates why local outcasts and refugees must choose the unstable land accretions (sandbars) as a point of entrance into a region that is continuously threatened by storms, floods, and land erosion as well as by a lack of connectivity, access to basic services like healthcare and education, and other necessities. Despite these difficulties, many Bangladeshi refugees choose to settle on the perilous sandbars, where they develop their ability to adapt to a changing environment. They frequently create original methods and tools for reducing the consequences of natural calamities while preserving their way of life and dwellings. This work needs more research is how well those living on the sandbars can adjust to what is often seen as an unstable environment. This paper's inquiry began with a series of questions on how prospective residents felt about the sandbars as a safe place to live. Why do people decide to live in the isolated sand bar area considering the great insecurity? This study shows that judgements of security and vulnerability are arbitrary and unimportant, but that immediate survival is essential.

Objectives of the Study

- > To clarify the paradoxical connection between changing fluvial environment and partition.
- > It explains why refugees choose to reside on the perilous sandbars.
- > Determine the causes of their physical and social isolation.
- > Examine their various viewpoints, resource management strategies, and survival tactics.

Review of Literature

According to Haroun er Rashid (*Geography of Bangladesh*, Dhaka, 1991, p. 18), "Char fields are perilous territory all year long, but especially during the rainy season. These 'chars' are the emblem of uncertainty, poverty, vulnerability, border disputes between states and countries, and a lack of governance leading to the exercise of different forms of crime and criminality." In her article, (*No Voice No Choice*) Gineya Mukherjee makes a very apparent discovery. She writes that due to the continuous emergence, submergence, re-emergence, and re-submergence of the 'chars', we find that the people living in the 'chars' (the erosion victims) suffer from the "settlement>displacement>re-settlement>re-displacement" ('SDRR') syndrome, where hazards (mainly in the form of river-bank erosion and inundation) easily transform them elsewhere.

Morisawa (*Rivers: Form and Process*, London: Longman, 1985) demonstrates how sandbars are referred to technically as "bars," "river islands," and "sloughs." Additionally, he has discussed the various characteristics of the residents of the sandbars. Sandbars and other associated wetland ecosystems are used by people in different ways in different countries. In the modern world, river islands are good candidates for environmental protection since they contain areas with uncommon and unusual plants and animals. Public leisure activities including boating, fishing, and hunting for game are frequently conducted in these regions. In this regard, M. Chowdhury (*Women's Technological Innovations and Adaptations for Disaster Mitigation: A Case Study of Charlands in Bangladesh*, 2001) stated that "lost people"—stranded Afghan refugees of various ethnic backgrounds who were "rediscovered" by the larger humanitarian and media worlds—find refuge on the sandbars in the Pjjang River on the border between Afghanistan and Tajikistan. In this context, M. Chowdhury, (*Women's Technological Innovations and Adaptations for Disaster Mitigation: A Case Study of Charlands in Bangladesh*, 2001), said "lost people"—stranded Afghan refugees of various

ethnic backgrounds who were "rediscovered" by the larger humanitarian and media worlds—find refuge on the sandbars in the Pjang River on the border between Afghanistan and Tajikistan. Samar Kanti Chakrabarty, (*A History of Receding Wetlands in West Bengal; Ecology, society and Environment (1947-2000)*), Unpublished Ph.D Thesis, The University of Burdwan, 2021) himself has investigated the misery of the people of the sandbars. Kumkum Bhattachayya, (*The Lower Damodar River, Understanding the Human Role in Fluvial Environment*’, Springer, 2011) has pointed out many aspects of changing fluvial environment of Lower Damodar basin in West Bengal.

This work explains that nowadays, the most susceptible refugees are facing the same plight, and they have no direct road communication. They have to cover a distance of 1-2 miles on a sandy-path every day to communicate with the nearest towns.³³ Moreover, they cannot avail of government facilities like medical assistance, education, the transport system, ration facilities, etc. They suffer a lot from environmental calamities and identity crises. Generally, they are poverty-stricken people, and the number of dropout students, child labour, and illiteracy is very high and increasing at an alarming rate. Their existence is always fraught with uncertainty and insecurity. From dawn to dusk, they have to work hard in the agricultural field, fishing, selling vegetables, as labourers, and so on. Very often, they become victims of sexual harassment.

Research Methodology

The present study's foundation is made up of four sets of data that have been gathered. It has been extensively utilized to follow the shifting course of the Lower Damodar and its flood history to use archived data from historical maps, official reports, legal deeds of refugees and *pattas*, and other necessary records. To trace the history of embankments, the original control structures, archival data has once again been utilized. The Damodar Valley Corporation (DVC), the Irrigation and Waterways Department (I&WD), and other departments have all provided quantified information on stream flow, sedimentation, rainfall, and cross sections.

In the current study, there are no specific models that can be replicated. Although the benefits of the DVC have been highlighted in several official papers and publications, no attempt has been made to evaluate the project's other facets. Numerous studies on flow regimes, riparian ecosystems, and sedimentation patterns below key control points have been conducted and published in numerous nations. None of these, however, highlight the dangerous sandbars that are still cut off from the mainland or discuss the social significance of local control structures in the riverbed. There is no a priori model for the current study because the emphasis is on socio-economic difficulties that arise from control structures. This study has placed a strong emphasis on field methods for a number of reasons. First off, because these micro landforms are so dynamic, multiple field trips are necessary. Second, field survey techniques were essential for the gathering of active data from repeated trips because air pictures and Land sat imagery were unavailable for all sections of the river or were inaccessible due to these issues. Third, government organizations do not have access to ongoing data on land usage in the riverbed. Due to the importance of this topic in this study, data on land use and river bed landscape characteristics were gathered through several field visits.

Results and Discussion

According to the results of the current study, the Damodar River's flood characteristics are quite unusual and determine the safety and unpredictability of life on the sandbars. Additionally, it learns that poor settlers and Bangladeshi refugees relocate to alluvial plains to meet their socioeconomic requirements rather than seeing them as permanent or transient. In other words, by describing how people, from refugees to local settlers, driven by a variety of cultural, economic, religious, and political forces, have changed the fluvial landscape and are living with hazards, this research reviews the impacts of control structures in the downstream environment and also attempts to understand anthropogenic changes to the river regime.

The results of the current study demonstrate that colonial and postcolonial artificial control techniques have both been useless and successful in accomplishing the desired socioeconomic goals, as demonstrated by the history of continuous flooding. (ii) In reality, sandbars are portions of the

that have been used carelessly and without regard for the surrounding ecosystem. (iii) This research reveals that the rapid anthropogenic stabilization of the river bottoms is to blame for the eroding sandbars and escalating channel degradation. It demonstrates how the fluvial ecology has been impacted by partition and how various steps have been made to regulate the river's mood. Last but not least, arbitrary changes to the river's path are enhancing the Damodar River's peculiar character.

Why Refugee Settled on Sandbars

After Partition, Bangali Hindus from Bangladesh (Formerly Eastern Pakistan) started migrating to this part of India in quest of a quick source of income and social security. The governments labeled all the sandbars as *khaslands* (government property). The newly relocated immigrants and other local residents, on the other hand, believed they have no legal rights and that these isolate landscapes are appropriate for their relocation.⁶ A few rehabilitated individuals displayed their *patta*, or legal documents, during the field survey. The migration into southern West Bengal over the Bangladesh border greatly increased after the Liberation Movement of 1971. Migration on sandbars accelerated as a result of the movement.⁷ However, in the vast Lower Damodar Basin (LDB), refugees have experienced knowledge on ecological management to prevent the occurrence of catastrophic disasters. The list of explanations for why refugees are relocating to the unstable sandy areas includes their practical solutions and resources based knowledge management :- (i) Grasses and soil-binding shrubs are allowed to grow to protect land erosion. (ii) Jute is grown alongside the banks that are prone to erosion. (iii) They cultivate different types of crops throughout the year on higher land above the inundation level. (iv) On the unauthorized (newly established) sandbar plots, more crops are cultivated. The local government is more accommodating to refugees. The cost of land is lower than on the mainland, making it simple for local settlers and refugees to buy land property for farming without encountering any administrative obstacles. They therefore give immediate security top priority before considering the study area's lack of protection. Thus, they are enabled them in the vulnerable parts of the changing fluvial environment of the Damodar river. In order to appropriately address them, the notion of refuge must be defined in this context.

The concept of a refugee is a legal, political, cultural, and sociological category). The technical meaning of the term "refugee" was developed between the two world wars.⁸ The 1951, "UN Convention Relating to the Status of Refugees", emerged due to the European experience of the Second World War. The Government of India's notes also refer to them as 'refugees'. A refugee is defined in Article 1 of the 1951 UN Convention as amended by the 1967 Protocol as: "A person who, owing to a well-founded fear of being persecuted for reasons of race, religion, nationality, membership in a particular social group, or political opinion, is outside the country of his nationality and is unable or, owing to such fear, is unwilling to avail himself of the protection of that country."⁹

The partition of India in 1947 gave birth to the refugee problem in West Bengal. The first phase of the refugee influx perhaps began after the *Noakhali* riots in 1946 and continued until March 1977.¹⁰ The Hindus who had crossed over to India from East Pakistan were issued a receipt for their entry into the country. These people are considered legal refugees. Between 1947 and 1952, millions of refugees migrated from erstwhile East Pakistan (present-day Bangladesh) to West Bengal. In 1947, the census found that 26.6 percent of what had become East Pakistan was Hindus. It was officially reported that 41.17 lakh refugees escaped to India differently between October 1946 and March 1958. Nearly 31.32 lakh of them are estimated to have remained in West Bengal, while the rest dispersed throughout India. From 1964 to 1970, 18.14 lakh refugees were displaced from Eastern Pakistan, and they chose to stay in West Bengal.¹¹ During the Liberation Movement of Bangladesh, West Bengal received 95 lakh people. Of course, a hefty proportion was settled in the Calcutta Metropolitan District; the third most significant concentration, after 24 Parganas and Nadia. But there were fewer opportunities for farming and fishing in the camps in urban and semi-urban areas for the Dalit Hindu refugees. Hence, a sizable number of refugees rejected this dole-sustained existence under the government's camps, and they searched *chars* lands/sand bars in the lower Damodar basin, which are fit for cultivation, animal husbandry, fishing, etc for immediate survival.¹²

The silty and sandy sandbars are physically on the border between the realms of land and water; they are the 'edges' where the cultures and ecologies of the two spheres collide and are separated from human habitation.¹³ The relationship between "partition" and "environment" has received the least attention in debates despite the fact that human use of these borderlands raises a wealth of metaphors and unique concerns of environmental dynamics and management. This essay is especially interested in investigating how well the disadvantaged can adapt to fluvial environments. In addition, the overall setting for this study is one of poverty and a lack of options.

Partly Water and Partly Land: Sandbars

'Ecologically, the "sand bars" of the Lower Damodar Basin in the Burdwan and Bankura districts of eastern India, are a singular illustration of the river's inner-delta development process. During the monsoon, the waves of rivers regularly create and erode sandbars. A significant area of sandbar is said to have been examined and inhabited in 1842, a few miles upstream of Burdwan (Ricketts, 1853).¹⁴ Captain C.H. Dicknes (1853) examined these grounds in 1854 and produced a map of them. These lands were likely developed as a result of the disastrous flood of 1840. Large floods have been demonstrated to alter the location and large floods have been proven to alter the size and placement of the sand bars along this section of river. There were more than 38 flowing sandbars between 1929 and 1943 that were all covered with a variety of bushes and grasses. According to the mouza maps surveyed between 1954 and 1957, some of the sand bars have developed a distinct shape. The government had resettled some refugees on the sand bars, which have been impacted by human involvement to the present day.¹⁵ Before the partition, such isolated landscapes had been a suitable abode for wild animals, birds, rare species of plants, and shrubs, including invisible creatures.

The Ganges, Brahmaputra, and Meghna rivers work together to form the biggest delta on earth in the eastern India, and their integrated river system is a crucial element of the Bengal Delta's scenery. The amount of silt carried by these rivers, which make up roughly 25% of the global total, and wind through the delta in countless branches before emptying into the Bay of Bengal, is the highest of any river system in the world. On its way to the Bay of Bengal, silt is thought to settle on the deltaic plain at a rate of about 40 billion cubic feet per year, forming the vast *chars* and *diaras* that make up the deltaic plain.¹⁶

Technical terms for sandbars include "bars," "river islands," and "sloughs." People's utilization of sandbars and other related wetland environments differs greatly from nation to nation. In the modern world, river islands are good candidates for environmental protection since they contain areas with uncommon and unusual plants and animals. Public leisure activities including boating, fishing, and hunting for game are frequently conducted in these regions.¹⁷ In this context, the "lost people"—stranded Afghan refugees of various ethnic backgrounds who were "rediscovered" by the larger humanitarian and media worlds—find refuge on the sandbars in the Pjäng River on the border between Afghanistan and Tajikistan.¹⁸ Few people are aware that there exist river islands and sandbars where people live, despite the fact that millions of people in low-lying regions of developing countries, such those in the Bengal delta, do.

The Bengal delta in South Asia is perhaps the best-known example of sandbars since it was formed by river-borne sediment from the Himalayas. Kumkum Bhattacharyya's 2010 study (The Lower Damodar) demonstrates how, recently, less flooding has caused the Lower Damodar River, one of the several important streams that feed the delta, to become increasingly "colonized" with sandbars.

¹⁹ Due to the significance of riparian zones to the lives and economics of the nation, the sandbars of Bangladesh further east have been the focus of resource management and policy discussions. According to Baqee, the pioneer of research into the human occupancy of Bangladeshi chars, they house "some of the most desperate people in the country," who, through their risk-taking behaviour, have established a unique subculture separate from the ways of the majority of the population.²⁰

The shifting sandbars and their people are mostly invisible to the larger economy and society in the Lower Damodar Valley, an area with high levels of urbanization and very prosperous agriculture.²¹

The locals exclusively utilized sandbars for pasture and regarded those uncultivated fields. In most cases, refugees occupied these areas and turned them into "green landscapes." The Bhasapur Sand Bar and adjacent sand bars are some of the best examples of dangerous terrain where people are

surviving using knowledge of resource management and sustainable development. For the sake of this study, some special featured sand bars like Bhasapur, Bara Mana, Shikarpur, Rangamati-Kenety of the Lower Damodar Basin (LDB) in Bengal delta of eastern India have been chosen as case studies.

Study Area: Human's Perceptions and Management

The term "perception" refers to both the way in which the senses react to outside stimuli and the deliberate effort of registering and filtering out specific occurrences. Culture, sex, education, upbringing, familial standing, neighbourhood standing, length of stay, and environmental attitudes are just a few of the variables that influence perception. There is a discernible difference between how explorers, colonists, and locals with different backgrounds and experiences evaluate the same landscape.²² Although Brookfield included perception in the approach of cultural and historical geography, the idea of perception may be applied to a number of different branches of geography, including human geography and geomorphology. He makes the distinction between "environmental perception" and the "perceived environment." The entire "monistic surface" on which judgments are made, encompassing natural and non-natural, visible and non-visible, geographical, political, economic, and sociological components, is referred to as the perceived environment.²³

Bhashapur Sand Bar

This sandbar is located under the jurisdiction of Golshi block in Burdwan district. It came into prominence after independence. Almost all Bengali Hindus of Eastern Pakistan and other local settlers of West Bengal (99%) have been living on the sand bar. There are several refugee colonies established on the sand bars of Lower Damodar Basin (LDB). On the right side of the river are seen several sand bars such as *Ranghamati, Nityanandapur, Chhoto Mana, Bara Mana, Patashpur, Kaitadi, Char, Gobindapur, Chair-Gaitanpur, Panchpara, Salkhara* etc., are situated on the right bank of the river. Whereas *Telenda Mana, Ramakrishna Palli, Pallishri and Sitarampur Mana, Lakshminipur, South Bhashapur, Satyanandapur-Kalimohanpur, Gaitanpur and Fakirpur sand bar* etc., are located on the left bank of the Lower Damodar river. On these sandbars, more than 150,000 people have been residing. In addition to these, seven sand bars are also located in the centre of the river. Their livelihood patterns and ecological management are different than other marginal people of the river. Every day life on these seven sandbars is very difficult for the residents. Such as susceptible people have to cross half km every on sand road to communicate local towns.²⁴ Within 20 km, there are no primary medical health centres or educational facilities. Patients die while travelling. The percentage of students that drop out is dramatically rising. There are no fundamental means of support. Because of this, there is a significant rate of labour migration, and child labour is always growing. These *sand bars* depicts in the following map to show its geographical location where refugee colonies were established after two-steps-partition.

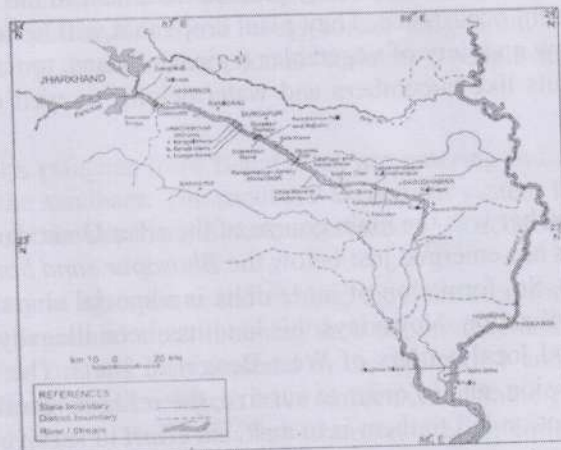


Fig. 1 Location of sand bars where refugees are predominant population

The sand bar's evolving biological configuration since 1930 is depicted on the lower map of the Baramana sand bar, which is under the control of the Bankura district. Here, we can observe how the cultivated area, human habitation, and roadways on the sand bar have occasionally changed sites. This occurs frequently in nature because of all the sand bars. Ecologically, the sand bar was joined to Sri Rampur's mainland in the 1960s under the Durgapur subdivision of Burdwan district in West Bengal. But the disastrous flood of 1978 cut it off from the mainland. In more recent times, it has reunited with the mainland once more. After 10 to 15 years, this type of ecological change has taken place in all of the Damodar basin's designated sandbars. Although the size of these sand bars varies, their landscape features are often the same.

It is a sand bar or land accumulation that is dominated by refugees. Due to issues with water and soil erosion, the area on this sand bar was unsuitable for agriculture until 1970. It was then a desolate land. When the refugees arrived, they started establishing bushes that would hold the soil together and plant trees on the edge of sandbars to stop land erosion. The silt deposited during the flood each year makes the entire land accretion fruitful. Around here, people grow a variety of crops all year round.²⁵ In the 1970s, farmers would only plant jute because there was no irrigation infrastructure and the sand bar was unsuitable for growing vegetables and legumes. They have been able to grow a variety of crops year-round since the 1980s because to the growth of the irrigation infrastructure, and the area along riverbeds is now suited for high-value crops owing to silt disposition every year. Today, every square inch of the land is used for agriculture, producing a variety of crops, including traditional ones as well as pulses, oil seeds, and vegetables.²⁶ In the vast Lower Damodar Basin (LDB), Bangladeshi refugees have experienced some ecological management to prevent the occurrence of catastrophic disasters. Their pragmatic measures and sensible actions include: (i) Grasses and soil-binding shrubs are allowed to grow on the erosion-prone banks. (ii) Jute is grown along banks that are prone to erosion (iii) They cultivate different types of crops throughout the year on higher land above the inundation level. (iv) On the unauthorized (newly established) sandbar plots, more crops are cultivated. However, the sand bar's land is ephemeral and vulnerable. High-yielding rice varieties (HYV) are grown here as silt de-poisoning progresses. In order to prevent crop loss, less important crops and vegetables are typically produced in the flood-free perimeter zone. An additional common employment among the locals is raising cattle. Schools and concrete homes are situated in elevated regions where they are hardly ever affected by flooding. In 1956, refugees started inhabiting the Telenda char/colony under the Mejia block of Bankura district. A short canal divides this sandbar into two halves. 28 households made up the *char*/sand bar's entire population of roughly 225. Previously, vegetation and wild grasses covered practically the whole sandbar.²⁷

The refugees arrived here and made the bushes bearable by cutting them back. For the purpose of reducing soil erosion, particularly during floods, they planted trees next to the chars. Here, during the rainy season, floods are a frequent occurrence. They plant crops that will be ready for harvest before the flood's onslaught. They grow a variety of vegetables (spinach, beans, tomatoes, carrots, potatoes, cabbage, cauliflower, etc.), fruits like cucumbers and watermelons, as well as rice and jute in the flood-free areas.

Shikarpur Sand Bar

Ecologically, the Shikarpur sand bar was the main course of the river Damodar until 2000. Recently, a group of small *chars*/sandbars has emerged just below the *Bhasapur sand bar* and together they are called *Shikarpur* land accretion. So, formation of inner-delta is a special character of the river and it continues since the dawn of civilization. Nowadays this land has been illegally occupied by the new infiltrators from Bangladesh and local settlers of West Bengal in India. The Bhashapur sand bar's eastern edge is still prone to erosion, and in order to survive, the refugees must adjust to the shifting fluvial environment. The only option left to them is to make an effort to survive.

Rangamati-Kenety Sand Bar

Rangamati-Kenety (RK) Char is under the jurisdiction of the Sonamukhi Block of Bankura district. Its width is about 2.5 km and its length is 3.5 km. This sand bar lies in the dam area of Rondiha Weir. In 1920, there were only fragmentary transit sandbars.²⁸ By 1957, land was added to the existing bars despite shape distortion and size reduction in some portions of the bars. Some new bars also appeared towards the left bank.²⁹ The 1978 floods caused extensive damage to these bars, and they were reduced in size. The thalweg has changed positions several times between 1921 and 2003 but has retained its braided channel pattern.³⁰ The households in R.K sandbar are about 800, and there have been about 15,000 people. Earlier, jute was a major cash crop when the water crisis was massive. Then, rice was the main crop in RK before the 1990s.³¹ Nowadays, potato cultivation has become more popular than the other crops in the winter season. Almost all types of vegetables are grown here because there are ready markets for them at Sonamukhi, Panagarh, Bankura, and Durgapur. Recently, marigold flower cultivation has become very popular in RkK sandbar. For more clarification, flower cultivation is now a common cash crop on all the sandbars in the Lower Damodar Basin. Generally, sandy soil is very suitable for marigold cultivation. Such flowers are grown at a low cost and in a short period.

Char lands are risky territory throughout the year, especially during the rainy season. These "chars" are the emblem of uncertainty, poverty, vulnerability, border disputes between states and countries, and a lack of governance leading to the exercise of different forms of crime and criminality. Due to the continuous emergence, submergence, re-emergence, and re-submergence of the 'chars', we find that the people living in the 'chars' (the erosion victims) suffer from the "settlement>displacement>re-settlement>re-displacement" ('SDRR') syndrome, where hazards (mainly in the form of river-bank erosion and inundation) easily transform them elsewhere.³² Nowadays, the most susceptible refugees are facing the same plight, and they have no direct road communication. They have to cover a distance of 1-2 miles on a sandy-path every day to communicate with the nearest towns. Moreover, they cannot avail of government facilities like medical assistance, education, the transport system, ration facilities, etc. They suffer a lot from environmental calamities and identity crises. Generally, they are poverty-stricken people, and the number of dropout students, child labour, and illiteracy is very high and increasing at an alarming rate. Their existence is always fraught with uncertainty and insecurity. From dawn to dusk, they have to work hard in the agricultural field, fishing, selling vegetables, as labourers, and so on. Very often, they become victims of sexual harassment.

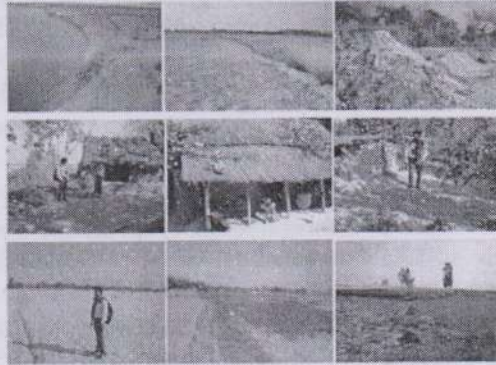
A Lesson of Survival Strategies

Analyses of human perceptions and behaviours in many environmental contexts, particularly those involving the natural world, have been comprehensive. Our understanding is that flood occurrences and the ensuing bank erosion are directly related to perceptions of security in the sand bars. However, the majority of the residents of Damodar have also dealt with social unrest brought on by political unrest, religious persecution, and cross-border migration. Ironically, because of the susceptibility brought on by these socioeconomic variables, people are now more accepting of natural disasters.

It has been said previously, refugees from Bangladesh are entering India through West Bengal and establishing colonies on the sandbars. The sandbars' ecological system has been compromised as a result. For those who live on the sandbars, it has exacerbated socioeconomic issues.

As a result of their ancestry in agriculture and fishing, they are accustomed to cultivating, farming, and fishing in flood-prone areas and are still honing their coping mechanisms for the natural disasters of the perilous char regions or sand bars depicted in the figures. -1 and 2. In the enormous Lower Damodar Basin (LDB), Bangladeshi refugees have implemented some practical methods to prevent the incidence of natural disasters. These survival strategies are: (i) Grasses and soil-binding shrubs are allowed to grow on the erosion-prone banks. (ii) Jute is cultivated by erosion-prone banks. (iii) They cultivate different types of crops throughout the year on higher land above the inundation level. (iv) Additional crops are grown on the unauthorized (newly formed) plots of the chars. (v) Linear

cottages and houses are found on the higher ground in flood-free areas. (vi) Nowadays floriculture is flourishing in the higher parts of the chars. (vii) A cooperative society, club, playground, and school are established in the flood-free zone. (viii) The people whose houses and lands have been engulfed by the river during the flood make huts in the unauthorized land of the char. (ix) Generally they built low-cost houses with jute sticks and bamboo and avoid clay houses. (x) Almost every house has an upper shelf to keep their valuables and take shelter during the flood. (xi) Almost all the families have boats and most can drive them.³³



Despite that, still today, they have to dance to the moods of the river. They are the poorest, the most industrious masses in the uncertain fluvial environment. Indeed, they are the people with no voice, hence no choice. Let's now take a closer look at the different perceptions and protection challenges that the individuals we spoke here with Bhashapur sand bar identified as crucial. Case studies finds out those same occurrences are happened in the all selected sand bars.

People Survives with Security and Insecurity

Physical Isolation

Individuals and populations frequently react to environments differently. Some people thrive in their environments more, while others do not. Some people can cope with adverse environmental conditions without problem, while others can only do so by changing their perceptions. Varied responses could result from varied environmental sensitivities or perceptions, or they might be the result of different environmental abilities.

The Bangladeshi immigrants who settle in the Damodar charlands frequently lack valid entrance documents. However, this is not a significant barrier to resettlement on its own. Relatives provide housing for the new immigrants so they can live without worrying about the authorities spying on them all the time or unpleasant neighbours. And over time, a loose network of local political figures, panchayat members, and community development block administrators helps people acquire legal documents like ration cards or voter identification cards. Therefore, vulnerability can be viewed as transitory or ephemeral phenomena since they serve as an entry point to mainland society and economy.

According to the settler, Swapan Sarkar:

We don't intend to stay here for an extended period of time. We are very aware of how fragile these sandbars are. Each year, due to bank erosion during the wet season, I have witnessed acres of land disappear into the river. The river might erode my house at any time during the upcoming flood. I've lived here for four years, and my wife and I both have citizenship papers. I'm still here since I still need to get my two sons' citizenship papers.

Swapan Sarkar and other residents of sandbars are vulnerable to flooding and river erosion as a result of their illegal immigration to India, which has complicated and interconnected effects on their poverty and vulnerability. Not all sandbar residents, however, are watching for a chance to flee. Regardless of whether they get citizenship credentials, some inhabitants choose to dwell in the sandbars because they view it as a safe neighbourhood. In this scenario, isolation, which is typically

to be avoided when choosing a place to live, is frequently a strong suggestion. A 35-year-old lady named Rani Sarkar described her life on a sandbar as follows:

We have improved a lot since we left Bangladesh. We never have hunger pains here. More or less all year round, we can find work as agricultural labourers. My spouse and I will go fishing in the river even if we ever lose our jobs. In order to catch fish every day, we must work hard.. The fish can be sold to the neighbours. We have set up the union of our eldest daughter with a man who also resides on the sandbar. We used our own labour to construct them a home. We don't lack for food here, and we are content to stay put since we lack any legal documents to leave.

Social Isolation

Strangely, one of the reasons individuals choose to live in the country occasionally is the lack of proximity to their social networks of family and friends. In several cases, whether in Bangladesh or elsewhere in West Bengal, people expressed satisfaction at how little about them was known outside of their previous existences.

Mood of River Controls the Lives

Our understanding of environmental uncertainty, susceptibility, and livelihood is lighted by an awareness of the circumstances in which people live in a setting that is perceived by the majority as marginal and unsafe. Our work has shown that people's feelings of security, insecurity, and vulnerability are all subjective and can vary greatly among various social groups—even locally. While some people obviously feel safer living in sandbars than they do in neighbourhoods with unfriendly neighbours, others see these locations as immediate life-supportive land without touch of local administration to dwell temporarily, while still others think the sandbars are completely unsuitable for occupancy. Others who live on sandbars are more aware of the defenselessness of the sandbars and only utilize them as a transitory haven while some strive to build permanent structures and make plans for a long-term settle.

Since the Damodar Valley Corporation (DVC, established-1948) dams were built, we have observed a decrease in the frequency and severity of floods in the Damodar sand bars. The residents of sand bars have felt more secure as a result of the flow and frequency of catastrophic floods, which has led to a greater use of the local resources at the same time. More intensive farming methods have, however, been implemented as a result of the growing competition for limited land. This raises the question of whether or not vulnerability has increased or lessened as a result of the constant influx of people into this vulnerable environment and the more intensive use of the sand bars.

Under the British government, the value of land ownership increased, and the agricultural department saw significant change. This reinforced the idea that land is more important than water and that perspective of rivers was altered. Rivers were re-conceived as disruptive factors that needed to be tamed in order to serve the land-based economy, in addition to changing agricultural practices, which earlier were frequently in harmony with this hybrid ecosystem.

Conclusion

This study investigates why Bangladeshi refugees decided to establish second houses in riverbeds. After India's independence in 1947, river resources were required to solve socioeconomic issues. There is no a priori model for the relationships between people and the environment, which further illustrates that decisions on specific land uses and assessments of the advantages of water from a DVC reservoir are based on personal experience. Environmentalists haven't paid much attention to the paradoxical relationship between "environment" and "partition" or its negative effects. Therefore, this study suggests some cutting-edge theories, discussions, and various points of view for the future of environmental history.

Acknowledgement

The University of Burdwan's Dean of Arts, Professor (Dr.) Pradip Chattopadhyay, and previous Vice-Chancellor Dr. Ranjan Chakrabarti, who helped make this study possible, have my sincere gratitude and respect. I also want to thank Sri Bidyapati Kumar and Principal Dr. Arup Kanti Konar.

References

1. A Case Study of the Damodar Valley Corporation and Its Projects, (1952), United Nations Economic Commission, *Ekistics*, Vol. 13, No. 77, 145-151, <https://www.jstor.org/stable/43615970>. Accessed, 17th Februray 2021
2. Mukherjee, G. (2011), *No voice, no Choice: Riverine Changes and Human Vulnerability in the 'chars' of Malda and Murshidabad*, Institute of Development of Studies, Calcutta, 13-16.
3. Chakrabarty, S.K. (2011) *A History Receding Wetlands in West Bengal (1947-2000): Society, Ecology and Environment*, 'The University of Burdwan, Burdwan, 195-96.
4. Basu, M. (1998) '*Marginalization and flood: A case of east Bengalee migrants in the Ajoy valley in Burdwan District*', University of Monitoba, Canada, 26-7.
5. Bhattacharyya, K.(1960) '*A Case Study of Damodar Valley Corporation and Its Project*, Flood Control Series No. 16, Bangkok, United Nation; Economic Commission for Asia and Far East, 9-33.
6. Lahiri-Dutt, K. (2000) '*Imagining Rivers*', in *Economic and Political Weekly*, Vol.35, no.27, 395-400
7. Lahiri-Dutt,K. (2003) '*People, Power and Rivers: Experiences from the Damodar River, India*', in *Water Nepal*, Vols.9/10, nos.1 & 2, 251-67
8. Kuper & J.Kuper, (1987), '*The Social Science Encyclopedia*', 1st edn. , Route ledge, New York, P.726.
9. Chakraborty, P. (1990), *The Marginal Man: The Refugee and Left Political Syndrome*, Lumiere books, Calcutta, 80-85
10. Chowdhuri, S. (1995), ed., *The Calcutta: The past and the Present*, Oxford / publications, New Delhi, 72-73.
11. Bhattacharyya, K. (1999), *Floods, Flood Hazards and Hazards Reduction Measures: A Model – The Case in the Lower Damodar Basin*, *Indian Journal of Landscape System and Ecological Studies*, Vol-I, No-II, Calcutta
12. Ghosh, S., Ghosh, S., (2014), eds., *Refugee Problem in Undivided Bengal*, Reader Publications, Calcutta, 72.
13. McCay, B. '*Edges, (2000), Fields and Regions*', in *The Common Property Digest*, Vol.54, .6-8.
14. D.Charles, (1854) '*Memorandum on the Survey of the Damodar and Question of the Abandonment of Bunds on Right Bank to Accompany*, the map received with superintending engineer South-eastern Province 's letters no. 1473, Bengal Government, Selection no. 15, Calcutta Bengal Military Orphan Press, Calcutta, 86-125
15. H. Rickets, (1853) '*Notes on the Management of the Embankment*', Bengal Govt., selection No., 12, Calcutta, Bengal Military Orphan Press, Calcutta, 1-12
16. I. Iftekhhar , (2010), *The Bengal Delta - Ecology, State and Social Change: 1840-1943*, Palgrave Macmillan, P. 15.
17. M. Morisawa, *Rivers: Form and Process* (London:Longman, 1985); and R.J. Chorley, S.A. Schumm and D.E. Sugden, *Geomorphology* (London:Methuen, 1984).
18. See <http://www.eurasianet.org/departments/rights/articles/eav100101.shtml>
19. Chowdhury, M. (2001), '*Women's Technological Innovations and Adaptations for Disaster Mitigation: A Case Study of Charlandsin Bangladesh*', Expert Group Meeting on Environmental Management and the Mitigation of Natural Disasters: A Gender Perspective, Ankara, 6- 9 November 2001.
20. Baqee, A. (1098), *Peopling in the Land of Allah Jaane: Power, Peopling and Environment, the Case of Charlands of Bangladesh* (Dhaka: The University Press Limited, 1.
21. Zaman, M.Q. (1989) '*The Social and Political Context of Adjustment to Riverbank Erosion Hazard and Population Resettlement in Bangladesh*', in *Human Organization*, Vol.48, no.3 197.

22. Burton I, Kates RW, (1964), The perception of natural hazards in resource management. 3:412-421
23. Brookfield HC, (1969), On the environment as perceived. In: Board C, Chorley RJ, Haggett P, Stoddart DR (eds) Progress in geography, vol 1. Edward Arnold, London, 53-80
24. Chakrabartty, S.K. (2016), 'The Marginal Men in the 'Charlands' of Lower Gangetic Basin and Lower Damodar Basin' Journal of People's History and Culture Volume 2, 20210510044102.pdf, 25-27.
25. Bhattacharyya, K, (2011), *The Lower Damodar River: India, Advances in Asian Human - Environmental Research*, P.151.
26. Saha, M, (2010), *Duranta Damodar*, Lesser Art Publication, Hooghly, 165.
27. Bergkenp, G. McCartney, M., Dugan, P., Mc Neely, J., Acreman, M., (2000), ' *World commission on Dams Thematic Review, Dams , Ecosystem, Functions and Environmental Restoration*, (Environmental Issue-II. 1, Cape Town, South Africa. 55.
28. Samanta, G., & Lahiri Dutta, K., (2017), 'Like the Drifting Grains of Sand: Vulnerability, Security and Adjustment by communities in the Char-lands of the Damodar Rivers', India, Journal of South Asian Studies, 342-45.
29. DVC (Damodar Valley Corporation), (1975a). 'Report of Lower Damodar Investigation Committee', DVC, Calcutta-I.
30. DVC (Damodar Valley Corporation), (1975b). 'Report of Lower Damodar Investigation Committee', DVC, Calcutta-II.
31. WL. Vooduin, (2007), *Preliminary Memorandum on the Unified Development of the Damodar'*, 1945, Central Technical Power Board, on behalf Government of India Press, Calcutta, P.156. (See, Original document from the University of Wisconsin, Digitized on 2007).
32. Samanta, G. & Lahiri Dutta, K. (2014), Dancing with the River: People and Life on the Chars of South Asia, Martin Luther University Halle-Wittenberg, 32-34.
33. S.K. Chakrabartty, 'Human Vulnerability in the Chars of Malda and Murshidabad and Lower Damodar Basin', in 'Modern Trends in Social and Basic Sciences', eds., Sailen Debnath, Bhaskar Bagchi and Subhra Mishra, (Reader Service, Calcutta, 2015), 667-670.



ISSN 2347-7180



Published by Dr. Angshuman Das, Secretary,
Dogo Rangsang Research Society, Guwahati &
Printed at Dream Graphics, Naokata, Tamulpur (BTR), Assam

Cover Designed at Dream Graphics by Kamal K Sarmah



ISSN : 2347-7180

(A Bilingual Research Journal, Indexed in UGC-Care list)

DOGO RANGSANG

Research Journal, Vol-13, Issue-6, No. 15, June 2023

दगो बाङ्छांग

CHIEF EDITOR (HON.)
EDITORS (HON.)

मुख्य सम्पादक (अबैतनिक)
सम्पादकद्वय (अबैतनिक)

: Dr. Upen Rabha Hakacham
: Dr. Lalit Chandra Rabha
: Dr. Dhaneswar Kavitha
: ड° उपेन बाभा हाकाचाम
: ड° ललित चन्द्र बाभा
: ड° धनेश्वर कलिता

A Peer Reviewed Bilingual Research Journal
(Indexed in UGC-CARE List)

ISSN 2347-7180

DOGO RANGSANG RESEARCH JOURNAL
দগো বাংছাং গবেষণা পত্রিকা

Chief Editor (Hon.) : Dr. Upen Rabha Hakacham
Editors (Hon.) : Dr. Lalit Chandra Rabha
Dr. Dhaneswar Kalita

মুখ্য সম্পাদক (অবৈতনিক) : ড° উপেন বাভা হাকাচাম
সম্পাদকদ্বয় (অবৈতনিক) : ড° ললিত চন্দ্র বাভা
ড° ধনেশ্বর কলিতা



Dogo Rangsang Research Society
Reg. No. KAM-M/263/L/ 595 of 2015-16

দগো বাংছাং গবেষণা সমিতি

PEOPLE'S WATER HARVESTING MANAGEMENT OF PURULIA DISTRICT (1947-2000): A GEO-HISTORICAL STUDY

Dr. Samar Kanti Chakrabartty Head Department of History Achhruram Memorial College, Sidho-Kanho-Birsha University Jhalda, Purulia, Pin-723202, W.B., India. Email id: samarkantichakrabartty@gmail.com

Abstract

It analyses how the native population of the Purulia district improved water harvesting management, which has sped up agricultural development and allowed them to live in and around artificial water bodies since the dawn of time. Particularly, our investigation has highlighted a number of services provided by various water body groupings in drought-prone areas between 1947 and 2000. It also looks at the socioeconomic advantages of water-taping techniques in the relevant research area, as well as how they affected the lives and means of subsistence of the oppressed people in the late 1980s and early 1990s. The majority of research on this area in West Bengal focuses on issues like migration, politics, cultural change, etc. The locals' concerns for the environment and a recent pattern of human involvement with water bodies, however, have received the least attention.

Key Words:

Agriculture, Migration, Culture, Sustainable Environment, Sustainable Environment

Introduction

The Purulia district is a peculiar location distinguished by enormous regions of plateaus, hills, woods, rivers, large deep tanks, and jor-bundh (medium-sized reservoirs), which are situated between the Chhotonagpur and the Ajodhya plateaus. With the ongoing threat of drought, a drinking problem, and storm surge, and several cultures can be witnessed. In a few West Bengal districts, including Bankura, Birbhum, West Midnapur, and Jhargram, especially Purulia district, which is distinct from the rest of the state, landscape and indigenous water-taping practices, are being successfully implemented. From prehistoric times to the twenty-first century, the westernmost areas of the state, including the study area, have been seriously threatened by dry temperatures and a lack of water. The district's ground water is insufficient because it is located on a rock-lying substrate. As a result, the district's water supply is derived from the storage of rainfall during wet monsoons. Because of this, the indigenous people of the area developed some unusual methods of collecting water, including: (i) ponds; (ii) bundh (big, deep tanks); (iii) jor-bundh (medium-sized reservoirs); (iv) hapa (extremely small size with an I-shaped deep water body); and (v) dug wells. Due to a wider use of local water-harvesting knowledge, the residents of the district conserve more water than the residents of the other districts in the state. According to the edited book *Water* by Debasish Sengupta, Paromesh Goswami, and Kalyan Rudra, this drought-prone region saves 21% of its water each year during the monsoon. Since the dawn of the Christian period, indigenous people have benefited from a number of these historical hydraulic engineering skills. However, since the 1980s and 1990s, the population's way of life and means of support have substantially improved because to the construction and maintenance of traditional water tapping practices. Despite the enormous threat posed by environmental crises and social pressures, they continue to persist and have been successfully cultivating these practices.

Statement of the Problem

In order to improve socioeconomic conditions, it intends to demonstrate how indigenous people have spread the Jor-bundh practise or new water-storing management in the drought-prone district. The farmers were able to establish themselves in and around the water bodies thanks to this creative, sustainable development. The work aims to promote flexibility in the drought-prone terrain and decrease socio-economic risks. The long-standing modes of subsistence of the indigenous people of

the district of South-West Bengal, India, have been impacted by both sustainable development and the growth of traditional water collecting.

Objective of the Study

- > Describe how the Jor-Bundh hydraulic system was found and developed by native people.
- > Determine the wisdom and collaboration of the entire community for holistic development.
- > Learn how crucial a single drop of water is in a drought area.

Review Literature

The relationship between water and society is integral to the larger interaction between man and nature. Social and political organisations of civilizations have been directly influenced in all ages by the ecology of water flows. Mahasweta Devi, has pointed out in her book entitled '*Puruliar Jol-Chitror Manushjhon*' (2013) that Purulia and other western regions of West Bengal need many *jor-bandhs*, ponds, and brick-made dug wells for the development of irrigation, fish cultivation, and meeting daily chores. Rainwater harvesting in *jor-bundhs*, or ponds, is important for maintaining a sound ecological balance. People of the Rarh region believed that water bodies were not only a manifestation of nature but also revered sectors of social customs observed by primitive communities since ancient times, some of which are still practiced today. Debasish Sengupta, Paramesh Goswami, and Kalyan Rudra's pioneering work '*Water*' (2013), has notably mentioned that each and every drought-prone district of North and South-West Bengal preserves rainwater artificially or naturally, but Purulia collects the maximum (21% of the total) of water through the application of traditional water management practice in West Bengal. Kalyan Rudra's recent work, '*Paschim Banger Jalasampad Sankater Utsasandhane* (2015), has highlighted the issues and factors relating to water scarcity faced by the people of West Bengal. Among various factors, failure of monsoon rain, deforestation, soil erosion, water waste, the extension of the process of urbanization, and global warming have been held responsible for water inadequacy in West Bengal. They have argued that there are basic similarities of thought between the 'environmental laws of *Arthashashtra*' and the principles of the '*Stockholm Conference*' in 1972. '*Banglar Dighi o Jolashoy* (2003) has narrated various issues related to the water bodies of the state. It deals with history, mythology, etc., and also discusses its ecology and management.

Research Methodology

This article was written using a combination of historical research techniques and primary source analysis. For producing an environmental history of water resources, information has also been gathered through field surveys in addition to secondary sources like books and journals. However, with the use of an interview schedule, they have been personally interviewed to better understand the various socio-economic patterns and stages of life of the indigenous people. Consequently, a field survey was carried out for this.

Results and Discussion

There are three factors; topographical location, present performance analysis, and the number of beneficiaries. This district having four water collection practices vis-à-vis the several services of the traditional knowledge, the current scenarios, and the status of the water managers. This study looked at almost many traditional water collection structures in West Bengal to collect authentic information on traditional water harvesting systems.

The discussion on water harvesting practices perhaps seems incomplete without a reference to the perceived threat of water-scarcity confronted now by all the nations of the world. Water, as one of the gifts of nature, is no longer considered inexhaustible, and with the passage of time and as a consequence of rising global warming, the water resource is also showing signs of depletion. In the closing decade of the 20th century, it has been calculated by geographers that approximately 110 corer people all over the world are still living in arid zones, and many of them have to undertake a journey

of more than five kilometers every day to fetch drinking water.¹ The severe water crisis in some parts of this planet has had an adverse impact on human societies. It is a problem on more or less all the continents, like India, Africa, Europe, Southeast Asia, etc. Even some highly developed countries like the USA, France, Britain, and Russia are also facing water-related problems today.²

Every person needs some water to meet his daily chores. It is reported that a person living in Phoenix, Arizona, in the state of Arizona, USA, needs 1000 litres of water every day, whereas a person living in an African city like Mozambique gets only 10 litres, and an Indian gets 139 litres of water per day.³ The two most important organizations—the WHO and the United Nations Children's Fund—both have suggested that every person should have 50 litres of water a day for drinking and other purposes in order to maintain good health. But the fact is that only 20 percent of the world's population can enjoy this minimum amount of water, and the rest have to remain satisfied with whatever little quantity of water is available.

Water deficiency is a global problem. In countries like India, Bangladesh, and China, the problem has become acute due to the tremendous growth in population. It is quite clear (*from the data of the West Bengal Pollution Corporation Board / Poribesh Bhavan, 2009*) that the demand for water in West Bengal was 121 cubic-kilometres per year up to 2011, and it seems to increase up to 143 cubic-kilometres per year by 2021. But, unfortunately, the state's present water resource can meet the demand of only 129 cubic-kilometer.⁴ This problem is very severe in the districts of Purulia, Bankura, Birbhum, West Burdwan, and Jhargram, and therefore these districts have been declared arid zones (Rarh). Drought in 1982 had affected the socio-economic life of the people of the region. In the 1970s and 1980s, the State Ground Water Board has reported that the ground water of many districts of West Bengal like Malda, North and North-South Dinajpur, Murshidabad, Midnapur, North 24 Parganas have diminished due to the massive extraction of ground water that has affected the surface water resources and its surrounding ecological set up.⁵ In the states like Chhattrishgrah, Madhya Pradesh, Rajasthan and some parts of Maharashtra, Gujarat, Andhra Pradesh, Karnataka and Jharkhand the crisis is even more acute and more than 45 per cent area of these states is under massive water crisis. For example, the villagers of Vadhavan village in Vadodara district of Gujarat have to get-down to about 24 meters deep well to collect muddy-water.⁵ According to NITI (National Institution for Transforming India, formed via a resolution of the Union Cabinet on 1 January 2015) Aayog report (on 18 June, 2018) of Central Government of India has rightly revealed that 600 million people have been facing high extreme water stress in the country, and 2, 00,000 people died every year due to inadequate water. About three-fourths of the households in the country do not have drinking water in their premises. With nearly 70% of water being contaminated, India is placed at 120th among 122 countries in the water quality index.⁷ According to the Niti Aayog's *Composite Water Management Index (CWMI)* of India has said and proved that twenty-one cities including Bangalore, Chennai, Delhi and Hyderabad will run out of ground water by 2020.⁷ Therefore, the government has launched a new department as "*Jal Shakti Ministry*" to mitigate drinking water crisis of the country.⁸

Due to insufficient rainfall, the Purulia district had severe droughts in 1953, 1966, 1972, and 1974, which had a negative impact on the region after partition (1947). As a result, there was a severe food crisis in several areas of the district. In response to this appalling condition, the district's political leaders in the 1980s spoke out in favour of rainwater conservation. ⁹ They sought an increasing number of *bundhs and jor-bundhs* (big ponds and tiny dams) in order to prevent the district's ongoing water issue. For the purpose of presenting their demand for water preservation to the State Ministry of Irrigation, a sizable contingent of district residents marched (*pada yatra*) from Purulia to Kolkata. In order to get people's attention, they also brought up this important subject in the State Assembly and Parliament.

New Water Management: Jor-bundh

The Rarh region's Jor-bundhs are also significant bodies of water. Both the socioeconomic and ecological balance of the area are greatly impacted by them. They are typically U-shaped, and a shallow

gate is installed on the Jor-bundh side to allow water to exit. In the vicinity's foothills, it excavates. There must be springs or streams at the top of the hills in order to build the Jor-bundh. Farmers in the area discovered a natural way to conserve water for farming. Such a Kuki Jor-bundh was built in Jhalda Block I at the base of the Parundih-Khamar Gramme Panchayat. In order to maintain the natural balance of the dam, the rainforest surrounding the jore-bundh is kept in this mountainous, jungle-covered area.. This is a jungle covered hilly area and the jungle around the jore-bundh is preserved for the ecological balance of the dam under the Bagmundi Forest Range. The most important dam in the district is Kumari dam that has been constructed down the two springs at Ghalbere village under the Ajodhya hills of Balarampur block. Hanumata is a drought-stricken area of Tamarsol Gram Panchayat and Tetlo Gram Panchayat under the same block. A spring of Dumri hills is the main source of water of the dam. Karior dam is located at Baro Gata village under the Karior G.P of Jhalda block I. Some Jor-bundhs like Golamator and Dimu have been constructed at the basin of its catchment area. Such Jor-bundhs are exceptional dams which are built without the water from the hills or streams. Earlier the surrounding arealay barren for want of water. And after the construction of the dam the area has become a highly cultivated zone. Bagmundi is the ending point of Purulia district where the dam Ukadha was constructed to preserve water of the Ukhada hill for the development of irrigation and cultivation. A list of major dams and their associated details of the district are given below.

Table-1. Jor-Bundhs in Purulia District

Sl. No.	Year of Completion	River & Dam	Height above lowest Foundation Level/ Mt	Volume Content of dam /h	Gross Storage capacity,	Effective storage capacity	Purpose	Desi gned spill way capacity	Year of Commen cement	Len gth of dam / mt.	Reser voir Area/ ha.
1	1984	Kumari	9.6	233	7521.5	4320	irriga tion	765.14	1970-71	976.8	2348
2	1982	Saharjore	22.9	1110	8384.7	7406	irriga tion	4.8.07	1976-77	2195	1721
3	1988	Rupai/ Kuki	12.07	110	1617.1	1559	irriga tion	362.73	1970-71	2615	761
4	1982	Kestobazar	7.2	158	796.5	707.2	irriga tion	119.02	1969-70	954.12	176
5	1989	Karior	11.5	125	389.6	388.5	irriga tion	117.6	1979-80	904.57	232.8
6	1982	Parga	15.76	163	2219.4	1580	irriga tion	129.96	1976-77	721.34	526.3
7	1984	Khairabera	21	184	2347.7	5195	irriga tion	119.87	1980-81	371.95	404.8
8	2004	Patloi	13.5	141	5548.7	4212	irriga tion	265.82	1976-77	952.74	1822
9	1984	Goalma rajore	13	196	24.4.40	1712	irriga tion	137.44	1976-77	1073.17	951.4
10	1989	Demu	12	157	926	677.6	irriga tion	48.97	1979-80	827.74	340
11	1982	Buridumur	6.93	54	191.1	117.2	irriga tion	22.84	1976-77	533.53	64.7

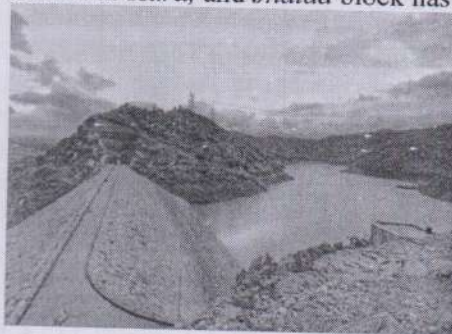
1	1982	Sankha	6.7	13	641.9	395.6	irriga	382.5	1974-75	67	217.6
2					2		tion	7			
1	1984	Turga	20.73	320	1372.	4213	irriga	96.86	1948-	360.	323.9
3					8		tion		1949	36	
1	1975	Nimgiri						26.5	1948-	99.3	1619
4									1949	9	

Source: This source has been collected by me from the irrigation the District Purulia, Submitted to the Director, Dam Safety Organization, I & W Director, Jalasampad Bhawan Salt Lake City, 13.03.08, Memo No. 476/S-140, (Third Minor Irrigation Census (2000-2001) in West Bengal Water Investigation and Development Department, GOWB, December 2003, PP.171-77)¹¹

UPPER-DAM AND LOWER-DAM IN AJODHYA

The Ajodhya pump storage hydroelectricity project was constructed on a 373.20-hectare area of dense rainforest between 1994 and 2002. Under the Baghmundi block, it is Asia's largest pump storage and power generation facility. Here, two reservoirs that go by the names of higher dam and lower dam have been built. The Kestobazar River existed before the dams were built. The dams' combined water storage capacity is currently at around 6.5 million cubic metres.¹²

The dense jungle around the Upper-Dam and the Lower-Dam on the Ajodhya hills destructed little during the construction of the two dams. Huge number of trees like eucalyptus, *sal*, and *mehagini* were planted as the substitute to restore ecological balance of the region. Despite construction of dams the natural vegetation has not changed much in the entire region. The bio-physical zone around the reservoirs is highly rich. Four types of plant species namely - dry peninsular *sal*, dry mixed deciduous plants, deciduous scrub and *butea* plants; mammal species like elephant, bat, wild bear, deer, leopard and birds' species etc., are found surrounding the dams.¹³ In addition to these, in each and every part of the district has numerous micro/major *jor-bundhs* namely *Shyam bundh*, *Cheliyamabundh*, *Baro-bundh at Manbazar block*, *Shuribundh at Hura*, and *Jhalda block* has more 150 big *bundhs*.



Ecological Set Up Around the Jor-Bundhs

Dams / *jor-bundhs* are thought to make good habitats for a variety of biological systems. Due to the abundance of natural foods around the *bundhs*, a variety of bird species can be found in the area around the *jor-bundh*. The aforementioned *jor-bundhs* offer the wild kingdom different types of food, refuge, breeding grounds, or other essentials. In most cases, the *jor-bundhs* had dug in the isolated parts of the districts. The *jor-bundhs'* surroundings provide a specific haven for wildlife, particularly elephants, deer, wild pigs, foxes, jackals, and bears. Prior to the 1980s, the region surrounding the *jor-bundhs* was mostly made up of open fields. Following construction, the *jor-bundhs'* surrounding vegetation, streams, and climatic conditions have improved and are now more favourable for wildlife.¹⁴

Different Water Harvesting Systems and Roles

Long-standing irrigation practises and accompanying water-tapping traditions have a significant impact on irrigation systems in the Rarh region. Water scarcity is a major obstacle to the region's plan

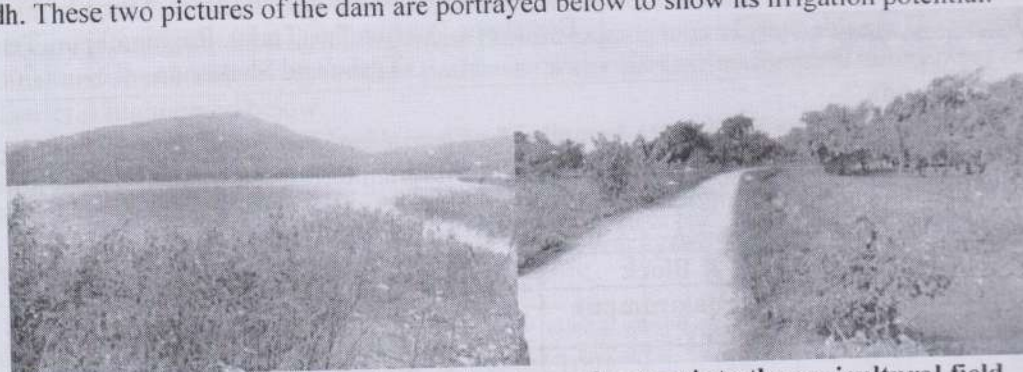
to increase irrigation. However, in the latter half of the 20th century, it was controlled and developed through the use of water conservation techniques, which decreased the farmers' socioeconomic susceptibility. The irrigation system in the area is built on three main principles: 1) rainwater conservation in the *jor-bundhs* and *bundhs*, 2) storing precipitation in dug-out wells, and 3) utilising rivers to raise irrigation water.

Role of *Jor-Bundh* Practice in Irrigation

By building *jor-bundhs*, the artificial irrigation system was expanded to dry terrain in the 1950s and 1980s. As a result, the installation of *jor-bundhs* brought 5–10% of the land in the Bankura and Purulia districts under a minor irrigation system.

The Purulia district has the best tradition of *jor-bundh* water management. Several *jor-bundhs* are contributing a lot to the advancement of irrigation in the district. About 42,953 thousand hectares' land came under irrigation systems after the 1980s. Consequently, many unproductive lands and one-crop lands have been transformed into multi-crop lands due to the availability of irrigation facilities, which have increased agricultural production in the entire district.¹⁶ The production of vegetables has also increased remarkably. The construction of *Khairabera-jor-bundh* was completed in 1982 in the Ayodhya Hills of Purulia district, which can irrigate about 1.5-thousand hectares of land in the rainy season. The villages around the dams, namely *Bhukadi, Burda, Mankidi, Koreng, Gurshu, Rotung, Kushadih, Pogradih, Sarjumata, and Bankadih* under *Bagmundi* block, have reaped agricultural benefits from the irrigation system facilitated by the dam. Paddy and other crops, including vegetables, are grown enormously here with the irrigation water. Thus, the single crop or barren lands have altered into multi-crop lands.

The *Khairabera-jor-bundh* is another important tank for irrigation under the *Bagmundi* block. The villages under the *Burdha Gram Panchayat* of *Jhalda* Subdivision are the main beneficiaries of the *jor-bundh*. These two pictures of the dam are portrayed below to show its irrigation potential.



Khairabera *jor-bundh* and its water channel enters into the agricultural field

Murguma *Jor-Bundh*

Saharjor *jor* or Murguma *bundh* is considered as the lifeline of the poor people of several mouzas under *Begunkodar Gram Pachayat*. It was built mainly for supply of drinking water and irrigation. The *Jhalda* municipality is fully dependent for its supply of drinking water that has minimized water crisis in the area. The water of the *jor-bundh* is also being used for irrigation purpose. The total irrigation area of the dam is about 5,095 thousand hectares.¹⁷ The main beneficiary villages are *Murguma, Laxmipur, Chatombhari, Bagandih, Keta, Gugui, Batoliya, Raghunathpur, Rampur, Harbaha, Jhari and Baram* under the *Jhalda-II* block. This zone is very famous as '*basket of rice and vegetables*'. **Kuki *jor*** is another important *jor-bundh* of the district. It was established for the expansion of irrigation in the fallow land. The irrigation potential area of the dam is about 1088.50 hectare.¹⁵ More than 80% vegetables of the area are grown here with the help of irrigation water. Earlier most of the villages are mono-cropped but after the construction of the *bundh* these villages have become multi-cropped area. The following beneficiary villages of the dam are mentioned in the table.

Table -2. Kuki Dam and Its Benefitted Mouzas

Name of Jore-Bundh	Gram Panchayat and Block	Benefited Villages
Kuki/ Rupai	Ichag under Jhalda -I	Mahaldih ,Sajumetapilai, Kuki,Palashdih, Bhutidih, Maisha, Jamlohar, Harahara, Birudih, Magha, Dharpa, Dibirtika,Jargo, Mathai, Ilu,Mahadih, Chandai, Nowadih, Rotiadih

Source: Field Survey

Kumari Jor-Bundh

The farmers are also receiving the same service from the Kumari Jor-bundh. Almost 3642 thousand hectares have the capacity to be irrigated as a result of the jor-bundh's construction. Following settlements are benefiting from the water preservation strategy of the dam since 1982 in terms of agriculture. The villages that received benefits are:

Table -3, Kumari Dam and Its Benefitted Mouzas

Name of Dam	G.P & Block	Benefited Mouzas
Kumari Dam	Baro Urma under Balarampur Block	Baradiya, Taltar, Valaidih, Bhagabundh,Chandanpur, Rawtara, Kharipari, Chipingdih,Kharipari, Dhatkidih, Nadiya, Bamandih,Manpur, Rangagara, Murgabere Bastebpur, Arabundha, Turku, Raghinathpur, Tetlo Tosho and Shukuruta

Hanumata Jor-Bundh

Similar picture is found in the **Hanumata-jor** under the *Choto Urma mouza of Balarampur* block. It provides the same irrigation facility in the advancement of agriculture in the region. The following table shows the benefitted villages under the Balarampur block.

Table -4

Name of Dam	G.P & Block	Benefited Mouzas
Hanumata Dam	Tetlo & Balarampur Block	Chhogadha, Chholagara, sabardih, Bonbadha, Hanshapur, Muradih, Lakhmapur, Pursha, Amagara, Gosaidih, Tuimabaradih, Baistamdih and Tumarsol

To address the serious groundwater and surface water crises in the state of West Bengal, the 'Jol Dhoro and Jol Bhoro' Scheme was created a programme designed to capture valuable rainfall during wet monsoons, was introduced in 2011-2012. The Water Resources Investigation & Development Department, GOWB, has taken on the significant role of large-scale rainwater collection as well as detention of surface runoff for enhancement and availability of priceless water resources through the erection and management of Minor Irrigation Constructions. This is necessary for the program's successful implementation.¹⁸

The aim of the project "Jal Dhoro-Jal Bhoro" programme is to detain rainwater in all kinds of water bodies, viz., *hapa*, (I shaped deep pond) tanks, ponds, reservoirs, canals, and underground artificial recharge through rooftop rainwater harvesting. For conservation and storage, rainwater and surface run-off is arrested in derelict or silted tanks after proper de-siltation, mainly for irrigation in the drought prone areas of West Bengal.¹⁹ Since December 2014, around 817 ponds and 7,319 water reservoirs have been excavated and renovated by the government, and approximately 3,000 ponds have been

further excavated under the scheme of "Jol Dahro and Jol Bharo" of the state Government in the year 2015-16. The Jal Tirtha Scheme under the West Bengal Accelerated Development of Minor Irrigation Project (WBADMIP) has spent Rs 1380 crore to make an additional 1.39 lakh hectares of land irrigable in the districts of Purulia, Birbhum, Bankura, and West Medinipur. About 15,000 hectares' of land have been made crop-worthy through micro-irrigation techniques.²⁰ This irrigation scheme has stressed water bodies across the state, which has enhanced job opportunities among the rural Bengalis through fish farming and cultivation. **Dug-Well Practice**
Dug wells in the Purulia district are the basic source of irrigation system throughout the year.



Nowadays around 31,370 hectares' lands are under the irrigation system owing to the contribution of 13,135 dug wells across the district.²¹ Needless to say that it has facilitated agricultural production in the region. In the past three decades to four decades, the irrigation through dug wells in Birbhum and Bankura has been hit hard with the construction of barrages. But nowadays the excellence of wells based agriculture is particularly appreciated in Purulia district.¹⁷ The farmers of the district are fully dependent on rain-fed wells cultivation owing to the capricious nature of monsoon and lack of whole water- net-work project. In order to these, configuration of land of the district is curse but dug well based cultivation has enhanced the settlement in study area. Whatever, the exact figures in terms of number are not available but many tones vegetables are being produced in the entire district through this practice. Presently the food-stricken district Purulia exports tons of vegetables in the neighbouring states Bihar and Jharkhand owing to these practices. Water harvesting scenario through the dug-well of the district is highlighted below.

Table-5. Source of Irrigation and Irrigated areas in Purulia: 1998-1999

Sl. NO.	Name of the Block	Canal Area	Wells Based Irrigation		River Lifting Irrigation	
			No	Area ha	No	Area ha
1	2	3	4	5	6	7
1	Arsha	3100	822	1442	7	190
2	Bagmundi	2830	1001	1480	6	170
4	Bandowan	880	304	3437	8	580
5	Barabazar	1931	600	1477	12	1005
6	Hura	635	524	2460	4	155
7	Jaipur	535	1523	1510	3	150
8	Jhlada	3717	330	740	13	315
9	Jhalda II	2825	339	1660	3	182
10	Manbazar	860	536	1821	10	384
11	ManbazarII	740	450	1470	5	180
12	Puncha	635	300	2240	9	151
13	Purulia	1885	1252	955	7	315
16	Neturia	725	237	802	4	66
17	Para	1096	1309	1155	6	190
18	R.N.Pur I	420	370	1818	4	167

19	R.N.Pur II	1115	211	1650	4	120
20	Santuri	1005	1034	694	4	85
	Total	28639	13135	31370	135	5285

Source: District Statistic Hand book, Purulia, Bureu of Applied Economics&Statistics, 1999 – 2000, P. 50²²

Rain-Fed Irrigation

Besides these, another rain-fed irrigation is being followed by the marginal farmers of the Purulia district. A high mound embankment is built around agricultural field to tap rain water. Each and every field has its own earthen-embankment to preserve water from top to bottom of the area. This picture shows an innovative rain-fed irrigation from top to bottom of the field.

After the 1980s, the gross production of Purulia district increased greatly due to well-maintained hydraulic structures and a huge amount of vegetables were exported to neighbouring states of the district like Bihar and Jhalkhand. The number of hats and bazaars (*Puncha hat, Rakhbar hat, Taltaol hat, Cheliyama hat, Adra, Borabazar hat, Kotshila hat, (Monday), Jhalda, Balarampur Ludhurka hat (Tuesday), Hura, Bandwan, Pundag, Bagmundi, Arsha, and Tulin hat (Thursday)* of Purulia district has developed owing to the extension of age-old water harvesting practices after partition of India.²³

Hapa Practice

For a very long time, this district has enjoyed the best hapa tradition. As a result of the expansion of minor irrigation and fishing, it has recently grown to be quite well known in the Kotshila and Arsh blocks of the district. Typically, a "hapa" is excavated in a field corner to collect rainwater during the wet monsoon. The command irrigation area now includes about 20–25 bigha unfarmed fields in these two blocks, which have more than 50–60 hapas combined. Additionally, it is crucial to cultivate a variety of veggies in the summer.

Impact on Labour Migration

The long-standing practice of labour migration in the district, as well as the newly developed jor-bundh practice has altered the rural economy of the study area and its surrounding regions. In the past, a sizable portion of the district's population had to leave in pursuit of work. Ben Rogal has demonstrated that seasonal migration in West Bengal is not just a necessary component of the debt cycle. Seasonal agricultural labourers from border regions like Bihar and West Bengal as well as other parts of West Bengal have a long history of working in the state's south central region.²⁵ With increase in rice production in west Bengal in the 1980s and early 1990s employment opportunities were created for seasonal migrants in transplanting and harvesting in a season which would be continuous rather than sporadic. Around 65,190 workers left Purulia for other locations in 1900. Nearly 30,777 labourers left the country in 1901. The rate of labour migration has definitely decreased. Only 15,492 labourers from the Purulia region moved to West Bengal, Assam, and Bihar in 1909. In 1911, H. Coupland recorded and published this official data in the Bengal District Gazetteer; Manbhum, statistics.²⁶ Even after India gained its independence, the trend of worker migration from the colonies has persisted. However, census statistics reveal the character and patterns of the migration process. 16.4% of the people in Purulia moved to other West Bengal districts, and 33.03% left the city for other states, per the census of 1961. Most of the modest emigration from Purulia (47, 101) took place in the Bankura and Burdwan (13,984). The district's agricultural labour facilities expanded after the 1980s and 1990s. They therefore have the opportunity to work in their home districts. Due to the greater growth of old water management systems; such labour migration has decreased in the present

Conclusion

Locals here actually believe that a body of water on the surface of the ground is not a hole or puddle. Instead, their cultures and beliefs are influenced by these water bodies either directly or indirectly.

Actually, they treat the water bodies they foster on a regular basis as their sons, and the water bodies offer everything they have to the area's poor. The societies of the district have enabled commercial growth through a considerable expansion of the district's historic infrastructure for water tapping. In order to survive and maintain ecological equilibrium, they are currently protecting themselves from environmental threats and conserving water gathering practices.

Acknowledgement

For helping to make this study possible, I sincerely thank Vice-Chancellor Dr. Ranjan Chakrabarti of the University of Vidyasagar and Professor (Dr.) Pradip Chattopadhyay of the University of Burdwan. I also want to thank Sri Bidyapati Kumar and Principal Dr. Arup Kanti Konar.

REFERENCES:

1. Debasish, S., Paromesh, G., & Kalyan, K. eds., (2014) ,*Water*, Avenal Publication: Memari, Burdwan, pp. 15-16.
2. S. Seth M, *Let There Be Water: Israel's Solution for A Water-Starved World*, 2015, Thomas Dunne Books, St. Martin's Press: New York, p. 4.
3. Debasish , S., Paromesh, G., & Kalyan ,K. op.cit., 19.
4. Debasish , S., Paromesh, G., & Kalyan ,K. , op.cit., P. 39.
5. *Semi-Detail Ground Water Survey in Purulia District*, (1977), Government of West Bengal, Rural Development Centre, Indian Institute of Technology, Kharagpur, pp.1-2.
6. *Ananda Bazar Patrika*, (written by an eminent journalist Jaya Mitra, *Ei Sujala Sufala Desher Emon Abostha Halo Ki Kore*, 21st July, 2019, Section – II, p. 8.
7. *Report of the NITI Aayog*, "Government of India", (12th June 2018), (Dahlberg Development Advisors Pvt. Ltd: New Delhi), pp.17-19.
8. *Semi-Detail Ground Water Survey in Malda & West Dinajpur District*, Government of West Bengal, Rural Development Centre, Indian Institute of Technology, Kharagpur, 1976, pp. 1-2.
9. *Ananda Bazar Patrika*, (2011), Jaya Mitra, *Ei Sujala Sufala Desher Emon Abostha Halo Ki Kore*, *Report of the NITI Aayog*, "Government of India", New Delhi, 12th June 2018, pp.17-19.
10. This source has been collected by me from the Department of Irrigation, Purulia District in West Bengal. India. Submitted to the Director, Dam Safety Organization, Director of Irrigation & Water, Jalasampad Bhawan, Salt Lake City, 13.03. 08, Memo No. 476/S-140, (Third Minor Irrigation Census (2000-2001) in West Bengal Water Investigation and Development Department, GOWB, December 2003, pp.171-77
11. Chowdhur, M., *Sanskriti Purulia*, (2012,),Raghnath Publishers, Ketaki, Purulia, West Bengal,p.71.
12. Biswas.A., '*Puruliar Jela Sankhya*', Information of Cultural Affairs, (, March 22, 2007) , Government of West Bengal, India, pp.63-65 .
13. Ray.S., *Puruliar Jela Sankhya*, Information of Cultural Affairs, (2008), Government of West Bengal, India, February 17, pp. 67-74.
14. Devi.M. *Puruliar Jol-Chitror Manushjhon*, (2003) (in Bengali) in the edited book, *Banglar Nadi Nadi O Jalashoy*, Pronab Saekar, Sarkar, p. Lok Patrika, Kolkata , p.76.
15. R.Kalyan, *Paschim Banger Jalasampad Samkater Utsasandhane*, (2015), Ppublisher - Sahitya Samsad, Kolkata, p.19.
16. Basu.K.*Jol Sankot*, (in Bengali), 'Bartaman Patrika', July7 , 2019
17. Water Resource Development Directorate,(2010-11) , "Government of West Bengal", p.21.
18. Hand Book of Fisheries Statistics, (2000) , Government of West Bengal, India, p.26.
19. Sarkar.K.*Banglar Dighi o Jolashoy*, 2004, (in Bengali),(Lokpatrika, Sonarpur, Kolkata) , pp. 393-396.
20. *Bureau of Applied Economics & Statistics*, (1999 – 2000), District Statistic Hand book, Purulia, "Government of West Bengal", "India", p.49.

21. Bureau of Applied Economics & Statistics, (1995 – 1996), District Statistic Hand book, Purulia, West Bengal, India, p.50.
22. Chakrabartty.S.K, *A History of Receding Wetlands (1947-2000): Ecology, Society and Environment*, Unpublished Thesis, The University of Burdwan, 2021, Burdwan, West Bengal, India, p. 45
23. Ben, R. *Workers on the Move: Seasonal Migration and Changing Social Relations in Rural India*, 1998, Gender and Development, Vol. 6, No. 1, (Mar.), p. 22.
24. Ibid.p. 24
25. West Bengal District Gazetteers of :Purulia,(1972), p.164.
26. R . Ben, (ed.) *Seasonal Migration, Social Change and Migrants' Rights: Lessons from West Bengal*, Economic and Political Weekly, Vol. 36, No. 49 (Dec. 8-14), pp.4551.



ISSN 2347-7180

Published by Dr. Angshuman Das, Secretary,
Dogu Rangsang Research Society, Guwahati &
Printed at Dream Graphics, Naokata, Tamulpur (BTR), Assam



Cover Designed at Dream Graphics by Kamal K Sarmah

Role of Youth in India's National Integration

Jayanta Pandey

Assistant Professor, Department of History
Achhruram Memorial College, Jhalda

Abstract: It is apodictic to assert that there is a close connection between youth and national integration. India is a land of unity in diversity. The future of this country lies in the hands of the young generation. They are considered to be the voice of the nation. They can make a huge difference. Youths can be involved actively in bringing up several changes - development, prosperity, and respect for our nation. This article first touches on India's vulnerability as a nation at the time of independence. It tries to identify various internal challenges relevant to India's national unity. Furthermore, it discusses elaborately how can our youth contribute through different ways to the national integration of India and concludes with a note that they would eradicate all internal threats and make our country stronger than ever before.

Keywords: Youth, National Integration, Communalism, Terrorism, Demographic dividend, Nation building.

Introduction:

On 15 August 1947, a hard earned, prized independence was won by the people of India after long, glorious years of struggle against the Britishers. India's freedom represents for its people the beginning of a long march to overcome the colonial legacy of economic underdevelopment, gross poverty, near total illiteracy, the wide prevalence of diseases, stark social inequality, and lack of political unity. Since the beginning, many critics have expressed doubts about India's ability to sustain its national integration and continue to progress as a nation. There have been vocal prophets of doom and gloom who predicted that neither freedom nor democracy would survive in India for long, that the Indian political system would collapse sooner or later, that the Indian Union would not survive and the nation-state would disintegrate into linguistic and ethnic fragments. They have repeatedly argued that India's numerous religious, caste, linguistic, and tribal

Conclusion:

Historian Ramchandra Guha said, "The forces that divide India are many...But there are also forces that have kept India together, that have helped transcend or contain the cleavages of class and culture, that - so far, at least - have nullified those many predictions that India would not stay united and not stay democratic."⁸ At the same time, we shouldn't take independence for granted. As mentioned earlier, India is enjoying a demographic dividend. India can reap the economic benefits of it as well as strengthen national unity by mobilising its huge young population. The role of the Youth is very important in nation building. They can easily influence society and can also solve problems by introducing innovative and impactful ideas that will only help in the betterment of the country. They have the ability to create an identity for themselves, which will help in creating an impact. All the youth need is the support of their family and friends, and they can make our country great. So our youth can play a vital role in promoting national integration.

References:

1. Chandra, Bipan, and others, India Since Independence, Penguin Books, New Delhi, 1999, p. 5.
2. Harrison, S. S., India-The Most Dangerous Decades, Princeton University Press, Princeton, 1960, p.338.
3. Upadhyay, S. P. and R. Robinson, Revisiting Communalism and Fundamentalism in India, EPW, Vol. 47, No. 36, Sep. 2012, pp. 40-41.
4. Deaton, Angus, and Jean Dreze, Poverty and Inequality in India: A Re-Examination, EPW, Vol. 37, No. 36, 2002, pp. 3729-48.
5. Bose, Nirmal, National Integration, The Indian Journal of Political Science, Vol. 52, No. 1, 1991, p. 2.
6. Mukherjee, Rohan, and David M. Malone, Indian Foreign Policy and Contemporary Security Challenges, International Affairs, Vol. 87, No. 1, 2011, p. 99.
7. Sharma, M. D., Paramilitary Forces of India, Kalpaz Publication, New Delhi, 2008, p. 305.
8. Guha, Ramchandra, India After Gandhi, Picador India, New Delhi, 2007, p. xxix.